


Enrichment study of hot intra-cluster gas through X-ray spectroscopy

Jelle de Plaa

Cover image: Chandra X-ray observatory image of the Centaurus cluster of galaxies (Image courtesy: NASA/IOA/J.Sanders & A.Fabian). The plume visible in the image is 70.000 light years wide, it weighs about 1 billion times the mass of our sun, it has a temperature of 10 million degrees Celcius, and it lies at a distance of 170 million light years from Earth.

Afbeelding omslag: Chandra waarneming van het Centaurus cluster van melkwegstelsels in röntgenstraling (Bron: NASA/IOA/J.Sanders & A.Fabian). De pluim op de foto is 70.000 lichtjaar lang, weegt een miljard keer meer dan onze zon, heeft een temperatuur van 10 miljoen graden Celcius en ligt op een afstand van 170 miljoen lichtjaar van de aarde.

Cover design / Ontwerp omslag:  snowcone|design

© 2007 Jelle de Plaa
Alle rechten voorbehouden.

ISBN-10: 90-393-4439-6
ISBN-13: 978-90-393-4439-2

Enrichment study of hot intra-cluster gas through X-ray spectroscopy

Verrijkingstudie van het hete intraclustergas met behulp van
röntgenspectroscopie
(met een samenvatting in het Nederlands)

Proefschrift

ter verkrijging van de graad van doctor aan
de Universiteit Utrecht op gezag van de
rector magnificus, prof. dr. W.H. Gispen, ingevolge het
besluit van het college voor promoties in het openbaar te
verdedigen op
maandag 12 februari 2007 des middags te 2.30 uur

door
Jelle de Plaa
geboren op 1 december 1979, te Vlissingen

promotor: : Prof. Dr. Ir. J.A.M. Bleeker

co-promotor: : Dr. J.S. Kaastra

Contents

1	Introduction	1
1.1	The enrichment history of clusters of galaxies	3
1.1.1	Population-III stars	3
1.1.2	The second generation of stars	4
1.1.3	Recent enrichment	5
1.1.4	Producing type Ia supernovae in the early universe	6
1.2	Enrichment studies with XMM-Newton	6
2	X-ray spectroscopy on Abell 478 with XMM-Newton	9
2.1	Introduction	10
2.2	Observations and data analysis	10
2.2.1	EPIC	11
2.2.2	RGS	12
2.2.3	Spectral models	14
2.3	Results	15
2.3.1	EPIC	15
2.3.2	RGS	17
2.4	Discussion	18
2.5	Conclusions	22
3	The temperature structure in the core of Sérsic 159-03	23
3.1	Introduction	24
3.2	Spectral models	24
3.3	Results	27
3.4	Conclusion	29

4	Chemical evolution in Sérsic 159-03 observed with XMM-Newton	31
4.1	Introduction	32
4.2	Observations and data analysis	33
4.2.1	EPIC Analysis	33
4.2.2	RGS analysis	39
4.3	Spectral Models	40
4.3.1	WDEM	41
4.3.2	GDEM	41
4.4	Results	42
4.4.1	EPIC/RGS spectral fitting	42
4.4.2	Abundances and SNIa/SNII/Population-III models	52
4.4.3	Non-thermal X-ray emission?	56
4.5	Discussion	60
4.5.1	Temperature structure	60
4.5.2	Abundance distribution and enrichment by supernova types Ia/II and Population-III stars	60
4.5.3	Soft excess and non-thermal X-ray emission	62
4.6	Conclusions	63
5	XMM-Newton Spectroscopy of the Cluster of Galaxies 2A 0335+096	65
5.1	Introduction	66
5.2	Observations and data reduction	67
5.2.1	EPIC analysis	67
5.2.2	RGS analysis	70
5.3	Spectral models	70
5.4	Global spectrum	73
5.4.1	EPIC	73
5.4.2	RGS	75
5.5	Radial profiles	77
5.5.1	Projected spectra	77
5.5.2	Deprojected spectra	80
5.5.3	RGS radial profiles	81
5.6	Temperature and iron abundance maps	82
5.7	Properties of the core on smaller scales	86
5.8	Abundances and enrichment by supernova types Ia, II, and Pop-III stars	88
5.9	Discussion	92
5.9.1	Intrinsic temperature structure	92
5.9.2	Abundance distribution	94
5.9.3	Possible merger scenario	94
5.9.4	Relative enrichment by supernova types Ia/II and Population III stars	95
5.10	Conclusions	97

6	Constraining supernova models using the hot gas in clusters of galaxies	99
6.1	Introduction	100
6.2	The sample and methodology	101
6.2.1	Sample selection	101
6.2.2	Methodology	103
6.3	Results	104
6.3.1	Basic properties of the sample	104
6.3.2	Abundance determination	105
6.4	Discussion	111
6.4.1	Solar abundances	112
6.4.2	Supernova type Ia models by Iwamoto et al.	113
6.4.3	Supernova type Ia models based on Tycho	113
6.4.4	Core-collapse models	115
6.4.5	The fraction of low mass stars that become Type Ia SNe	119
6.5	Conclusions	120
7	Summary & Outlook	123
7.1	Outlook	124
7.1.1	Transition-Edge Sensors	125
7.1.2	Future X-ray missions using TES detectors	126
8	Nederlandse Samenvatting	131
8.1	Clusters van melkwegstelsels	131
8.1.1	Heet gas	132
8.1.2	Koele kern	133
8.2	De oorsprong van elementen	134
8.2.1	Type Ia supernovae	135
8.2.2	Chemische handtekening	135
8.3	De chemische historie van clusters	137
8.4	De vooruitgang met XMM-Newton en Chandra	138
8.5	Nieuwe ontdekkingen	139
	References	143
	Curriculum Vitae	149
	Nawoord	151

Chapter 1

Introduction

Most of the volume of the current-day universe is considered to be cold and empty, but most of the baryonic mass is actually hot and concentrated in a structure called the cosmic web. This structure of filaments and junctions consists of a huge amount of galaxies and gas. Since gravitation started to become the dominating force in the universe shortly after the big bang, the matter collapsed into sheets due to its own gravity. Meanwhile, the large mass concentrations formed on the intersections of the sheets which are known as clusters of galaxies.

Clusters are the biggest gravitationally bound objects that we know. Many of these cosmic intersections contain hundreds of galaxies in a volume which is not much larger than a few tens of cubic megaparsecs. The stars in the galaxies dominate the emission of the cluster in the visual wave band. However, only a small fraction of the baryonic mass in a cluster is in the form of stars.

For that reason most of the baryonic mass in clusters remained hidden to the human eye for a long time. It took until the sixties of the twentieth century to uncover a part of this hidden mass in the universe. X-ray detectors aboard balloons and rockets performed measurements that showed extended diffuse X-ray emission in the direction of extra-galactic sources. The first objects of this kind were found at the position of Coma, Perseus and M87 in the Virgo cluster (Byram et al. 1966; Bradt et al. 1967; Kellogg et al. 1971). After these discoveries Cavaliere et al. (1971) suggested that these X-ray sources are indeed connected to the cluster environment.

Because balloons and rockets do not allow long observations on particular objects, the real breakthrough came with the launch of the Uhuru X-ray satellite. The first catalogues compiled from the data (Giacconi et al. 1972) strongly suggested that some of the sources co-incided with rich clusters of galaxies (Kellogg 1973). The low-resolution spectra of the clusters showed that the X-ray emission originates from hot thermal plasma with a temperature of about 10^7 Kelvin. For the first time astronomers saw that large over-dense regions in the universe are hot.



Figure 1.1: *Artist impression of XMM-Newton in orbit above Africa. Image courtesy of ESA.*

In his paper, Edwin Kellogg anticipated a great future for the study of this hot gas: “It is to be expected that further study of the powerful extended X-ray sources in clusters of galaxies will tell us much about the evolution of clusters and perhaps about cosmological phenomena. If the X-ray emission from these clusters is due to hot gas, we may be seeing the active galaxies in Virgo and Perseus heating up the gas contemporaneously, whereas in Coma we see the thermalized remnant of a heating process which ended more than 10^9 years ago.” Kellogg’s thoughts about the physics of the hot gas turned out to be remarkably correct, the main issues that he pointed out are still subject of investigation.

After Uhuru, data from the X-ray satellite missions Einstein, Exosat, Ginga, Rosat and ASCA continued the study of clusters of galaxies with great success. As new sensor and mirror technologies became available, every new mission was a step forward in terms of either effective area, spatial or spectral resolution. A major improvement in spectral resolution came with the Japanese ASCA satellite which was launched on February 20, 1993. For the first time it was possible to measure the abundances of elements other than iron and silicon (e.g. Fukazawa et al. 1994).

The ability of measuring abundances in clusters raised questions about how the clusters have been enriched during their evolution. In principle, the hot gas contains a

major fraction of the metals that have been ejected by supernovae since the first stars formed. In this thesis, I derive abundances in clusters from data obtained with the European XMM-Newton X-ray observatory (Jansen et al. 2001). XMM-Newton, shown in Fig. 1.1, was launched in 1999 and is currently the best suited observatory to study chemical enrichment in clusters, because of its large effective area and spectral resolution. I use both the European Photon-Imaging Cameras (EPIC, Turner et al. 2001) and Reflection Grating Spectrometer (RGS, den Herder et al. 2001) aboard XMM-Newton to obtain accurate abundances of clusters and try to sharpen our view on the chemical history of the hot X-ray gas in clusters.

Another major X-ray observatory, which is also in orbit since 1999, is a US X-ray telescope facility named Chandra. This observatory is also well suited for observing clusters, however, it is optimised for a different purpose. Its high spatial resolution allows us to resolve shocks and giant bubbles in images of cluster cores (for example, Fabian et al. 2006). But the effective area of Chandra is about a factor of ten less than the total effective area of XMM-Newton. Although Chandra is therefore less well suited to do high-resolution spectroscopy and enrichment studies of extended sources, it is a great instrument to study mergers of clusters and the interaction between active galactic nuclei and the hot gas.

1.1 The enrichment history of clusters of galaxies

Our current views on the chemical enrichment of the universe are, of course, based on observations in multiple wavelengths and on many theoretical considerations. In this general view, hydrogen and helium dominated the baryonic mass in the universe shortly after the 'Big Bang'. Apart from these elements, there were only small traces of lithium and beryllium present. It took until the formation of the first stars before heavier elements were produced. The continuous enrichment with metals that followed by various populations of stars, resulted in a mass fraction of heavy elements of about 2% (solar) at the current epoch. This relatively small level of enrichment that occurred over billions of years is already sufficient to accommodate the formation of low-mass stars, planets, and eventually life.

1.1.1 Population-III stars

The first stars that enriched the universe are thought to have formed about 100-200 million years after the 'Big Bang' (e.g. Couchman & Rees 1986; Tegmark et al. 1997). Gas clouds that reached $10^{5-6} M_{\odot}$ were for the first time able to collapse into stars. The zero-metallicity gas in the cloud cannot cool efficiently due to the scarcity of line emission. Therefore, the gas clouds need to gain a lot of mass before the onset of gravitational collapse. The first stars that formed were probably much more massive than the typical stars that form out of metal-rich gas. These massive stars of about 50–200 M_{\odot} , also known as Population-III stars, may be able to enrich the gas in the early universe up to 10^{-3} times the solar value (Bromm et al. 2001).

The strongest indication for the existence of Population-III stars can be found in the Lyman-alpha forest. In the blue wing of the Ly α emission line from very distant quasars, many absorption lines can be observed. They are associated with density fluctuations in the inter-galactic medium at high redshift. High-resolution spectra of this Ly α forest have revealed that the metallicity of the gas in the IGM is around 10^{-3} solar, even at redshifts $z > 3$ (Cowie et al. 1995). The metallicity of the Ly- α forest is consistent with the values that are expected for Population-III stars. However, in principle, these metals could also have been mixed into the IGM by galactic winds from the first galaxies. Observations show that even the low column-density filaments show the presence of carbon absorption lines (Ellison et al. 2000). This suggests that the gas was enriched by a first generation of stars at redshifts $z > 6$.

Once the Population-III stars had enriched the gas in the high density regions of the universe, line cooling became much more efficient and gas clouds could collapse more easily (Bromm & Larson 2004). Because of the changes in metallicity, the Initial-Mass Function (IMF) presumably also changed. The presence of metals allowed low-mass stars to form and that triggered the first starbursts of the types of stars that we know today.

1.1.2 The second generation of stars

The second generation of stars dominate the elliptical galaxies in clusters at present day. Already a few million years after these stars formed, the most massive stars exploded as core-collapse supernova. These first starbursts were therefore rapidly causing massive enrichment through galactic winds driven by the ongoing supernova explosions.

About 30 million years after the starburst, the first white dwarfs formed. If these white dwarfs form in a binary, they can in some cases form a type Ia supernova. Because iron is mostly a product of supernova type Ia, the iron abundance should increase as soon as the binaries have evolved. At $z=3$, just about 2 Gyr after the 'Big Bang', the average abundance of the universe is thought to be 0.1 solar already (Renzini 2004). However, if the iron abundance is indeed 0.1 solar at that point in time, then the delay time between the starburst and the first type Ia supernovae should be relatively short in order to produce enough iron. In Section 1.1.4, I address this problem in more detail.

Unfortunately, we do not have a complete view of the metal abundances at $z=3$ from an observational point of view. The magnitude of enrichment appears to be very dependent on the scales of the objects (Pettini 2004; Renzini 2004). Our current knowledge about metallicities at $z=3$ is summarised in Fig. 1.2. Small objects, like quasars (QSOs) can already have solar or even super-solar metallicity. Galaxies, like young spheroids and Lyman-Break Galaxies (LBGs), also possess a considerable amount of enrichment. However, on large scales the metallicity does not reach 0.1 solar. Damped Lyman- α systems, detected in the Ly α forest, and the Ly α forest itself, have metallicities below 0.1 solar.

Since clusters of galaxies are thought to be built up out of galaxies and groups, we can see from the abundance of the young spheroids that the bulk of the metals in

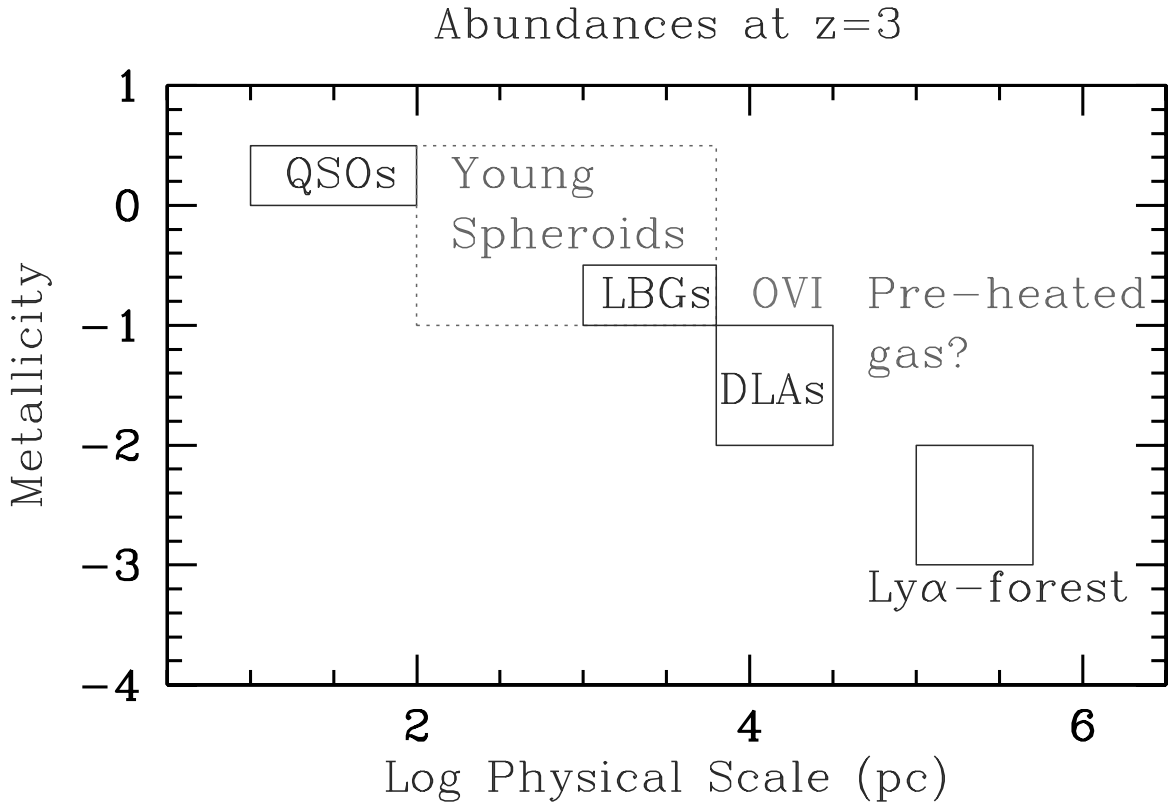


Figure 1.2: Abundances at $z=3$ according to our current knowledge and observations, adapted from Renzini (2004) and Pettini (2004). The vertical axis shows the log of the abundance with respect to solar. The plot shows the metallicity of Quasi-Stellar Objects (QSOs), Young Spheroids, Lyman-Break Galaxies (LBGs), Damped Lyman- α absorbers, and the Lyman- α forest.

clusters was already there at $z=3$. This means that the enrichment of the Intra-Cluster Medium (ICM) that started to form around that period of time was in an advanced stage. As the ICM increased in mass and temperature due to accretion (Cen & Ostriker 1999), it started to suppress star formation in the member galaxies. This effect probably starts playing a role at $z \lesssim 1.5$. Around that time we also start seeing the the first X-rays from the hot ICM. Presently, the most distant cluster detected in X-rays is at $z=1.45$ (Stanford et al. 2006).

1.1.3 Recent enrichment

In the last 10 Gyr, from $z=1.5-0$, the ICM was enriched by winds induced by supernova type Ia and ram-pressure stripping. The supernovae type Ia in elliptical galaxies keep exploding at a relatively low rate of $10^{-13}-10^{-14}$ supernovae per year per M_{\odot} , even 10 Gyrs after the starburst (Portinari et al. 2004). If the starburst indeed occurred early in the universe ($z \geq 3$), the expected current supernova type Ia rates in clusters are consistent with the supernova rate observed (Maoz & Gal-Yam 2004). In cooling-core

clusters, the explosions occur mainly in the giant elliptical galaxy in the centre. Because mixing in the ICM is relatively inefficient, this would lead to a peaked abundance profile of type Ia products.

Ram-pressure stripping of in-falling galaxies also causes a peaked metallicity profile in clusters, but for both type Ia and core-collapse products. When a spiral galaxy falls into a cluster, it will lose all of its gas, because the inter-stellar medium of the galaxy collides with the hot gas. The pressure exerted on the gas of the galaxy (P_{ram}) is proportional to the density of the ICM (ρ_{ICM}) and the in-fall velocity v (Gunn & Gott 1972):

$$P_{\text{ram}} \approx \rho_{\text{ICM}} v^2. \quad (1.1)$$

Since the density profiles of cool-core clusters peak in the centre, the ram-pressure is also most efficient there. According to recent simulations (Domainko et al. 2006; Schindler et al. 2005) ram-pressure stripping could have caused a metallicity increase in the cluster of about 10% since $z=1$.

1.1.4 Producing type Ia supernovae in the early universe

Our current idea about the progenitors of supernova type Ia is that they are produced from intermediate-mass binaries. When one of the stars of the binary evolves into a white dwarf and starts to accrete matter from its companion, the white dwarf is pushed over the Chandrasekhar limit at some point, and explodes. Thus, a type Ia supernova generally occurs long after the formation of the stars, because it has to wait for the stellar and binary evolution to complete. It is therefore surprising that we already see a high Fe/Mg ratio in quasars at $z > 3$, only about 2 Gyr after the ‘Big Bang’ (e.g. Kawara et al. 1996; Taniguchi et al. 1997).

Several solutions to this problem have been put forward. Mannucci et al. (2006) suggest that there are two channels for the formation of type Ia’s: one with a very short delay time (10^8 yr) and one with a long delay time (2–4 Gyr). The origin of the differences in delay time may be in the IMF at high redshift. A top-heavy IMF could, in principle, preferably create more massive intermediate-mass binaries that have shorter delay times (Loewenstein 2006). In his scenario, he suggests that also a large part of the iron could come from heavy core-collapse supernovae.

The high Fe/Mg ratio in quasars may also be solved using Population-III stars. If these stars had masses around $130 M_{\odot}$, then the Fe/Mg ratio that they produce closely resembles that of a type Ia supernova (Heger & Woosley 2002). In this scenario, the products of the Population-III star should remain in the over-dense region where the star formed. Probably, quasars later also form in these over-dense regions and find themselves embedded in Population-III enriched material with SNIa-like metallicity.

1.2 Enrichment studies with XMM-Newton

The XMM-Newton observatory has three main advantages over other X-ray observatories, namely large effective area, high-spectral resolution, and the capability to do

spatially-resolved spectroscopy. Especially, the latter advantage allows us to derive radial abundance profiles with the best accuracy ever. Because RGS also has spatial resolution in one dimension, the consistency of the results from EPIC and RGS can be checked and cross-correlated independently. These properties make XMM-Newton very suitable for enrichment studies of clusters of galaxies.

In principle, XMM-Newton can determine the abundances of nine elements in the 0.3–10 keV band: oxygen, neon, magnesium, silicon, sulfur, argon, calcium, iron, and nickel. However, not all of the lines emitted by these elements can be independently measured. Line-blending effects, calibration uncertainties and background uncertainties can cause substantial systematic offsets in the measured abundances. It is therefore absolutely essential to carefully model these effects and take them into account in the results. One of the most important advances in this thesis is a substantial improvement in the data-analysis methodology by a robust and careful modelling process of all background components.

Once the abundances and systematic uncertainties are obtained, they can be compared to the yields of supernovae. When there are enough accurately determined abundances, the number ratio of type Ia supernovae over core-collapse supernovae can be derived. The accuracy of the determination will also increase when a larger range of abundances is known. At the same time, abundances provide constraints on supernova models, and perhaps the metallicity and Initial-Mass Function (IMF) with which the progenitors of the supernovae formed.

When radial profiles of clusters are derived from the EPIC data, then the uncertainties of the background spectrum are the main limiting factor. Due to the high eccentric orbit of XMM-Newton, the background level is relatively high. So-called soft protons and other particles originating from the solar wind and cosmic rays induce events in the cameras that act as an additional time-variable background. Moreover, the galactic X-ray background also varies spatially across the sky. Therefore, subtracting an average background will not be sufficient to obtain credible values for the cluster outskirts. More work is needed to take into account the correct background spectrum.

From the radial profiles of certain elements, the spatial distribution of core-collapse and type Ia supernovae can be derived. Core-collapse products, like oxygen, are expected to have a more extended profile, because most of the core-collapse supernovae are thought to have exploded directly after the initial starburst. Therefore, the elements had a lot of time to mix into the ICM. Type Ia supernovae explode more gradually over time and are thought to be more peaked in the centre, where most of the stars reside.

We have seen in Sect. 1.1.1 that Population-III stars are expected to raise the metallicity of the gas about 10^{-3} times solar (Bromm et al. 2001). With XMM-Newton, one can get the statistical error on a typical abundance value down to about 10^{-2} times solar, although without accounting for systematic uncertainties or intrinsic scatter. In principle, we therefore do not expect to detect a Population-III star contribution, but indirect evidence for their existence might possibly be found.

X-ray spectroscopy on Abell 478 with XMM-Newton

J. de Plaa^{1,2}, J. S. Kaastra¹, T. Tamura^{1,3}, E. Pointecouteau⁴, M. Mendez¹, and J. R. Peterson⁵

¹ SRON National Institute for Space Research, Utrecht, The Netherlands

² Astronomical Institute, Utrecht University, Utrecht, The Netherlands

³ Institute of Space and Astronautical Science, JAXA, Kanagawa, Japan

⁴ CEA/DSM/DAPNIA Saclay, Service d'Astrophysique, Gif-sur-Yvette, France

⁵ KIPAC, Stanford University, Stanford, USA

Received 2 February 2004 / Accepted 7 May 2004

Published in *Astronomy & Astrophysics*, volume 423, pages 49–56, 2004

Abstract

We report the results from a spatially resolved spectroscopy study with XMM-Newton on the relaxed cluster of galaxies Abell 478. From the EPIC data we extract a temperature profile and radial abundance profiles for Ne, Mg, Si, S, Ca, Fe and Ni. The abundance profiles follow the same trends as observed in other clusters. The spectra of the core of the cluster can be best fitted with a multi-temperature model. We argue that this multi-temperature behavior is mostly due to projection effects, because of the strong temperature gradient in the core. Contributions from other effects, for example, intrinsic temperature stratification cannot be fully excluded. For the first time we measure an underabundance of oxygen in the Galactic absorption component toward a cluster. The measured oxygen abundance in this absorber is about 0.5 times the solar oxygen abundance as determined by Anders & Grevesse (1989).

2.1 Introduction

The evolution and hydrodynamical structure of the hot diffuse X-ray emitting gas in clusters of galaxies is still not well understood. Several clusters show excess X-ray emission in their cores. The so-called cooling flow models (for a review see Fabian 1994) propose radiative cooling of gas in the core to explain the observed surface brightness and temperature profiles. The pressure decrease in the core due to the cooling gas causes a net inflow toward the center of the cluster, hence the name cooling flow. XMM-Newton observations show that the amount of cool gas in the core of cooling-flow clusters is much lower than predicted (Peterson et al. 2001; Kaastra et al. 2001; Tamura et al. 2001b; Peterson et al. 2003; Kaastra et al. 2004). Therefore, the standard cooling-flow model needs to be adjusted. Several mechanisms to explain the observations have been proposed (see Peterson et al. 2001, for a list of possible explanations).

The Abell 478 cluster of galaxies is a good example of a highly relaxed cluster. Earlier X-ray observations with EXOSAT (Edge & Stewart 1991), Ginga and Einstein (Johnstone et al. 1992), ROSAT (Allen et al. 1993; White et al. 1994), ASCA (Markevitch et al. 1998; White 2000) and Chandra (Sun et al. 2003) show a significant excess of X-ray emission in the core, suggesting the presence of a massive cooling flow. The observations performed by missions with sufficient spatial resolution (e.g. ROSAT, ASCA and Chandra) are consistent with a radial temperature decrease toward the core. In a recent Chandra observation an X-ray cavity was discovered in the core which seems to be associated with a lobed radio source (Sun et al. 2003).

In this paper we study the properties of Abell 478 using high-resolution and spatially-resolved spectra obtained with the European Photon Imaging Camera (EPIC, Turner et al. 2001) and the Reflection Grating Spectrometer (RGS, den Herder et al. 2001) aboard XMM-Newton (Jansen et al. 2001). We focus on the physics and metal abundances in the core of Abell 478. In an associated paper Pointecouteau et al. (2004) describe the large scale temperature, gas and dark matter distribution in this cluster using a pointed and an offset XMM-Newton EPIC observation.

Throughout this paper we use $H_0 = 50 \text{ km s}^{-1} \text{ Mpc}^{-1}$ and $q_0 = 0.5$. Using this cosmology $1'$ is 157 kpc at the cluster redshift of 0.0881.

2.2 Observations and data analysis

The observation of Abell 478 was performed as part of the Guaranteed Time program on February 15 2002 and had a total duration of 126 ks. Both EPIC MOS cameras were operated in Full Frame mode and the EPIC pn camera in Extended Full Frame mode. For all EPIC cameras the thin filter was used.

For the analysis we use the event lists produced by the XMM-Newton SOC and the 5.4.1 version of the XMM Science Analysis System (SAS). To correct for enhanced and variable background due to soft proton flares we use the events with energies larger than 10 keV from pn and CCD 9 of RGS. The data are filtered using upper and lower count-rate thresholds. The thresholds are calculated in a way analogous to the method

Table 2.1: *Maximum count rates and resulting useful exposure times after screening for solar flares.*

Detector	Max. count rate (counts s ⁻¹)	Useful exposure time (ks)
PN	0.53	51
MOS		51
RGS	0.36	119

used in Pratt & Arnaud (2002). We first make a histogram of the light curve above 10 keV with a binsize of 100 s and pattern equal to 0, which we fit it with a Poissonian function. The count rate thresholds are subsequently fixed to $N \pm 3\sqrt{N}$, where N is equal to the mean number of counts within a bin. Because the pn is most sensitive to solar flares, we merge the Good Time Intervals (GTI) derived from the pn data also with the preliminary GTI for MOS. Therefore pn and MOS have roughly the same exposure time. The maximum count rates and the resulting useful exposure times are shown in Table 2.1. This simple variable background procedure aims at obtaining maximum statistics in the core region, where the background is relatively less important, but excludes contributions from the large solar flares. Because the cluster signal in the 0–4′ region dominates over the background, it is not necessary to perform a double background subtraction nor a multi-band flare search like described in Pointecouteau et al. (2004). The countrate thresholds we chose are well within the advised threshold of <1.0 cts s⁻¹ (PN) provided by the XMM-Newton SOC (Kirsch 2003).

2.2.1 EPIC

Because the cluster is slightly elongated along the north-east to south-west axis, we extract the source and background spectra from elliptical annuli allowing patterns ≤ 12 for MOS and ≤ 4 for pn. We use a ratio of 1.2 between the major and minor axis of the ellipse, which we obtain from an empirical 2D β -model fit to the EPIC image. Although the data show some minor deviations from this 2D model, the value is in the range of 1.2–1.4 (ROSAT, White et al. 1994) and compatible with 1.22 derived by Pointecouteau et al. (2004) who uses the same method and data. Further on in this paper we characterize the extraction region by its semi major axis. We extract the EPIC background spectra from the blank sky event files provided by Read & Ponman (2003). Relatively bright point sources in the EPIC field of view have been excluded both from the Abell 478 and background datasets.

To gain statistics in each spatial bin we extract the spectra from annuli with a width of more than 30′′. This way, we are less sensitive to the energy dependent shape of the PSF and therefore we neglect this effect in the rest of the analysis. The downside of choosing large binsizes is that mixing of temperatures within the bin also increases with binsize if there are strong temperature gradients present. This effect may become important during multi-temperature fitting.

Table 2.2: Systematic errors included in the EPIC spectral fits. (Adapted from Kaastra et al. 2004)

Energy band	Error source	Error background
0.4–0.5	10%	35%
0.5–0.7	5%	25%
0.7–2.0	5%	15%
2.0–10.0	5%	10%

Although we neglect the influence of the energy dependent part of the PSF, a substantial broadening effect in the core remains. To correct the normalization of each annulus for PSF effects we calculate correction factors by fitting the surface brightness profile from the Advanced Camera Imaging System (ACIS) on board Chandra (Sun et al. 2003) with a double King profile. We normalize both the ACIS fit and the EPIC surface brightness profile and calculate the ratios between the two for each bin. These factors range from 0.73 in the core up to 1.03 at 4'. Then, we multiply the effective area of each annulus with this factor and obtain a PSF corrected response.

For the spectral analysis we use the SPEX package (Kaastra et al. 2003b) and fit the spectra over the 0.4–10 keV range. We include systematic errors due to uncertainties in the calibration and the background in the spectral fit. The applied systematic errors are shown in Table 2.2; they have been adapted from Kaastra et al. (2004). These systematic errors enclose possible variations of the Cosmic X-ray Background (CXB), background normalization and errors in the calibration.

After a preliminary analysis, the pn appears to have a gain problem, resulting in a significantly lower value for the redshift of the source than measured by the MOS instrument. From MOS we obtain a redshift of 0.0889 ± 0.0003 , which is consistent with the optical value of 0.0881 ± 0.0009 (Zabludoff et al. 1990). But, our fits of the pn spectra result in a redshift of 0.0775 ± 0.0002 . To correct for this, we measure the centroid energies of the aluminum, nickel, copper and zinc background lines. A linear fit ($E_{\text{new}} = aE_{\text{old}} + b$) through the measured and expected energies for these lines yields $a = 1.0066 \pm 0.0007$ and $b = (-1.04 \pm 0.24) \times 10^{-2}$. After correcting the energy values in the original eventfile according to this relation, we fit the resulting spectra again. The corrected spectra show large discrepancies at low energies. Therefore, we conclude that the observed gain problem is probably not linear, in line with the argumentation of Pointecouteau et al. (2004). Unfortunately, the number and distribution of background lines is insufficient to derive the exact shape of the gain correction. For the rest of the analysis we therefore use the original event file, fit MOS and pn separately and let the redshift free in the fit.

2.2.2 RGS

We extract the RGS spectra with SAS version 5.4.1 following the same method as described in Tamura et al. (2001a). We select the events from a rectangular area on the

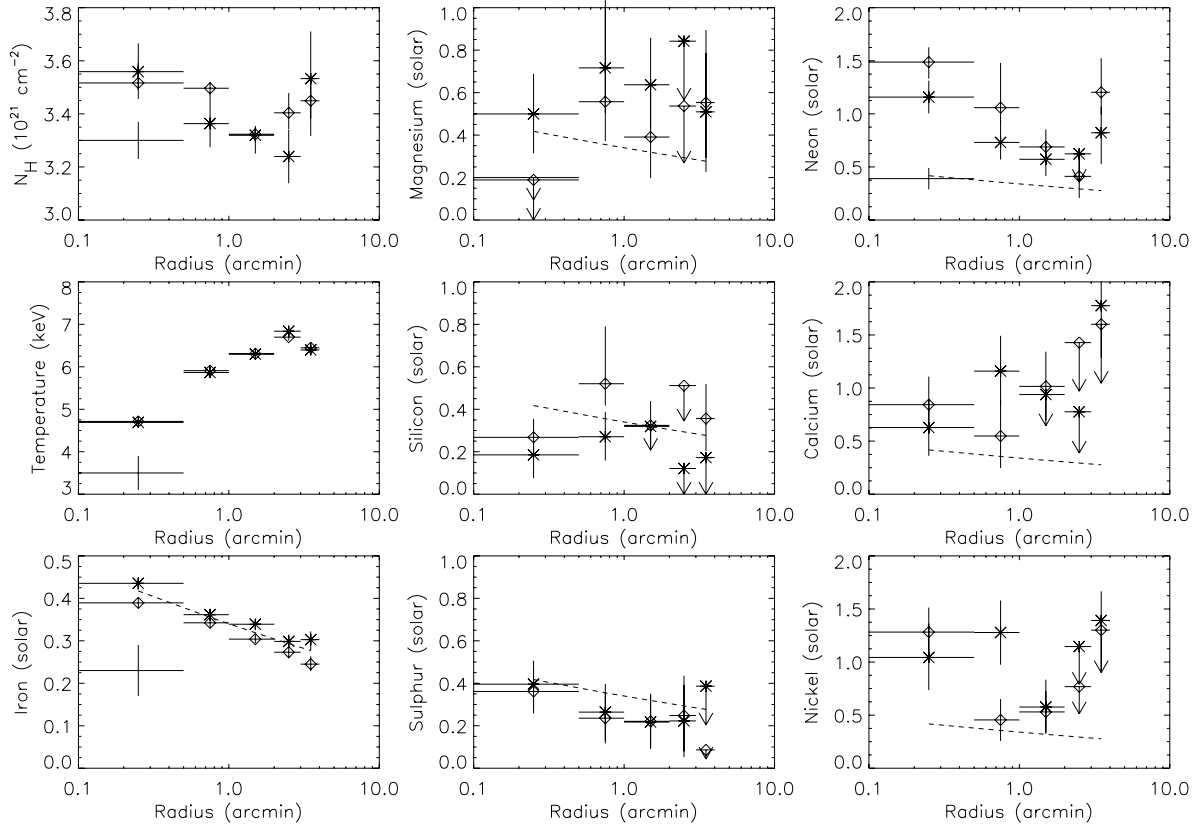


Figure 2.1: Single-temperature fit results. EPIC MOS (stars), pn (diamonds) and RGS (plus-sign) are shown. The dashed line shows an empirical powerlaw fit to the Fe abundance distribution for comparison.

CCD strip with a full width of $1'$ in the cross-dispersion direction and centered on the core of the source. We extract the background spectra from several blank field observations (Tamura & den Herder 2003). Because the observation was performed before the cooling of the RGS instruments, the spectra contain a relatively high number of bad columns due to warm pixels. These bad columns appear as absorption-like features in the spectra. Unfortunately, also CCD gaps are present in the wavelength ranges where line emission is expected. Together with the relatively high thermal Bremsstrahlung component due to the high temperature of the cluster, the lines are difficult to resolve. Therefore, we also include the second order spectrum in the fit to increase the statistics. All RGS spectra are fitted over the 8–35 Å range.

Because the RGS gratings operate without a slit, the resulting spectrum of an extended source is the sum of all spectra in the (in our case) $1' \times \sim 12'$ field of view, convolved with the PSF (see for a complete discussion about grating responses Davis 2001). Extended line-emission appears to be broadened depending on the spatial extent of the source along the dispersion direction. In order to describe the data properly, the spectral fits need to account for this effect. In practice, this is accomplished by convolving the spectral models with the surface brightness profile of the source along the dispersion direction (Tamura et al. 2004). For that purpose we extract the cluster inten-

Table 2.3: Averaged EPIC results for Abell 478 for the single temperature (1) and *wdem* (2) fits. Errors are given at the 1σ confidence level and the $<$ -sign denotes a 2σ upper limit. We leave the abundance of oxygen in the absorption component free to fit the oxygen edge near 0.5 keV. This parameter is called O_{abs} . The abundances are given relative to solar abundances measured by Anders & Grevesse (1989).

		EPIC				
		0–0.5'	0.5–1.0'	1.0–2.0'	2.0–3.0'	3.0–4.0'
$\chi^2/\text{d.o.f. (MOS)}$	1	318 / 327	286 / 327	290 / 327	288 / 327	281 / 303
	2	247 / 326	285 / 326	292 / 326	278 / 326	281 / 302
$\chi^2/\text{d.o.f. (pn)}$	1	216 / 179	204 / 179	228 / 179	211 / 179	166 / 158
	2	177 / 178	193 / 178	228 / 178	209 / 178	161 / 157
$N_{\text{H}} (10^{21} \text{ cm}^{-2})$	1	3.54 ± 0.06	3.40 ± 0.05	3.32 ± 0.03	3.34 ± 0.06	3.49 ± 0.11
	2	3.60 ± 0.04	3.44 ± 0.04	3.32 ± 0.04	3.34 ± 0.05	3.52 ± 0.05
O_{abs}	1	0.40 ± 0.02	0.44 ± 0.03	0.41 ± 0.02	0.39 ± 0.04	0.32 ± 0.05
	2	0.50 ± 0.02	0.45 ± 0.02	0.43 ± 0.03	0.38 ± 0.03	0.34 ± 0.06
kT (keV)	1	4.70 ± 0.03	5.88 ± 0.04	6.30 ± 0.04	6.76 ± 0.07	6.42 ± 0.07
kT_{max} (keV)	2	8.31 ± 0.08	7.7 ± 0.3	7.0 ± 0.4	8.8 ± 0.4	9.5 ± 0.5
$1/\alpha$	2	$1.12^{+0.12}_{-0.3}$	0.39 ± 0.15	0.12 ± 0.03	0.40 ± 0.11	0.8 ± 0.4
O	1	< 0.06	< 0.14	< 0.09	< 0.09	< 0.11
	2	< 0.07	< 0.06	< 0.09	< 0.06	< 0.05
Ne	1	1.32 ± 0.11	0.90 ± 0.12	0.63 ± 0.11	< 0.5	1.04 ± 0.17
	2	< 0.18	0.52 ± 0.11	0.60 ± 0.11	0.4 ± 0.2	0.43 ± 0.16
Mg	1	0.49 ± 0.19	0.63 ± 0.15	0.51 ± 0.15	< 0.5	0.53 ± 0.19
	2	< 0.08	0.46 ± 0.14	0.49 ± 0.15	< 0.4	0.31 ± 0.17
Si	1	0.23 ± 0.07	0.40 ± 0.08	0.20 ± 0.07	< 0.5	0.36 ± 0.16
	2	0.22 ± 0.06	0.35 ± 0.07	0.20 ± 0.07	< 0.4	0.32 ± 0.13
S	1	0.38 ± 0.08	0.25 ± 0.09	0.22 ± 0.09	0.24 ± 0.12	< 0.08
	2	0.41 ± 0.06	0.25 ± 0.09	0.22 ± 0.09	0.23 ± 0.11	< 0.09
Ar	1	< 0.4	< 0.2	< 0.2	< 0.15	< 0.6
	2	0.35 ± 0.15	< 0.2	< 0.2	< 0.16	< 0.6
Ca	1	0.73 ± 0.19	0.8 ± 0.2	0.7 ± 0.2	< 0.8	1.1 ± 0.4
	2	1.1 ± 0.2	1.0 ± 0.2	0.7 ± 0.2	< 0.9	1.2 ± 0.4
Fe	1	0.410 ± 0.010	0.351 ± 0.009	0.320 ± 0.008	0.285 ± 0.011	0.268 ± 0.014
	2	0.425 ± 0.010	0.367 ± 0.009	0.322 ± 0.008	0.294 ± 0.011	0.292 ± 0.014
Ni	1	1.2 ± 0.2	0.78 ± 0.19	0.55 ± 0.17	< 0.8	0.9 ± 0.3
	2	0.79 ± 0.19	0.7 ± 0.2	0.54 ± 0.17	< 0.8	0.7 ± 0.3

sity profile from MOS1 along the dispersion direction of RGS, which we convolve with the RGS response during spectral fitting. Because the radial profile of an ion can be different from the mean profile, this method is not ideal. We let the scale of the width and the position of the profile free in the fit to match the profiles of the main emission lines.

2.2.3 Spectral models

We fit the spectra both with a single temperature collisionally ionized plasma model (MEKAL) and a differential emission measure (DEM) model called *wdem*. In this particular model the emission measure (Y) is distributed as a function of temperature (T)

as shown in Eq. (2.1) adapted from Kaastra et al. (2004):

$$\frac{dY}{dT} = \begin{cases} cT^\alpha & T < T_{\max} \\ 0 & T > T_{\max} \end{cases} \quad (2.1)$$

This model is an empirical parametrization of the DEM distribution found in the core of many clusters. In this form the limit $\alpha \rightarrow \infty$ yields the isothermal model. For convenience we will use $1/\alpha$ in this paper, because then the isothermal model is obtained when $1/\alpha = 0$. The classical cooling-flow model corresponds to a dY/dT of $1/\Lambda(T)$, where $\Lambda(T)$ is the cooling function.

To investigate the role of projection effects, we fit the spectra of the core also with an extra temperature component of 6.5 keV. This way we emulate the spectral contribution of the outer parts of the cluster.

We notice from a preliminary analysis that the oxygen edge near 0.5 keV is not well fitted. Therefore, we use an absorption model component with variable element abundances and leave the oxygen abundance free. We call this particular oxygen abundance O_{abs} further on in the paper.

2.3 Results

2.3.1 EPIC

The results of the EPIC single-temperature fits are presented in Fig. 2.1 and Table 2.3. The upper left plot in Fig. 2.1 shows that the absorption is not a constant across the cluster. The temperature profile shows a steep decrease toward the core with a hint for a bend outside the 2.0' radius. The abundances of neon, sulfur and iron are consistent with an increase toward the center. However, neon and sulfur are also consistent with a flat distribution, like the other abundances. Because of low statistics we had to discard the 8–10 keV band in the 3–4' annulus.

Fig. 2.2 shows the residuals of the combined MOS spectra of the 0–0.5' region, fitted with a single temperature component for which the abundances have been set to zero afterward. In this way we show the lines that are detected in the EPIC spectrum. Except for neon, the abundance of all elements can be fitted independently. Since the main neon line is close to the Fe-L complex blend at ~ 1 keV, it is difficult to constrain the neon abundance with EPIC. Because the Fe-K line is the strongest line, this line mainly determines the iron abundance. The strength of the Fe-L complex is mostly dependent on the temperature structure.

In the core of the cluster the χ^2 value from the single-temperature fit is higher than can be expected from the high signal-to-noise in that area. We therefore also fit the core with the multi-temperature *wdem* component defined in Sect. 2.2.3. These results are also listed in Table 2.3. The *wdem* abundances are all consistent with the single temperature abundances, apart from neon, which is blended by Fe-L. From the χ^2 values the multi-temperature model appears to be preferable over the single-temperature model in the 0–0.5' region.

Table 2.4: Averaged results from the single-temperature (3) and *wdem* (4) fits with an extra 6.5 keV temperature component.

	Model	EPIC	
		0–0.5′	0.5–1.0′
$\chi^2/\text{d.o.f. (MOS)}$	3	244 / 326	284 / 326
	4	247 / 325	282 / 325
$\chi^2/\text{d.o.f. (pn)}$	3	178 / 178	192 / 178
	4	176 / 177	200 / 177
$N_{\text{H}} (10^{21} \text{ cm}^{-2})$	3	3.60 ± 0.03	3.45 ± 0.06
	4	3.58 ± 0.03	3.43 ± 0.06
O_{abs}	3	0.453 ± 0.016	0.41 ± 0.04
	4	0.488 ± 0.017	0.48 ± 0.03
kT (keV)	3	2.46 ± 0.04	4.14 ± 0.08
kT_{max} (keV)	4	3.04 ± 0.05	4.95 ± 0.17
$1/\alpha$	4	0.38 ± 0.07	1.0 ± 0.3
O	3	< 0.08	< 0.12
	4	< 0.08	< 0.05
Ne	3	0.83 ± 0.16	0.65 ± 0.14
	4	0.26 ± 0.12	0.20 ± 0.10
Mg	3	0.27 ± 0.07	0.50 ± 0.15
	4	< 0.09	0.43 ± 0.13
Si	3	0.23 ± 0.05	0.36 ± 0.08
	4	0.22 ± 0.05	0.33 ± 0.06
S	3	0.38 ± 0.06	0.27 ± 0.09
	4	0.39 ± 0.06	0.26 ± 0.08
Ar	3	0.31 ± 0.14	< 0.18
	4	0.34 ± 0.15	< 0.2
Ca	3	1.1 ± 0.2	1.0 ± 0.2
	4	1.09 ± 0.19	1.0 ± 0.2
Fe	3	0.436 ± 0.010	0.362 ± 0.009
	4	0.429 ± 0.010	0.363 ± 0.009
Ni	3	0.83 ± 0.18	0.7 ± 0.2
	4	0.77 ± 0.19	0.69 ± 0.19

Then, we add a single temperature component fixed at 6.5 keV to emulate the projection effect from the hot gas in front of the core. The value of 6.5 keV is roughly the mean temperature outside the 1′ radius. In Table 2.4 we show the results of this fit. The abundances are again consistent apart from neon. We notice that the fitted temperatures for the core are now significantly cooler than without the hot component. The value for $1/\alpha$ in the *wdem* component is 0.38 ± 0.07 , lower than the value we previously found, $1.12_{-0.3}^{+0.12}$.

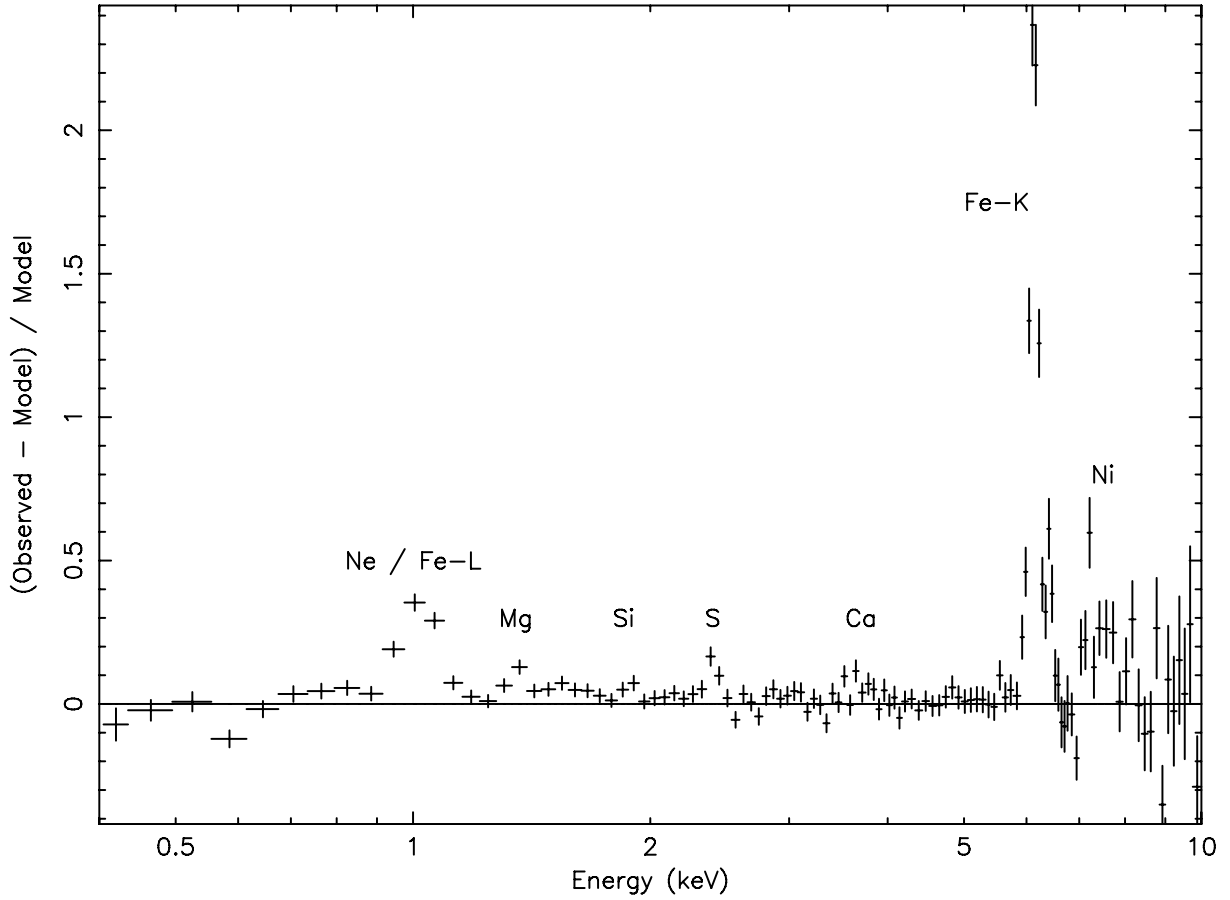


Figure 2.2: Residuals of the averaged MOS spectrum of the core of Abell 478 with the abundances put to zero.

2.3.2 RGS

We obtain a reasonable fit to the RGS spectra of the core (0–0.5′) with the single-temperature model. The $\chi^2 / \text{d.o.f.}$ is 887 / 754. Unfortunately, the O VIII line complex is partly within a CCD bad-column on RGS1 and falls in the dead area of RGS2, which makes the derived oxygen abundance more uncertain. The Fe-L complex and Ne line near 12 Å are detected and resolved.

Because the EPIC spectra from the core region are best fitted with a multi-temperature model, we also fit the RGS spectra with the *wdem* component. This results in a slightly better $\chi^2 / \text{d.o.f.}$ of 867 / 753. The results of this fit and the single-temperature model are shown in Table 2.5 and Fig. 2.3. Because the temperature determination with RGS depends mostly on the line emission, the weakness of the lines in this spectrum causes the temperature to be less well constrained. Furthermore, the energy range of the RGS is much smaller than EPIC and concentrated on the soft energy part of the spectrum, making it more sensitive to the cool component of the spectrum. Therefore, the fit is less sensitive to the multi-temperature distribution. Because of the increased freedom of the fit due to the use of multi-temperature components, the *wdem* fit is marginally better than the single-temperature fit. We have also attempted to fit the

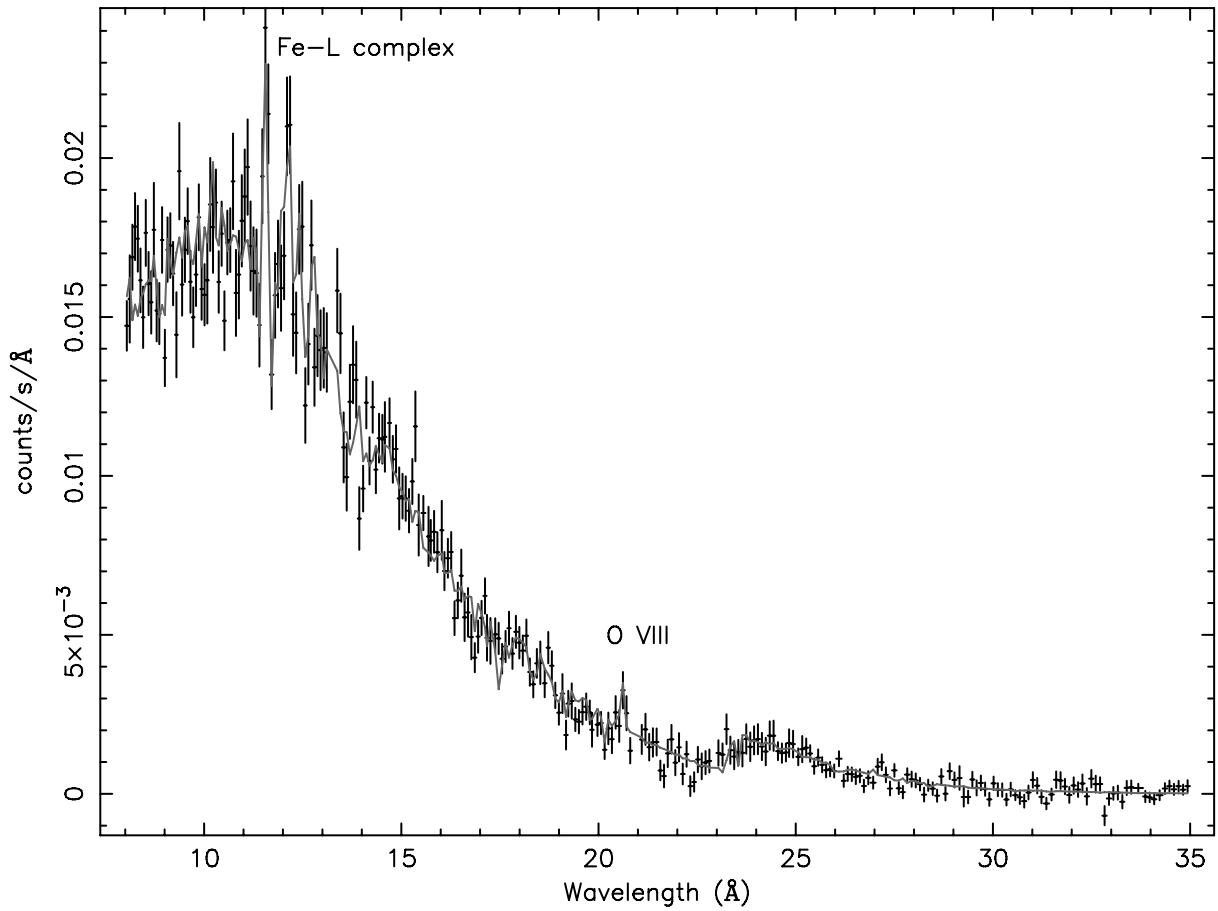


Figure 2.3: RGS averaged spectrum (0–0.5') of Abell 478. Only the first order spectrum is shown for clarity. Data points from bad columns were removed from the RGS1 and RGS2 spectra before they were averaged.

RGS spectrum with an extra hot component of 6.5 keV which we added to both a single-temperature and *wdem* model. Because the temperatures in this model could not be constrained, we have not pursued this model any further.

2.4 Discussion

We analyze the high-resolution spectra of the Abell 478 cluster of galaxies and we derive, for the first time, radial abundance profiles for several elements in this hot cluster. The exposure time of 126 ks allows us to resolve the main emission lines. By fitting these lines and the continuum emission we are able to put constraints on the temperature structure in the core and the abundance distribution of Ne, Mg, Si, S, Ca, Fe and Ni. Furthermore, by fitting the oxygen edge near 0.5 keV we measure an underabundance of oxygen in the absorption component.

The temperature profile obtained from the single-temperature fits (see Fig. 2.1 and

Table 2.5: Results from the RGS spectral fits of the core region ($0-0.5'$) of Abell 478. The RGS spectra were fitted using the *wdem* model component and a single-temperature model. Errors are given at the 1σ confidence level and the $<$ -sign denotes a 2σ upper limit. We left the abundance of oxygen in the absorption component free to fit the oxygen edge near 0.5 keV. This parameter is called O_{abs} .

	RGS wdem	RGS single-temperature	Unit
$\chi^2/\text{d.o.f}$	867 / 753	887 / 754	
N_{H}	3.15 ± 0.08	3.30 ± 0.07	10^{21} cm^{-2}
O_{abs}	0.67 ± 0.04	0.63 ± 0.04	Z_{\odot}
kT		3.5 ± 0.4	keV
kT_{max}	$11.1^{+1.2}_{-2.3}$		keV
$1/\alpha$	1.3 ± 0.3		
O	0.15 ± 0.07	0.09 ± 0.05	Z_{\odot}
Ne	0.46 ± 0.13	0.39 ± 0.10	Z_{\odot}
Mg	0.17 ± 0.12	< 0.2	Z_{\odot}
Fe	$0.61^{+0.10}_{-0.17}$	0.23 ± 0.06	Z_{\odot}

Table 2.3) of the core ($< 2'$) are consistent with the temperature profile measured with Chandra (Sun et al. 2003) and ROSAT (White et al. 1994; Allen et al. 1993). It confirms that Abell 478 has one of the steepest temperature gradients observed so far.

In the outer regions, outside $2'$ from the core, our pn temperature profile shows a hint of a bend which is consistent with the more extended temperature determination by Pointecouteau et al. (2004), but is inconsistent with Sun et al. (2003). The ACIS aboard Chandra, which has a lower sensitivity at high energies and a smaller field of view than pn, is therefore more vulnerable to systematic background effects in the temperature. The bend in the pn temperature profile is comparable with profiles observed in other clusters, for example the core of Sérsic 159-03 (Kaastra et al. 2001), and has been interpreted as the transition from the cooling core to the inter-cluster medium.

In the core region, within $0.5'$, a multi-temperature (*wdem*) model fits better than the single-temperature model. The value of $1/\alpha = 1.3 \pm 0.3$ from RGS is high compared to the cluster samples studied by e.g. Peterson et al. (2003) and Kaastra et al. (2004). These studies find values for $1/\alpha$ which are roughly of the order of 0.5. If we add an extra temperature component of 6.5 keV to account for the emission from the outer regions in front of the core, then the difference between the single-temperature and *wdem* component vanishes (see Table 2.4). This suggests that the projection effect of the hot cluster material along the line of sight strongly affects the $1/\alpha$ value in the fits.

The multi-temperature behavior is not necessarily explained by contamination from the outer parts of the cluster. Although the X-ray cavities reported by Sun et al. (2003) are not spatially resolved with XMM-Newton, the value of $1/\alpha$ and the cool area associated with the X-ray cavity may be related. Together with the high resolution study of the temperature profile (Pointecouteau et al. 2004), which reveals a steep temperature gradient in the core region, these effects could also partially account for the multi-

temperature behavior observed in the central bin. Unfortunately, the spatial resolution of XMM-Newton does not allow us to draw conclusions from these data on the complex structure in the core.

From the single-temperature fits we measure a central increase of the iron abundance from ~ 0.3 at about $4'$ to ~ 0.4 in the center which is consistent with the mean abundance profile of Abell 478 derived by White (2000) using ASCA. The central abundance is also consistent with earlier EXOSAT measurements by Edge & Stewart (1991). The significant central increase of Fe is similar to the profiles of other hot (> 6 keV) clusters (Tamura et al. 2004). Also neon and sulfur seem to follow the same trend in our results. However, due to the large error bars these profiles could still be consistent with a flat distribution. The central increase of sulfur was also found in the cluster sample of Tamura et al. (2004). Neon is not resolved in EPIC, because of the lower spectral resolution and blending with lines from the iron L complex. Therefore, the systematic uncertainty on the abundance of neon is quite large. Moreover, the single-temperature model tries to fit the Fe-L complex by enhancing the Ne abundance, while the reason for the Fe-L to be enhanced is the presence of colder material. Because RGS resolves the neon line, its value for the neon abundance is much more robust. Neon and oxygen are thought to have the same origin. Therefore, we expect their values and spatial behavior to be comparable, which excludes the very high numbers for neon from the single-temperature EPIC fits. The nickel abundance we find is likely to be overestimated due to an error in the nickel line energies (see also Gastaldello & Molendi 2004).

The oxygen abundance could not be constrained in our EPIC fits, but despite the occurrence of bad columns in the line resolved by the RGS we could get a value for the oxygen abundance consistent with the EPIC upper limits. We can compare our result with the predicted O/Fe ratios from theoretical models for supernovae Ia and II. The O/Fe ratio obtained from the RGS *wdem* fit is 0.25 ± 0.13 , which is lower than the average value of 1.2 ± 1.6 for hot clusters reported by Tamura et al. (2004), but not significantly different because of the large spread. The theoretical models predict an O/Fe ratio of < 0.05 and 1.5 – 4 for supernova types Ia and II, respectively. Our value of 0.25 ± 0.13 is in between the two predictions, like in the other hot clusters.

In Table 2.3 and Table 2.5 the values for N_{H} and O_{abs} appear to be different between EPIC and RGS. This is partly due to the fact that the EPIC/RGS cross-calibration near the oxygen edge is still not optimal. The EPIC results are also slightly affected by correlations between N_{H} , O_{abs} and the oxygen abundance, because of blending due to the lower CCD resolution. The O_{abs} anti-correlates with absorption, but because fixing the edge results in large residuals at lower energies, we decided to let the oxygen abundance in the absorption component free. Fig. 2.4 shows the error ellipses for the oxygen abundance against N_{H} . From the plot it is apparent that N_{H} and O_{abs} are anti-correlated. If we fix the O_{abs} abundance to 1.0, the N_{H} values we find are consistent with those from Pointecouteau et al. (2004) and Sun et al. (2003). This plot also shows that O_{abs} is significantly different from solar. Weisskopf et al. (2004) report from their Chandra observation of the Crab nebula that, using the abundances from Anders & Grevesse (1989), they find an underabundance of oxygen in the Galactic absorption component of 0.41 ± 0.07 . Takei et al. (2003) find values in the range from 0.63 ± 0.12 to 0.74 ± 0.14 using a Chandra observation of Cyg X-2. Within the calibration uncer-

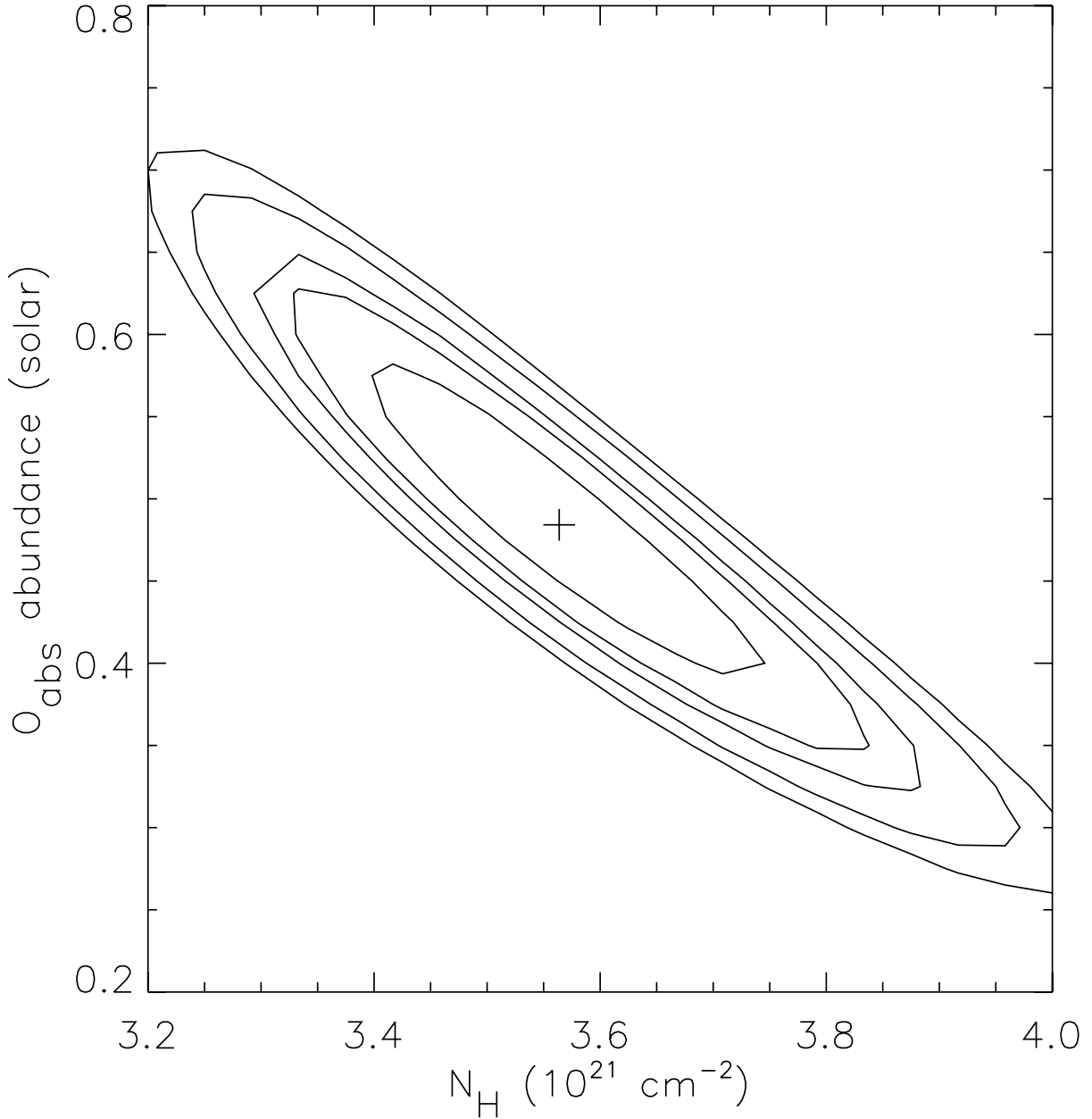


Figure 2.4: Error ellipses for N_{H} against O_{abs} calculated from the MOS fit of the core (0.0–0.5') region. Contours are drawn for $\Delta\chi^2 = [2.30, 4.61, 6.71, 9.21, 11.8]$.

tainties our results are consistent with these numbers. It is likely that the observed underabundance is an artifact of the solar abundances we use. Allende Prieto et al. (2001) reported a new solar photospheric abundance of $\log \epsilon(\text{O}) = 8.69 \pm 0.05$ dex. This is 0.58 ± 0.08 times smaller than the value of Anders & Grevesse (1989) and in between our values for O_{abs} . Pointecouteau et al. (2004) show that the origin of the absorption in the direction of Abell 478 is most likely Galactic and correlated with infra-red data. Although O_{abs} is consistent with the solar oxygen abundance of Allende Prieto et al. (2001) we cannot fully exclude the existence of a real underabundance of oxygen in the

absorbing material along the line of sight.

Finally, we find that the average redshift measured in the pn detector is 0.0775 ± 0.0002 , compared to 0.0881 ± 0.0009 measured in the optical by Zabludoff et al. (1990). This is probably a gain-related problem which was not corrected for during the XMM-Newton SOC data processing. Problems with the redshift determinations are not unique. Discrepancies between X-ray measured redshifts and optical redshifts have been reported earlier by Zhang et al. (2004) and Takahashi & Yamashita (2003).

2.5 Conclusions

We analyze the high-resolution XMM-Newton spectra of the Abell 478 clusters of galaxies and conclude that:

- We measure an underabundance of oxygen in the Galactic absorption component. This is measured for the first time using an observation of a cluster of galaxies.
- We derive radial abundance profiles for Ne, Mg, Si, S, Ca, Fe and Ni, which confirm the trends observed in other clusters (Tamura et al. 2004).
- The core of the cluster shows multi-temperature behavior, which is mostly explained by projection effects partly because of the steep temperature gradient.

Acknowledgements

We would like to thank Monique Arnaud for providing useful comments and for the fruitful discussions we had while completing this paper. This work is based on observations obtained with XMM-Newton, an ESA science mission with instruments and contributions directly funded by ESA member states and the USA (NASA). The Space Research Organization of the Netherlands (SRON) is supported financially by NWO, the Netherlands Organization for Scientific Research.

The temperature structure in the core of Sérsic 159-03

J. de Plaa^{1,2}, *J. S. Kaastra*¹, *M. Méndez*¹, *T. Tamura*³, *J. A. M. Bleeker*¹, *J. R. Peterson*⁴,
*F. B. S. Paerels*⁵, *M. Bonamente*⁶, and *R. Lieu*⁶

¹ SRON National Institute for Space Research, Utrecht, The Netherlands

² Astronomical Institute, Utrecht University, Utrecht, The Netherlands

³ Institute of Space and Astronautical Science, JAXA, Kanagawa, Japan

⁴ KIPAC, Stanford University, Stanford, USA

⁵ Department of Astronomy, Columbia University, New York, USA

⁶ Department of Physics, University of Alabama, Huntsville, USA

Published in *Advances in Space Research*, Volume 36, Issue 4, 2005, Pages 601-604

Abstract

We present results from a new 120 ks XMM-Newton observation of the cluster of galaxies Sérsic 159-03. In this paper we focus on the high-resolution X-ray spectra obtained with the Reflection Grating Spectrometer (RGS). The spectra allow us to constrain the temperature structure in the core of the cluster and determine the emission measure distribution as a function of temperature. We also fit the line widths of mainly oxygen and iron lines.

Received 9 November 2004 / Accepted 11 april 2005

3.1 Introduction

X-ray emission from clusters of galaxies is dominated by diffuse emission from virialized hot plasma which is trapped in the clusters gravitational potential. Current X-ray missions like XMM-Newton and Chandra show that the structures in the hot diffuse plasma can be very complex.

Recent high-resolution X-ray spectra of cool-core clusters by the RGS instrument aboard XMM-Newton (Peterson et al. 2001, 2003) show that the cores of many clusters lack strong Fe XVII emission lines. This indicates that the amount of cool gas in the cores is too little to be explained by classical cooling-flow models (see e.g. Fabian 1994). From the studies of larger samples of cool-core clusters with XMM-Newton (Peterson et al. 2003; Kaastra et al. 2004) we learn that the cores are not isothermal, but probably multi-phase. The implication of the lack of cool gas is that cool-core clusters need an additional heat source to balance the radiative cooling of the gas.

In this paper we discuss the results of a 120 ks XMM-Newton RGS observation of the cluster of galaxies Sérsic 159-03. This cluster is relatively nearby and has a redshift of $z = 0.0564$. We concentrate on the temperature structure of the core and the widths of the emission lines.

3.2 Spectral models

The temperature distribution in the complex cores of clusters and the amount of cool gas, can be determined from its spectrum and does not necessarily have to be resolved spatially. From the XMM-Newton data of a large sample of clusters we know that cluster cores can be best fitted with a differential emission measure (DEM) model (e.g. Peterson et al. 2003; Kaastra et al. 2004, and Chapter 2). In this model the emission measure ($Y = \int n_e n_H dV$) of a number of thermal components is distributed as a function of temperature (T). This is shown in Eq. (3.1) adapted from Kaastra et al. (2004):

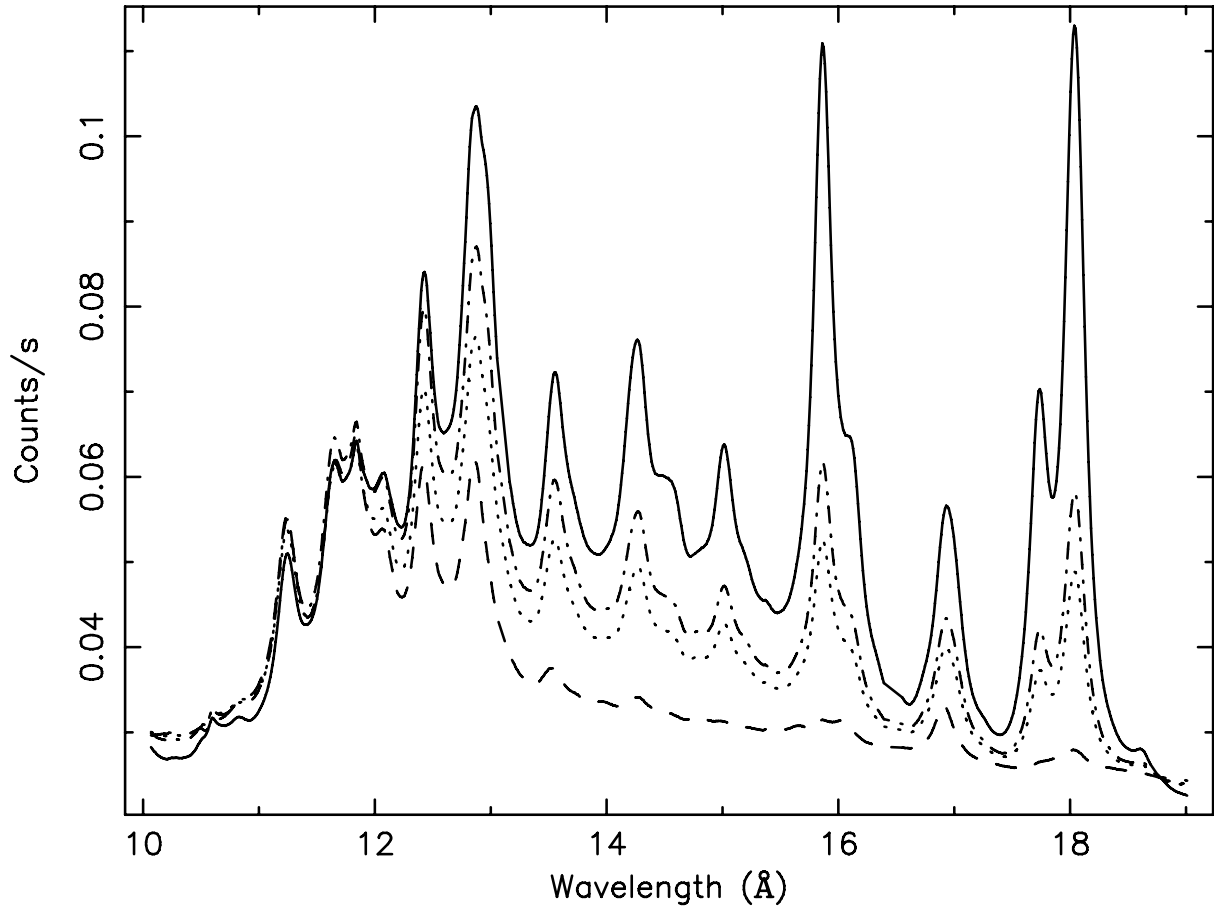
$$\frac{dY}{dT} = \begin{cases} cT^{1/\alpha} & T < T_{\max}, \\ 0 & T > T_{\max}. \end{cases} \quad (3.1)$$

This distribution is cut off at some fraction of T_{\max} which is set to 0.1 times kT_{\max} in this study. The model above is an empirical parametrization of the DEM distribution found in the core of many clusters. In this form the limit $\alpha \rightarrow 0$ yields the isothermal model.

Well resolved spectral lines are important for this model to give an accurate result, because the strength of each line has a unique dependence on the temperature. As an example, we show simulated RGS spectra of the Fe-L complex in Fig. 3.1. These spectra are simulated using four different sets of model parameters listed in Table 3.1. We assume a cluster spectrum emitted at the redshift of Sérsic 159-03 ($z=0.0564$). The respective DEM profiles corresponding to these spectra are shown in Fig. 3.2. From this figure we see that the model with $\alpha = 1.0$ has a larger contribution of cold gas than $\alpha = 0.4$. In the spectrum (Fig. 3.1) this leads to enhanced line emission above 11 Å from

Table 3.1: *The model parameters used to produce Fig. 3.1 and Fig. 3.2.*

Model	Linestyle	kT_{\max}	α	Mean kT	Cut-off
DEM	-----	3.0 keV	0.4	2.33 keV	$0.1kT_{\max}$
DEM	-.-.-.	3.0 keV	1.0	2.02 keV	$0.1kT_{\max}$
DEM	3.47 keV	1.0	2.33 keV	$0.1kT_{\max}$
Cooling-flow	———	3.0 keV			0.1 keV

**Figure 3.1:** *Simulated RGS spectra of the Fe-L complex using the model parameters listed in Table 3.1.*

ions like Fe XVII. Thus, by fitting high-resolution spectra with this model we are able to derive the shape of the temperature distribution.

The first two models listed in Table 3.1 show the difference between two values for α . In order to compare the outcome of these models with single-temperature fit results found in other studies, we also calculate the weighted mean temperature of the DEM distribution. The third model in Table 3.1 is chosen in a way that the mean temperature of the distribution is the same as the one in the first model. Finally, the fourth model

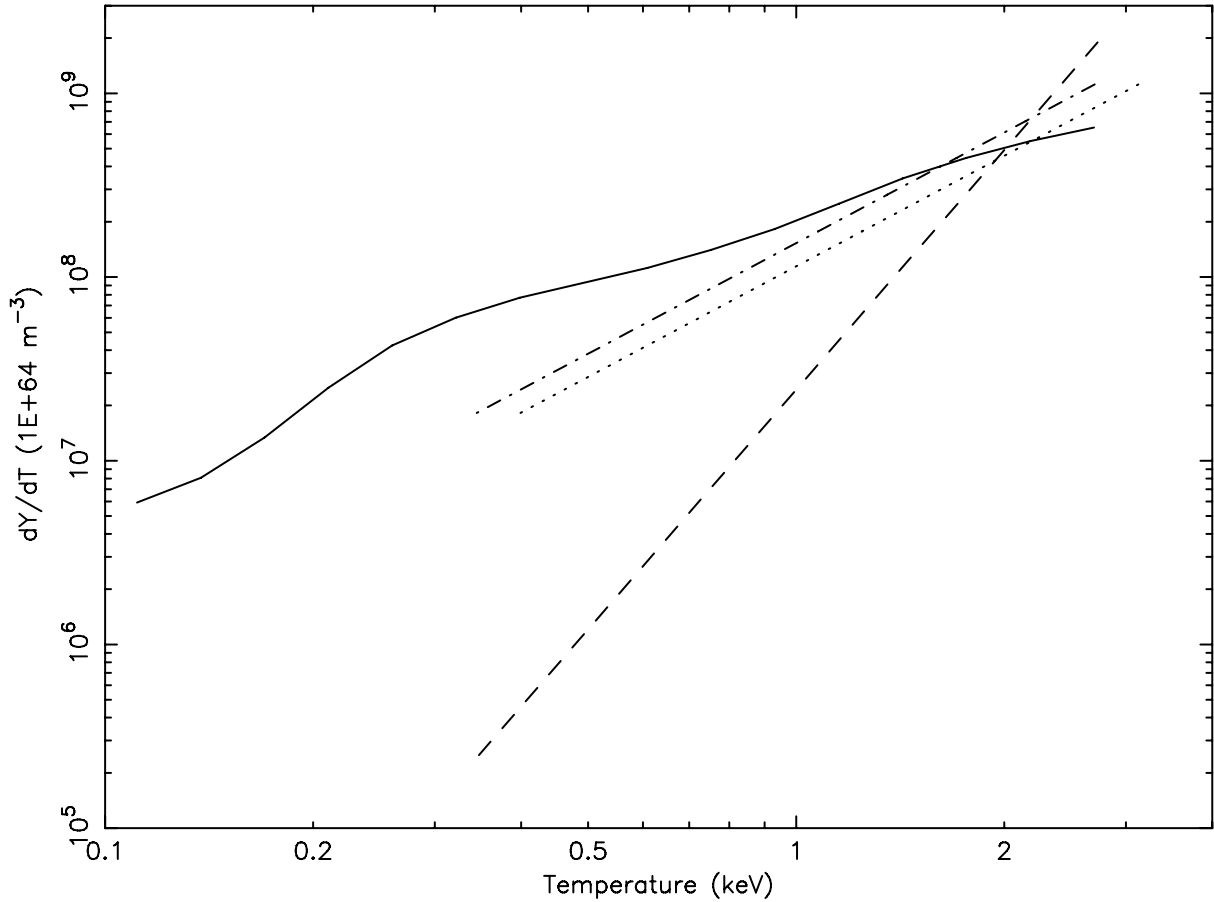


Figure 3.2: DEM distributions for the models listed in Table 3.1.

represents the isobaric cooling-flow model.

Because the RGS gratings operate without a slit, the resulting spectrum of an extended source is the sum of all spectra in the (in our case) $1' \times \sim 12'$ field of view, convolved with the PSF (for a complete discussion about grating responses see Davis 2001). Extended line-emission appears to be broadened depending on the spatial extent of the source along the dispersion direction. In order to describe the data properly, the spectral fits need to account for this effect. In practice, this is accomplished by convolving the spectral models with the surface brightness profile of the source along the dispersion direction. For that purpose we extract the cluster intensity profile from MOS1 along the dispersion direction of RGS, which we convolve with the RGS response during spectral fitting. This procedure is described in Tamura et al. (2004) and was also applied in studies like, for example, Kaastra et al. (2001) and Chapter 2. Because the radial profile of an ion can be different from the wide-band surface brightness profile, this method is not ideal. In order to account for this, we let the scale of the width and the position of the profile free in the fit to match the profiles of the main emission lines.

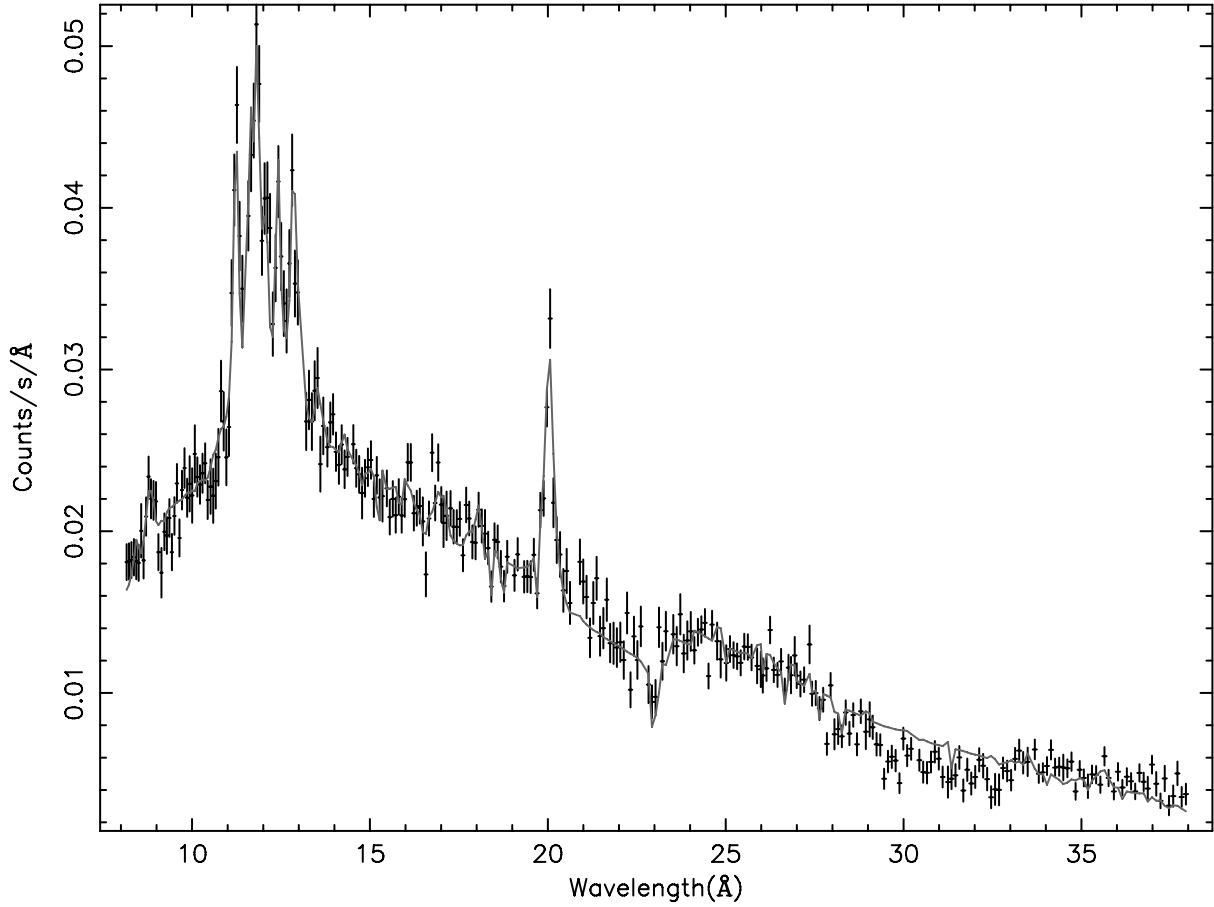


Figure 3.3: RGS spectrum of Sérsic 159-03 fitted with a DEM model with a variable width for the oxygen and iron lines. The wavelength plotted here is the observed (redshifted) wavelength. From the left to the right we see emission lines from Mg (9 Å), Fe-L and Ne (11–14 Å) and O (20 Å).

3.3 Results

In Table 3.2 we show the results of a fit to the RGS spectrum of Sérsic 159-03 shown in Fig. 3.3. We extract this spectrum from a 4 arcmin wide region in the cross-dispersion direction of the RGS. The spectrum shows line emission from Fe-L, Ne, Mg and O. In the region between $\sim 14\text{--}19$ Å no strong features from Fe XVII lines can be observed and therefore the fitted value of α is moderate: 0.43 ± 0.03 . Together with the kT_{max} from the fit we find a mean temperature of the core of 3.14 ± 0.13 keV. This value is not so different from the value of 2.80 ± 0.08 keV obtained when fitting a single-temperature model to the data.

When we look into the 10–19 Å wavelength range and compare the best fit DEM model with the classical cooling-flow model, we obtain a spectrum like in Fig. 3.4. The lower and upper temperature limits of the cooling-flow model (continuous line) have been set to 0.1 and 4.0 keV respectively. The dashed-line represents the best fit DEM model and is the same as the model presented in Fig. 3.3. From this plot it is clear that

Table 3.2: Best fit results from a DEM model fit to the spectrum extracted from a 4 arcmin wide extraction region. The line width relative to the FWHM of the cluster line profile is also given. This cluster line profile derived from the clusters surface brightness profile has a FWHM of 0.14 \AA .

Parameter	Value	Parameter	Value
kT_{max} (keV)	4.08 ± 0.16	cut off	0.05 ± 0.04
α	0.43 ± 0.03	mean kT	3.14 ± 0.13
Line width (C,N,O)	1.5 ± 0.3	Line width (Ne,Mg,Fe)	0.57 ± 0.07

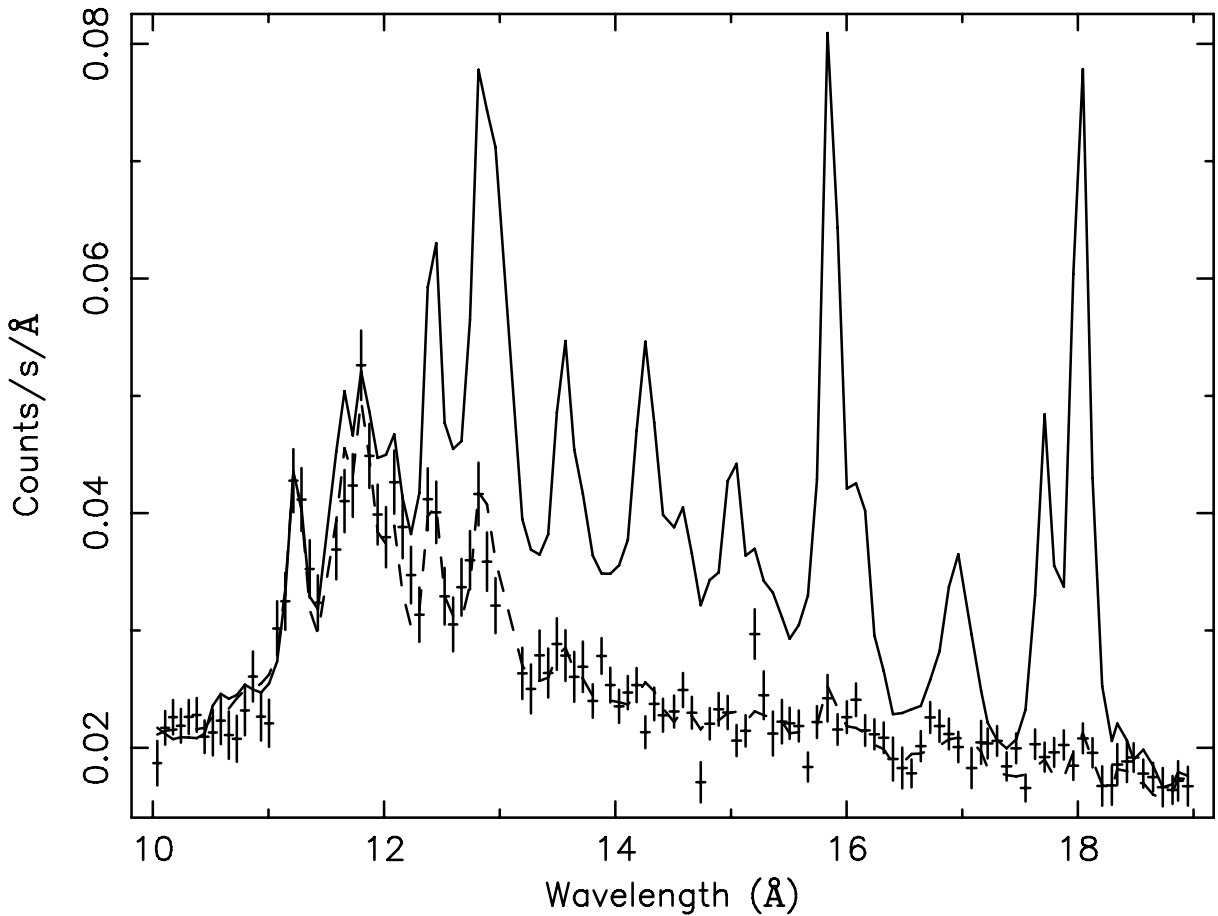


Figure 3.4: RGS combined spectrum of the 10–19 \AA wavelength range. The dashed line represents the best-fit DEM model and the continuous line shows a typical cooling-flow model.

the iron lines associated with the cold gas, which are predicted by the cooling-flow model, are not observed.

In Fig. 3.3 we can see by eye that the oxygen line near 20 \AA is broader than the individual iron lines in the Fe-L complex at around $11\text{--}13 \text{ \AA}$. A fit to the width of the lines confirms this view and shows that the line width of oxygen is nearly 3 times larger than the width of the iron lines. The lines of the other fitted elements (carbon, nitrogen, neon and magnesium) do not have a large signal-to-noise, therefore we couple their

widths to either iron or oxygen. The line widths of carbon and nitrogen are coupled to oxygen, while neon and magnesium are coupled to iron. In Table 3.2 we show the widths of these lines with respect to the broad band cluster profile.

3.4 Conclusion

We performed a spectral analysis of the cool-core cluster Sérsic 159-03 using the RGS instrument aboard XMM-Newton. The high-resolution spectra of the core confirm the lack of cool gas in the core of the cluster in agreement with the results found by Peterson et al. (2001) and Peterson et al. (2003) in this and other clusters. From the line width of O and Fe we can derive the spatial distribution of the elements. Fe has a line width of 0.57 ± 0.07 with respect to the profile of the continuum emission derived from EPIC MOS, while the O line is much broader with a value of 1.5 ± 0.3 . This means that the Fe distribution in the cluster is much more centrally peaked than the oxygen distribution. This is consistent with earlier measurements by e.g. Tamura et al. (2004).

Chemical evolution in Sérsic 159-03 observed with XMM-Newton

J. de Plaa^{1,2}, N. Werner¹, A. M. Bykov³, J. S. Kaastra¹, M. Méndez¹, J. Vink^{1,2}, J. A. M. Bleeker¹, M. Bonamente⁴, and J. R. Peterson⁵

¹ SRON Netherlands Institute for Space Research, Utrecht, The Netherlands

² Astronomical Institute, Utrecht University, Utrecht, The Netherlands

³ A.F. Ioffe Institute for Physics and Technology, St. Petersburg, Russia

⁴ Department of Physics, University of Alabama, Huntsville, Alabama, USA

⁵ KIPAC, Stanford University, Stanford, California, USA

Received 20 July 2005 / Accepted 26 February 2006

Published in *Astronomy & Astrophysics*, volume 452, pages 397–412, 2006

Abstract

Using a new long X-ray observation of the cluster of galaxies Sérsic 159-03 with XMM-Newton, we derive radial temperature and abundance profiles using single- and multi-temperature models. The fits to the EPIC and RGS spectra prefer multi-temperature models especially in the core. The radial profiles of oxygen and iron measured with EPIC/RGS and the line profiles in RGS suggest that there is a dip in the O/Fe ratio in the centre of the cluster compared to its immediate surroundings. A possible explanation for the large scale metallicity distribution is that SNIa and SNII products are released in the ICM through ram-pressure stripping of in-falling galaxies. This causes

a peaked metallicity distribution. In addition, SNIa in the central cD galaxy enrich mainly the centre of the cluster with iron. This excess of SNIa products is consistent with the low O/Fe ratio we detect in the centre of the cluster. We fit the abundances we obtain with yields from SNIa, SNII and Population-III stars to derive the clusters chemical evolution. We find that the measured abundance pattern does not require a Population-III star contribution. The relative contribution of the number of SNIa with respect to the total number of SNe which enrich the ICM is about 25–50%. Furthermore, we discuss the possible presence of a non-thermal component in the EPIC spectra. A potential source of this non-thermal emission can be inverse-Compton scattering between Cosmic Microwave Background (CMB) photons and relativistic electrons, which are accelerated in bow shocks associated with ram-pressure stripping of in-falling galaxies.

4.1 Introduction

Hot diffuse X-ray emitting gas dominates the visible mass in clusters of galaxies, but the structure and evolution of the cluster is not yet fully understood. During its formation, supernova explosions and galactic winds of member galaxies have enriched the Intra-Cluster Medium (ICM) substantially (De Young 1978). The abundances can provide the relative contribution of Supernova type Ia (SNIa), Supernova type II (SNII) and population-III stars (PopIII) to the enrichment of the ICM (e.g. Iwamoto et al. 1999; Tsujimoto et al. 1995), because the abundance ratios of the various elements are signatures of supernova types Ia and II and possibly of the remains of PopIII stars (e.g. Gibson et al. 1997; Loewenstein 2001; Baumgartner et al. 2005). The radial distribution of the metals provides information about dynamical ways to enrich the ICM like, for example, ram-pressure stripping (e.g. Schindler et al. 2005).

Clusters of galaxies appear as knots in the cosmic web. They accrete gas from the surrounding filaments, which consist of warm gas with a temperature in the range of 10^{5-6} K. According to numerical hydro-dynamical simulations by e.g. Cen & Ostriker (1999) and Davé et al. (2001), this Warm-Hot Intergalactic Medium (WHIM) could contain about half of the missing baryons in the universe,

There have been several attempts to detect this WHIM in emission. In the late 90's Lieu et al. (1996) and Mittaz et al. (1998) discovered a soft X-ray excess in EUV and ROSAT spectra of several clusters. More recent observations with XMM-Newton appear to confirm the presence of a soft excess in some cluster spectra (Kaastra et al. 2003a; Finoguenov et al. 2003). The detection of a possibly redshifted O VII line, which traces gas with a temperature of $\sim 10^6$ K, suggests that the gas might be the WHIM. Unfortunately, current instruments do not have sufficient spectral resolution to prove that the emission is indeed extragalactic.

Recent measurements of Sérsic 159-03 by Bonamente et al. (2005) and Kaastra et al. (2003a) show that the soft-excess can be fit both using thermal and non-thermal models. Inverse-Compton scattering of CMB photons with relativistic electrons can also contribute a non-thermal power-law component to the spectra. This mechanism was already proposed by Sarazin & Lieu (1998) to explain the extreme-ultraviolet emission

from clusters. In the hard X-ray band up to 80 keV, detections of non-thermal emission have been claimed in several clusters, for example Coma and Abell 2256 (Fusco-Femiano et al. 1999, 2005). But these BeppoSAX detections of the hard-excess are still subject to debate (Rossetti & Molendi 2004).

The cluster of galaxies Sérsic 159-03, also known as ACO S 1101, was discovered by Sérsic (1974). Since then it was studied in X-rays as part of several cluster samples: e.g. EXOSAT (Edge & Stewart 1991) and ROSAT (Allen & Fabian 1997). Kaastra et al. (2001) reported results from an XMM-Newton observation with a useful exposure time of about 35 ks showing a radial temperature profile which peaks at $kT = 2.7$ keV at a radius of $2'$ from the core. The temperature drop in the core is relatively modest, while the temperature outside the $2'$ radius drops rapidly to values around 0.5 keV. Because Sérsic 159-03 is thought to show a large soft X-ray excess, the cluster was also included in the sample of Kaastra et al. (2003a).

In this paper we present results from a 121 ks long XMM-Newton (Jansen et al. 2001) observation of Sérsic 159-03. The main goal of the paper is to obtain accurate temperature and abundance profiles as far out from the core as possible using a new method for handling the background. We exploit the large effective area of XMM to obtain temperature and abundance profiles with EPIC (Turner et al. 2001) and RGS (den Herder et al. 2001). This deep observation also allows us to study the nature of the previously detected soft excess in more detail, and in addition it provides more accurate radial profiles of the temperature and metal abundances. We then fit the derived abundances to yields of Supernovae type Ia and II, and PopIII stars. Moreover, we discuss the potential presence of non-thermal emission in the cluster.

Throughout this paper we use $H_0 = 70 \text{ km s}^{-1} \text{ Mpc}^{-1}$, $\Omega_m = 0.3$ and $\Omega_\Lambda = 0.7$. Using this cosmology $1'$ is 73 kpc at the cluster redshift of 0.0564 (Maia et al. 1987). The elemental abundances presented in this paper are given relative to the solar abundances from Lodders (2003).

4.2 Observations and data analysis

The XMM-Newton observation of Sérsic 159-03 was performed on November 20, 2002 and had a total duration of 121 ks. The two EPIC MOS cameras were operated in Full Frame mode and the EPIC pn camera in Extended Full Frame mode. For all EPIC cameras the thin filter was used. The RGS instruments were operated in the standard spectroscopy mode. All data were analysed with the 6.1.0 version of the XMM Science Analysis System (SAS).

4.2.1 EPIC Analysis

One of the most important things to account for in extended source analysis is the background. Because we intend to measure the cluster properties as far from the core of the cluster as possible, we need an accurate estimate of the local background, especially for the dim outer parts of the cluster. In general the source fills the entire field of

view, which makes a direct measurement of the local background very difficult. Common practice is to extract spectra from a combined event list of several observations of empty fields, like the ones compiled by Lumb et al. (2002) or Read & Ponman (2003), and use them as best estimate for the local background. The spectra extracted from this blank field are scaled and then subtracted from the source spectra. This method works fine in areas in which the surface brightness of the source is high, and with clusters that have similar background conditions (e.g. particle background, local cosmic background and instrumental background) compared to the blank fields.

The Cosmic X-ray Background (CXB), however, consists of multiple components, which are more extensively described in Sect. 4.2.1. The emission can be roughly divided in two parts: a soft thermal component originating from hot plasma in our own galaxy and a non-thermal power-law component caused by unresolved distant point sources, predominantly AGN. The soft galactic CXB component varies spatially across the sky. Therefore, the total photon background at low energies can vary up to 30–60% from pointing to pointing (Read & Ponman 2003). It is clear that when the background conditions in the source observation are very different from the average blank-sky background, this can lead to systematic uncertainties in the fitted parameters from the outer parts of the cluster.

In Fig. 4.1 we show the systematic effect of background subtraction on a temperature profile extracted from the EPIC data of Sérsic 159-03. For this plot we deliberately introduced an error of +10% and -10% in the background normalisation. The crosses show a profile derived with no background scaling at all, while the circles and triangles show the temperature profile for a scaling of -10% and +10%, respectively. From this plot we see that overestimating the background results in a lower temperature, and vice versa. Note that we included a 10% systematic error on the background during fitting. We conclude that the uncertainties in the temperature are mainly caused by the background scaling and therefore we can gain a lot in accuracy by constraining the background normalisations.

In order to find the best estimate for the local background we divide the background into three components: soft-protons, instrumental background, and the CXB. By separating these components in our analysis, we will be able to constrain the normalisation and accuracy of each component. The method we use is similar to the one used by De Luca & Molendi (2004), but with a few modifications. The steps are described below.

Soft Protons

In order to minimise the effect of soft protons in the spectra, we cut out the time intervals which show enhanced soft-proton flux using the method described in Pratt & Arnaud (2002). We make a light curve using the events with energies between 2–12 keV and with a bin size of 100 s. From this light curve we extract the distribution of counts per bin. The resulting histogram is then fitted with a Poissonian function to determine the average number of counts per bin. The thresholds are subsequently fixed to $N \pm 2\sqrt{N}$, where N is equal to the mean number of counts within a 100 s bin. This way we cut out every flare which reaches the 2σ level. This method is more strict in rejecting soft-proton flares than using the conventional >10 keV light curve with 3σ

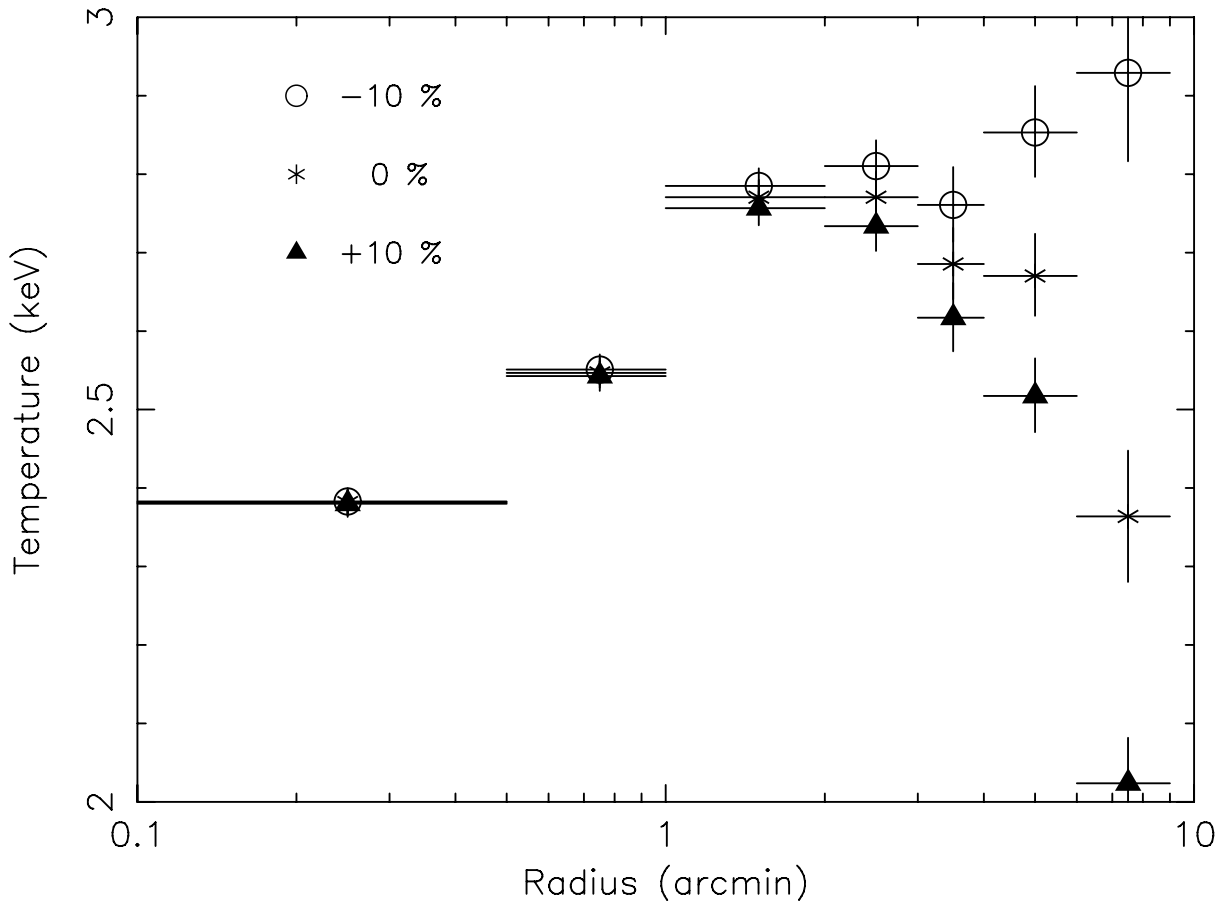


Figure 4.1: Systematic effects in a temperature profile obtained with a blank-sky background dataset (Read & Ponman 2003). The points with the cross are derived from spectra with no background scaling. The background for the circled data points is scaled with 0.9 and the triangles with 1.1.

clipping. Because of the broad energy interval we choose, the signal-to-noise in the light curve is very high and even small flares stand out from the quiescent level. By putting a strict 2σ threshold we exclude also small flares without losing a lot of usable data ($\sim 4\%$ max. is lost in this case). This way we minimise the effect of soft-proton flares which can bias our temperature determination like in Fig. 4.1. After applying the threshold we obtain an effective exposure time of 81 ks for both MOS instruments and 60 ks for pn.

The disadvantage of this method is that we do not necessarily subtract the quiescent level of soft protons. We can get an indication of the magnitude of the soft-proton count rate by using CCD9 of the RGS instrument. For this CCD the photon count rate from the source is very low, so the count rate is dominated by soft protons and instrumental noise. For our observation we find that the RGS CCD9 count rate is 0.086 cnts/s in the quiescent periods. Compared to all the soft-proton background count rates measured during the lifetime of XMM-Newton, this residual soft proton background is low (González-Riestra 2004). Therefore, the influence on our analysis should be very small.

Table 4.1: *The closed filter observations that we use for the EPIC background subtraction.*

Instrument	Obs. date	Obs. ID	Exposure
MOS	2003-04-06	0150390101	200 ks
pn	2003-08-12	0160362801	35 ks

Instrumental background

A good template for the instrumental background can be obtained from a closed-filter observation. For this analysis we use a closed-filter observation which was performed after the cooling of the EPIC and RGS instruments in November 2002. The properties of the observations are listed in Table 4.1.

The instrumental background contains roughly two components: fluorescence lines and a power law. A study of the EPIC-pn background by Katayama et al. (2004) shows that the variation of the fluorescence lines is much lower than the variation in the continuum. We use the power-law component to model the variable hard-particle background and the intrinsic instrumental noise. This background component is mainly caused by hard-particles which are able to reach the detector even when the filter wheel is in closed position. We especially choose a long closed-filter observation, not taken during the passage of the Earth radiation belts, to avoid getting a too large variation in the hard-particle flux with respect to our Sérsic 159-03 observation.

Because these variations can have a significant effect on fitted parameters (see Fig. 4.1), we would like to be able to modify the normalisation of the hard-particle power law by a few percent without changing the normalisations of the instrumental lines. In order to find the scaling factors for this normalisation, we can use the events registered outside the field of view (out-of-FOV) of the EPIC instruments in both the closed-filter and source observations. These non-illuminated parts of the CCD chips provide unbiased data on the power-law normalisation, also when a bright source is present in the field of view.

We start by determining the power-law index of the instrumental power law by fitting a closed-filter spectrum extracted from the full field of view. We assume that this power-law index will be constant over the whole detector, since the observation does not suffer from vignetting and PSF effects of the mirror. We fit the spectrum with just a spectral redistribution file and no effective area file. From these fits we obtain a photon index (Γ) of 0.15 for MOS and 0.37 for pn. The MOS value is consistent with the value of ~ 0.2 obtained in the same way by De Luca & Molendi (2004)

We extract the events labelled as out-of-FOV events (`FLAG==#XMMEA_16`) to determine the normalisation of the instrumental background. To be sure that photons and soft-protons that scatter into the shielded out-of-FOV region of the detector are not polluting the measurement, we only count events registered outside a radius of 15.4' from the centre of the field-of-view. We divide the out-of-FOV count rates in our Sérsic 159-03 observation with the closed-filter out-of-FOV count rates in the 8–12 keV band to obtain an instrumental background scaling factor (c). The c values are 1.03 ± 0.02 ,

0.97 ± 0.02 and 0.97 ± 0.06 for MOS1, MOS2 and pn respectively. In this case the correction on the power-law normalisation is only $\pm 3\%$ and within the statistical error, but we prefer to use the most likely value for c . Despite the fact that our values for c are consistent with being 1, this is a useful exercise, because the normalisation of closed filter spectra is known to vary by about 15% (De Luca & Molendi 2004). Already a deviation of a few percent can lead to discrepancies in the temperature determination.

We cannot simply multiply the closed-filter spectra with our values for c , because then the instrumental lines would not be well subtracted. The only component that we have to scale is the power-law component. Therefore, we add (or subtract) a power law with the same slope (Γ) to the original closed filter spectra (S_{orig}). The normalisation of the power law (n) we add is derived as follows. We first solve this simple system for S_{orig} to approximate the scaled spectrum S_{scal} :

$$\begin{cases} S_{\text{scal}} = cS_{\text{orig}} \\ S_{\text{scal}} = nE^{-\Gamma} + S_{\text{orig}}, \end{cases} \quad (4.1)$$

and work out n :

$$n = \frac{(c-1)}{E^{-\Gamma}} S_{\text{orig}}. \quad (4.2)$$

We can subsequently calculate n for every energy bin of energy E . We exclude energy intervals affected by instrumental lines. The mean value of n over all these bins is determined by fitting a Gaussian to a histogram of n . This value will be used to add or subtract the power law from the closed filter spectra. Finally, we subtract this scaled spectrum from the source spectra.

Cosmic X-ray background

Instead of subtracting the CXB from the spectra, like it is done with blank-field data, we include the CXB components during fitting. Because the CXB can vary spatially across the sky we can more easily adapt the flux of each component to the local conditions. Unlike the case of the instrumental background and soft-protons, all the photons enter through the XMM mirrors in the same way as the source photons. Therefore, the response files (rmf) and effective area files (arf) must be applied and we must fit the CXB simultaneously with the source spectra.

For the fitting we use the spectral components described by Kuntz & Snowden (2000) and De Luca & Molendi (2004). For the thermal components in this paper we use MEKAL models, but the thermal components in Kuntz & Snowden (2000) are fitted with Raymond-Smith models (Raymond & Smith 1977). There are, however, significant differences in ionisation balance and line strengths between MEKAL and Raymond-Smith, because the MEKAL code includes many more ions and up-to-date atomic constants. Hence, a temperature determined from a spectrum using the Raymond-Smith model is different from a temperature determined using MEKAL for the same dataset. To obtain consistency, we choose to convert the model temperatures from Kuntz & Snowden (2000) to MEKAL temperatures to match the measured spectra by Kuntz & Snowden (2000) in our modelling. Unfortunately, this transformed Kuntz & Snowden (2000) model does not fit a spectrum extracted from the Read & Ponman

Table 4.2: The CXB background components we use in the fits of Sérsic 159-03. The integrated absorbed intensity over the 0.3–10 keV energy range was calculated using an N_{H} value of $1.79 \times 10^{20} \text{ cm}^{-2}$. In the thermal components the abundances are set to solar values.

Component	kT (keV)	Γ	Z_{\odot}	Integrated intensity ($\text{erg cm}^{-2} \text{ s}^{-1} \text{ deg}^{-2}$)
Soft thermal	0.070		0.3	2.23×10^{-12}
Hard thermal	0.20		1.0	1.03×10^{-11}
Power law		1.41		3.16×10^{-11}

Table 4.3: Boundaries of the annular extraction regions used in our EPIC analysis. The annuli are centred on the cluster centre.

Annulus	Inner boundary (')	Outer boundary (')
1	0.0	0.5
2	0.5	1.0
3	1.0	2.0
4	2.0	3.0
5	3.0	4.0
6	4.0	6.0
7	6.0	9.0

(2003) blank-fields. Therefore, we empirically fit the Read & Ponman (2003) blank-fields with a power law, a soft, and a hard thermal component, which turns out to be a good description of the data. Based on the best fit and the model by Kuntz & Snowden (2000) we fix the temperatures and metallicities to the values listed in Table 4.2

In order to estimate the normalisations of the local background components around Sérsic 159-03 we fit them to the outermost annulus (9–12' from the core of the cluster) using the temperatures derived from the Read & Ponman (2003) blank-fields. We add an additional thermal component for the cluster emission. In our final fits for all annuli we fix the normalisations of the background components to the fitted values of the 9–12' annulus, which are listed in Table 4.2. For comparison, the 2–10 keV absorbed integrated intensity of the power-law component is $2.26 \times 10^{-11} \text{ erg cm}^{-2} \text{ s}^{-1} \text{ deg}^{-2}$, which is consistent with the value of $(2.24 \pm 0.16) \times 10^{-11} \text{ erg cm}^{-2} \text{ s}^{-1} \text{ deg}^{-2}$ found by De Luca & Molendi (2004).

In order to avoid large background fluctuations in our extraction regions we cut out bright point sources which were identified by eye. The unresolved point sources are taken into account by the CXB power law.

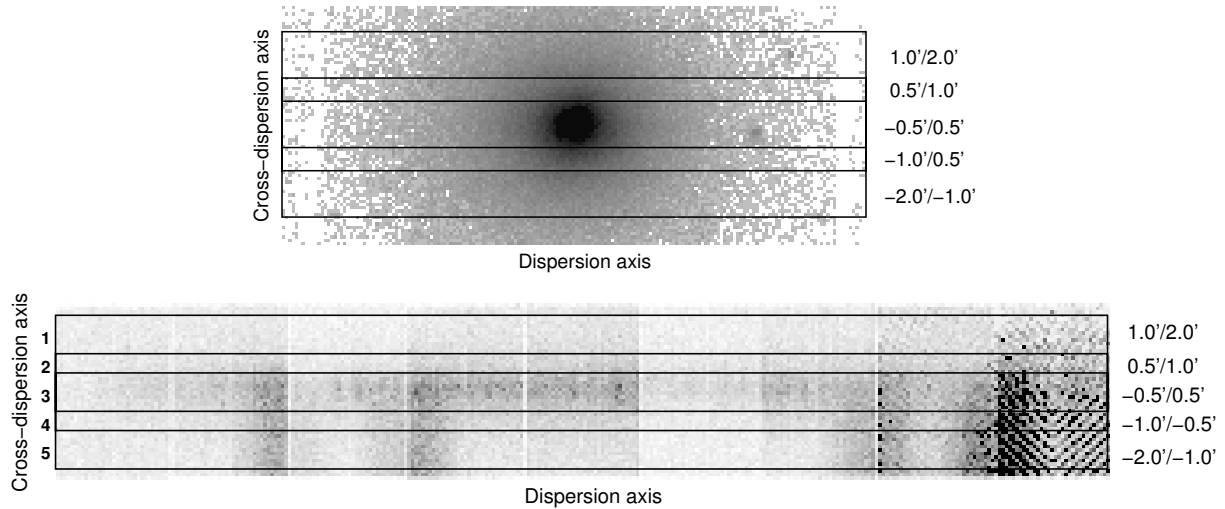


Figure 4.2: RGS extraction regions projected on top of a MOS1 image (top panel) and projected on top of a combined RGS1/RGS2 detector image (bottom panel). In the eighth and ninth CCD of RGS the instrumental effect of fixed-pattern noise causes the fish-bone shaped patterns.

Data extraction and fitting

As we are interested in the spectral parameters as a function of radius, we extract spectra from annuli as defined in Table 4.3. To gain statistics we choose a width for the annuli which is $\geq 30''$. By using these relatively wide annuli, we are also less sensitive to the energy dependent shape of the PSF and therefore we neglect this effect in the rest of the analysis. Because of small calibration differences between MOS and pn we include a 5% systematic error on the source and background spectra. This error is added in quadrature to the poissonian error of the data points.

4.2.2 RGS analysis

We extract the RGS spectra following the method described in Tamura et al. (2001a). In addition, we do spatially resolved spectroscopy using the RGS data: with RGS it is possible to extract spectra from different regions in the inner $4'$ of the cluster. The different regions can only be separated if they lie along the cross-dispersion axis of the instrument. We select the events from several rectangular areas on the CCD strip in the cross-dispersion direction. In Fig. 4.2 we show how these extraction regions are projected on the sky (MOS1, upper panel) and on the chips of the RGS (lower panel).

Because the cluster fills the entire field-of-view of the RGS, we need a blank field observation to extract the background spectrum. For this observation, which was taken prior to the cooling of RGS1 but after cooling of RGS2, we choose a Lockman Hole observation with an effective exposure time of 100 ks performed just 3 XMM-Newton orbits after our observation, also still before the cooling of RGS1. This way we minimise systematic effects due to hot pixels and instrument response. The flare subtraction is analogous to the method used with EPIC, but now we use the events from CCD 9 out-

side the central area. We select only events that have a position greater than $30''$ from the dispersion axis to make the light curve. This method was applied to both source and background datasets.

The RGS spectrometer operates without a slit. This means that all photons from within the (in our case) $5' \times \sim 12'$ field of view end up in the final spectrum, but not necessarily at the right wavelength. Only photons which are emitted in the cluster centre end up at the dispersion coordinate which corresponds to the correct wavelength. If the photon originates from the outskirts at an angle θ (projected on the dispersion axis) from the cluster centre, then the instrument will register it at a different dispersion coordinate and assign a wavelength to it which is shifted with respect to the true wavelength. This shift in wavelength depends linearly on incidence angle θ (arcmin) projected on the dispersion axis:

$$\Delta\lambda = 0.138\text{\AA} \Delta\theta. \quad (4.3)$$

Because of this effect, the line-emission appears to be broadened depending on the spatial extent of the source along the dispersion direction (see Davis 2001, for a complete discussion about grating responses).

In order to describe the data properly, the spectral fits need to account for the effect described above. In practice, this is accomplished by convolving the spectral models with the surface brightness profile of the source along the dispersion direction (Tamura et al. 2004). Therefore, we extract the cluster intensity profile from MOS1 along the dispersion direction of RGS. For each extraction region we can convert the spatial profile, which is a function of θ , into a line profile in \AA using Eq. 4.3. We convolve this profile with the model spectrum during spectral fitting. However, the width of the measured line profile can be different from the line profile that we derive from MOS1, because the surface brightness at the wavelength of a spectral line is not necessarily the same as the surface brightness in a broad energy band. To take this effect into account, we multiply the wavelength axis of the derived line profile with a scale factor. A scale factor of 1.0 corresponds directly to the wavelength scale of the profile we derive from the continuum. A scale factor of 2.0 stretches the line profile in wavelength space by a factor of two compared to the original line profile. In this way, we are able to fit the widths of the line profiles and to have a measure of the spatial extent of the line-emission region.

4.3 Spectral Models

In our analysis we fit several models to the spectra using the SPEX package (Kaastra et al. 1996). These models can be a combination of a number of thermal models (MEKAL) and a power-law model. Two models, however, include a more sophisticated combination of thermal models that we call Differential Emission Measure (DEM) models. Previous papers (e.g. Peterson et al. 2003; Kaastra et al. 2004, and Chapter 2) show that many clusters can be fitted better when we use a distribution of temperatures instead of a single temperature model. Actually, we expect that the plasma within our annuli should contain multiple temperatures and not one. An observational proof of this is given in Chapter 5. In the case of Sérsic 159-03 we fit two

types of distributions: a truncated power-law distribution (*wdem*) and a Gaussian distribution (*gdem*).

4.3.1 WDEM

We use the so-called *wdem* model, where the emission measure, $Y = \int n_e n_H dV$, of a number of thermal components is distributed as a truncated power law. This is shown in Eq. (4.4) adapted from Kaastra et al. (2004):

$$\frac{dY}{dT} = \begin{cases} cT^{1/\alpha} & \beta T_{\max} \leq T < T_{\max} \\ 0 & T > T_{\max} \vee T < \beta T_{\max}. \end{cases} \quad (4.4)$$

This distribution is cut off at a fraction of T_{\max} which is βT_{\max} . The value of β is set to 0.1 in this study. The model above is an empirical parametrisation of the DEM distribution found in the core of many clusters. In this form the limit $\alpha \rightarrow 0$ yields the isothermal model at T_{\max} .

In order to compare the outcome of the *wdem* model with single-temperature models, we can calculate the emission weighted mean of the DEM distribution. The mean temperature kT_{mean} follows from Eq. 4.5:

$$T_{\text{mean}} = \frac{\int T \frac{dY}{dT} dT}{\int \frac{dY}{dT} dT}. \quad (4.5)$$

When we integrate this equation between βT_{\max} and T_{\max} , we obtain a direct relation between T_{mean} and T_{\max} as a function of α and β :

$$T_{\text{mean}} = \frac{(1 + 1/\alpha) (1 - \beta^{1/\alpha+2})}{(2 + 1/\alpha) (1 - \beta^{1/\alpha+1})} T_{\max}. \quad (4.6)$$

The values for kT_{mean} we present in this paper are calculated using Eq. 4.6.

A detailed comparison of the *wdem* model with the classical cooling-flow model can be found in Chapter 3. In general the *wdem* model contains less cool gas than the classical cooling-flow model, which is consistent with recent observations (Peterson et al. 2001, 2003).

4.3.2 GDEM

Another DEM model that we use is a Gaussian differential emission measure distribution, *gdem*, in $\log T$:

$$Y(x) = \frac{Y_0}{\sigma_T \sqrt{2\pi}} e^{-(x-x_0)^2/2\sigma_T^2}. \quad (4.7)$$

In this equation $x = \log T$ and $x_0 = \log T_0$ where T_0 is the average temperature of the distribution. The width of the Gaussian is σ_T . Compared to the *wdem* model this distribution contains more emission measure at higher temperatures.

4.4 Results

4.4.1 EPIC/RGS spectral fitting

In this section we fit both the EPIC and RGS spectra with the models described in Sect. 4.3. From the fits we obtain temperatures and abundances for which we also derive spatial information. In all the fits we fix N_{H} to $1.79 \times 10^{20} \text{ cm}^{-2}$ which is the value deduced from H I data (Dickey & Lockman 1990). This value is the same as the one used in Kaastra et al. (2004). We use the Verner et al. (1996) cross-sections in our absorption model. Throughout the paper we use errors at the $\Delta\chi^2 = 1$ (68%) level for one interesting parameter.

The EPIC spectra are rebinned to the optimal binning of $\sim 1/3$ FWHM of the resolution of the instrument. We use the response matrix to derive the FWHM for every energy. The spectra are fitted over the 0.3–10 keV range. We are aware that below 0.6 keV there are some calibration uncertainties of the order of 5–10% when using SAS 6.1.0. This is partially accounted for by the 5% systematic error that we add to the spectra during fitting. The remaining calibration uncertainties are still small compared to the uncertainties in the soft X-ray background. Because of the importance of the soft-excess problem and the role of O VII we choose to include the 0.3–0.6 keV energy band in our fits.

For RGS we discuss the spectrum which was extracted from a 4' wide strip in the cross-dispersion direction, with which we obtain the highest signal-to-noise. In addition we also present spatially-resolved spectra extracted from smaller strips in the cross-dispersion direction. This provides a radial profile of the temperature and abundances in the core region (0–2').

After preliminary analysis, the RGS spectra show a discrepancy with any thermal model around 29–33 Å. The data points are significantly below the models in this interval, as can be seen in Fig. 4.5. Since the wavelength range coincides with a read-out node of CCD2, we believe this feature is instrumental in nature. If we perform the same analysis on an earlier observation of Sérsic 159-03 the discrepancy disappears, which supports our view. In Peterson et al. (2003) some other RGS observations of clusters of galaxies show the same problem, namely Hydra A, Abell 496 and MKW 3s. A large study of many RGS observations shows that about $\sim 5\%$ of the observations show an anomaly in the count rate of CCD2 (A. Pollock, priv. comm.). We therefore believe the feature we observe is instrumental in nature and we ignore the 29–33 Å interval in our analysis.

Integrated spectrum within 4'

In Table 4.4 we show the results from fits to a spectrum extracted from a circular region which has a radius of 4' and is centred on the core. In this circular region the cluster signal is well above the background. We can use the high signal-to-noise ratio of this spectrum to obtain accurate values for all the fitted parameters. The χ^2 value of the single-temperature fit (1228/916) indicates that a single-temperature model is potentially not the best description of the data. Multi-temperature models, however,

Table 4.4: Fit results for an EPIC spectrum extracted from a circle with a radius of $4'$ and centred on the core. Fluxes are calculated over the 0.3–10 keV range and presented in 10^{-10} erg cm $^{-2}$ s $^{-1}$ deg $^{-2}$. Emission measure ($Y_{\text{thermal}} = \int n_e n_H dV$) is given in 10^{66} cm $^{-3}$ and Y_{pow} is given in 10^{51} ph s $^{-1}$ keV $^{-1}$ at 1 keV.

Parameter	single-temp	<i>w</i> dem-model	<i>g</i> dem-model
Y_{thermal}	20.31 ± 0.15	20.55 ± 0.15	21.07 ± 0.15
F_{thermal}	19.26 ± 0.14	19.40 ± 0.14	19.46 ± 0.15
kT	2.568 ± 0.009		2.472 ± 0.010
kT_{mean}		2.60 ± 0.03	
kT_{max}		3.41 ± 0.03	
α		0.45 ± 0.02	
σ_T			0.226 ± 0.005
O	0.36 ± 0.05	0.30 ± 0.04	0.19 ± 0.03
Ne	0.89 ± 0.08	0.16 ± 0.08	0.000 ± 0.013
Mg	0.02 ± 0.04	0.11 ± 0.04	0.08 ± 0.04
Si	0.196 ± 0.017	0.239 ± 0.017	0.252 ± 0.018
S	0.122 ± 0.017	0.18 ± 0.02	0.20 ± 0.02
Ar		0.14 ± 0.04	0.19 ± 0.05
Ca	0.31 ± 0.05	0.36 ± 0.05	0.44 ± 0.06
Fe	0.360 ± 0.007	0.346 ± 0.008	0.242 ± 0.005
Ni	0.42 ± 0.09	0.45 ± 0.08	0.35 ± 0.08
χ^2 / dof	1228 / 916	1017 / 915	949 / 915

do produce a χ_r^2 close to 1.0. Hence, our abundance analysis will be based on the multi-temperature models. There are other models that fit the data equally well. These alternative models will be discussed in Sect. 4.4.3. The potential presence of a relatively small contribution of other emission components however is of no consequence for the observed trends we present in this section.

An example of a spectrum fitted with a DEM model is shown in Fig. 4.3. When we set the line emission to zero in our model and plot the residuals, we obtain the plot shown in Fig. 4.4. The lines from all elements for which we fit abundances are evident in the spectrum. Especially the iron lines are very strong, but also silicon, sulfur and calcium have a high signal-to-noise. Oxygen, magnesium, argon and nickel are clearly visible: this plot shows the total spectrum; the strengths of these lines are weaker in individual annuli.

The spectral models constrain the abundances very well, except for neon and magnesium, because these lines are blended with iron at this spectral resolution (see Fig. 4.4). The determination of the oxygen abundance becomes difficult in the outer parts of the cluster. Here, the oxygen in the galactic foreground emission starts to play a more important role and could bias the abundance measurement. In the central region ($\lesssim 4'$) the cluster flux is high enough to get an accurate measurement. In general, all abundances are between 0.1 and 0.6 times their solar value (Table 4.4). Only neon

Table 4.5: Fit results for RGS spectra extracted from a $4'$ wide strip and fitted over a $8\text{--}38 \text{ \AA}$ range ignoring data from CCD2 (see text). Emission measures ($Y = \int n_e n_H dV$) are given in 10^{66} cm^{-3} . The iron abundance is given with respect to solar abundances. The scale factors for oxygen and iron mentioned below are those explained in Sect. 4.2.2.

Parameter	single-temp	<i>w</i> dem-model	<i>g</i> dem-model
Y	7.27 ± 0.06	7.08 ± 0.07	7.25 ± 0.06
kT (keV)	2.6 ± 0.09		3.25 ± 0.18
kT_{mean} (keV)		3.04 ± 0.16	
kT_{max} (keV)		4.0 ± 0.2	
α		0.46 ± 0.03	
σ			0.28 ± 0.02
C/Fe	0.00 ± 0.19	0.0 ± 0.4	0.0 ± 0.3
N/Fe	0.00 ± 0.18	0.1 ± 0.5	0.0 ± 0.5
O/Fe	0.85 ± 0.10	0.87 ± 0.10	0.91 ± 0.13
Ne/Fe	1.04 ± 0.15	0.73 ± 0.12	0.71 ± 0.14
Mg/Fe	0.32 ± 0.11	0.35 ± 0.11	0.32 ± 0.12
Fe	0.98 ± 0.06	1.20 ± 0.08	1.14 ± 0.09
Scale (O)	1.1 ± 0.2	1.6 ± 0.3	1.5 ± 0.3
Scale (Fe)	0.35 ± 0.05	0.36 ± 0.05	0.31 ± 0.05
χ^2 / dof	997 / 856	925 / 854	963 / 855

shows high values up to 1, but since the lines of this element are blended with the Fe-L complex, the value is highly correlated with the temperature distribution.

In Fig. 4.5 we present the total RGS spectrum of Sérsic 159-03 extracted from a $4'$ wide strip in the cross-dispersion direction and centred on the core. Because of the high statistics, we can also use the second order spectrum. In both orders the Fe-L spectral line complex between $10\text{--}15 \text{ \AA}$ and the Mg line near 9 \AA are well resolved. Above 19 \AA the first order spectrum shows a prominent O VIII Ly α line.

The fit results for RGS are shown in Table 4.5. The elemental abundances determined from the different models are consistent with each other within 3σ . Unfortunately, the carbon and nitrogen abundances are not well constrained. The width of the oxygen line is consistent with the width of the line profile derived from the continuum emission in MOS1, and the width of the iron lines is about $1/3$ smaller (Fig. 4.6). This suggests that the oxygen distribution is more extended across the cluster centre, while the iron abundance is strongly peaked in the centre. Looking at the χ^2 values we see that the fit to the RGS data does not strongly prefer a DEM distribution over a single-temperature model. All models are acceptable, contrary to the merging cluster 2A 0335+096 described by Chapter 5.

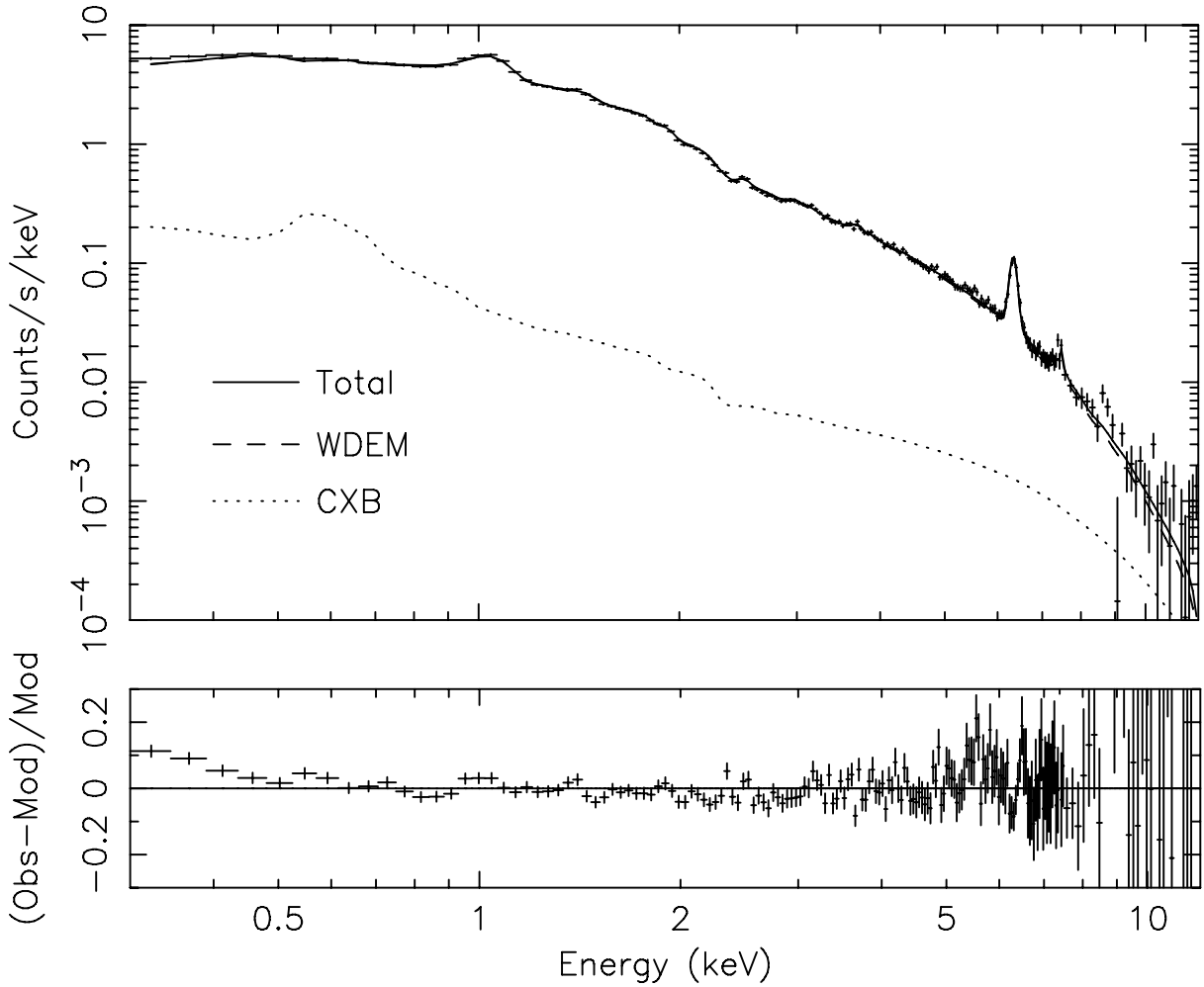


Figure 4.3: EPIC spectrum extracted from a circular region of $4'$ around the core. The total best-fit model, the *wdem* model component and the background component are shown.

Radial profiles using thermal DEM models

By fitting the spectra extracted from the annuli for EPIC and from strips for RGS, we can make radial profiles of temperatures and abundances. Again, we fit the spectra with a single-temperature model, a *wdem* model and a *gdem* model (Table 4.6). In Fig. 4.7 (left panel) we present the temperature profile obtained for these models. For *wdem* the maximum temperature (kT_{\max}) and mean temperature (kT_{mean}) are shown. The profile shows a slight increase of the temperature within a $2'$ radius. Beyond $3'$ the temperature rapidly drops to about 1.5 keV. The single-temperature profile is consistent with the profile derived from the earlier XMM-Newton observation by Kaastra et al. (2001).

The DEM parameters α (*wdem*, Fig. 4.7 middle panel) and σ_T (*gdem*, Fig. 4.7 right panel) are quite constant, but increase slightly in the outer parts, where the temperature gradient is large. This means that the fit needs a broader range of temperatures to fit the spectrum.

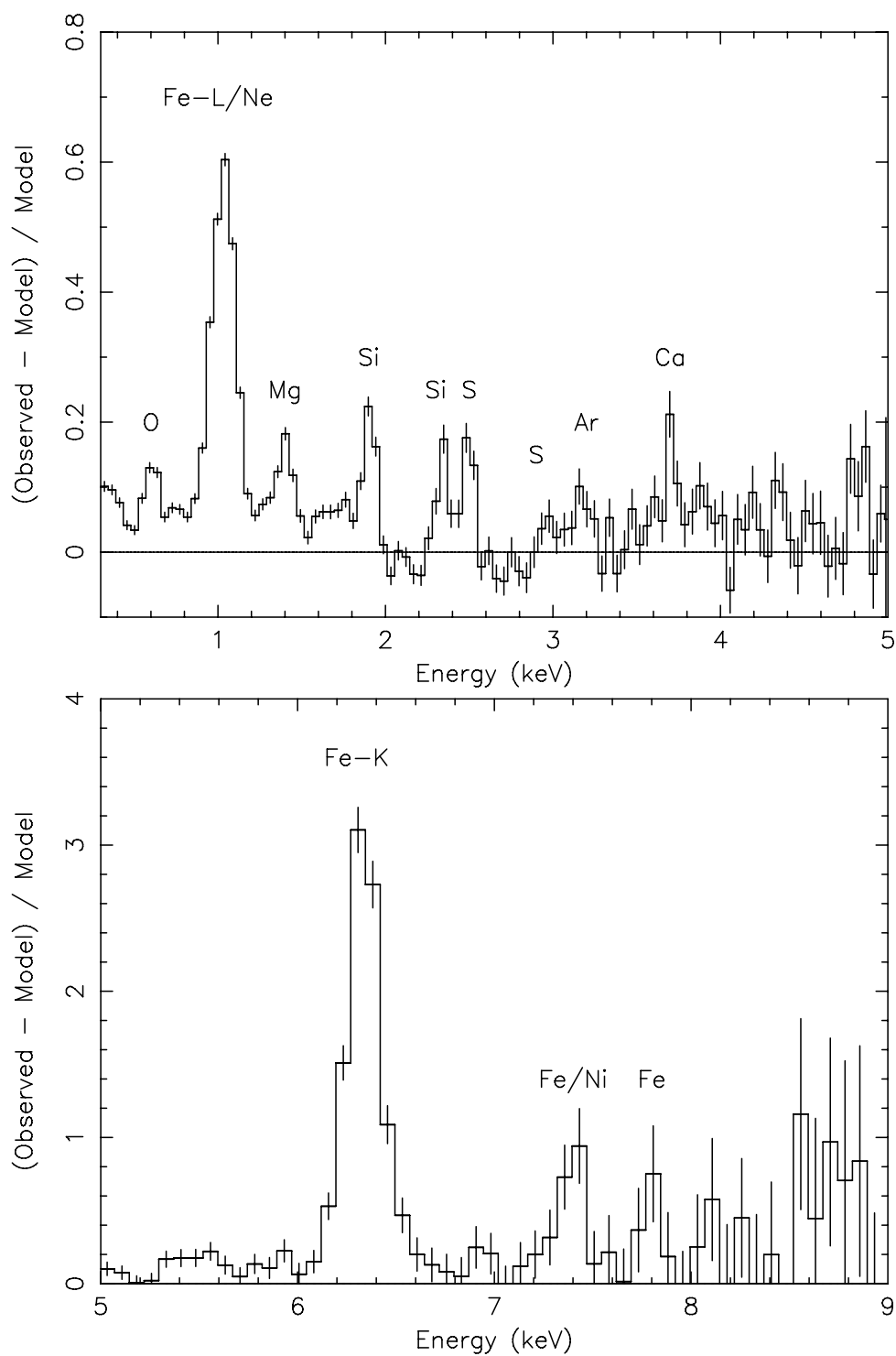


Figure 4.4: Residuals of a *wdem* fit to the EPIC total spectrum extracted from a circle with a radius of $4'$. The line emission in the model is set to zero to show the line emission on top of the continuum. The upper panel shows the residuals from 0.3–5 keV and the lower panel the 5–10 keV range.

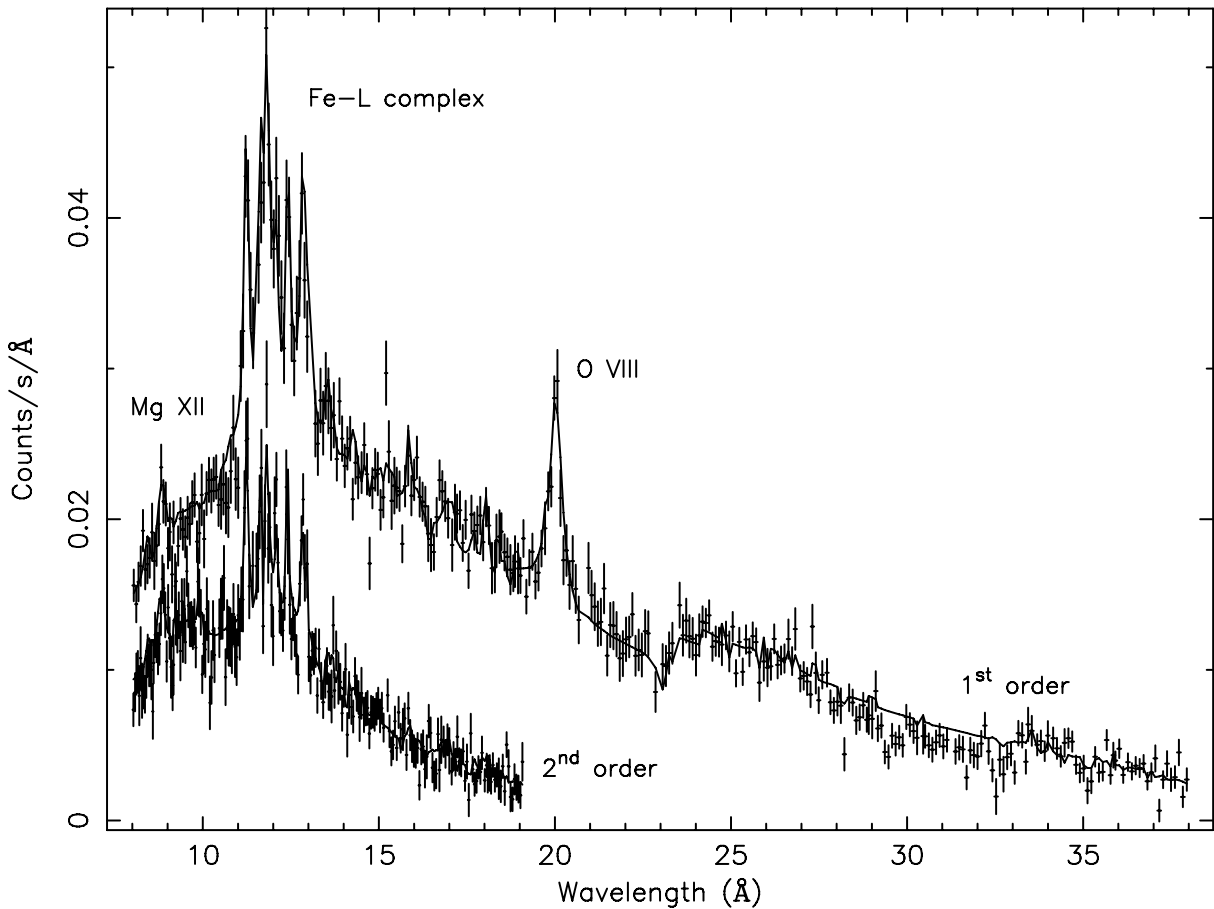


Figure 4.5: 1^{st} and 2^{nd} order RGS spectrum of Sérsic 159-03 extracted from a $4'$ wide strip centred on the core. The continuous line represents the fitted *wdem* model. On the x-axis we show the observed wavelength.

From the fits we obtain radial profiles of the abundances of several elements. The radial profiles of oxygen, silicon, and iron are shown in Fig. 4.8. We detect a clear decrease of the silicon and iron abundance with radius. For oxygen the situation is less clear: the O/Fe ratio in the 0–0.5' bin is lower than the ratio in the 0.5–4' interval at 3σ confidence level. There is a hint of a decrease of the oxygen abundance like we see for iron, but a flat distribution cannot be excluded.

While silicon is quite well constrained independent of the DEM model used, the iron abundance derived from the *gdem* model is significantly different from the other two models. The absolute values of the *gdem* oxygen and iron abundances are consistent with the ones from silicon. The iron abundance from the single-temperature and *wdem*, however, show a steeper gradient. From these plots it is clear that the used temperature distribution is very important when measuring elemental abundances.

An overview of all the fitted parameters is given in Table 4.6. Apart from the elements we discussed in the previous paragraph, only sulfur is reasonably well constrained up to 9'. In the outermost spatial bin, however, the abundance increases to unphysical values. In the core region sulfur shows the same profile as silicon. The

Table 4.6: Fit results for spatially resolved EPIC spectra. The fitted models are single-temperature CIE (s), *wdem* (w) and a Gaussian DEM model (g). Fluxes are calculated over the 0.3–10 keV range and are given in unit $\text{erg s}^{-1} \text{cm}^{-2} \text{deg}^{-2}$. Emission measures ($Y = \int n_e n_H dV$) are given in 10^{66}cm^{-3} .

	M	0–0.5′	0.5–1.0′	1.0–2.0′	2.0–3.0′
Y	s	4.75 ± 0.05	5.55 ± 0.05	6.17 ± 0.05	2.88 ± 0.03
	w	4.72 ± 0.05	5.58 ± 0.05	6.23 ± 0.05	2.91 ± 0.03
	g	4.86 ± 0.04	5.72 ± 0.05	6.36 ± 0.05	2.97 ± 0.03
F	s	$(2.59 \pm 0.02) \times 10^{-8}$	$(1.038 \pm 0.009) \times 10^{-8}$	$(2.76 \pm 0.02) \times 10^{-9}$	$(7.72 \pm 0.09) \times 10^{-10}$
	w	$(2.60 \pm 0.03) \times 10^{-8}$	$(1.042 \pm 0.010) \times 10^{-8}$	$(2.77 \pm 0.02) \times 10^{-9}$	$(7.79 \pm 0.09) \times 10^{-10}$
	g	$(2.61 \pm 0.02) \times 10^{-8}$	$(1.047 \pm 0.010) \times 10^{-8}$	$(2.78 \pm 0.02) \times 10^{-9}$	$(7.84 \pm 0.08) \times 10^{-10}$
kT (keV)	s	2.353 ± 0.012	2.557 ± 0.013	2.640 ± 0.015	2.64 ± 0.03
	g	2.280 ± 0.011	2.471 ± 0.013	2.547 ± 0.015	2.57 ± 0.02
kT_{mean}	w	2.39 ± 0.03	2.59 ± 0.05	2.67 ± 0.05	2.69 ± 0.08
kT_{max}	w	3.01 ± 0.03	3.27 ± 0.04	3.42 ± 0.05	3.51 ± 0.08
α	w	0.350 ± 0.019	0.36 ± 0.03	0.39 ± 0.03	0.44 ± 0.05
σ_T	g	0.203 ± 0.005	0.208 ± 0.007	0.209 ± 0.008	0.236 ± 0.012
O/Fe	s	0.76 ± 0.12	1.12 ± 0.13	1.17 ± 0.17	1.3 ± 0.3
	w	0.76 ± 0.11	1.05 ± 0.14	1.06 ± 0.17	1.2 ± 0.3
	g	0.77 ± 0.10	1.05 ± 0.13	1.05 ± 0.17	1.0 ± 0.3
Ne/Fe	s	2.6 ± 0.2	2.0 ± 0.2	1.4 ± 0.3	1.4 ± 0.4
	w	0.9 ± 0.2	0.4 ± 0.3	0.00 ± 0.15	0.0 ± 0.2
	g	0.00 ± 0.16	0.00 ± 0.07	0.00 ± 0.05	0.00 ± 0.09
Mg/Fe	s	0.10 ± 0.10	0.00 ± 0.12	0.00 ± 0.08	0.01 ± 0.19
	w	0.29 ± 0.10	0.18 ± 0.13	0.13 ± 0.15	0.3 ± 0.3
	g	0.34 ± 0.14	0.20 ± 0.18	0.1 ± 0.2	0.5 ± 0.4
Si/Fe	s	0.58 ± 0.05	0.45 ± 0.06	0.57 ± 0.07	0.38 ± 0.12
	w	0.69 ± 0.05	0.56 ± 0.06	0.70 ± 0.08	0.51 ± 0.13
	g	1.07 ± 0.08	0.88 ± 0.09	1.08 ± 0.12	0.8 ± 0.2
S/Fe	s	0.43 ± 0.06	0.34 ± 0.07	0.19 ± 0.09	0.22 ± 0.16
	w	0.56 ± 0.06	0.47 ± 0.08	0.35 ± 0.09	0.40 ± 0.15
	g	0.90 ± 0.09	0.76 ± 0.11	0.57 ± 0.13	0.7 ± 0.2
Ar/Fe	s	0.02 ± 0.13	0.20 ± 0.17	0.4 ± 0.2	0.0 ± 0.4
	w	0.19 ± 0.14	0.39 ± 0.18	0.7 ± 0.2	0.2 ± 0.4
	g	0.4 ± 0.2	0.7 ± 0.3	1.2 ± 0.4	0.4 ± 0.7
Ca/Fe	s	0.59 ± 0.18	1.1 ± 0.2	1.1 ± 0.3	1.0 ± 0.5
	w	0.67 ± 0.18	1.3 ± 0.2	1.2 ± 0.3	1.0 ± 0.6
	g	1.2 ± 0.3	2.3 ± 0.4	2.2 ± 0.5	1.7 ± 1.1
Fe	s	0.453 ± 0.012	0.381 ± 0.010	0.294 ± 0.009	0.239 ± 0.011
	w	0.458 ± 0.011	0.371 ± 0.011	0.282 ± 0.009	0.224 ± 0.012
	g	0.314 ± 0.007	0.253 ± 0.007	0.191 ± 0.007	0.148 ± 0.008
Ni/Fe	s	1.0 ± 0.2	0.9 ± 0.2	0.0 ± 0.3	0.0 ± 0.2
	w	1.2 ± 0.2	1.0 ± 0.3	0.2 ± 0.3	0.0 ± 0.5
	g	1.4 ± 0.3	1.1 ± 0.4	0.0 ± 0.5	0.0 ± 0.8
χ^2 / dof	s	1213 / 829	1084 / 846	1240 / 852	1191 / 804
	w	1045 / 828	969 / 845	1136 / 851	1109 / 803
	g	981 / 828	890 / 845	1083 / 851	1034 / 803

Table 4.7: Annuli from 3–9' (Table 4.6 continued).

	M	3.0–4.0'	4.0–6.0'	6.0–9.0'
Y	s	1.40±0.02	1.62±0.04	1.21±0.04
	w	1.42±0.02	1.62±0.03	1.21±0.03
	g	1.44±0.02	1.55±0.03	0.94±0.04
F	s	$(3.17±0.05)×10^{-10}$	$(1.08±0.02)×10^{-10}$	$(2.59±0.08)×10^{-11}$
	w	$(3.20±0.05)×10^{-10}$	$(1.093±0.019)×10^{-10}$	$(2.59±0.08)×10^{-11}$
	g	$(3.24±0.05)×10^{-10}$	$(1.112±0.018)×10^{-10}$	$(2.59±0.09)×10^{-11}$
kT (keV)	s	2.50±0.04	2.21±0.05	1.41±0.04
	g	2.48±0.04	2.40±0.05	1.83±0.09
kT_{mean}	w	2.56±0.12	2.27±0.11	
kT_{max}	w	3.31±0.13	2.90±0.12	1.42±0.08
α	w	0.42±0.07	0.38±0.07	0.01±0.09
σ_{T}	g	0.244±0.019	0.24±0.02	0.14±0.04
O/Fe	s	1.2±0.4	0.2±1.0	0.0±1.7
	w	1.1±0.4	0.4±0.6	0.0±1.7
	g	0.4±0.4	0.00±0.05	0.00±0.06
Ne/Fe	s	1.5±0.6	1.7±1.1	0.0±0.9
	w	0.0±0.5	0.2±0.9	0.0±0.9
	g	0.0±0.2	0.0±0.5	0.0±0.7
Mg/Fe	s	0.00±0.09	0.1±0.5	0.0±0.4
	w	0.00±0.11	0.3±0.5	0.0±0.4
	g	0.0±0.2	1.3±0.6	0.0±0.7
Si/Fe	s	0.43±0.09	0.8±0.3	0.5±0.5
	w	0.5±0.2	0.8±0.2	0.4±0.5
	g	0.9±0.3	1.4±0.4	0.7±0.6
S/Fe	s	0.3±0.3	0.97±0.17	5.6±1.7
	w	0.5±0.2	1.0±0.4	5.6±1.8
	g	0.9±0.4	1.3±0.5	3.5±1.2
Ar/Fe	s	0.6±0.7	1.9±1.1	16.8±6.4
	w	0.8±0.7	1.8±1.1	17.0±6.4
	g	1.4±1.2	1.6±1.5	5.4±3.5
Ca/Fe	s	1.6±1.0	3.6±1.5	36.6±15.6
	w	1.6±1.0	3.0±1.6	36.2±15.9
	g	2.2±1.8	0.4±2.3	0.0±6.5
Fe	s	0.209±0.013	0.14±0.02	0.049±0.009
	w	0.196±0.017	0.140±0.016	0.049±0.009
	g	0.134±0.012	0.134±0.012	0.13±0.02
Ni/Fe	s	0.3±0.8	0.0±0.3	0.0±2.3
	w	1.1±1.0	0.0±0.3	0.0±2.4
	g	2.8±1.5	0.3±1.6	6.0±2.5
χ^2 / dof	s	1270 / 772	1113 / 777	1045 / 757
	w	1218 / 771	1095 / 776	1045 / 756
	g	1131 / 771	1042 / 776	1079 / 756

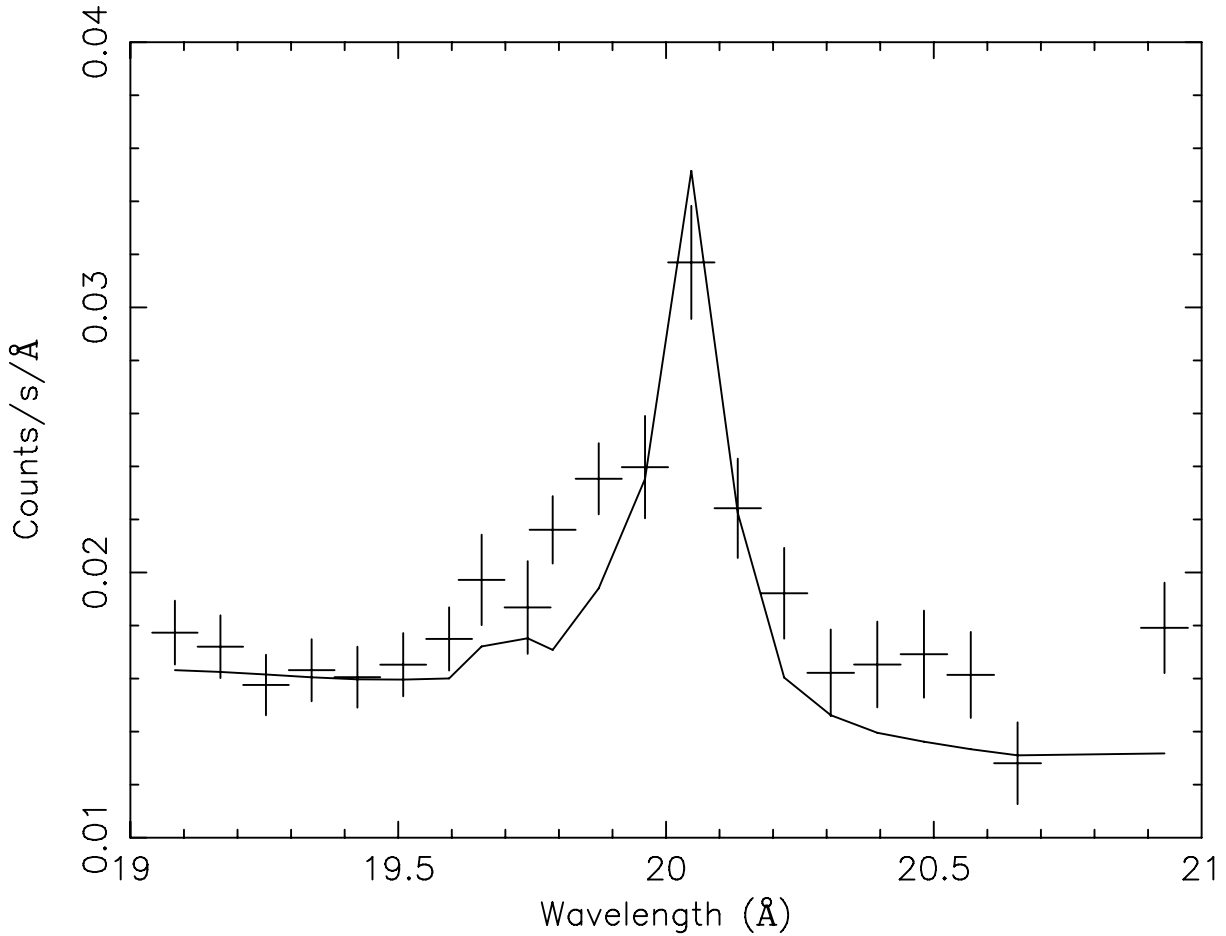


Figure 4.6: RGS spectrum in the 19–21 Å band featuring the O VIII Ly- α line. The data points represent the measured spectrum, while the model line shows the line when the scale factor is frozen to ~ 0.3 , which is the best-fit value for the iron lines.

other elements are less well constrained. Neon is always difficult to measure at CCD resolution because it is blended with the Fe-L complex near 1 keV. Calcium and nickel are only constrained in the core, but the derived values are not affected by systematics due to different DEM models. In every radial bin the values are consistent with each other. The magnesium and argon abundances are poorly determined. Only in the core region some points are measured at a significance larger than 2σ . In general these two elements have upper limits of about 0.2 times the solar abundances.

The χ^2 values for the three models are also shown in Table 4.6. In the core region all fits are acceptable when we use the condition $\chi_r^2 < 1.5$. However, the χ_r^2 for the single temperature model in the core is much less than in Chapter 5 in the cluster 2A 0335+096. In the outer parts multi-temperature fitting still results in a better fit, but we do not see significant differences between the models.

From RGS we also extract rectangular regions in the cross-dispersion direction of the instrument. The regions we use are defined in Sect. 4.2.2. Because the cluster does not show significant spatial asymmetries in the cross-dispersion direction, we add the

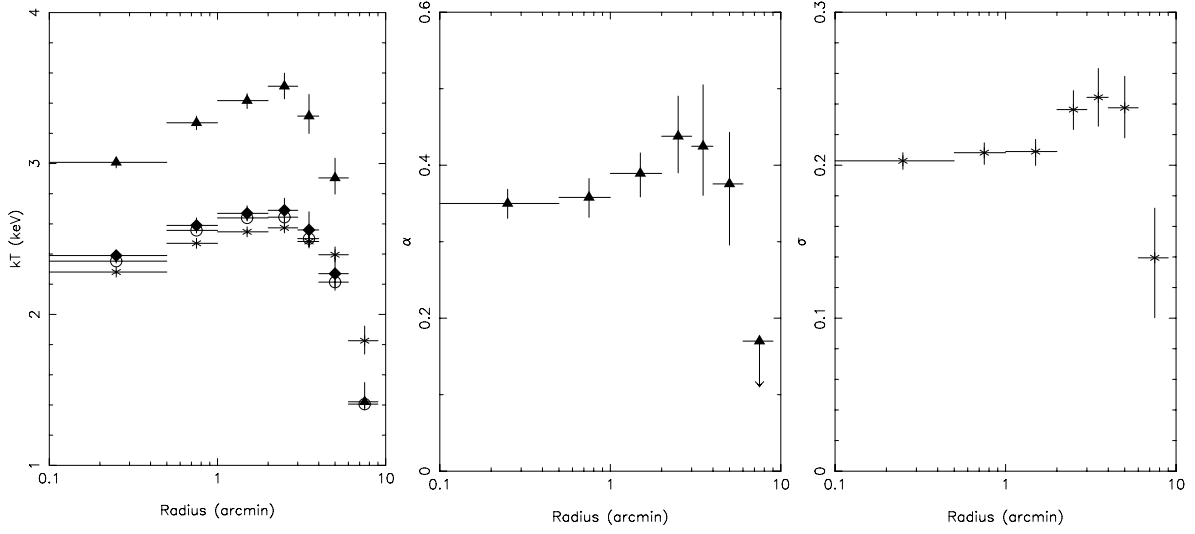


Figure 4.7: DEM model fit results for the three models: single-temperature (\circ), *wdem* (\blacktriangle) and *gdem* (*). In the left panel we show the radial temperature profiles for all models, including the kT_{\max} (\blacktriangle) and kT_{mean} (\blacklozenge) from the *wdem* parameters. In the middle and right panel we show the radial profiles of the DEM parameters α and σ_T .

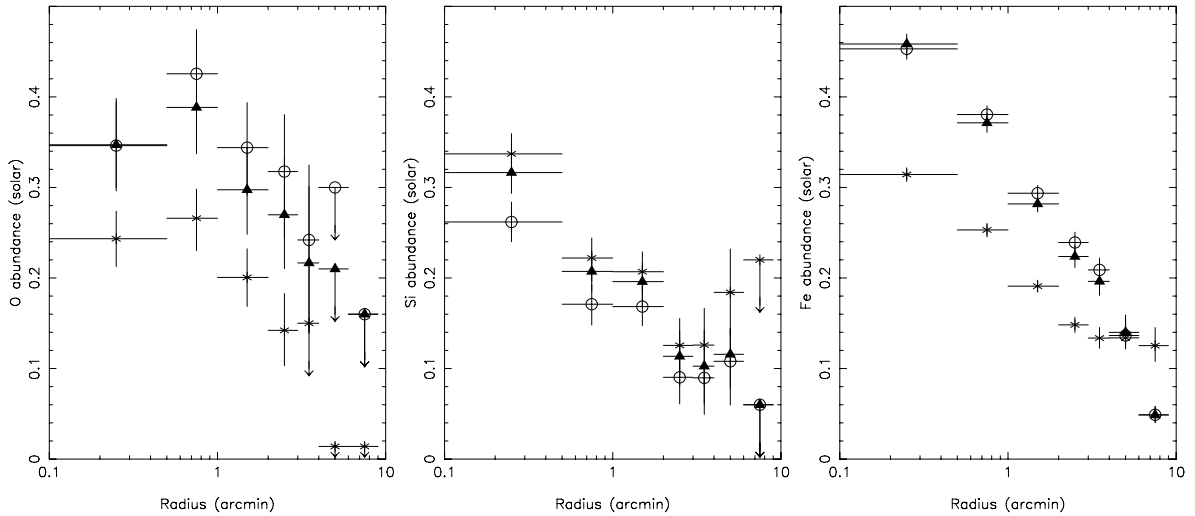


Figure 4.8: Abundance profiles of oxygen, silicon and iron derived using three models: single-temperature (\circ), *wdem* (\blacktriangle) and *gdem* (*).

spectra extracted from regions with equal distance to the dispersion axis: region 1 + 5 and 2 + 4 as defined in the lower panel of Fig. 4.2. This way we are able to derive radial profiles of the core up to a radius of $2'$. The best fit values for three models are presented in Table 4.8. The fit results show signs of a temperature decrement in the core. However, the temperatures we determine from RGS are systematically higher than those from EPIC. This is not surprising, because the RGS spectrum also contains emission from the hot gas just outside $2'$ which falls within the rectangular field-of-view. From the *wdem* model fits we see that the value of α increases with radius, while the

width of the Gaussian DEM distribution shows a drop in the 1.0–2.0′ bin. As expected from the EPIC profiles, the O/Fe ratio is lower in the core than in the outer parts. The Ne/Fe ratio, however, is consistent with being flat within 2′ from the core. Finally, the width of the lines, indicated by the scale parameter (see Sect. 4.2.2), increases outside the core. There it is consistent with being 1.0. In these models we fit the average of all the line widths with respect to the continuum surface brightness.

From the O and Fe abundances measured with EPIC and RGS in the inner 2′ of the cluster, we detect a jump in the O/Fe ratios between the inner 0.5′ and the annulus from 0.5–2.0′. To illustrate this, we combine the single-temperature EPIC and RGS results in the 0.5–2.0′ region. From EPIC we obtain $(\text{O}/\text{Fe})_{0.5'-2.0'} = 1.14 \pm 0.10$ which is significantly higher than the central $(\text{O}/\text{Fe})_{0.0'-0.5'} = 0.76 \pm 0.12$. The combined O/Fe ratio from the 0.5–2.0′ RGS results is also significantly higher, $(\text{O}/\text{Fe})_{0.5'-2.0'} = 0.84 \pm 0.09$, compared to the central value $(\text{O}/\text{Fe})_{0.0'-0.5'} = 0.53 \pm 0.05$. This jump has a confidence of 2.5σ and 3σ in EPIC and RGS respectively, which corresponds to a combined significance of 3.9σ . Despite the fact that the absolute values of the O/Fe ratio are different for the EPIC and RGS results, the relative increase of the O/Fe ratio is the same for both instruments: 1.5 ± 0.3 (EPIC) and 1.6 ± 0.2 (RGS). In the *wgem* and *gdem* results the relative jump in O/Fe is equal or lower, but still consistent with the result for the single temperature model: 1.4 ± 0.3 (EPIC/*wdem*), 1.4 ± 0.2 (EPIC/*gdem*), 1.6 ± 0.3 (RGS/*wdem*) and 1.5 ± 0.3 (RGS/*gdem*).

4.4.2 Abundances and SNIa/SNII/Population-III models

From the single-temperature (CIE) and DEM models we fit to the data, we obtain the abundances of the elements for which line emission is detected. Assuming that all the elements originate from SNIa, SNII and PopIII stars, we can construct a simple model to obtain the relative contribution of these objects to the enrichment of the ICM.

We use several SNIa yields obtained from two physically different models adapted from Iwamoto et al. (1999) to fit our abundances. The W7 model describes a so-called slow deflagration model, while the WDD2 is calculated using delayed-detonation (DD) models, which is the currently favoured Type Ia explosion scenario. Note that with SNII we mean all types of core-collapse supernovae including types Ib and Ic. We use the SNII yields integrated over the stellar population calculated by Tsujimoto et al. (1995) and Iwamoto et al. (1999). For the PopIII-star SN yields we use two models from Heger & Woosley (2002) with different core masses of the PopIII star: $65 M_{\odot}$ and $130 M_{\odot}$. These two masses are the lowest and the highest core mass considered in Heger & Woosley (2002).

For every element i the total number of particles N_i is a linear combination of the number of atoms produced by supernova type Ia ($Y_{i,\text{Ia}}$), type II ($Y_{i,\text{II}}$) and PopIII stars ($Y_{i,\text{III}}$).

$$N_i = aY_{i,\text{Ia}} + bY_{i,\text{II}} + cY_{i,\text{III}}, \quad (4.8)$$

where a , b and c are multiplication factors of SNIa, SNII, and PopIII stars respectively. The total number of particles for an element can be easily converted into a number abundance. This reduces to a system of three variables (a , b and c) and nine data points

Table 4.8: Fit results for spatially resolved RGS spectra between 8–38 Å excluding CCD2. The fitted models are single-temperature CIE (s), *wdem* (w) and a Gaussian DEM model (g). Emission measures ($Y = \int n_e n_H dV$) are given in 10^{66} cm^{-3} . The iron abundance is fixed to 1.0 with respect to solar abundances.

Parameter	Mod	0–0.5′	0.5–1.0′	1.0–2.0′
Y	s	3.69 ± 0.04	1.80 ± 0.04	1.46 ± 0.03
	w	3.60 ± 0.04	1.78 ± 0.04	1.30 ± 0.05
	g	3.74 ± 0.04	1.88 ± 0.05	1.46 ± 0.04
kT (keV)	s	3.23 ± 0.09	4.2 ± 0.2	4.3 ± 0.3
	g	4.09 ± 0.16	5.1 ± 0.6	4.3 ± 0.3
kT_{mean}	w	3.53 ± 0.14	4.7 ± 0.4	4.3 ± 0.5
kT_{max}	w	4.76 ± 0.18	6.6 ± 0.5	6.5 ± 0.7
α	w	0.53 ± 0.04	0.66 ± 0.09	1.06 ± 0.18
σ_T	g	0.342 ± 0.018	0.35 ± 0.06	0.00 ± 0.12
O/Fe	s	0.53 ± 0.05	0.77 ± 0.12	0.96 ± 0.15
	w	0.51 ± 0.05	0.72 ± 0.12	1.2 ± 0.3
	g	0.54 ± 0.05	0.68 ± 0.18	0.93 ± 0.17
Ne/Fe	s	1.10 ± 0.12	1.7 ± 0.3	0.8 ± 0.4
	w	0.79 ± 0.11	0.9 ± 0.3	0.00 ± 0.10
	g	0.75 ± 0.12	0.9 ± 0.4	0.8 ± 0.4
Mg/Fe	s	0.16 ± 0.10	0.00 ± 0.10	0.00 ± 0.04
	w	0.32 ± 0.11	0.0 ± 0.2	0.00 ± 0.12
	g	0.28 ± 0.11	0.00 ± 0.11	0.00 ± 0.05
Scale	s	0.50 ± 0.08	1.14 ± 0.17	1.3 ± 0.3
	w	0.45 ± 0.07	1.1 ± 0.2	2.8 ± 0.4
	g	0.40 ± 0.07	0.8 ± 0.3	1.3 ± 0.2
$\chi^2 / \text{d.o.f.}$	s	1100 / 858	970 / 858	925 / 858
	w	1000 / 855	953 / 855	885 / 855
	g	1039 / 857	971 / 857	926 / 857

(O, Ne, Mg, Si, S, Ar, Ca, Fe and Ni). We present the ratio of the relative numbers of SNIa, SNII and PopIII with respect to the total number.

We fit the abundances we obtain from the EPIC results of the core region to a model consisting of SNIa, SNII and PopIII-star yields in order to determine their relative contribution to the ICM. In Table 4.9 we compare two SNIa yield models fitted together with the SNII and PopIII yield models to the measured abundances in Table 4.4. We use the abundances derived from the fits with the *wdem* model. If we include the calcium abundance, none of the fits are statistically acceptable. However, if we ignore the calcium data point, we obtain a χ_r^2 of about 1 for the WDD2 model. We also test other SNIa models listed in Iwamoto et al. (1999): W70, WDD1, WDD3, CDD1 and CDD2. Their best-fit ratios were in general similar to the WDD2 and W7 models, but with a higher χ^2 .

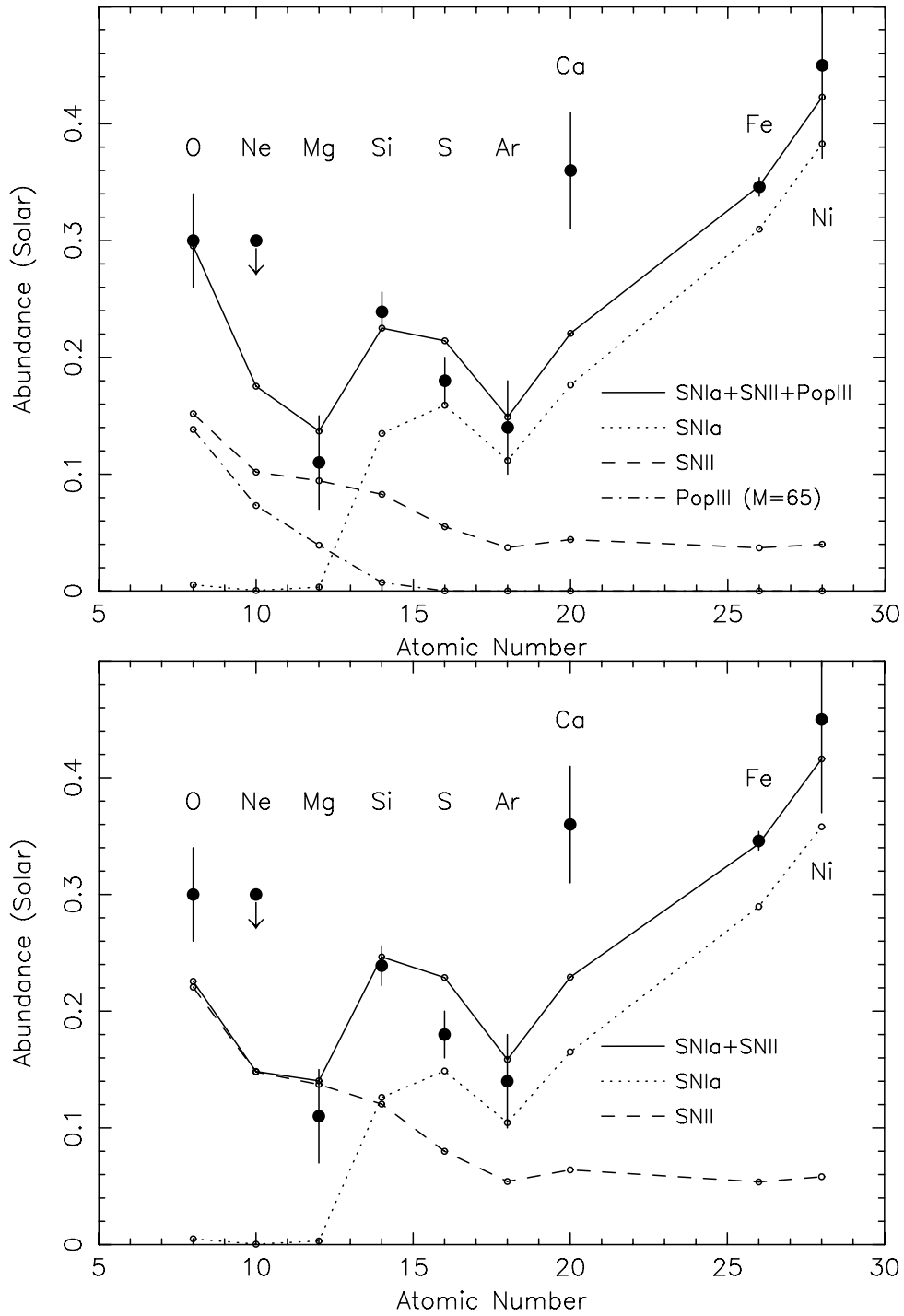


Figure 4.9: The elemental abundances derived from a *wdem* fit, fitted with the WDD2 SNIa-yield model. The best fit from Table 4.9 is shown in the upper panel with a PopIII mass of $65 M_{\odot}$. In the plot we also show the SNIa, SNII and PopIII contribution separately. In the lower panel we show a fit without a PopIII contribution. In both plots the calcium abundance is included in the fit.

Table 4.9: Relative contribution of SNIa, SNII and PopIII stars to the enrichment of the ICM. We compare two SNIa models in Iwamoto et al. (1999) with the data. We only show results from *wdem* fits, because we could only get an acceptable fit using these data. The values shown here are the fractions with respect to the sum of all contributions (SNIa + SNII + PopIII).

Type	$M_{\text{PopIII}} = 130M_{\odot}$		$M_{\text{PopIII}} = 65M_{\odot}$	
	Value	χ^2 / dof	Value	χ^2 / dof
W7				
SNIa	0.33 ± 0.09		0.30 ± 0.04	
SNII	0.7 ± 0.2	41 / 6	0.70 ± 0.14	55 / 6
PopIII	$(3.4 \pm 1.4) \times 10^{-3}$		$(-3 \pm 7) \times 10^{-3}$	
WDD2				
SNIa	0.38 ± 0.08		0.48 ± 0.10	
SNII	0.63 ± 0.15	12 / 6	0.5 ± 0.2	12 / 6
PopIII	$(-1.8 \pm 1.2) \times 10^{-3}$		$(1.7 \pm 1.1) \times 10^{-2}$	
<i>Fits with the calcium abundance excluded:</i>				
Type	$M_{\text{PopIII}} = 130M_{\odot}$		$M_{\text{PopIII}} = 65M_{\odot}$	
	Value	χ^2 / dof	Value	χ^2 / dof
W7				
SNIa	0.34 ± 0.09		0.32 ± 0.05	
SNII	0.7 ± 0.2	29 / 5	0.69 ± 0.15	41 / 5
PopIII	$(2.9 \pm 1.3) \times 10^{-3}$		$(-2 \pm 7) \times 10^{-3}$	
WDD2				
SNIa	0.38 ± 0.08		0.50 ± 0.10	
SNII	0.62 ± 0.15	4.9 / 5	0.5 ± 0.2	4.1 / 5
PopIII	$(-1.9 \pm 1.2) \times 10^{-3}$		$(1.9 \pm 1.2) \times 10^{-2}$	

The relative contribution of PopIII stars is in all fits smaller than three times its error, thus it is not significantly detected. Because of the large yields per PopIII event, a small number of PopIII stars can in principal contribute a lot to the abundance. The abundance pattern of PopIII stars, however, resemble the patterns of SNIa and SNII depending on the core mass. The SNIa or SNII patterns can mostly compensate for the PopIII contribution, when it is left out in the fit. The χ^2 does improve only marginally when we add PopIII star yields to a model containing only SNIa and SNII yields. The best fit using just SNIa and SNII models including calcium gives a χ^2/dof of 15 / 7 and a SNIa contribution of 0.35 ± 0.03 . In fact some models fit the data best by putting a negative value to the PopIII or SNII contribution, which is unphysical. The $65 M_{\odot}$ PopIII model produces a slightly higher PopIII contribution than the one for $130 M_{\odot}$. But since the mass of the expelled material is higher for the latter model, the number of stars needs to be higher in the $65 M_{\odot}$ model to get a comparable effect. The errors on these bigger values are also too large to claim a significant PopIII-star contribution.

In Fig. 4.9 we plot the abundances from the *wdem* model with the best-fit model

(WDD2) listed in Table 4.9. Note that the WDD2 model is also the type Ia model favoured by Iwamoto et al. (1999) on observational grounds. The data points we use are taken from the third column of Table 4.4. From this plot we see that the calcium abundance might be underestimated by the nucleosynthesis models and the cause of the high χ^2 values. But the actual uncertainties in the measured calcium abundance might be bigger than the statistical error indicated here. This calcium overabundance is also seen in the analysis of 2A 0335+096 (Chapter 5), confirming that the overabundance is probably not a statistical deviation. Every other abundance is consistent with the model within the error bars. The contribution of PopIII can be seen mainly in oxygen and neon, but the uncertainties are large.

We applied the same procedure to the abundances obtained from RGS. The relative abundances determined from RGS are very well constrained, but the number of elements that we can measure is too small to get a reasonable fit. If we fit the abundances we obtain errors which are equal to the measured values. Therefore, we do not show these fits in this paper.

4.4.3 Non-thermal X-ray emission?

In previous papers about Sérsic 159-03 (e.g. Kaastra et al. 2003a; Bonamente et al. 2005) the larger χ_r^2 for the single-temperature model is attributed to a soft X-ray excess. There are, however, a number of solutions to fit this soft excess and to obtain an acceptable χ_r^2 of about 1.0. From the spectral fits in Sect. 4.4.1 we confirm that a single-temperature model is not the best description for the observed spectra. If we fit the data with a multi-temperature model, then we obtain a χ_r^2 of about 1.0. In this section we explore the possibility of the existence of a soft excess in Sérsic 159-03 and speculate about its nature. The *wdem* and *gdem* models already provide acceptable fits to the spectra. We verified that the non-thermal component presented in this section does not affect the trends observed in the thermal analysis listed in Sect. 4.4.1.

One possibility is that the soft X-ray emission originates from warm thermal emission from the WHIM (Kaastra et al. 2003a). Here we explore the possibility that inverse-Compton emission from CMB photons which are up-scattered to X-ray energies by relativistic electrons can also cause a soft excess. The same emission mechanism is also thought to be the origin of the hard excess in clusters of galaxies detected by BeppoSAX (e.g. Fusco-Femiano et al. 2005). A power-law component describing this inverse-Compton emission might be able to fit both this hard and soft excess.

A single non-thermal component as illustrated in Fig. 4.10 with a Γ of 2.0 can explain both hard and soft X-ray excess with respect to a single-temperature model. At low energies $\lesssim 0.5$ keV the power-law component is comparable in flux to the thermal component, hence causing a soft excess. Above ~ 5 keV the power-law component in this example is even stronger than the thermal component, causing a hard X-ray excess. In Sérsic 159-03 the power-law emission is not as strong as in this example, but a similar model is consistent with the data.

In order to learn whether the data allow the soft excess to be thermal or non-thermal in nature, we fit the spectra from all annuli (see Table 4.3) with a single-temperature

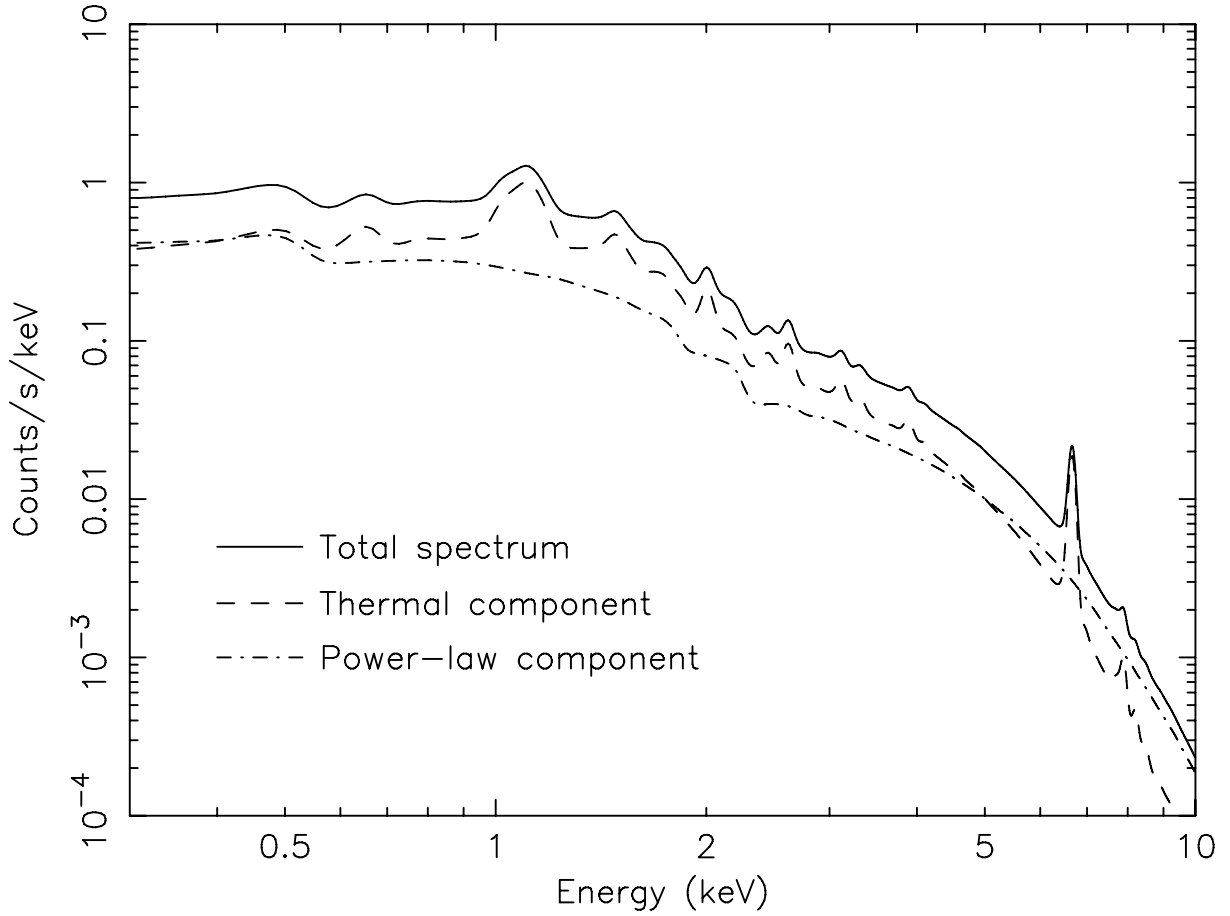


Figure 4.10: This spectrum shows that an underlying power-law component can cause both a soft and a hard excess. The figure shows a power-law component with $\Gamma = 2$, a single-temperature CIE component with a temperature of 2.5 keV and the total spectrum. The contribution of the power-law component is mostly noticeable below ~ 0.5 keV and above ~ 5 keV, hence causing a soft and hard excess with respect to the thermal component.

cluster component, a cold thermal component representing the WHIM, and a power-law component representing the soft and hard non-thermal emission. We first fit all annuli with the photon index and the kT of the cool component as a free parameter. Because the photon index and temperatures were not well constrained in the outer annuli, we fix the photon index and cool temperature in the final fits of all annuli to the mean value in the core region, which is 1.9 for the power-law index and 0.25 keV for the cool thermal component. This assumption for Γ is valid if the relativistic electrons are produced by acceleration in shocks, which behave similarly regardless of the position in the cluster. The radial profiles of the fitted components are shown in Fig. 4.11. The profile of the hot gas and the soft component have the same shape, which suggests that they have the same origin. The power-law component, however, has a more extended radial distribution. The flux is still the highest in the core of the cluster, but the slope of the radial profile is more shallow than the thermal emission. The ratio between the components is plotted in the right panel of Fig. 4.11. This figure

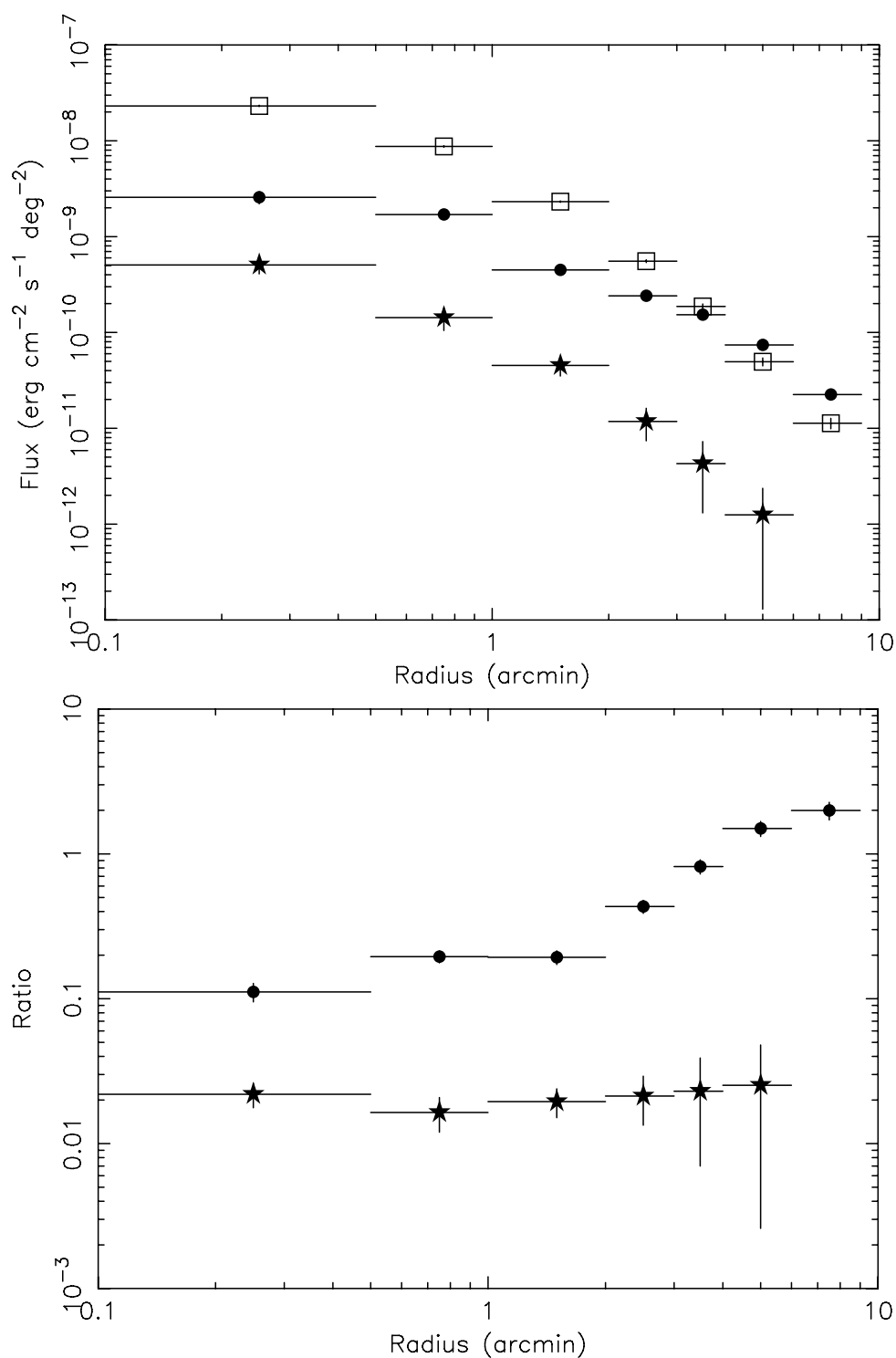


Figure 4.11: Upper panel: The 0.3–10 keV integrated intensities for three model components: Cluster hot gas (□), power law (●) and soft-excess (★). Lower panel: Ratio between the intensities: power law/hot cluster gas (●) and soft-excess/hot cluster gas (★).

Table 4.10: Fit results for an EPIC spectrum extracted from a circle with a radius of $4'$ and centred on the core including a single-temperature thermal component + power law and multi-temperature thermal components + power law. Fluxes are calculated over the 0.3–10 keV range and presented in 10^{-10} erg cm^{-2} s^{-1} deg^{-2} . Emission measure ($Y_{\text{thermal}} = \int n_e n_H dV$) is given in 10^{66} cm^{-3} and Y_{pow} is given in 10^{51} ph s^{-1} keV^{-1} at 1 keV.

Parameter	single-temp + pow	wdem + pow	gdem + pow
Y_{thermal}	16.8 ± 0.3	17.6 ± 0.3	18.9 ± 0.4
F_{thermal}	16.2 ± 0.2	16.9 ± 0.3	18.0 ± 0.5
kT	2.45 ± 0.02		2.50 ± 0.03
kT_{mean}		2.53 ± 0.07	
kT_{max}		3.14 ± 0.06	
α		0.32 ± 0.04	
σ_T			0.208 ± 0.012
O	0.27 ± 0.05	0.26 ± 0.05	0.17 ± 0.03
Ne	1.00 ± 0.11	0.42 ± 0.11	0.11 ± 0.09
Mg	0.18 ± 0.04	0.21 ± 0.05	0.18 ± 0.04
Si	0.32 ± 0.02	0.33 ± 0.02	0.33 ± 0.02
S	0.22 ± 0.02	0.25 ± 0.02	0.25 ± 0.02
Ar	0.20 ± 0.05	0.23 ± 0.05	0.26 ± 0.06
Ca	0.42 ± 0.06	0.45 ± 0.06	0.52 ± 0.07
Fe	0.433 ± 0.011	0.409 ± 0.011	0.275 ± 0.009
Ni	0.62 ± 0.11	0.60 ± 0.10	0.54 ± 0.10
Y_{pow}	6.6 ± 0.4	5.3 ± 0.4	3.5 ± 0.8
F_{pow}	3.5 ± 0.2	2.8 ± 0.2	1.6 ± 0.4
Γ	2.06 ± 0.03	2.10 ± 0.04	2.30 ± 0.15
χ^2 / dof	897 / 914	853 / 913	861 / 913

indeed shows that the ratio between the soft excess and the cluster gas is constant. This is not what you expect if the excess is due to WHIM which should be picked up preferably at the outskirts of the cluster. On the other hand, the power-law component does become relatively more important in the outskirts of the cluster. This is to be expected for Inverse-Compton emission because it scales with density n instead of n^2 which is true for thermal emission. The different profile of the power-law emission therefore strongly suggests that if there is an excess, it is non-thermal in nature.

In the following fits we drop the cool component and fit the spectra with just a thermal (DEM) components and an additional power-law component to fit the soft-excess (Table 4.10). The models including a power law generally result in a lower χ^2 . This effect is most strongly present in the single-temperature fit: $\chi^2 = 897 / 914$ with a power-law component and $\chi^2 = 1228 / 916$ without. But also for the DEM models there is an improvement in χ^2 that provides an argument for the presence of a non-thermal component.

The absolute values of the abundances change when an additional power law is

used, but the general trends do not change considerably. The spatial abundance distributions are also consistent with the trends observed in the single-temperature models. In particular, fits including a power-law component show that the jump in O/Fe in the centre of the cluster remains. However, the significance of the jump decreases compared to the single-temperature result when a power-law component is added.

Our suggestion that a single power-law component can both explain a possible soft as well as a hard excess of Sérsic 159-03, may also be relevant for several clusters for which non-thermal emission has been detected by BeppoSAX (Fusco-Femiano et al. 2000, 2004, 2005). However, the Coma-cluster is, so-far, the only cluster for which both a hard X-ray component and a soft excess has been reported (Fusco-Femiano et al. 2004; Kaastra et al. 2003a). For Sérsic 159-03, it does indeed seem to be the case that a single non-thermal component explains both the soft and hard X-ray excess: Extrapolating the BeppoSAX flux in the 20–80 keV range, $(1.5 \pm 0.5) \times 10^{-11}$ erg s⁻¹ cm⁻², to the 0.3–10 keV band, assuming $\Gamma = 2.0$, we obtain a flux of $(3.8 \pm 1.3) \times 10^{-11}$ erg s⁻¹ cm⁻². This is consistent with the XMM-Newton flux for the putative non-thermal component reported by Kaastra et al. (2003a), $(6.8 \pm 2.0) \times 10^{-11}$ erg s⁻¹ cm⁻². For this calculation we assume that all the non-thermal emission originates from within a circle of 12' from the core.

4.5 Discussion

4.5.1 Temperature structure

The parameters of the DEM distributions which we obtain from multi-temperature fitting, are well determined for this cluster. However, we cannot discriminate between different shapes of DEM distributions and the presence of a non-thermal component. The DEM parameters α (w_{dem}) and σ_T (g_{dem}) values show a slight increase to the outer parts of the cluster. This can be explained by the steep temperature gradients we see both in the cooling core and in the outer parts of the cluster. The values we derive for α are higher than the value of 0.20 ± 0.05 derived by Kaastra et al. (2004) based on a shorter exposure. However, their background subtraction method and handling of spectral excess is different, which can lead to systematic differences. Also projection effects can have an influence on the broadness of the DEM distribution, but as Kaastra et al. (2004) and Chapter 5 show, multi-temperature models are also needed for fitting deprojected spectra.

4.5.2 Abundance distribution and enrichment by supernova types Ia/II and Population-III stars

From the EPIC and RGS spectra we obtain radial abundance profiles for the most abundant metals. The EPIC and RGS radial profiles for oxygen show a jump in the centre of the cluster. The key data point is the point in the 0–0.5' bin. If we compare the O/Fe ratio of the central bin with the neighbouring bins, its value is significantly lower. This

means that either the iron abundance is relatively high or oxygen is low in the centre of the cluster.

Recently, using cluster simulations, Schindler et al. (2005) found that ram-pressure stripping acting on in-falling galaxies can result in centrally peaked abundance profiles, while early galactic winds produce an extended distribution of the oxygen abundance. The spatial distribution of oxygen, which is difficult to determine, is the key to understand the evolution history of the cluster.

Contrary to the iron and oxygen lines in Sérsic 159-03, the widths of these lines are the same in the cluster 2A 0335+096 (Chapter 5). A possible explanation is that the cluster 2A 0335+096 shows a much stronger temperature drop in the centre of the cluster. Since spectral lines are stronger when the temperature is lower, the RGS spectrum is dominated by line emission from the cool core of the cluster. In this case, the line profiles of iron and oxygen should follow the temperature structure more than the abundance distribution of the elements. In Sérsic 159-03 the temperature profile within the RGS extraction region is relatively flat. The temperature is about 2.5 keV with a spread of 10%. Because a strong thermal gradient is absent in the core of this cluster, the line profile should follow the abundance distribution of the elements. The observed line profiles in RGS therefore strongly suggest that in Sérsic 159-03 oxygen emission is lower in the centre of the line profile compared to iron, which is consistent with the radial profiles extracted from EPIC and RGS.

From several abundance yield simulations for Supernova type Ia and II we know that oxygen dominates the yield of type II supernovae, while iron originates mostly from type Ia supernovae. If the iron abundance is more peaked in the centre of the cluster, we can formulate a scenario of the possible enrichment history of the ICM in Sérsic 159-03. In the early universe the Inter-Galactic Medium (IGM) might have been enriched by PopIII-star explosions. The star bursts in the young galaxies that form after PopIII enrichment produce a lot of SNII which produce mainly oxygen. Because clusters are still in an early stage of development, the oxygen becomes well mixed through the IGM. Then, 1 billion years after the 'Big Bang', also SNIa explosions start enriching the local ISM in galaxies continuously. If a galaxy containing both SNIa and SNII products falls into a cluster, the ISM is stripped off by ram-pressure stripping, preferably in the denser core of the cluster, hence leading to a more centrally peaked abundance distribution of all SNIa and SNII products (Schindler et al. 2005). Because iron is also produced by SNIa explosions in the central cD galaxy, this could enhance the iron abundance in the centre of the cluster (Tamura et al. 2001a). The drop in the centre of the observed O/Fe fits within this scenario.

In order to check whether the absolute abundance of iron can be consistent with the interpretation we just formulated, we calculate the total iron mass in the cluster. We find about $4 \times 10^9 M_{\odot}$ within a radius of 300 kpc of the core. If all this iron originates from SNIa explosions, we would need at least 5×10^9 explosions in the cluster lifetime, which is of the order of 10^{10} years. Since there are typically 10^2 galaxies, there should be about 1 SNIa explosion per 200 years per galaxy, which is consistent with the rate of SNIa in our own galaxy.

We then fit the abundances from EPIC to a model of the yields of SNIa, SNII and PopIII stars (Iwamoto et al. 1999; Heger & Woosley 2002). Using a linear combination

of the yields we can estimate the expected abundances and fit them to the data. From the fit we obtain the relative contributions of the three types of metal-enriching sources.

We have to be careful, though, when we interpret the fitted supernova ratios. The mechanisms by which the elements are ejected into the ICM are not yet fully understood and are certainly not included in our simplified model. A small part of the supernova products can also be locked up in low-mass stars, so the abundance distribution we observe in the ICM is not entirely representative for the total abundance distribution in the cluster. A more detailed description of the problems when one uses this simplified model is described in Matteucci & Chiappini (2005). The derived supernova ratios should be interpreted as the number fraction of supernovae that would be needed to enrich the ICM, not the actual number of supernovae during the history of the cluster.

Our analysis shows that PopIII stars are not required to fit the data. The contributions from this early generation of stars are probably too small to be detectable in current cluster abundance patterns. We cannot confirm the results from a sample of clusters observed with ASCA that suggest that low mass PopIII stars are necessary to explain the observed silicon and sulfur abundance (Baumgartner et al. 2005). Our analysis, which includes more elements with about the same error bars on the abundances as in Baumgartner et al. (2005), shows that a PopIII-star contribution is not detected in Sérsic 159-03. Considering the single-temperature spectral models used by Baumgartner et al. (2005), we think that a temperature bias in the iron abundance makes their Si/Fe and S/Fe ratios unreliable. We also cannot confirm the underabundance of argon and calcium in the Baumgartner et al. (2005) sample. We actually measure an overabundance of calcium with respect to the nucleosynthesis models, which is in line with the result in Chapter 5 in the cluster 2A 0335+096. This might be an indication that the SNI and SNIa models have difficulties predicting the right yield for this element, but the actual uncertainties in our measured value might also be bigger than the quoted statistical error. When we compare the supernova fractions found in Chapter 5 in 2A 0335+096, we see that the SNIa contribution in Sérsic 159-03 tends to be 5–25% higher.

4.5.3 Soft excess and non-thermal X-ray emission

An alternative solution to obtain an acceptable fit for the spectra of Sérsic 159-03 is to add a soft-excess component to a single-temperature model. We explore the possibility that the deviations from the single-temperature model are due to a different component, like the WHIM or inverse-Compton emission.

A non-thermal component can explain both a soft and hard excesses for both Sérsic 159-03 and Coma, is consistent with inverse-Compton emission of CMB photons on relativistic electrons (Hwang 1997). The alternative explanation, non-thermal Bremsstrahlung emission from a non-thermal tail to the Maxwellian energy distribution of the electrons, would only result in a hard X-ray excess.

There are several possible sources that can produce a population of relativistic electrons in a cluster that would explain the observed power-law emission. The acceleration of electrons can occur, for example, in active galactic nuclei, supernovae and

pulsars (Sarazin & Lieu 1998). But also plasma waves or shocks in the ICM can accelerate electrons (see Enßlin et al. 1999, for a discussion). Using our results from Sérsic 159-03, we propose a new scenario where electrons are accelerated by the shock waves associated with in-falling galaxies.

We already discussed the possibility that the centrally peaked iron distribution might be due to an efficient ram-pressure stripping of in-falling galaxies in the dense core of the cluster. Some fraction of these galaxies being stripped would have moderate supersonic velocities. The galaxies will drive bow shocks of Mach numbers up to ~ 3 in the intra-cluster gas that can accelerate electrons to relativistic energies. To produce photons of ~ 10 keV due to inverse-Compton up-scattering of CMB photons, electrons with a Lorentz factor $\gamma \sim 7 \times 10^3$ are required. The life-time of such an electron in the cluster core is about $2.3 \times 10^{12} \gamma^{-1}$ years (assuming that the magnetic field in the core is below $2 \mu\text{G}$ and the energy densities of optical and IR radiation field in the core are below 0.1 eV cm^{-3}). It is worth noting here that the central galaxy in Sérsic 159-03 is one of the brightest cD galaxies detected in IR (Hansen et al. 2000), but the energy density of the IR photon field produced by the galaxy is below 0.1 eV cm^{-3} .

The electron acceleration time at a shock of velocity $\geq 1000 \text{ km s}^{-1}$ in the cluster core is typically much shorter than 3×10^8 years. Thus, to provide a steady non-thermal X-ray emission the stripping galaxies must cross the cluster core at a frequency ν of about 1 in 3×10^8 years. The mechanical power, L_{kin} , dissipated by the galactic shocks of velocity v_g and average radius R_g in the core region of diameter D_c and average number density n_c can be written as:

$$L_{\text{kin}} \approx 2 \times 10^{43} \left(\frac{R_g}{15 \text{ kpc}} \right)^2 \left(\frac{D_c}{300 \text{ kpc}} \right) \left(\frac{v_g}{10^3 \text{ km s}^{-1}} \right)^2 \left(\frac{n_c}{3 \times 10^{-3} \text{ cm}^{-3}} \right) \left(\frac{\nu}{3 \times 10^{-9} \text{ yr}^{-1}} \right) \text{ erg s}^{-1} \quad (4.9)$$

For the parameters assumed above, galaxies with velocity $v_g \sim 2000 \text{ km s}^{-1}$ would provide $L_{\text{kin}} \sim 10^{44} \text{ erg s}^{-1}$. A few percent of the power would be enough to maintain the relativistic electrons required to provide the 10 keV regime non-thermal emission. Note that the lifetime of the electrons with Lorentz factor below 100 would be about the Hubble time. This implies that the spectrum of electrons accelerated by multiple successive shocks of Mach number about 3 will have power-law distribution of index about 3 at $\gamma \sim 10^4$, and a flat distribution at $\gamma \leq 100$, where the Compton losses are not important. The electron distribution index 3 corresponds to the photon index of the photon emission of 2, close to that observed.

4.6 Conclusions

We have analysed high-resolution X-ray spectra of the cluster of galaxies Sérsic 159-03 obtained with XMM-Newton and conclude that:

1. For the first time we accurately determine the abundances in a cluster of galaxies which fit to a linear combination of current supernova yield models.

2. From the line width in RGS and the radial profiles from EPIC/RGS we find a jump in the O/Fe ratio around a radius of $0.5'$ from the cluster centre. The O/Fe ratio in the centre of the cluster is lower compared to its immediate surroundings. A combination of ram-pressure stripping (Schindler et al. 2005) and enrichment by SNIa in the central elliptical galaxy (Tamura et al. 2001a) can explain the observed profile.
3. We do not detect a contribution of PopIII stars in Sérsic 159-03. This result is not in line with the claim by Baumgartner et al. (2005) that PopIII stars are necessary to explain the abundances measured in an ASCA sample of clusters. The number contribution of SNIa with respect to the total number of supernovae we find, based on the measured abundances, is about 25–50%.
4. The spectra can also be fitted with an additional non-thermal component with a power-law index of about 2.1 on top of the thermal emission. The χ_r^2 of these fits is comparable to the χ_r^2 using only multi-thermal models. If a non-thermal component is present in Sérsic 159-03, it can be explained by Inverse-Compton scattering of CMB photons and relativistic electrons.

Acknowledgements

We would like to thank the anonymous referee for providing comments that helped to improve the presentation of our results and conclusions in this paper. This work is based on observations obtained with XMM-Newton, an ESA science mission with instruments and contributions directly funded by ESA member states and the USA (NASA). The Netherlands Institute for Space Research (SRON) is supported financially by NWO, the Netherlands Organisation for Scientific Research.

XMM-Newton Spectroscopy of the Cluster of Galaxies 2A 0335+096

N. Werner¹, J. de Plaa^{1,2}, J.S. Kaastra¹, J. Vink^{1,2}, J. A. M. Bleeker^{1,2}, T. Tamura³, J. R. Peterson⁴, and F. Verbunt²

¹ SRON Netherlands Institute for Space Research, Utrecht, The Netherlands

² Astronomical Institute, Utrecht University, Utrecht, The Netherlands

³ Institute of Space and Astronautical Science, JAXA, Yoshinodai, Sagamihara, Kanagawa, Japan

⁴ KIPAC, Stanford University, Stanford, California, USA

Received 20 July 2005, Accepted 30 November 2005

Published in *Astronomy & Astrophysics*, volume 449, pages 475–491, 2006

Abstract

We present here the results of a deep (130 ks) XMM-Newton observation of the cluster of galaxies 2A 0335+096. The deep exposure allows us to study in detail its temperature structure and its elemental abundances. We fit three different thermal models and find that the multi-temperature *wdem* model fits our data best. We find that the abundance structure of the cluster is consistent with a scenario where the relative number of Type Ia supernovae contributing to the enrichment of the intra-cluster medium is $\sim 25\%$, while the relative number of core collapse supernovae is $\sim 75\%$. Comparison of the observed abundances to the supernova yields does not allow us to put any constraints on the contribution of Pop III stars to the enrichment of the ICM. Radial

abundance profiles show a strong central peak of both Type Ia and core collapse supernova products. Both the temperature and iron abundance maps show an asymmetry in the direction of the elongated morphology of the surface brightness. In particular the temperature map shows a sharp change over a brightness edge on the southern side of the core, which was identified as a cold front in the Chandra data. This suggests that the cluster is in the process of a merger with a subcluster. Moreover, we find that the blobs or filaments discovered in the core of the cluster by Chandra are, contrary to the previous results, colder than the ambient gas and they appear to be in pressure equilibrium with their environment.

5.1 Introduction

Clusters of galaxies are the largest known gravitationally bound structures in the universe. According to the standard cosmological scenario they form and grow along the filaments through merging with groups and individual galaxies. Optical and X-ray studies reveal that clusters of galaxies are still forming at the present epoch.

The large effective area and superb spectral resolution of *XMM-Newton* together with the high spatial resolution of *Chandra* allow us to study clusters of galaxies with unprecedented detail. Analysis of data obtained by these satellites led to a number of important results in the recent years. In the central parts of many clusters of galaxies the gas density is high enough that the radiative cooling time of the gas is shorter than the age of the cluster. As the gas cools the pressure decreases, which causes a net inflow toward the center of the cluster. Many clusters of galaxies indeed show a temperature drop by a factor of three or more within the central 100 kpc radius (for a review on cooling flows see Fabian 1994). However, the spectra obtained by the XMM-Newton Reflection Grating Spectrometer (RGS) show no evidence for strong cooling rates of gas below 30 – 50% of the maximum temperature of the ambient gas, which forces us to look for additional heating mechanisms in the cores of clusters (Peterson et al. 2001; Tamura et al. 2001b; Kaastra et al. 2001). The high resolution images from Chandra led recently to the discovery of *cold fronts*, associated with motion of the cluster cores and to the identification of filamentary structure in the cores of a number of clusters (Markevitch et al. 2000). Spatially resolved spectroscopy of many clusters of galaxies shows a strongly centrally peaked distribution of metal abundances (Tamura et al. 2004).

Because of their large potential wells, clusters of galaxies retain all the enriched material produced in the member galaxies. This makes them a unique environment for elemental-abundance measurements and for the study of the chemical enrichment history of the universe.

In this paper we study the X-ray bright cluster 2A 0335+096 using spatially-resolved and high-resolution spectra obtained during a 130 ks observation with the European Photon Imaging Camera (EPIC, Turner et al. 2001; Strüder et al. 2001) and the Reflection Grating Spectrometer (RGS, den Herder et al. 2001) aboard *XMM-Newton* (Jansen et al. 2001). The properties of 2A 0335+096 allow us to address here some of the above mentioned issues.

2A 0335+096 was first detected as an X-ray source by *Ariel V* (Cooke et al. 1978), and was found to be associated with a medium compact Zwicky cluster (Zwicky et al. 1965; Schwartz et al. 1980). The presence of a cooling flow was first noted by Schwartz et al. (1980) in the data obtained by *HEAO 1*. X-ray observations with *EXOSAT* (Singh et al. 1986, 1988) and *Einstein* (White et al. 1991) confirmed the presence of the cooling flow. Observations with *ROSAT* (Sarazin et al. 1992; Irwin & Sarazin 1995) show a filamentary structure in the central region of the cooling flow. Observations with *ASCA* (Kikuchi et al. 1999) show a hint of a centrally peaked metallicity distribution. Using data obtained by *BeppoSAX*, De Grandi & Molendi (2001, 2002) analyzed the metallicity and temperature profile of the cluster and found a centrally peaked metallicity gradient. Using the same dataset, Ettori et al. (2002) estimated the total mass of the cluster within the region with overdensity of 2500 times the critical density to be $\sim 1.6 \times 10^{14} M_{\odot}$, while the mass of the gas was found to be $\sim 2.0 \times 10^{13} M_{\odot}$.

Recent *Chandra* observation shows a complex structure in the core of the cluster: a cold front south of the center, unusual X-ray morphology consisting of a number of X-ray blobs and/or filaments on scales $\gtrsim 3$ kpc, along with two prominent X-ray cavities (Mazzotta et al. 2003). Moreover, the *Chandra* observation shows that the cluster has a cool dense core and its radial temperature gradient varies with position angle. The radial metallicity profile has a pronounced central drop and an off-center peak (Mazzotta et al. 2003). A previous shorter observation with *XMM-Newton* shows an increase of the Fe abundance toward the center with a strong central peak (Tamura et al. 2004). The central galaxy of 2A 0335+096 is a cD galaxy with a very extended optical emission line region ($H\alpha + [\text{NII}]$) to the northeast of the galaxy. Moreover, the central region of the galaxy is anomalously blue, indicating recent star formation (Romanishin & Hintzen 1988). Edge (2001) reports a detection of CO emission (implying $2 \times 10^9 M_{\odot}$ of molecular gas) and IRAS 60 μm continuum. These observations indicate a mass deposition rate of a cooling flow of $< 5 M_{\odot} \text{ yr}^{-1}$. A radio study of 2A 0335+096 shows a radio source coincident with the central galaxy, which is surrounded by a mini-halo (Sarazin et al. 1995).

Throughout the paper we use $H_0 = 70 \text{ km s}^{-1} \text{ Mpc}^{-1}$, $\Omega_M = 0.3$, $\Omega_{\Lambda} = 0.7$, which imply a linear scale of $42 \text{ kpc arcmin}^{-1}$ at the cluster redshift of $z = 0.0349$. Unless specified otherwise, all errors are at the 1σ confidence level.

5.2 Observations and data reduction

2A 0335+096 was observed with *XMM-Newton* on August 4th and 5th 2003 with a total exposure of 130 ks. The EPIC MOS and pn instruments were operated in Full Frame mode using the thin filter. The exposure times of both MOS cameras and RGS were 130 ks and the exposure time of pn was 93 ks.

5.2.1 EPIC analysis

The raw data are processed with the 6.0.0 version of the XMM-Newton Science Analysis System (SAS), using the EPPROC and EMPROC tasks. We apply the standard fil-

tering, for EPIC/MOS keeping only single, double, triple and quadruple pixel events ($\text{PATTERN} \leq 12$), while for EPIC/pn we make use of single and double events ($\text{PATTERN} \leq 4$). In both cases only events with $\text{FLAG}==0$ are considered. The redistribution and ancillary response files are created with the SAS tasks `rmfgen` and `arfgen` for each camera and region we analyze.

In the spectral analysis we remove all the bright X-ray point-sources with a flux higher than $4.8 \times 10^{-14} \text{ erg s}^{-1} \text{ cm}^{-2}$.

At the low energies, the EPIC cameras are currently not well calibrated below 0.3 keV. For pn we take a conservative lower limit of 0.5 keV, below which, at the time of our analysis, there are still some uncertainties in calibration. At energies higher than 10 keV our spectra lack sufficient flux. Therefore, in most of the analyzed regions, our analysis of the MOS and pn spectra is restricted to the 0.3 – 10 keV and 0.5 – 10 keV range respectively. Bonamente et al. (2005) showed that the systematic uncertainties of the EPIC detectors in the energy range of 0.3 to 1 keV are less than 10%. We include systematic errors to account for the uncertainties in the calibration and background in the spectral fit. The applied systematics are adopted from Kaastra et al. (2004). After a preliminary analysis we find that the pn instrument has a small gain problem. We minimize this effect by shifting the pn energy grid by 10 eV. The spectra obtained by MOS1, MOS2 and pn are then fitted simultaneously with the same model, while their relative normalizations are left as free parameters.

To test whether our abundance measurements can be influenced by narrow band regions where the calibration of EPIC might still be problematic, we fit the spectrum of PKS 2155-304, a bright BL Lac object observed with thin filter on 2004 November 23. The X-ray spectra of BL Lac objects are generally well fitted by simple absorbed power-law, or broken power-law models. We find that the fit residuals at the position of the measured spectral lines are always consistent within the 1σ uncertainty with the best fit absorbed power-law model. Thus, we can rule out the possibility that the measured abundances are seriously influenced by narrow band calibration uncertainties.

Background modeling

Since we want to investigate the cluster properties up to at least $9'$ from its core, we need a good estimate for the background, especially at the dim outer parts of the cluster. The source fills the entire field of view, which makes a direct measurement of the local background very difficult. The commonly used combined background event lists of Lumb et al. (2002) and Read & Ponman (2003), can be used in areas where the surface brightness of the source is high, or when the cluster has similar background properties as the combined background fields. As shown in Chapter 4 relatively small systematic errors in the background normalization can have a big influence on the spectral fits in the outer parts of clusters.

The background can be divided into three main components: instrumental background, low energy particles (with energy of a few tens of keV) accelerated in the Earth's magnetosphere (so called *soft-protons*) and the Cosmic X-ray Background (CXB).

To minimize the effect of soft protons in our spectral analysis, we cut out time intervals where the total 10 – 12 keV count rate deviates from the mean by more than 3σ .

Table 5.1: The CXB components used in the fitting of 2A 0335+096. The power-law index of the extragalactic component is frozen to $\gamma = 1.41$. The fluxes are determined in the 0.3 – 10 keV band and, apart of the Local hot bubble, corrected for Galactic absorption using a column of $N_{\text{H}}=2.5 \times 10^{21} \text{ cm}^{-2}$ (the local hot bubble is inside of the Galactic absorbing column).

Component	kT (keV)	Flux ($\text{erg s}^{-1} \text{ cm}^{-2} \text{ deg}^{-2}$)
Local bubble	0.082	3.58×10^{-12}
Soft distant component	0.068	6.57×10^{-14}
Hard distant component	0.127	6.19×10^{-13}
Extra galactic power-law		2.16×10^{-11}

The cleaned MOS1, MOS2 and pn event files have useful exposure times of 107 ks, 108 ks and 77 ks, respectively.

To deal with the instrumental background we adopt a method developed in Chapter 4. As a template for the instrumental background we use data from closed filter observations, which we scale to the source observation using events detected outside of the field of view (the values of the scaling factors are 1.00 ± 0.02 , 1.04 ± 0.02 and 1.10 ± 0.07 for MOS1, MOS2 and pn respectively). The scaling is performed by adding or subtracting a powerlaw with a photon index of $\gamma = 0.15$ for MOS and $\gamma = 0.24$ for pn. For detailed description of the method see Chapter 4.

We correct for the Cosmic X-ray Background (CXB) during the fitting. Since all the CXB photons enter the mirrors together with the source photons, we can fit the CXB simultaneously with the source spectra. In our models, we use CXB components described by Kuntz & Snowden (2000). They distinguish 4 different components: *the extragalactic power law* (EPL), *the local hot bubble* (LHB), *the soft distant component* (SDC) and *the hard distant component* (HDC). The EPL component is made from the integrated emission of faint discrete sources, mainly from distant Active Galactic Nuclei (AGNs). According to one of the most recent determinations by De Luca & Molendi (2004) the power law index of the EPL is 1.41 ± 0.06 and its 2 – 10 keV flux is $2.24 \pm 0.16 \times 10^{-11} \text{ erg cm}^{-2} \text{ s}^{-1} \text{ deg}^{-2}$ (with 90% confidence). Since in our spectral analysis we cut out all the point sources with a flux higher than $4.8 \times 10^{-14} \text{ erg s}^{-1} \text{ cm}^{-2}$ we reduce the EPL flux in our extraction area. Moretti et al. (2003) have made a compilation of number counts of X-ray point sources in two energy bands (0.5 – 2 and 2 – 10 keV) from a large source sample and determined analytic formula for the number of point sources $N(S)$ with a flux higher then S . To determine, the contribution of the point sources brighter then our cut-off to the total flux of the EPL we calculate the integral $\int_{S_{\text{cut-off}}}^{\infty} \left(\frac{dN}{dS} \right) S dS$. We find, that the point sources we cut out make up $\approx 20\%$ of the total EPL flux. The 0.3 – 10 keV flux of the EPL in our model is thus $2.16 \times 10^{-11} \text{ erg cm}^{-2} \text{ s}^{-1} \text{ deg}^{-2}$. The LHB is a local supernova remnant, in which our Solar System resides. It produces virtually unabsorbed emission at a temperature of $\sim 10^6$ K. The SDC and HDC originate at a larger distance, they might be identified with the Galactic halo, Galactic corona or the Local group emission and are absorbed by almost the full Galactic column density. They have a temperature of 1 – 2 million K. We model each

of the three soft background components (the LHB, SDC and the HDC) by a MEKAL model with temperatures of 0.082 keV, 0.068 keV, 0.127 keV respectively (based on Kuntz & Snowden 2000). We determine the normalizations of these soft components by fitting the spectrum extracted from an annulus, with inner and outer radii of $9'$ and $12'$ respectively, centered at the core of the cluster. The contribution to the total flux from cluster emission at these radii is $\sim 60\%$, the rest of the emission comes from the CXB. To account for the cluster emission we use an additional thermal model. In our final spectral fits we fix the normalizations of the background components. The temperatures and the 0.3 – 10 keV fluxes of the background components are given in Table 5.1.

5.2.2 RGS analysis

We extract the RGS spectra with SAS version 6.1.0 following the same method as described in Tamura et al. (2001a). In order to get spatial information we select the events from several rectangular areas on the CCD strip in the cross-dispersion direction. Because the cluster fills the entire field-of-view of the RGS, we need a blank field observation to extract the background spectrum. For this observation we choose a Lockman Hole observation with an effective exposure time of 100 ks. The flare subtraction is analogous to the method used with EPIC, but now we use the events from CCD 9 outside the central area with a cross-dispersion of $|xdsp| > 30''$ to make the lightcurve. This method was applied to both source and background datasets.

Because the RGS gratings operate without a slit, the resulting spectrum of an extended source is the sum of all spectra in the (in our case) $5' \times \sim 12'$ field of view, convolved with the PSF (see Davis 2001, for a complete discussion about grating responses). Extended line-emission appears to be broadened depending on the spatial extent of the source along the dispersion direction. In order to describe the data properly, the spectral fits need to account for this effect. In practice, this is accomplished by convolving the spectral models with the surface brightness profile of the source along the dispersion direction (Tamura et al. 2004). For that purpose we derive for each extraction region the cluster intensity profile from MOS1 in the 0.8 – 1.4 keV band along the dispersion direction of RGS and we convolve this MOS1 profile with the RGS response in order to produce a predicted line spread function (lsf). Because the radial profile for an ion can be different from the mean MOS1 profile, this method is not ideal. Therefore we introduce two scale parameters, namely the width and centroid of the lsf. These parameters are left free during spectral fitting in order to match the observed profiles of the main emission lines. The scale parameter s for the width is the ratio of the observed lsf width to the nominal MOS1 based lsf width.

5.3 Spectral models

For the spectral analysis we use the SPEX package (Kaastra et al. 1996). We model the Galactic absorption using the *hot* model of that package, which calculates the transmission of a plasma in collisional ionisation equilibrium with cosmic abundances. We

mimic the transmission of a neutral plasma by putting its temperature to 0.5 eV. To find the best description of the cluster emission we fit several combinations of collisionally ionised equilibrium (CIE) plasma models (MEKAL) to the spectra: a single-temperature thermal model; a combination of two thermal models; a differential emission measure (DEM) model with a cut-off power-law distribution of emission measures versus temperature (*wdem*). The *wdem* model appears to be a good empirical approximation for the spectrum in cooling cores of clusters of galaxies (e.g. Kaastra et al. 2004, and Chapter 2). The emission measure $Y = \int n_e n_H dV$ (where n_e and n_H are the electron and proton densities, V is the volume of the source) in the *wdem* model is shown in Eq. (5.1) adapted from Kaastra et al. (2004):

$$\frac{dY}{dT} = \begin{cases} AT^{1/\alpha} & T_{\min} < T < T_{\max}, \\ 0 & \text{elsewhere.} \end{cases} \quad (5.1)$$

The emission measure distribution has a cut-off at $T_{\min} = cT_{\max}$. The cut-off c is set in this study to 0.1. For $\alpha \rightarrow \infty$ we obtain a flat emission measure distribution. The emission measure weighted mean temperature T_{mean} is given by:

$$T_{\text{mean}} = \frac{\int_{T_{\min}}^{T_{\max}} \frac{dY}{dT} T dT}{\int_{T_{\min}}^{T_{\max}} \frac{dY}{dT} dT}. \quad (5.2)$$

By integrating this equation between T_{\min} and T_{\max} we obtain a direct relation between T_{mean} and T_{\max} as a function of α and c :

$$T_{\text{mean}} = \frac{(1 + 1/\alpha)(1 - c^{1/\alpha+2})}{(2 + 1/\alpha)(1 - c^{1/\alpha+1})} T_{\max}. \quad (5.3)$$

A comparison of the *wdem* model with the classical cooling-flow model can be found in Chapter 3. We note that the *wdem* model contains less cool gas than the classical cooling-flow model, which is consistent with recent observations (Peterson et al. 2001, 2003).

The spectral lines in the MEKAL model are fitted self consistently. From the fits we obtain the numbers of atoms of all elements with detected line emission. To see whether different elements show similar abundances with respect to solar, it is convenient to normalize these numbers with respect to the relative solar abundances. To make the comparison with previous work easier, we use the solar abundances as given by Anders & Grevesse (1989) for this normalization. The more recent solar abundance determinations (e.g. Grevesse & Sauval 1998; Lodders 2003) give significantly lower abundances of oxygen and neon than those measured by Anders & Grevesse (1989). Use of these new determinations would only affect the *representation* of the elemental abundances in our paper, but not the actual measured values, which can be reconstructed by multiplication of the given values with the normalizations.

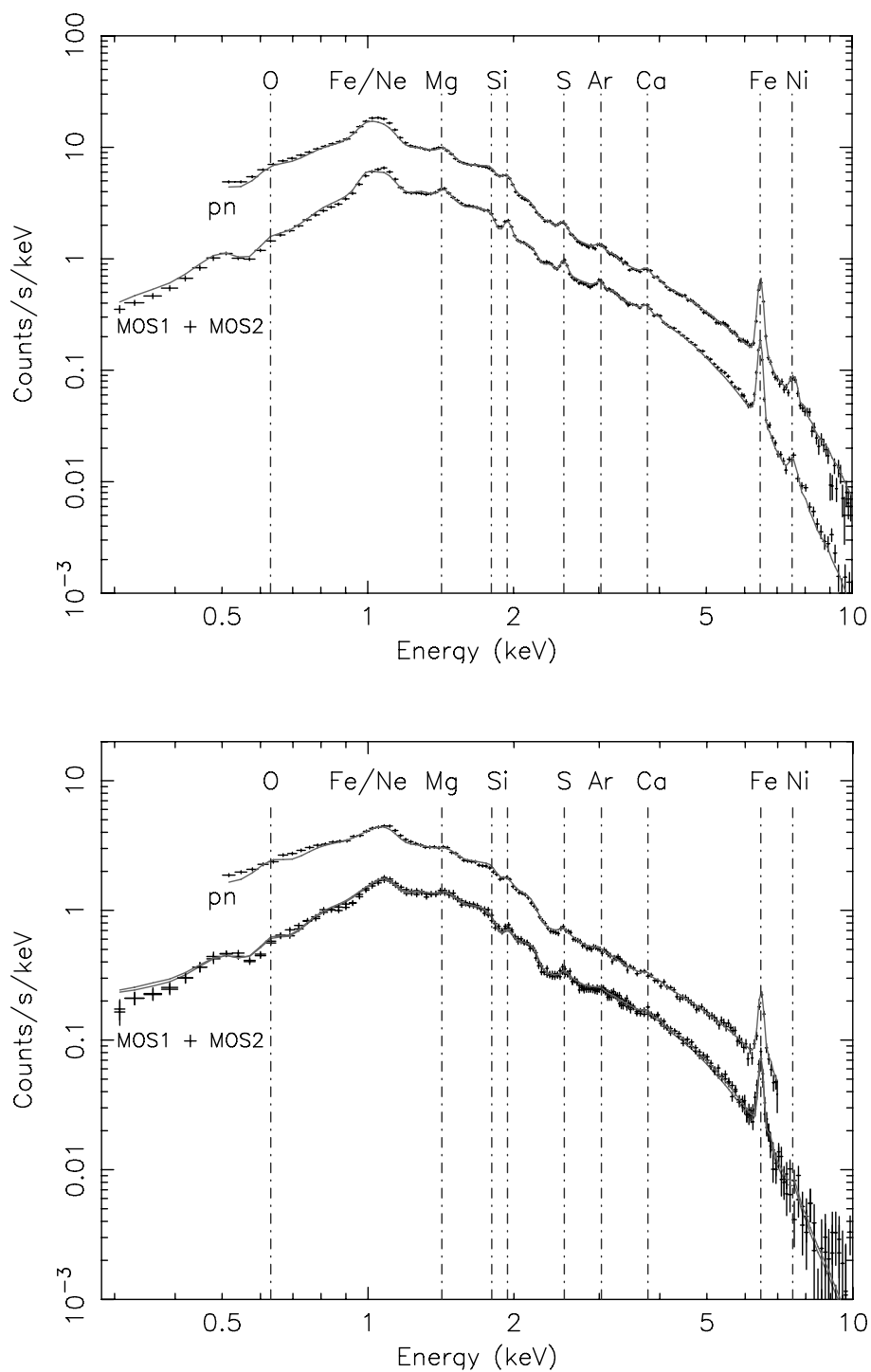


Figure 5.1: The total spectrum of the core of the cluster (with a radius of $3'$), which contains the cooling core (upper panel) and the spectrum of the $3' - 9'$ region (lower panel). The continuous line represents the fitted wdem model. The EPIC pn and MOS1 + MOS2 spectra are indicated.

Table 5.2: Fit results obtained by fitting the *wdem* model to the spectrum extracted from a circular region with a radius of $3'$ centered on the core of the cluster and from an annulus with inner and outer radii respectively $3'$ and $9'$. For the Galactic absorption we use a value of $N_{\text{H}}=2.5 \times 10^{21} \text{ cm}^{-2}$. Emission measures ($Y = \int n_{\text{e}}n_{\text{H}}dV$) are given in 10^{66} cm^{-3} . Abundances are given with respect to solar.

Parameter	0 – 3'	3 – 9'
Y	15.89 ± 0.13	6.53 ± 0.01
kT_{max} (keV)	3.75 ± 0.02	5.36 ± 0.06
α	0.75 ± 0.02	1.34 ± 0.10
kT_{mean}	2.64 ± 0.02	3.46 ± 0.05
Mg	0.57 ± 0.08	0.21 ± 0.06
Si	0.72 ± 0.03	0.37 ± 0.03
S	0.61 ± 0.03	0.27 ± 0.04
Ar	0.42 ± 0.05	0.14 ± 0.09
Ca	0.84 ± 0.06	0.62 ± 0.12
Fe	0.532 ± 0.007	0.383 ± 0.006
Ni	1.46 ± 0.10	0.77 ± 0.15
$\chi^2 / \text{d.o.f.}$	948/525	666/491

5.4 Global spectrum

5.4.1 EPIC

To compare the properties of the cluster in its cooling core region with the properties outside of the cooling core region we extract two spectra. One is from a circular region with a radius of $3'$ centered on the X-ray maximum of the cluster and one is from an annulus with inner radius of $3'$ and outer radius of $9'$. The large temperature gradient and projection effects make it necessary to fit the spectra with a multi-temperature model. We use the *wdem* model, described in Sect. 5.3 and fix the abundances of elements with weak lines, which we do not fit, to 0.6 and 0.3 times solar in the inner and outer region respectively. The high statistics of the spectra allow us to determine the temperature structure and elemental abundances of several elements in these regions very precisely. The best-fit parameters are shown in Table 5.2.

We find that the core is cooler than the outer region. We also find that the outer part has a broader temperature distribution than the core. The spectra with the indicated important spectral lines are shown in Fig. 5.1. All the detected spectral lines are shown in Fig. 5.2, which shows the residuals of the EPIC spectrum with line emission put to zero in the model, so all spectral lines are clearly visible. For the first time we see a feature at the expected energy of chromium in a cluster of galaxies, which corresponds to a detection with 2σ significance. First, we attempt to measure the abundances of elements shown in Table 5.2.

Since oxygen is predominantly produced by type II supernovae, it is an important element for constraining the enrichment scenarios. Oxygen has strong H-like lines at 0.65 keV. The strong absorption toward 2A 0335+096, uncertainties in the calibration

Table 5.3: Abundance upper limits for elements with weak lines, which could not be reliably detected, determined from the fluxes at the expected line energies of their helium-like emission. We also show the abundance of calcium calculated with the same method (it is consistent with the abundance determined in MEKAL).

Element	I (phot m ⁻² s ⁻¹)	Abund. (solar)
Ca	0.252 ± 0.019	0.80 ± 0.05
Ti	0.017 ± 0.013	1.5 ± 1.1
Cr	0.020 ± 0.010	0.5 ± 0.2
Mn	-0.003 ± 0.009	-0.2 ± 0.5
Co	0.000 ± 0.008	0 ± 2

of EPIC and relatively nearby iron lines do not allow us to constrain the oxygen abundance accurately by EPIC. However, the RGS with its high spectral resolution allows us to determine the oxygen abundance in the core of the cluster (see Table 5.4). The 2p–1s neon lines at 1.02 keV are in the middle of the iron L complex (lying between about 0.8 to 1.4 keV). The resolution of the EPIC cameras is not sufficient to resolve the individual lines in the iron L complex which makes the neon abundance determination by EPIC unreliable. However, the high resolution of RGS allows us to determine the neon abundance at least in the core of the cluster (see Table 5.4). The K shell lines of magnesium at 1.47 keV are also close to the iron L complex, which makes our magnesium abundance determinations by EPIC somewhat sensitive to our temperature and iron abundance model. The magnesium abundance determinations at larger radii, where the surface brightness of the cluster is relatively low might be influenced by the instrumental aluminum line at 1.48 keV. The silicon, sulfur, argon and calcium lines lie in a relatively uncrowded part of the spectrum and their abundances are in general well determined. Iron has the strongest spectral lines in the X-ray band. At temperatures above 3 keV its K α lines are the strongest at about 6.67 keV and 6.97 keV, while the iron L-shell complex ranging from about 0.8 keV to 1.4 keV dominates at lower temperatures. These spectral lines make the iron abundance determinations the most reliable of all elements. The nickel abundance is determined mainly from its K-shell line blends at 7.80 keV and 8.21 keV, which are partially blended with iron lines.

In Table 5.2 we see that the abundances in the outer part are always lower than in the core of the cluster.

We also attempt to estimate the abundance upper limits for elements with weak lines (titanium, chromium, manganese, cobalt), which can not yet be fitted in MEKAL in a self-consistent way. We determine their abundances from the fluxes at the expected line energies of their helium-like emission (see Table 5.3). The feature at the expected energy of chromium corresponds to a detection at a 2σ level, while the feature at the expected energy of titanium corresponds to a 1σ detection.

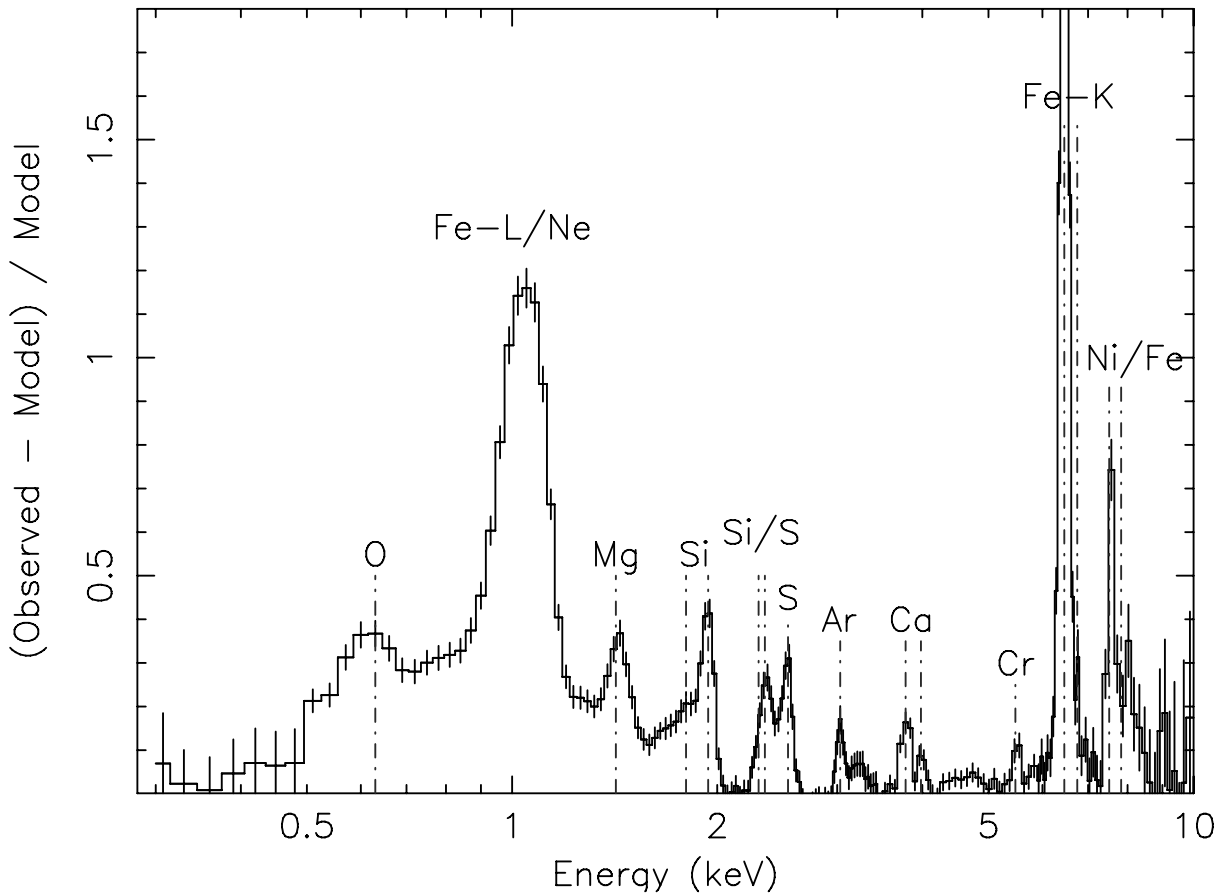


Figure 5.2: Residuals of the fit to the EPIC total spectrum extracted from a circular region with a radius of $3'$, with the line emission put to zero in the model.

5.4.2 RGS

In Fig. 5.3 we show the first and second order RGS spectra extracted from a $4'$ wide strip in the cross-dispersion direction of the instrument. The extraction region is centered on the core of the cluster. Despite the spatial broadening, the strong spectral lines of magnesium, neon, iron and oxygen are well resolved in both spectral orders. In Table 5.4 we list the fit results for these spectra, for both the single temperature and *wdem* model.

The χ^2 values of the fits show that the *wdem* model fits better than the single-temperature model. However, the χ^2 for the *wdem* is still high, probably because of the disturbed nature of the core of the cluster. There are some systematic differences between the two models. The abundances found fitting the spectrum with the *wdem* model are in general twice the single-temperature values and the line widths of oxygen and iron, indicated with the scale parameters s_O and s_{Fe} , are also higher for *wdem*. Because of these differences, we divide the abundances of the other elements, by the value for iron. Since the continuum is not well determined by the RGS, these ratios are more reliable than the absolute value. The relative abundances, given in units with respect to solar, for neon and magnesium are similar to iron, while the oxygen abundance is

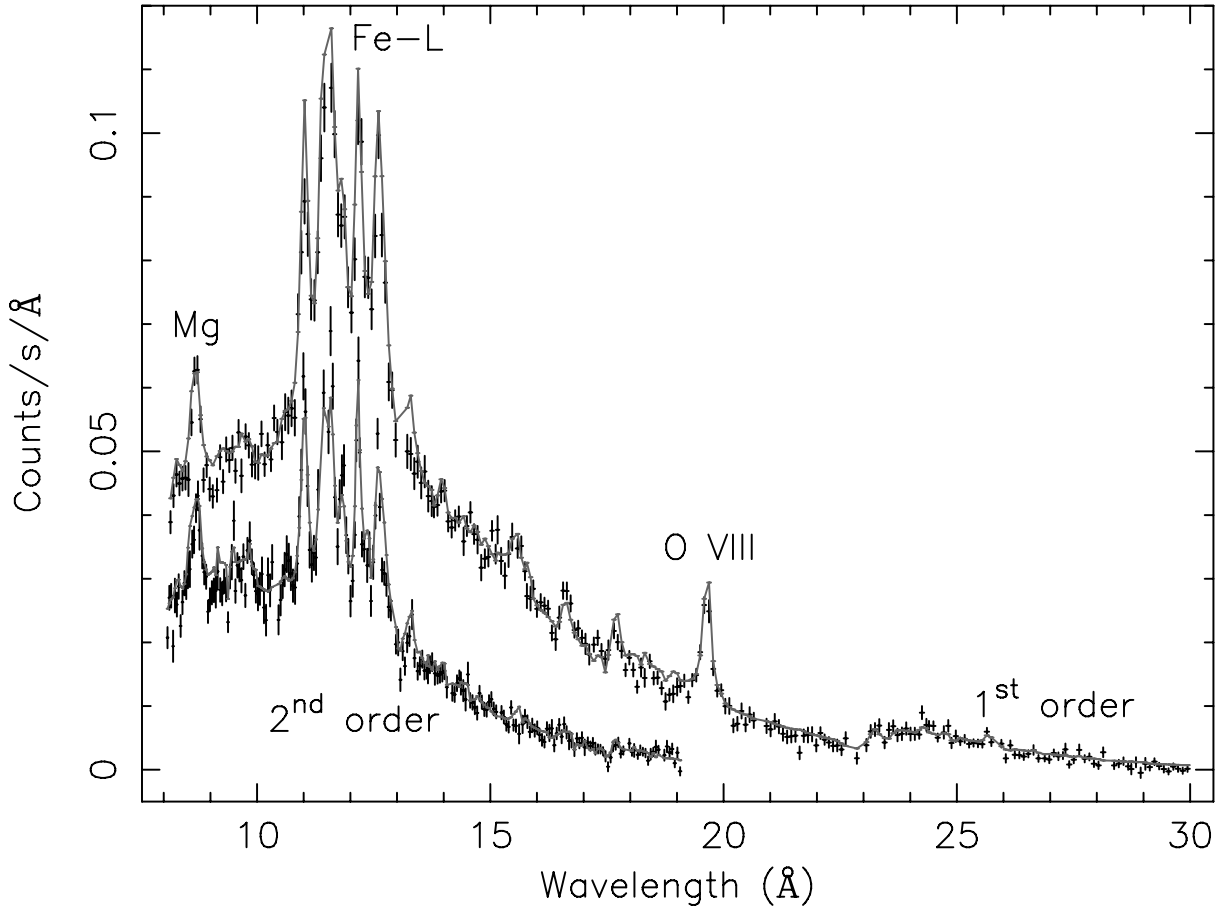


Figure 5.3: 1^{st} and 2^{nd} order spectrum of 2A 0335+096 extracted from a $4'$ wide strip centered on the core. The continuous line represents the fitted *wdem* model. Between 15 and 18 Å Fe XVII and Fe XVIII emission lines are visible. On the x-axis we show the observed wavelength.

about half the value for iron. We are also able, using the excellent statistics, to derive the abundance for nitrogen. This value is also consistent with that for iron, although the error bars are large. The widths of the oxygen and iron lines, indicated by the scale values, are very similar in this cluster, which shows that the spatial distribution of oxygen and iron might be similar.

Regarding the DEM temperature structure, the value of α (0.52 ± 0.03) for *wdem* is smaller than the EPIC value of 0.75 ± 0.02 from within $3'$ from the core, probably, because of the different extraction regions. The different extraction regions and the disturbed nature of the core (see sections 5.6 and 5.7) make the abundances determined from the EPIC and RGS difficult to compare. The mean temperature kT_{mean} of the *wdem* results is 2.51 ± 0.10 keV, which is higher than the single-temperature fit.

Because the solar oxygen abundance in Anders & Grevesse (1989) is slightly overestimated, we need to free the oxygen-abundance in the Galactic absorption component (O_{abs}) in our spectral model. This effect in absorption was first observed by Weisskopf et al. (2004) in an observation of the Crab pulsar and later confirmed in a cluster observation of Abell 478 in Chapter 2. The values of 0.47 ± 0.02 and 0.54 ± 0.03 that we

Table 5.4: Fit results for the RGS spectra extracted from a 4' wide strip. The value for N_{H} is in 10^{21} cm^{-2} . Iron is given with respect to solar and the other abundances with respect to iron.

Parameter	single-temp	<i>wdem</i> -model
N_{H}	3.14 ± 0.03	2.95 ± 0.04
kT (keV)	1.80 ± 0.02	
kT_{max}		3.36 ± 0.13
kT_{mean}		2.51 ± 0.10
α		0.52 ± 0.03
O_{abs}	0.47 ± 0.02	0.54 ± 0.03
N/Fe	1.7 ± 0.6	1.3 ± 0.4
O/Fe	0.55 ± 0.05	0.49 ± 0.05
Ne/Fe	1.11 ± 0.10	0.85 ± 0.08
Mg/Fe	0.97 ± 0.10	0.97 ± 0.08
Fe	0.524 ± 0.018	1.07 ± 0.06
Scale s_{O}	0.59 ± 0.12	0.81 ± 0.14
Scale s_{Fe}	0.60 ± 0.04	0.73 ± 0.04
χ^2 / d.o.f.	1552 / 790	1173 / 788

find for the oxygen-abundance in the Galactic absorption component O_{abs} are slightly lower than the RGS values found in Chapter 2, but consistent with the expected value of 0.58 ± 0.08 based on an updated value for the solar oxygen abundance by Allende Prieto et al. (2001).

5.5 Radial profiles

We determine the radial temperature and abundance profiles of several elements using projected and deprojected spectra extracted from circular annuli, centered on the X-ray maximum of the cluster. We use annuli with outer radii indicated on the top of Table 5.5. We also extract radial temperature and abundance profiles from RGS in the cross-dispersion direction.

5.5.1 Projected spectra

We fit the spectra extracted from the annuli with three different models, and compare the results. Due to high background in the 6th and 7th annulus we ignore the pn data at energies higher than 7.5 keV. In our model we fix the abundances of elements which we do not fit to 0.3 solar. The results are presented in Fig. 5.4 and Table 5.5. First we fit the spectra with a single temperature model. We find that the model fits our data poorly and the χ^2 in the core of the cluster is unacceptably high. Based on the large χ^2 of the fit, in the central region we can discard the single temperature model. We therefore try to fit 2 thermal models simultaneously, with coupled abundances and

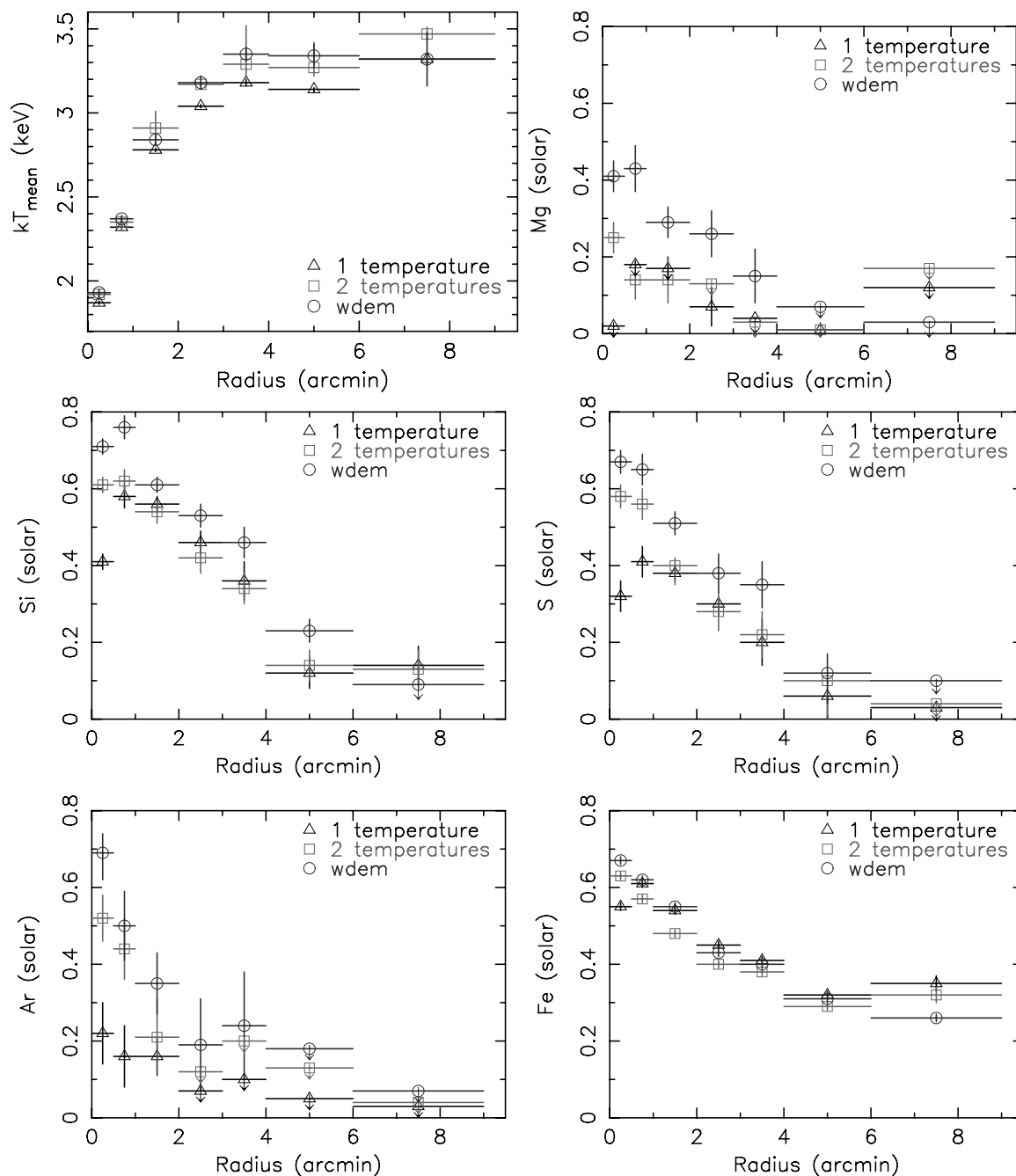


Figure 5.4: Comparison of fit results obtained by fitting the EPIC data with a single-temperature model, two-temperature model and the *wdem* model.

Table 5.5: Fit results obtained by fitting the EPIC data with a single-temperature model (1), two-temperature model (2) and the *wdem* model (3). Emission measures ($Y = \int n_e n_H dV$) are given in 10^{66} cm^{-3} . Abundances are given with respect to solar.

		0 – 0.5'	0.5 – 1.0'	1.0 – 2.0'	2.0 – 3.0'	3.0 – 4.0'	4.0 – 6.0'	6.0 – 9.0'
Y	1	3.55	4.65	5.22	3.19	2.01	2.85	2.97
	2	3.42	4.82	5.45	3.31	2.08	2.75	2.56
	3	3.21	4.52	5.30	3.26	2.05	2.85	2.23
kT	1	1.87 ± 0.01	2.32 ± 0.01	2.78 ± 0.01	3.04 ± 0.01	3.18 ± 0.02	3.14 ± 0.02	3.32 ± 0.04
kT_2	2	$2.154^{+0.005}_{-0.002}$	2.72 ± 0.04	3.51 ± 0.09	3.08 ± 0.01	$3.92^{+0.23}_{-0.07}$	$4.10^{+0.15}_{-0.05}$	4.39 ± 0.04
kT_{max}	3	2.64 ± 0.02	3.14 ± 0.02	3.95 ± 0.03	4.39 ± 0.04	4.81 ± 0.05	4.97 ± 0.05	5.84 ± 0.14
kT_{mean}	3	1.93 ± 0.02	2.37 ± 0.02	2.84 ± 0.03	3.18 ± 0.04	3.35 ± 0.04	3.34 ± 0.08	3.32 ± 0.16
α	3	0.58 ± 0.01	0.48 ± 0.02	0.65 ± 0.02	0.62 ± 0.04	0.79 ± 0.04	$1.01^{+0.23}_{-0.02}$	8.02^{+13}_{-3}
Mg	1	< 0.02	< 0.18	0.17 ± 0.03	0.07 ± 0.05	< 0.04	< 0.01	< 0.12
	2	0.25 ± 0.04	0.14 ± 0.05	0.14 ± 0.06	< 0.13	< 0.03	< 0.01	< 0.17
	3	0.41 ± 0.04	0.43 ± 0.06	0.29 ± 0.04	0.26 ± 0.06	0.15 ± 0.07	< 0.07	< 0.03
Si	1	0.41 ± 0.02	0.58 ± 0.03	0.56 ± 0.02	0.46 ± 0.03	0.36 ± 0.05	0.12 ± 0.04	0.14 ± 0.05
	2	0.61 ± 0.02	0.62 ± 0.03	0.54 ± 0.03	0.42 ± 0.04	0.34 ± 0.04	0.14 ± 0.04	0.13 ± 0.05
	3	0.71 ± 0.02	0.76 ± 0.03	0.61 ± 0.02	0.53 ± 0.03	0.46 ± 0.04	0.23 ± 0.03	< 0.09
S	1	0.32 ± 0.04	0.41 ± 0.04	0.38 ± 0.02	0.30 ± 0.02	0.20 ± 0.06	< 0.06	< 0.03
	2	0.58 ± 0.03	0.56 ± 0.04	0.40 ± 0.04	0.28 ± 0.05	0.22 ± 0.06	< 0.10	< 0.04
	3	0.67 ± 0.03	0.65 ± 0.04	0.51 ± 0.03	0.38 ± 0.05	0.35 ± 0.06	0.12 ± 0.07	< 0.10
Ar	1	0.22 ± 0.08	0.16 ± 0.08	0.16 ± 0.05	< 0.07	< 0.10	< 0.05	< 0.03
	2	0.52 ± 0.06	0.44 ± 0.08	0.21 ± 0.10	< 0.12	< 0.20	< 0.13	< 0.04
	3	0.69 ± 0.06	0.50 ± 0.09	0.35 ± 0.08	0.19 ± 0.12	0.24 ± 0.14	< 0.18	< 0.07
Ca	1	0.51 ± 0.12	0.66 ± 0.10	0.85 ± 0.07	0.68 ± 0.09	0.53 ± 0.15	0.57 ± 0.15	0.27 ± 0.21
	2	0.66 ± 0.09	0.96 ± 0.10	0.92 ± 0.12	0.71 ± 0.16	0.66 ± 0.14	0.70 ± 0.14	0.30 ± 0.23
	3	0.74 ± 0.09	0.98 ± 0.11	1.02 ± 0.10	0.77 ± 0.15	0.74 ± 0.17	0.66 ± 0.17	0.70 ± 0.23
Fe	1	0.55 ± 0.01	0.61 ± 0.01	0.54 ± 0.01	0.45 ± 0.01	0.41 ± 0.01	0.32 ± 0.01	0.35 ± 0.02
	2	0.63 ± 0.01	0.57 ± 0.01	0.48 ± 0.01	0.40 ± 0.01	0.38 ± 0.01	0.29 ± 0.01	0.32 ± 0.02
	3	0.67 ± 0.01	0.62 ± 0.01	0.55 ± 0.01	0.43 ± 0.01	0.40 ± 0.01	0.31 ± 0.01	0.26 ± 0.01
Ni	1	0.68 ± 0.11	1.08 ± 0.13	0.57 ± 0.08	0.35 ± 0.11	0.37 ± 0.20	un.	un.
	2	0.89 ± 0.09	0.90 ± 0.12	0.53 ± 0.13	0.29 ± 0.15	0.22 ± 0.17	un.	un.
	3	1.65 ± 0.10	1.52 ± 0.14	0.99 ± 0.10	0.64 ± 0.20	0.69 ± 0.17	un.	un.
χ^2/dof	1	2444/525	1278/525	1066/525	774/525	717/525	909/499	816/476
	2	844/525	753/525	883/525	680/525	664/525	789/499	742/476
	3	782/525	664/525	707/525	596/525	532/525	607/499	880/476

with a fixed separation between the two temperatures as $T_2 = 2T_1$ (where T_1 and T_2 are the temperatures of the two thermal components). Fixing the temperature to $T_2 = 2T_1$ is a good first approximation of the multi-temperature structure, since Kaastra et al. (2004) and Peterson et al. (2003) found that in almost all cases of their cluster samples, at each radius, there is negligible emission from gas with a temperature less than one-third to half of the fitted upper temperature. Using the two temperature model our fits improve significantly. The χ^2 improves most significantly in the core of the cluster, but we can see a slight improvement also at outer radii. However, fitting the data with the *wdem* model further improves the χ^2 of our fits in 6 of 7 extraction annuli.

Fitting the data with a single-temperature thermal model we see that the abundances of all elements except argon drop in the core of the cluster and have a off-center

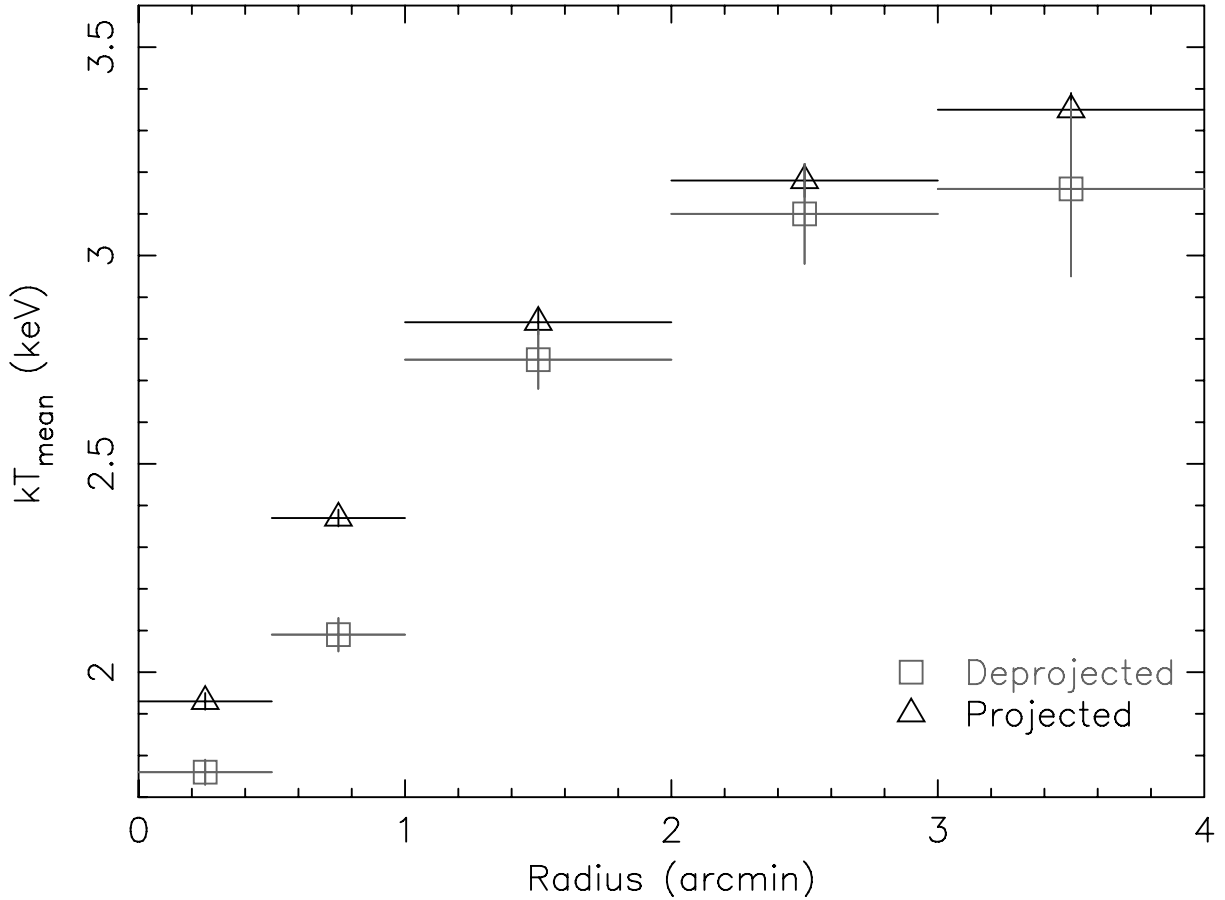


Figure 5.5: Comparison of the projected and deprojected mean temperatures obtained by fitting the *wdem* model.

peak. As we go from the single-temperature model to the two-temperature model and further to the *wdem* model, abundances of all elements in general increase, especially in the central regions of the cluster. The *wdem* model shows that most of the abundances peak in the core of the cluster, we detect a slight hint of a drop in the center only for calcium, silicon and magnesium. The dependence of the iron abundance on the temperature model is known as the Fe-bias (see, e.g. Buote 2000; Molendi & Gastaldello 2001). As we go from one model to the other, the abundance value of magnesium varies the most. Due to its vicinity to the Fe-L complex its abundance is very sensitive to the temperature and iron abundance model.

In general, all three models show a drop of abundances toward the outer parts of the cluster.

5.5.2 Deprojected spectra

To account for projection effects in the core of the cluster we extract spectra, deprojected under the assumption of a spherical symmetry. We use the background event files of Lumb et al. (2002). We extract the deprojected spectra from 5 annuli in the inner $0' - 4'$, where the cluster is still bright enough and the background subtraction does not

have a significant influence on our results. The deprojected spectra represent the count rates from spherical shells centered on the core of the cluster. Our extraction method and data analysis for the deprojected spectra is described extensively in Kaastra et al. (2004).

The fit results for the deprojected spectra are shown in Table 5.6. The temperatures determined from deprojected and projected spectra are compared in Fig. 5.5. Since, in the process of deprojection we account for the hot plasma lying in front of the relatively cool core, the observed temperatures of the deprojected shells are lower than those determined without deprojection. While the χ^2 of the fit of the single-temperature model improves significantly if we deproject the spectrum (compare with the χ^2 in Table 5.5), the single temperature thermal model still does not describe our spectra well. The *wdem* model describes the deprojected spectra extracted from the core of the cluster significantly better than the single-temperature model. It shows, that the temperature gradients in the extraction regions and the intrinsic multi-temperature structure make it necessary to use multi-temperature models also when fitting deprojected spectra. Although the deprojected spectra give a better value for the temperature, with the deprojection we introduce more noise into the spectra so the determination of abundances becomes more uncertain.

5.5.3 RGS radial profiles

Because of the high statistics of the RGS spectrum shown in Fig. 5.3, we are also able to extract smaller strips in the cross-dispersion direction and make a radial profile up to $2'$ from the center. The results of these fits are shown in Table 5.7. It confirms the radial temperature profile in the core found with EPIC, although the temperature determined with RGS is slightly higher. The reason for this discrepancy is probably the difference in extraction regions. The RGS spectra also contain a small contribution of photons originating outside the core radius due to the spatial extent of the source. Again, like in the full field-of-view case, the mean temperatures kT_{mean} are slightly higher than the single-temperature fits, although the values are consistent within the error-bars. The value for α is rather well constrained in the region between $-2'$ and $0.5'$ and shows a slight discontinuity around $0'$, but the statistics do not allow to draw a conclusion. From the χ^2 values it is clear that a DEM model (*wdem*) fits the RGS spectra better.

From the RGS abundance profiles in the cross-dispersion direction, which are listed in Table 5.7, we confirm the spatial distribution of oxygen and iron indicated by the line widths in the full RGS spectrum. The O/Fe ratio is consistent with a value between 0.3–0.4 over the whole profile. The neon and magnesium abundance tend to peak in the center slightly more than iron. Because the individual spectra in the RGS spatial profile have lower statistics than the total RGS spectrum, we use one scale parameter s for all measured lines. Therefore, the fitted scale parameter, which accounts for the broadening of the lines because of the spatial extend of the source, is the average of all line widths given in units of the width of cluster emission. These widths increase naturally toward the outer part of the cluster, because the spatial profile of the cluster also flattens.

Table 5.6: Fit results of the deprojected EPIC spectra extracted from 5 annuli in the inner 4' and fitted with a single-temperature model (1) and *wdem* model (3). This region contains the cooling core, where the projection effects are the most important. Abundances are given with respect to solar.

Parameter	Model	0 – 0.5'	0.5 – 1.0'	1.0 – 2.0'	2.0 – 3.0'	3.0 – 4.0'
N_{H} (10^{21}cm^{-2})	1	2.36 ± 0.02	2.37 ± 0.02	2.47 ± 0.03	2.48 ± 0.05	2.53 ± 0.05
	3	2.52 ± 0.06	2.58 ± 0.05	2.64 ± 0.08	2.64 ± 0.11	2.66 ± 0.16
kT (keV)	1	1.65 ± 0.02	2.07 ± 0.02	2.68 ± 0.02	3.04 ± 0.03	3.11 ± 0.05
kT_{max} (keV)	3	2.36 ± 0.04	2.72 ± 0.04	3.65 ± 0.08	4.28 ± 0.13	4.25 ± 0.21
kT_{mean} (keV)	3	1.76 ± 0.03	2.09 ± 0.04	2.75 ± 0.07	3.10 ± 0.12	3.16 ± 0.21
α	3	0.52 ± 0.03	0.43 ± 0.03	0.49 ± 0.04	0.62 ± 0.08	0.53 ± 0.14
	3	0.6 ± 0.2	0.7 ± 0.2	0.3 ± 0.2	0.3 ± 0.2	< 0.5
Mg	1	0.11 ± 0.08	0.34 ± 0.10	0.65 ± 0.07	0.35 ± 0.13	< 0.16
	3	0.55 ± 0.10	0.53 ± 0.11	0.76 ± 0.14	0.36 ± 0.15	< 0.26
Si	1	0.46 ± 0.04	0.73 ± 0.05	0.80 ± 0.04	0.73 ± 0.07	0.52 ± 0.09
	3	0.74 ± 0.06	0.84 ± 0.06	0.84 ± 0.07	0.71 ± 0.08	0.50 ± 0.10
S	1	0.42 ± 0.04	0.61 ± 0.05	0.52 ± 0.04	0.47 ± 0.08	0.19 ± 0.12
	3	0.66 ± 0.06	0.75 ± 0.06	0.61 ± 0.07	0.51 ± 0.09	0.25 ± 0.10
Ar	1	0.40 ± 0.11	0.50 ± 0.11	0.25 ± 0.10	< 0.14	0.3 ± 0.2
	3	0.57 ± 0.14	0.69 ± 0.12	0.33 ± 0.15	< 0.21	0.4 ± 0.3
Ca	1	0.64 ± 0.20	0.81 ± 0.18	1.00 ± 0.13	0.9 ± 0.2	0.4 ± 0.3
	3	0.41 ± 0.20	0.88 ± 0.16	1.06 ± 0.18	1.0 ± 0.3	0.5 ± 0.4
Fe	1	0.50 ± 0.02	0.65 ± 0.02	0.61 ± 0.02	0.46 ± 0.02	0.41 ± 0.03
	3	0.67 ± 0.03	0.66 ± 0.03	0.57 ± 0.02	0.45 ± 0.02	0.40 ± 0.03
Ni	1	0.62 ± 0.17	1.8 ± 0.2	1.53 ± 0.18	0.9 ± 0.4	0.6 ± 0.5
	3	1.3 ± 0.3	2.0 ± 0.3	1.8 ± 0.3	0.8 ± 0.4	0.6 ± 0.5
$\chi^2 / \text{d.o.f.}$	1	1090/587	668/570	892/587	515/587	520/587
	3	622/587	489/587	526/587	481/587	515/587

5.6 Temperature and iron abundance maps

In order to investigate the spatial variations of the temperature and metallicity we extract temperature and iron abundance maps of the $5.5' \times 5.5'$ region centered on the core of the cluster.

First, we determine the temperature and iron abundance on a grid with bin-size of $30'' \times 30''$. For every bin we compute a redistribution and an ancillary file. We fit the spectrum of each bin individually by the multi-temperature *wdem* model. The spectral fits are done with a hydrogen column density fixed to the global value $2.5 \times 10^{21} \text{cm}^{-2}$. The redshift is fixed to the spectroscopically determined value of the central cD galaxy ($z = 0.0349$). The abundances of all elements except iron in our model are fixed to 0.3 times the solar value (the exact value of these abundances does not influence the temperature and iron abundance determinations), while the iron abundance is left as a free parameter. We fix the parameter α to 0.58, which is the value determined for the

Table 5.7: Fit results for spatially resolved RGS spectra between 8–25 Å. The fitted models are (1) single-temperature CIE and (3) *wdem*. We use 2σ upper limits.

Par	Mod	-2.0 / -1.0'	-1.0 / -0.5'	-0.5 / 0'	0 / 0.5'	0.5–1.0'	1.0–2.0'
kT (keV)	1	4.12 ± 0.13	3.37 ± 0.10	2.89 ± 0.06	2.53 ± 0.05	3.21 ± 0.12	4.4 ± 0.3
kT_{\max}	3	6.6 ± 0.3	5.2 ± 0.2	4.6 ± 0.2	3.73 ± 0.14	5.3 ± 0.8	7.8 ± 0.9
kT_{mean}	3	4.6 ± 0.2	3.70 ± 0.15	3.12 ± 0.15	2.72 ± 0.11	3.8 ± 0.7	5.1 ± 0.6
α	3	0.79 ± 0.08	0.70 ± 0.06	0.94 ± 0.10	0.60 ± 0.05	0.7 ± 0.4	1.3 ± 0.3
O/Fe	1	0.28 ± 0.07	0.34 ± 0.05	0.40 ± 0.04	0.36 ± 0.04	0.35 ± 0.07	0.57 ± 0.18
	3	0.29 ± 0.06	0.34 ± 0.05	0.41 ± 0.04	0.36 ± 0.04	0.36 ± 0.06	0.47 ± 0.14
Ne/Fe	1	1.34 ± 0.17	1.34 ± 0.15	1.83 ± 0.14	1.54 ± 0.12	1.00 ± 0.17	1.4 ± 0.5
	3	0.60 ± 0.15	0.73 ± 0.13	0.98 ± 0.10	0.98 ± 0.10	0.56 ± 0.15	< 0.3
Mg/Fe	1	< 0.4	0.66 ± 0.17	0.40 ± 0.12	< 0.4	< 0.5	< 0.2
	3	0.5 ± 0.2	1.19 ± 0.17	1.09 ± 0.12	0.68 ± 0.11	0.42 ± 0.18	1.0 ± 0.5
Scale s	1	1.5 ± 0.2	0.98 ± 0.10	1.01 ± 0.10	0.90 ± 0.07	0.77 ± 0.13	4.5 ± 1.0
	3	1.30 ± 0.16	0.78 ± 0.10	0.69 ± 0.06	0.62 ± 0.05	0.58 ± 0.11	3.0 ± 0.7
χ^2 / d.o.f.	1	852 / 701	977 / 701	1491 / 701	1337 / 701	932 / 701	923 / 701
	3	757 / 698	802 / 698	800 / 698	853 / 698	851 / 698	839 / 698

core of the cluster (see Table 5.5). The free parameters are the maximum temperature T_{\max} , the iron abundance and the normalization of the *wdem* component.

The temperature map, which shows the mean temperature T_{mean} of the *wdem* model, reveals an elongated temperature structure in the South-Southeast North-Northwest direction and a sharp temperature change over the brightness edge south of the core. The iron abundance map shows a highly centrally peaked iron abundance with an extension to the North (see the panel *c* and *d* in Fig. 5.6).

High count rates in the $5.5' \times 5.5'$ central region allow us to reduce the size of the bins to $15'' \times 15''$ (which is roughly the FWHM of the point spread function of the pn detector) and extract a higher resolution temperature and iron abundance map fitting a single temperature model to each bin (see panel *a* and *b* in Fig. 5.6). The map shows a sharp temperature change on the southern side of the core and a large extension of the cool temperature gas to North-Northwest. In contrast to the *wdem* model fit, the iron abundance map extracted using a single-temperature model shows a central drop of iron abundance, with an abundance peak in a "high metallicity ring" around the X-ray core with an extension to the North. We verified that the central drop of iron abundance is evident also in a temperature map with $30'' \times 30''$ bins fitted with a single temperature model. The central abundance drop is rather the result of the oversimplified model for the temperature structure of the core of the cluster, than a real feature (see subsection 5.5.1).

To verify the azimuthal differences in the temperature and the metallicity we extract spectra from 4 circular regions with a radius of $0.5'$ and fit them with the *wdem* model. The extraction regions are shown in Fig. 5.7. The regions 1, 2 and 3 are centered at the same distance from the core ($2'$) but at different position angles (North, West, South).

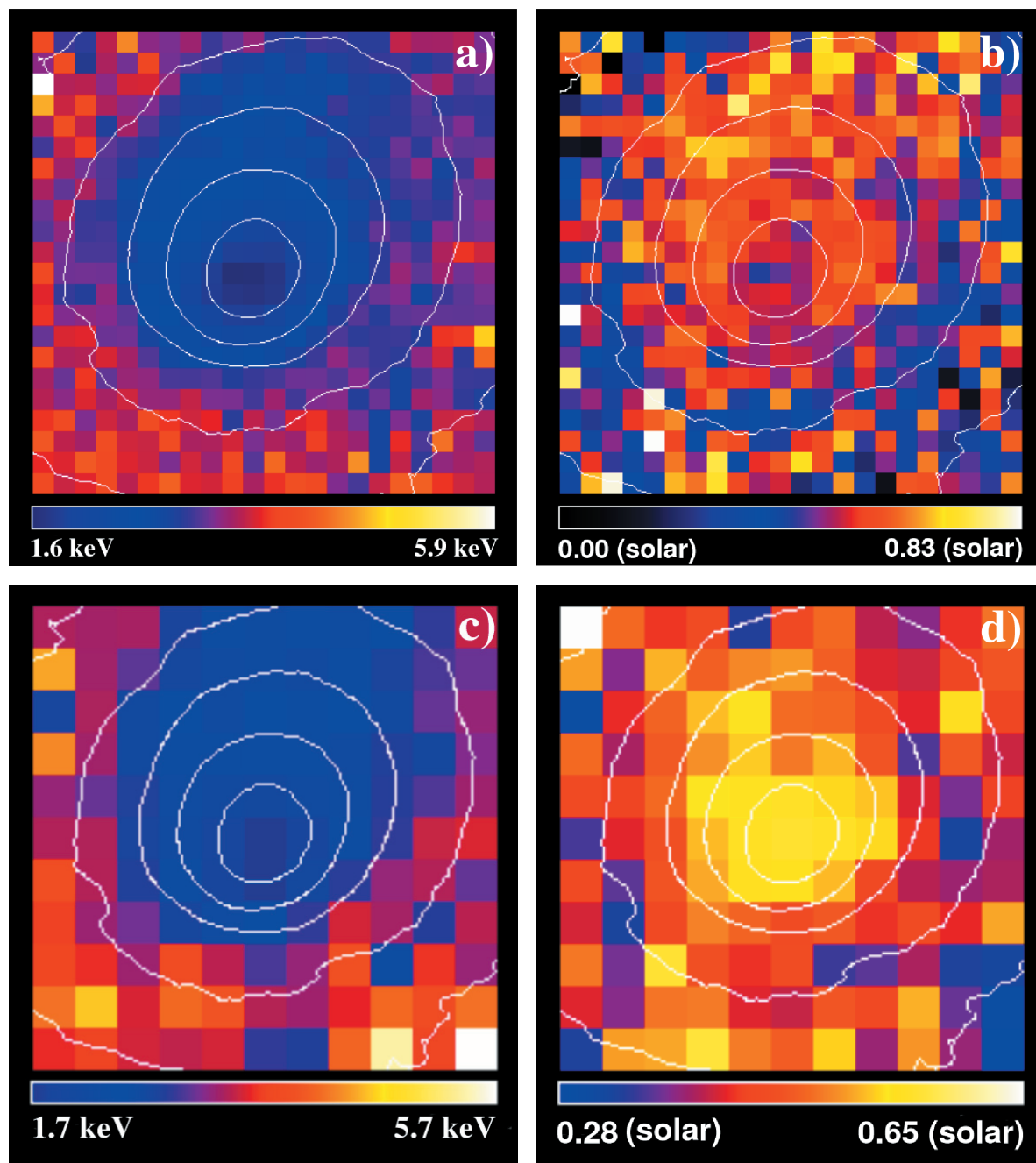


Figure 5.6: Temperature and iron abundance maps of the inner $5.5' \times 5.5'$ region of the cluster. Panel a and b: temperature and iron abundance map with each $15'' \times 15''$ pixel fitted with a single-temperature model. Panel c and d: mean temperature and iron abundance map with each $30'' \times 30''$ pixel fitted with a wdem model. Note that North is up, West is to the right. All maps have overplotted the same X-ray isophots.

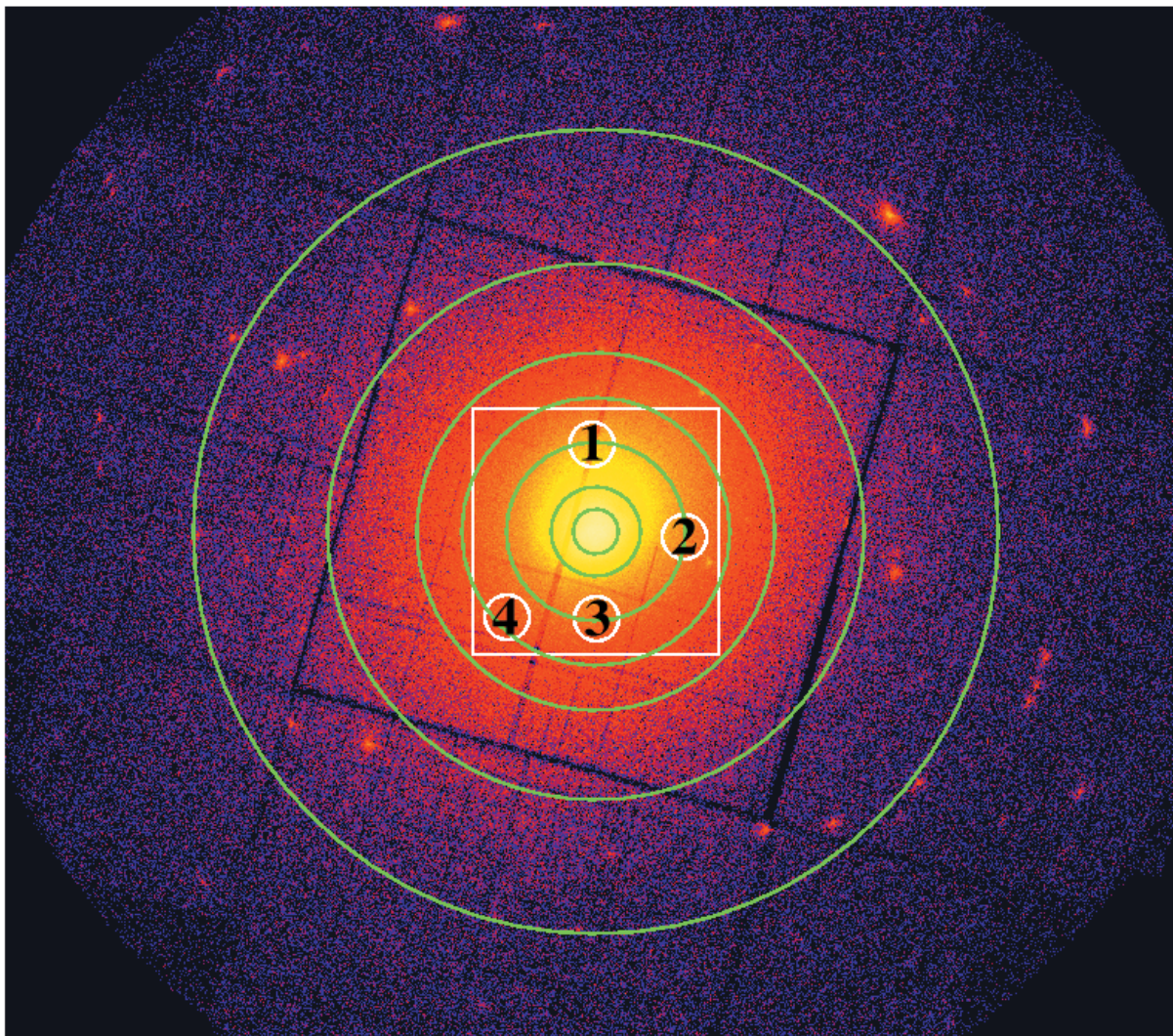


Figure 5.7: MOS1 + MOS2 image of 2A 0335+096 with overplotted extraction regions. The concentric circles correspond to our extraction annuli used to investigate the radial profiles, the square shows the $5.5' \times 5.5'$ region used to extract the temperature and iron abundance maps and the small circles correspond to extraction regions 1, 2, 3 and 4 used to verify that the temperature and abundances vary with position angle.

Region 4 is at a distance of $2.75'$ from the core at South-Southeast. Apart from the *wdem* normalization, T_{\max} and the iron abundance we leave free and fit the parameter α , N_{H} and the silicon and sulfur abundance. The best-fit parameter values are given in Table 5.8. We confirm the temperature and iron abundance asymmetry seen in the temperature maps.

Table 5.8: Parameter values obtained by fitting regions 1, 2, 3 and 4 indicated in Fig. 5.7 with the *wdem* model. Emission measures ($Y = \int n_e n_H dV$) are given in 10^{66} cm^{-3} , temperatures are given in keV, N_H in 10^{21} cm^{-2} and abundances are given with respect to solar.

Par.	1 (N)	2 (W)	3 (S)	4 (SSE)
Y	4.55	2.63	1.84	1.16
N_H	2.54 ± 0.05	2.32 ± 0.1	2.49 ± 0.09	2.38 ± 0.17
kT_{max}	3.18 ± 0.10	4.15 ± 0.20	4.2 ± 0.25	4.9 ± 0.4
kT_{mean}	2.69 ± 0.13	3.22 ± 0.20	3.25 ± 0.24	3.5 ± 0.4
α	0.22 ± 0.06	0.41 ± 0.10	0.41 ± 0.11	0.6 ± 0.3
Si	0.60 ± 0.06	0.70 ± 0.10	0.59 ± 0.11	0.50 ± 0.24
S	0.46 ± 0.08	0.43 ± 0.14	0.17 ± 0.14	0.31 ± 0.19
Fe	0.51 ± 0.02	0.39 ± 0.03	0.36 ± 0.03	0.37 ± 0.04
$\chi^2 / \text{d.o.f.}$	605/509	512/509	551/509	598/509

5.7 Properties of the core on smaller scales

The high statistics of the data obtained during our deep XMM-Newton observation allow us to better study the thermal properties of the blobs/filaments found in the core of 2A 0335+096 with Chandra (Mazzotta et al. 2003). We use a smoothed Chandra ACIS image in the energy band of 0.5 – 1.5 keV to locate the blobs/filaments. We create three extraction masks: one for the region of bright *blobs/filaments*; one for the bright region around the blobs, but excluding the blobs (*the ambient gas*); and one for the bright core but excluding the complex structure (*the envelope*); see Fig. 5.8. We use these masks to extract spectra from our EPIC-MOS data. The Full Width Half Maximum (FWHM) of the on-axis Point Spread Function (PSF) of MOS1 and MOS2 at 1.5 keV is 4.3'' and 4.4'' respectively, while the FWHM of the on-axis PSF of EPIC-pn at the same energy is 12.5''. Since the large PSF of EPIC-pn would cause a strong contamination of the spectra extracted from the region of blobs/filaments, we analyze only the data obtained by MOS.

We fit the three spectra simultaneously. The envelope is fitted by a thermal model. The ambient inter-blob gas is fitted by two thermal models, while all the parameters of the second thermal model are coupled to the model with which we fit the envelope. The region of blobs/filaments is fitted with three thermal models, where the parameters of the second and third model are coupled respectively to the model we use to fit the ambient gas, and the envelope. This way we de facto deproject the temperature of the blobs. The only free parameters in the fit are the normalizations of the thermal components, the temperatures, and the iron abundances. The values of the other abundances are fixed to the values determined by fitting the central region with *wdem*. The redshift is fixed to the redshift of the central cD galaxy. The best fit parameters are shown in Table 5.9 and the fitted spectra are shown in Fig. 5.9. The fit shows that the deprojected temperature of the blobs/filaments is 1.14 ± 0.01 keV, while the temperature of the ambient gas is 1.86 ± 0.01 keV. The iron abundance of the blobs is coupled to the iron abundance of the ambient gas, while the iron abundance of the envelope is fit-

Table 5.9: Temperature and iron abundance of the blobs/filaments, the ambient gas around these features and of the envelope of gas surrounding the inner core. The superscript *a* indicates that the parameters are coupled.

	blo./fil.	amb. gas	envelope
kT	1.14 ± 0.01	1.86 ± 0.01	2.79 ± 0.01
Fe (solar)	$0.63^a \pm 0.02$	$0.63^a \pm 0.02$	0.61 ± 0.01

Table 5.10: Relative numbers of SN Ia, SN II and Pop III contributing to the enrichment of the intra-cluster medium. We show the results of fits of linear combinations of the yields of SN Ia, SN II and Pop III stars, with two SN Ia yield models, to the abundances of 7 elements shown in Table 5.2 determined for the core and the outer region of 2A 0335+096. For the core we show the results of fits with two different Pop III star models and the results of fits without Pop III stars.

Model	Par	$0' - 3'$		$3' - 9'$	
		$M_{\text{popIII}} = 130 M_{\odot}$	$M_{\text{popIII}} = 65 M_{\odot}$	no Pop III	no Pop III
W7	SN Ia	0.24 ± 0.04	0.18 ± 0.01	0.20 ± 0.01	0.39 ± 0.04
	SN II	0.76 ± 0.04	0.85 ± 0.01	0.80 ± 0.01	0.61 ± 0.04
	Pop III	$(4 \pm 1) \times 10^{-3}$	$(-2.7 \pm 0.4) \times 10^{-2}$	–	–
	χ^2	36 / 4	60 / 4	70 / 5	44 / 5
WDD2	SN Ia	0.25 ± 0.04	0.27 ± 0.03	0.26 ± 0.01	0.37 ± 0.04
	SN II	0.75 ± 0.04	0.72 ± 0.03	0.74 ± 0.01	0.63 ± 0.04
	Pop III	$(-2 \pm 1) \times 10^{-3}$	$(6 \pm 18) \times 10^{-3}$	–	–
	χ^2	35 / 4	43 / 4	43 / 5	8 / 5

ted separately and is found to be somewhat lower. Coupling the iron abundance of the blobs with that of the ambient gas is necessary to avoid anti-correlation between the two parameters and it has no effect on the determined temperature difference between the two components.

Mazzotta et al. (2003) assumed that the blobs are ellipsoids and selected eight regions. We assume the regions and the luminosities given by Mazzotta et al. (2003) and with our new temperature we calculate with a MEKAL model the density of the blobs. We find a value of $\sim 8.5 \times 10^{-2} \text{ cm}^{-3}$. From our best fit emission measure of the thermal model of the ambient gas we calculate the density of the gas and find a value of $\sim 5.5 \times 10^{-2} \text{ cm}^{-3}$. These density estimates and our new values of the temperatures of these two components therefore indicate, that the cold blobs/filaments and the ambient gas are in thermal pressure equilibrium ($nkT \simeq 0.1 \text{ keV cm}^{-3}$).

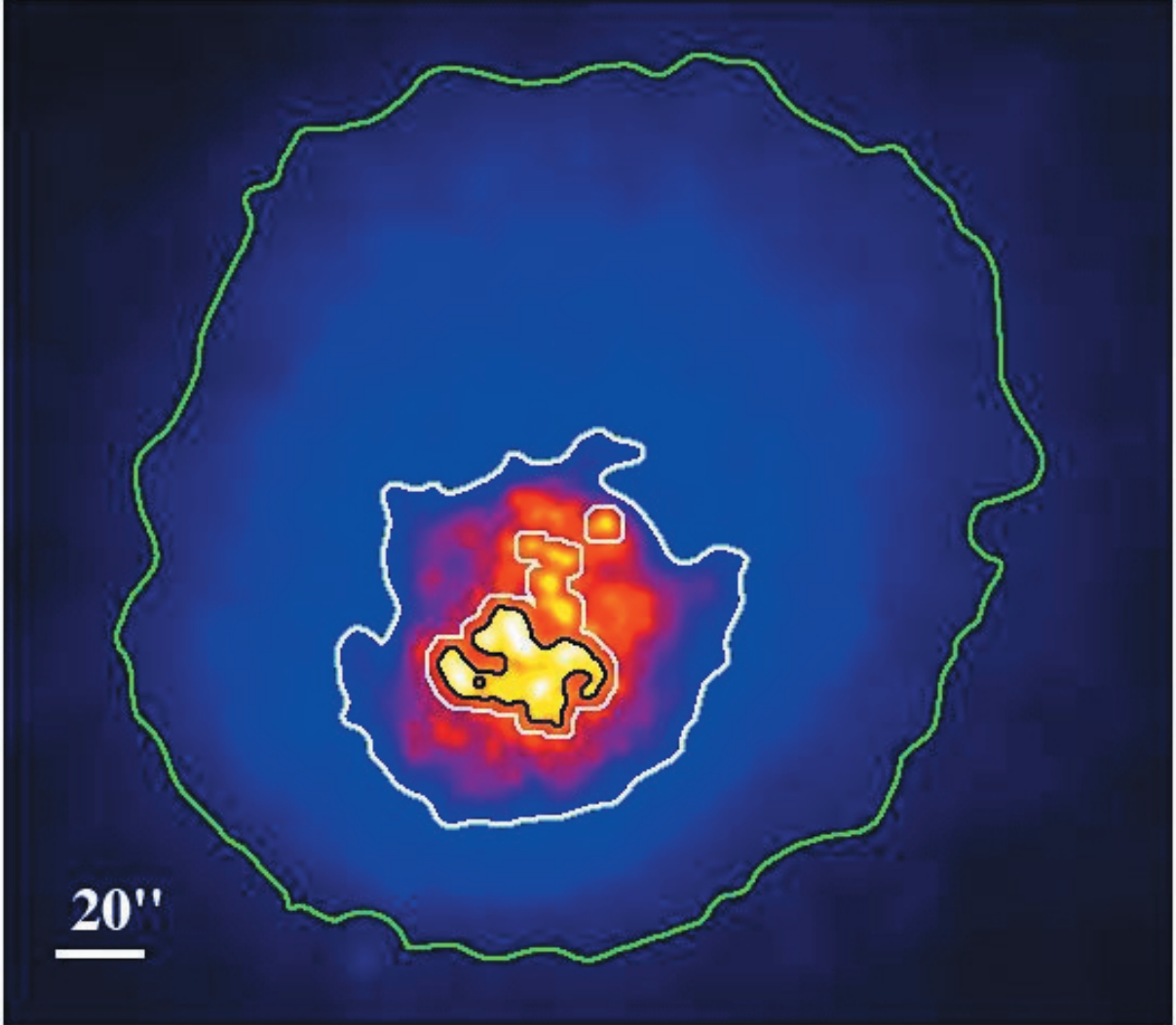


Figure 5.8: Smoothed Chandra image of the core of 2A 0335+096 with overplotted areas used to extract spectra from the data obtained during our deep XMM-Newton observation. The spectra of blobs/filaments, ambient gas and the envelope were extracted respectively from the area indicated by black, white and gray contours.

5.8 Abundances and enrichment by supernova types Ia, II, and Pop-III stars

We investigate the relative contribution of the number of supernova types Ia/II to the total enrichment of the intra-cluster medium (ICM). We also investigate the possibility of putting constraints on the contribution by Population III stars. We try to determine the relative numbers of different supernovae

$$\frac{N_{\text{Sx}}}{N_{\text{Ia}} + N_{\text{II}} + N_{\text{popIII}}}, \quad (5.4)$$

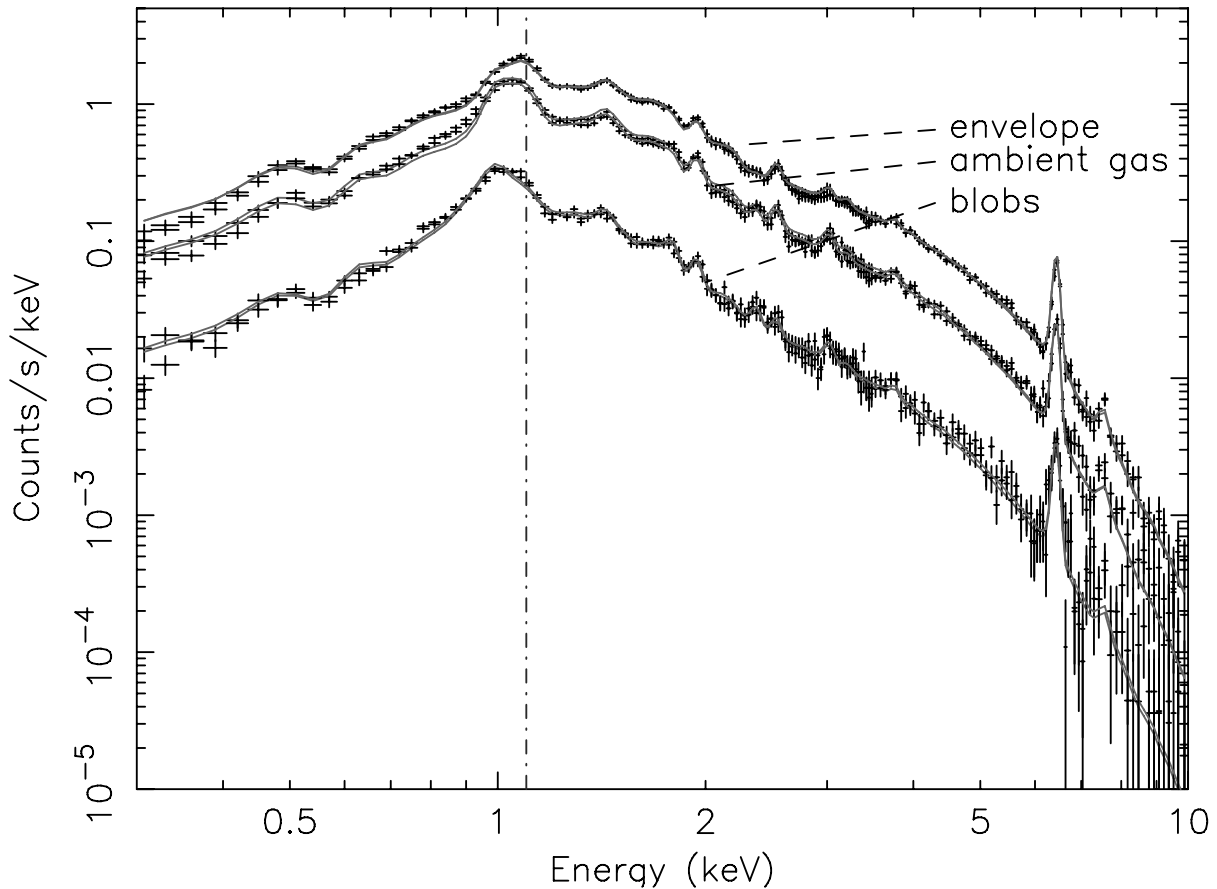


Figure 5.9: Spectra of the blobs/filaments, the ambient gas around these features and of the envelope of gas surrounding the inner core. The vertical line helps to see that there is more Fe-L emission at low energies in the spectrum of the blobs.

where N_{Sx} is either the number of Type Ia supernovae (SNe Ia), Type II supernovae (SNe II) or Population III stars (Pop III) contributing to the enrichment of ICM. Since the progenitors of Type II supernovae and Type Ib and Ic (SNe Ib/Ic) are massive stars, we associate the heavy-element yields from SNe II with those from SNe Ib/Ic. For nucleosynthesis products of SN II we adopt an average yield of stars on a mass range from $10 M_{\odot}$ to $50 M_{\odot}$ calculated by Tsujimoto et al. (1995) assuming a Salpeter initial mass function. For nucleosynthesis products of SN Ia we adopt values calculated by Iwamoto et al. (1999) and investigate two different models (see Table 5.10). The W7 model is calculated using a slow deflagration model, while the WDD2 model is calculated using a delayed-detonation model. Note that delayed-detonation models are currently favored over deflagration models by the supernova community, whereas the WDD2 is favored by Iwamoto et al. (1999). The intergalactic medium might also have been significantly enriched by Pop III stars which exploded as pair instability supernovae. We investigate two models for heavy element yields of Pop III stars calculated by Heger & Woosley (2002), with a core mass of $130 M_{\odot}$ and $65 M_{\odot}$.

We assume that the observed total number of atoms N_i of the element i (determined from its abundance and the emission measure distribution) is a linear combination of

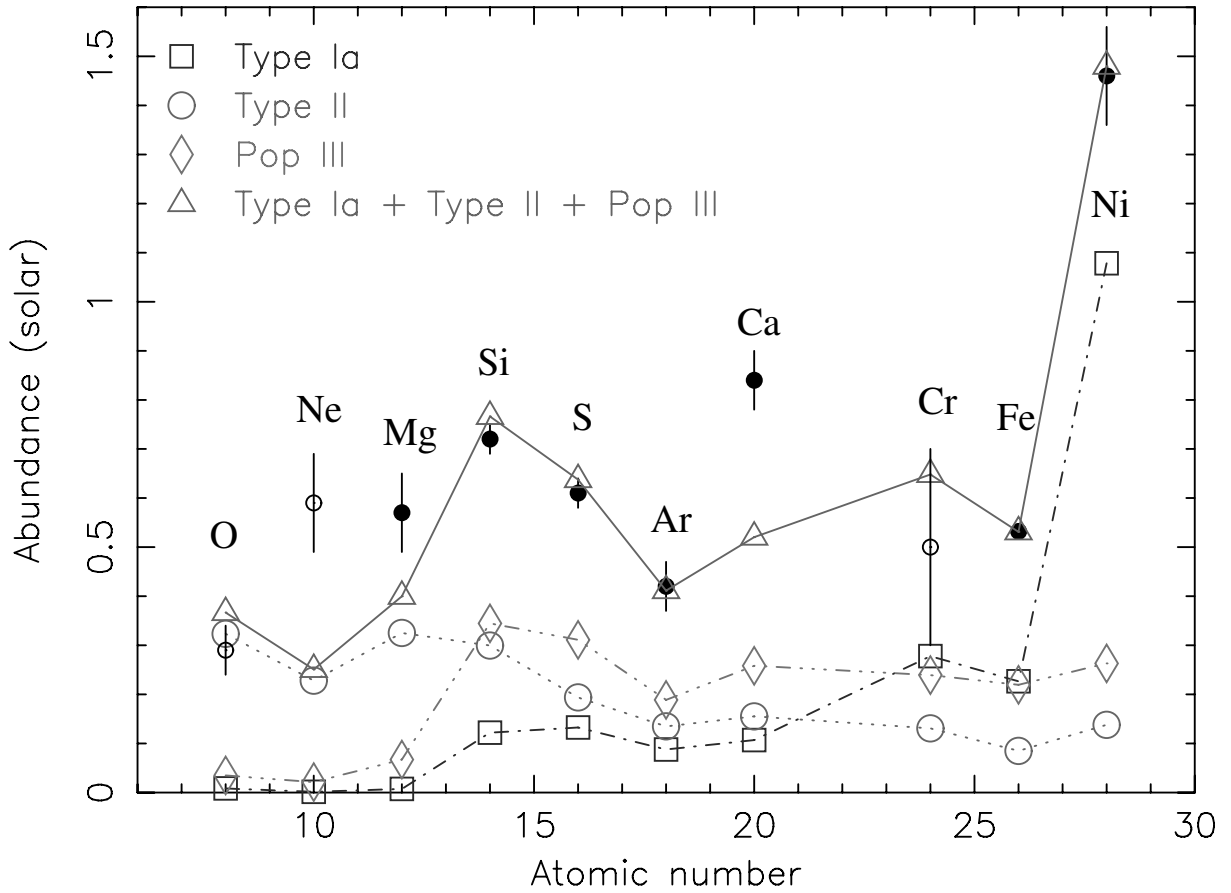


Figure 5.10: The elemental abundances derived from a *wdem* fit of the inner 3' of 2A 0335+096, fitted by a linear combination of the yields of SN Ia, SN II and Pop III, for the SN Ia model W7 and Pop III model with a core mass of $130 M_{\odot}$. The black empty circles indicate elements not used in the fit.

the number of atoms Y_i produced per individual supernova Type Ia ($Y_{i,\text{Ia}}$), Type II ($Y_{i,\text{II}}$) and Population III star ($Y_{i,\text{III}}$):

$$N_i = aY_{i,\text{Ia}} + bY_{i,\text{II}} + cY_{i,\text{III}}, \quad (5.5)$$

where a , b and c are multiplication factors representing the total number of each supernovae that went off in the cluster and enriched the ICM.

First we fit the abundances obtained for the cooling-core region (the inner 3') and determine the best-fit values for a , b and c , which we use to estimate the relative numbers of supernovae. We fit the abundance values obtained for the inner 3' region shown in Table 5.2. The best fit values of the relative contributions are shown in Table 5.10 and Fig. 5.10. In the Fig. 5.10 we also show our best measurement of the chromium abundance and the measured oxygen and neon abundances determined by the RGS and normalized to the iron abundance determined by EPIC (the absolute abundances are not well determined by RGS). Since the low significance makes the value of the chromium abundance uncertain and the abundance values of the oxygen and neon may be affected by systematic uncertainties arising from using different extraction regions for the RGS and EPIC, we do not include them in the fitting. We see that all

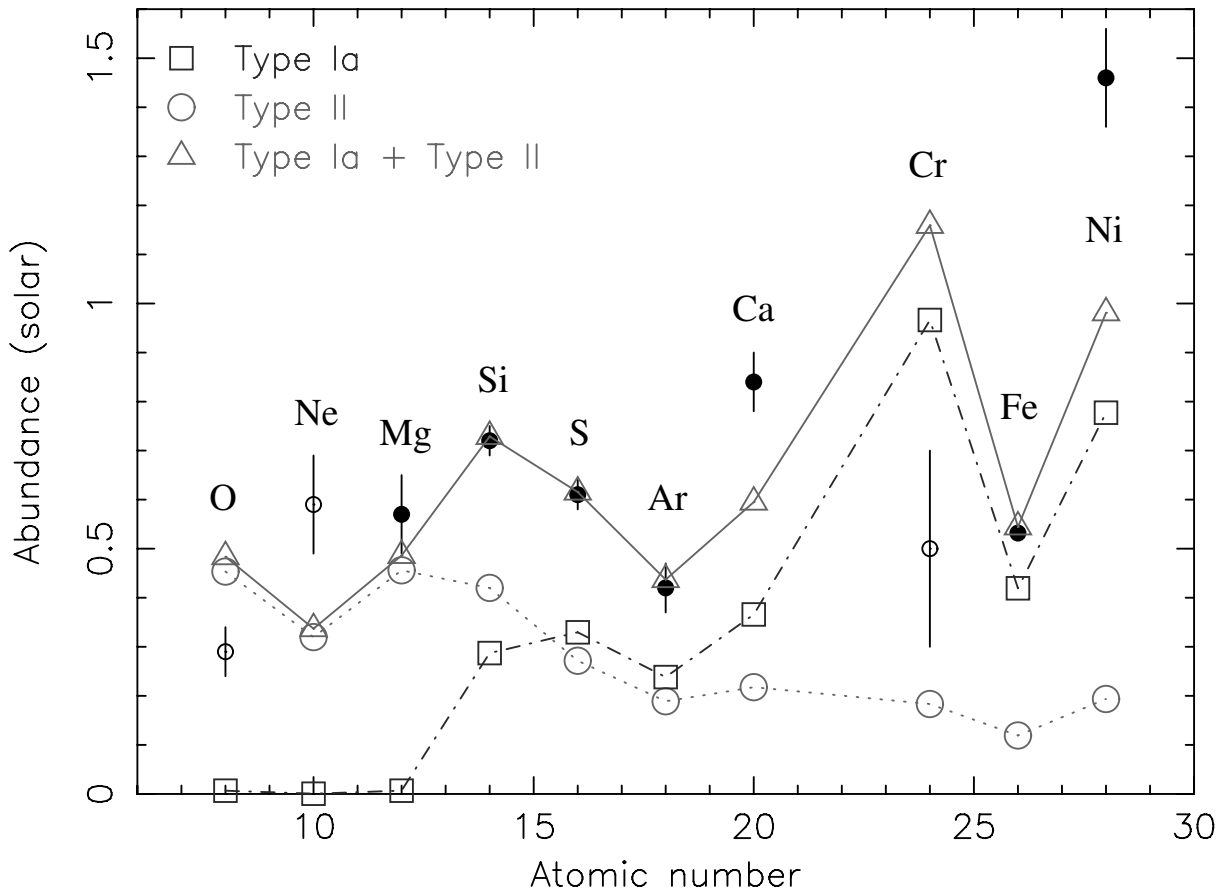


Figure 5.11: The elemental abundances derived from a *wdem* fit of the inner 3' of 2A 0335+096, fitted by a linear combination of the yields of SN Ia and SN II. For SN Ia we use the WDD2 model. The black empty circles indicate elements not used in the fit.

models are consistent with a scenario where the relative number of Type Ia supernovae contributing to the enrichment of the intra-cluster medium is 20 – 30%, while the relative number of Type II supernovae is 70 – 80%.

The $130 M_{\odot}$ Pop III star model fits show, that their relative number contributing to the enrichment is about two orders of magnitude lower than the number of SN Ia/II. However, they produce according to the models about two orders of magnitude more mass per star than SN Ia/II so their contribution to the enrichment of ICM could still be significant. However, the relative numbers determined for Pop III are model dependent and the high values of the χ^2 s do not allow us to confirm their contribution. The $65 M_{\odot}$ Pop III star model fits give unphysical values for their relative numbers. In Fig. 5.11 we show our best-fit model of the observed abundances as a linear combination of only SN Ia and SN II. This model gives us the same relative number of SN Ia as the models containing Pop III stars. Also, using the WDD2 SN Ia model, the χ^2 does not change with respect to models containing Pop III stars. The fit results show that Pop III stars are not necessary to explain the observed abundance patterns, although their contribution to the enrichment of the ICM cannot be excluded. We conclude that this analysis does not allow us to put any constraints on the enrichment by Pop III stars.

In Fig. 5.10 and 5.11 we see that the measured abundance of calcium is significantly higher than that predicted by the models. The abundance of nickel is well fitted only using the W7 model of Type Ia supernovae with Pop III stars. Fitting the abundances as a linear combination of SN Ia and SN II, the W7 model predicts more and the WDD2 model predicts less nickel than observed. Mainly the discrepancies between the model and the measured abundances of calcium and nickel are responsible for the large χ^2 s. The WDD2 model always predicts significantly more chromium than the upper limit derived from our data-point. The best measured abundances of oxygen and neon are also not well reconstructed by the models. This may be either due to problems in the supernova models or due to the fact that they were determined from a different extraction region with a different instrument. We note that the involved uncertainties and complications when interpreting the observed abundances (see Matteucci & Chiappini 2005) do not allow us to differentiate between the two SN Ia models.

Since our fits of the core show that we cannot put constraints on the contribution of Pop III stars we fit the “outskirts” ($3' - 9'$) with models containing only SN Ia and SN II. The fits show a higher contribution of SN Ia in the outer region than in the cooling core region, however the large χ^2 values and the involved systematic uncertainties do not allow us to make a firm statement.

5.9 Discussion

We have used three different thermal models in our analysis of 2A 0335+096 and find that the multi-temperature *wdem* model fits the data best. We note that a good description of the temperature structure is very important to obtain correct values for elemental abundances. Fitting the EPIC and RGS data we determine the radial temperature and abundance profiles for several elements. The elemental abundances have a peak in the core of the cluster and show a gradient across the whole cluster. The abundance structure of the cluster is consistent with a scenario where the relative number of SN Ia is 20 – 30% of the total number of supernovae enriching the ICM. Contrary to the findings of Baumgartner et al. (2005), the Population III stars are not necessary to explain the observed abundance patterns. However, their contribution to the enrichment of the ICM cannot be excluded. Extracting temperature and iron abundance maps we find an asymmetry across the cluster. We find that the deprojected temperature of the blobs/filaments in the core of the cluster is lower than the temperature of the ambient gas and the blobs appear to be in thermal pressure equilibrium with the ambient gas. Below, we discuss the implications of these results.

5.9.1 Intrinsic temperature structure

Our results show a presence of plasma emitting at a range of different temperatures within every extraction bin. In the core of the cluster, this may be caused in part by projection effects and by the strong temperature gradient. The multi-temperature structure we find around the central bin may also be caused in part by the large scale

temperature asymmetry of the cluster, so in one extraction annulus we extract the spectrum of both the colder and of the warmer gas from North and South of the cluster center respectively. However, the non-isothermality detected by fitting the deprojected spectra cannot be caused only by the width of our extraction annuli in combination with the temperature asymmetry. The temperature gradients across our annuli and the temperature differences between North and South are not large enough for that. The results can be interpreted as intrinsic multi-temperature structure at each position, which is in agreement with the results of Kaastra et al. (2004). Furthermore, these results show that fitting the spectrum of the intra-cluster gas with a single-temperature thermal model is in general not sufficient and introduces systematic errors especially in the determination of elemental abundances.

Spatial temperature distribution

The temperature distribution has a strong gradient in the core. In the inner 3' the deprojected temperature drops by a factor of ~ 1.8 toward the center. In the outer part (3' – 9') the radial temperature distribution is flat. We do not see a temperature drop toward the outskirts. We find an asymmetry in the temperature distribution and iron abundance distribution. The temperature maps show the asymmetry in temperature distribution in the direction of the elongated surface brightness morphology, roughly in the South-Southeast North-Northwest direction. The temperature drops faster toward the core from the South than from the North. The temperature change is the strongest over the cold front South of the core identified by Mazzotta et al. (2003) in Chandra data. The cold fronts are interpreted as boundaries of a dense, cooler gas moving through the hotter, more rarefied ambient gas (Markevitch et al. 2000). From the pressure jump across the cold front Mazzotta et al. (2003) conclude that the dense central gas core moves from North to South with a Mach number of $M \simeq 0.75 \pm 0.2$. The elongated, comet-like shape of the cold central core shown in our temperature maps supports this picture. The elongated shape of the cold gas core may hint that we see a surviving core of a merged subcluster moving through and being stripped by a less dense surrounding gas. The possible merger scenario is discussed in subsection 5.9.3.

X-ray blobs/filaments

Mazzotta et al. (2003) found that the deprojected temperature of the blobs is consistent with that of the less dense ambient gas, so these gas phases do not appear to be in thermal pressure equilibrium. Therefore they propose a possibility of a significant unseen non-thermal pressure component in the inter-blob gas, possibly arising from the activity of a central active galactic nucleus (AGN). They also discuss two models to explain the origin of the blobs: hydrodynamic instabilities caused by the motion of the cool core and “bubbling” of the core caused by multiple outbursts of the central AGN.

However, the temperature measurements of Mazzotta et al. (2003) have large uncertainties due to the low statistics of the Chandra data. The superior spectral quality of our XMM-Newton data allows us to measure the temperature of the blobs much more accurately. In contrast to the previous findings we find that the deprojected tempera-

ture of the region where they identified the blobs/filaments is colder by a factor of 1.6 than the temperature of the ambient gas and the blobs appear to be in thermal pressure equilibrium with the ambient gas. In the light of this new result a non-thermal pressure component in the inter-blob gas is not necessary to explain the observed blobs.

5.9.2 Abundance distribution

The high statistics of the data allow us to determine the abundances of the most abundant metals. For the first time we put constraints on the abundance of chromium, and upper limits on abundances of titanium, manganese and cobalt. The abundance distribution has a peak in the core of the cluster. The radial profiles show an abundance gradient toward the core across the whole analyzed region of the cluster. The abundance gradient is not restricted to the cooling-flow region. We observe centrally peaked abundance distributions for both SN Ia products (iron, nickel) and elements contributed mainly by SN II (magnesium, silicon). Contrary to our results from 2A 0335+096, cooling core clusters (e.g. see the sample of Tamura et al. (2004)) in general show a centrally peaked distribution of SN Ia products with respect to SN II products. The different abundance distribution in 2A 0335+096 might point toward a different enrichment history. In Sérsic 159-03 the widths of the RGS lines also indicate that the iron abundance is much more centrally peaked than oxygen (Chapter 4). Contrary to Sérsic 159-03, the RGS data in 2A 0335+096 indicate that the spatial distributions of oxygen and iron might be very similar. However, we have to be careful with interpreting the RGS results, because the strong temperature drop in the center of this cluster might cause that the RGS spectrum is dominated by the line emission from the cool core and the line profiles of iron and oxygen follow the temperature structure more than the abundance distribution of the elements.

We estimate that the total mass of iron within the radius of 126 kpc is $\sim 2.1 \times 10^9 M_{\odot}$. If all iron originates from SN Ia, we need $\sim 2.8 \times 10^9$ SN Ia explosions to explain the observed amount of iron. Assuming 1.1×10^{10} years and 50 galaxies contributing iron via galactic winds and gas stripping we get an average SN Ia rate of one explosion per 200 years per galaxy.

We show that the determined abundance values are sensitive to the applied temperature model. Especially single-temperature thermal models can introduce a bias in the abundance determination, resulting in a detection of off-center abundance peaks reported for example by Sanders & Fabian (2002) and Johnstone et al. (2002).

The abundance maps show an asymmetry in the iron abundance distribution, with a higher abundance to the North of the cluster core. The abundance asymmetry further highlights and supports the picture of great dynamical complexity.

5.9.3 Possible merger scenario

We observe an asymmetry of the temperature and iron abundance distribution across the cluster, along the surface brightness elongation, which points toward the possibility of an ongoing merger in 2A 0335+096. Mazzotta et al. (2003) note that the orientation of

the cold front and the asymmetry of the temperature distribution suggest that the cool core is moving along a projected direction that goes from North to South. However, it is not known whether the motion is due to a merger, or due to gas sloshing induced by an off-axis merger or by a flyby of another cluster. Mazzotta et al. (2003) also reason that if the cool core is indeed a merging subcluster, then in projection the position of the subcluster is close to the cluster center. However, the impact parameter cannot be measured hence the subcluster may be passing through the cluster at any distance along the line of sight. Our detection of an asymmetry in the abundance distribution across the cluster, with a higher metallicity North of the core with respect to the South, supports the merger scenario, in which the subcluster had a higher metallicity. The most important enrichment processes, like ram pressure stripping of cluster galaxies and galactic winds, are not expected to produce the observed asymmetry in the spatial distribution of the iron abundance. In the dense cores of clusters of galaxies the internal kinematics of the ICM is expected to quickly smooth out any existing inhomogeneities in the abundance distribution.

In Fig. 5.12 we show an archival *Hubble Space Telescope* (HST) image of the core of the cluster with overplotted EPIC-MOS X-ray isophots. The HST image shows the central cD galaxy and a companion galaxy to the North-West (the bright source in the lower left is a foreground star). We see, that the X-ray brightness peak is offset to the South from the central cD galaxy, which also shows that the core is not in a relaxed state. This was already shown by Mazzotta et al. (2003) who found that the centroid positions of the best fit double β -model to the cluster surface brightness do not coincide with the position of the central cD galaxy, but are offset to the South-East and North-West. It is interesting to note, that the alignment of the central cD galaxy and the alignment of the central galaxy with the projected companion nucleus are following the same direction as the possible merger axis inferred from the X-rays. Dubinski (1998) has shown that the long axis of a brightest cluster galaxy always aligns with the primordial filament along which the cluster collapsed and with the long axis of the cluster galaxy distribution. If 2A 0335+096 formed along a filament aligned as the long axis of the central cD galaxy, we might be seeing the traces of the latest phase of the formation of the cluster, in which a subcluster is falling in along the same primordial filament.

Although there is growing evidence for the merger scenario, with the available data we still cannot rule out an alternative scenario of gas sloshing. Radial velocity measurements of the individual galaxies in 2A 0335+096 are necessary to provide the decisive evidence.

5.9.4 Relative enrichment by supernova types Ia/II and Population III stars

All our fits show that the contribution of SN Ia is 20 – 30% of the total number of supernovae enriching the ICM. Tsujimoto et al. (1995) found that the ratio of the total numbers (integrated over time) of supernovae Type Ia to Type II that best reproduces the Galactic abundances is $N_{\text{Ia}}/N_{\text{II}} = 0.15$, while the ratio determined for the Magellanic Clouds is 0.2 – 0.3, which correspond to relative numbers of $N_{\text{Ia}}/N_{\text{Ia+II}} = 0.13$

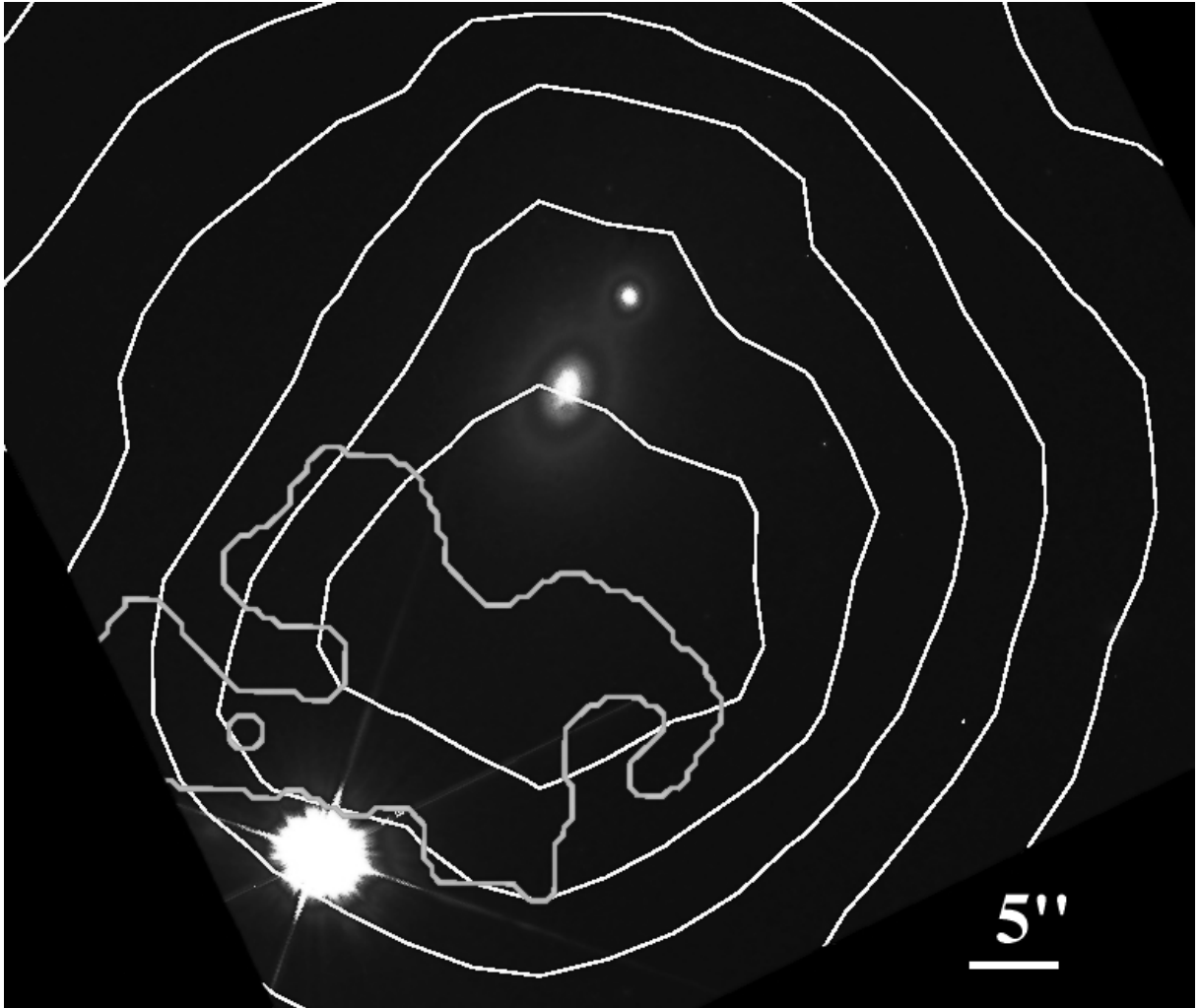


Figure 5.12: An image of the core of the cluster obtained by the Hubble Space Telescope with overplotted X-ray isophots. North is up, West is right. The X-ray isophots are off-set from the central cD galaxy. The gray contour indicates the location of the cold blobs/filaments detected in X-rays.

and 0.17 – 0.23 in the Galaxy and in the Magellanic clouds respectively. Supernova types Ia/II produce heavy-elements on different time scales during the chemical evolution of galaxies, with SN II causing the enrichment usually in the early phases of galactic evolution and SNe Ia on a much longer time-scale, in the later phases of galactic evolution. The current relative frequencies of SNe Ia and II also depend on types of galaxies. According to the Lick Observatory Supernova Search (LOSS) about 42% of the supernovae observed in galaxies within a redshift of $z = 0.03$ are SN Ia, while SNe II are rare in early-type galaxies and SNe Ia occur in all types of galaxies (van den Bergh et al. 2005). The relative contribution to the enrichment of ICM by SN Ia in the cluster of galaxies 2A 0335+096 is between the Galactic value and the value of the current relative frequencies determined by LOSS (van den Bergh et al. 2005). The value of $N_{\text{Ia}}/N_{\text{Ia+II}} = 20 - 30\%$ is consistent with a picture of an early enrichment by SNe II material from star-burst galaxies and later contribution by Type Ia supernovae

material.

However, the scenario proposed by Tamura et al. (2001a) and Finoguenov et al. (2001), where an early and well mixed SN II enrichment is followed by SN Ia enrichment in the central galaxy, produces over the Hubble time a centrally peaked distribution of SN Ia products relative to SN II products. As discussed in 5.9.2, we observe a centrally peaked abundance distribution of both SN Ia and SN II products. Moreover, contrary to the expectations, comparing the relative enrichment in the inner and outer regions of the cluster the Mg/Fe, Si/Fe and S/Fe ratios point toward a higher contribution of SN Ia in the outer parts compared to the cool core. Such a difference in the enrichment history between the core and the outer parts would strongly support the scenario according to which the cool core is the surviving ICM of a merged subcluster (see 5.9.3). However, the involved uncertainties in the determination of the relative enrichment are high.

As discussed by Matteucci & Chiappini (2005) the interpretation of the observed abundance ratios is not easy. The observed abundance ratios strongly depend on the star-formation history in cluster galaxies. Part of the supernova products might still be locked in the stars or in the potential wells of cluster galaxies. Therefore, the relative number of supernovae contributing to the enrichment of the ICM, which we infer from the abundance ratios, might be somewhat different from the relative number of supernovae which exploded in the cluster over its life-time.

The results also show that it is not necessary to include the Pop III stars in our models to explain the observed abundance patterns. Our magnesium, silicon, sulfur, argon and iron abundances can be reconstructed with a linear combination of yields of SN Ia and II for all tested SN Ia yield models. In the cluster 2A 0335+096 we cannot confirm the results of Baumgartner et al. (2005) claiming, that especially in the hotter clusters, Pop III stars are necessary to explain the observed silicon, sulfur, calcium and argon abundances. However, to test the results of Baumgartner et al. (2005) an analysis of a large cluster sample including hotter clusters will be necessary.

All fitted models give a significantly lower calcium abundance than we observe. This points toward uncertainties in the models of SN II yields, e.g. different explosion energies in the models can result in a difference of an order of magnitude in calcium production (Woosley & Weaver 1995).

5.10 Conclusions

We have analyzed spatially resolved and high resolution spectra of the cluster of galaxies 2A 0335+096 obtained during a deep XMM-Newton observation. We found that:

- We unambiguously detect multi-temperature structure in the core of 2A 0335+096: for the determination of elemental abundances, a multi-temperature model is mandatory. The *wdem* model is a good description of the temperature structure of the gas in 2A 0335+096.
- The blobs/filaments found in the core of 2A 0335+096 are significantly colder than the ambient gas and they appear to be in pressure equilibrium with their

environment.

- We detect a strong central peak in the abundance distributions of both SN Ia and SN II products.
- The relative number of SN Ia contributing to the enrichment of the intra-cluster medium in the central 130 kpc of 2A 0335+096 is $\sim 25\%$, while the relative number of SN II is $\sim 75\%$. Comparison of the observed abundances to the supernova yields does not allow us to put any constraints on the contribution of Pop III stars to the enrichment of the ICM. We observe significantly higher calcium abundance than predicted by supernova models.
- The detected asymmetry in the temperature and iron abundance distribution further supports the merger scenario, in which the subcluster had a higher metallicity.

Note: the online edition of this paper contains an appendix describing the effect of the background subtraction and absorption on the results. The appendix is available on the website of A&A (<http://www.aanda.org/>) or through astro-ph using reference number 0512401.

Acknowledgements

This work is based on observations obtained with XMM-Newton, an ESA science mission with instruments and contributions directly funded by ESA member states and the USA (NASA). The Netherlands Institute for Space Research (SRON) is supported financially by NWO, the Netherlands Organization for Scientific Research.

Constraining supernova models using the hot gas in clusters of galaxies

J. de Plaa^{1,2}, *N. Werner*¹, *J. A. M. Bleeker*^{1,2}, *J. S. Kaastra*¹, *M. Méndez*¹, and *J. Vink*^{1,2}

¹ SRON Netherlands Institute for Space Research, Utrecht, The Netherlands

² Astronomical Institute, Utrecht University, Utrecht, The Netherlands

Submitted 12 September 2006

Submitted to *Astronomy & Astrophysics*, 2006

Abstract

Context. The hot X-ray emitting gas in clusters of galaxies is a very large repository of metals produced by supernovae. During the evolution of clusters, billions of supernovae eject their material into this Intra-Cluster Medium (ICM).

Aims. We aim to accurately measure the abundances in the ICM of many clusters and compare these data with metal yields produced by supernovae. With accurate abundances determined using this cluster sample we will be able to constrain supernova explosion mechanisms.

Methods. Using the data archive of the XMM-Newton X-ray observatory, we compile a sample of 22 clusters. We fit spectra extracted from the core regions and determine the abundances of silicon, sulfur, argon, calcium, iron, and nickel. The abundances from the spectral fits are subsequently fitted to supernova yields determined from several supernova type Ia and core-collapse supernova models.

Results. We find that the argon and calcium abundances cannot be fitted with currently favoured supernova type Ia models. We obtain a major improvement of the fit, when we use an empirically modified delayed-detonation model that is calibrated on the Tycho supernova remnant. The two modified parameters are the density where the sound wave in the supernova turns into a shock and the ratio of the specific internal energies of ions and electrons at the shock. Our fits also suggest that the core-collapse supernovae that contributed to the enrichment of the ICM had progenitors which were already enriched.

Conclusions. The Ar/Ca ratio in clusters is a good touchstone for determining the quality of type Ia models. The core-collapse contribution, which is about 50% and not strongly dependent on the IMF or progenitor metallicity, does not have a significant impact on the Ar/Ca ratio. The number ratio between supernova type Ia and core-collapse supernovae suggests that binary systems in the appropriate mass range are very efficient (~ 5 –16%) in eventually forming supernova type Ia explosions.

6.1 Introduction

Clusters of galaxies are the largest gravitationally bound objects in the universe. About 80% of the baryonic matter in the clusters is in the form of hot X-ray emitting gas that has been continuously enriched with metals since the first massive stars exploded as supernovae. The abundances of elements in this hot Intra-Cluster Medium (ICM) therefore correspond to the time-integrated yield of the supernova products that reached the ICM. About 20–30% of the supernova products is being locked up in stars in the member galaxies (Loewenstein 2004). Because of the huge mass of the accumulated metals in the ICM, clusters of galaxies provide a unique way to test nucleosynthesis models of supernovae on a universal scale.

Since the launch of the ASCA satellite, it has been possible to do abundance studies using multiple elements. Several groups (e.g. Finoguenov et al. 2000; Fukazawa et al. 2000; Finoguenov et al. 2001; Baumgartner et al. 2005) used ASCA observations of a sample of clusters to study the enrichment of the ICM. They were able to measure the abundances of iron, silicon, and sulfur. Also neon, argon, and calcium were sometimes detected, but with relatively low accuracy. The spatial distributions of iron and silicon indicated that the core of the clusters is dominated by SN Ia products (Fe), while the outer parts of the clusters appear to be dominated by core-collapse supernova products (O). Using ASCA observations some authors already tried to constrain the specific flavour of supernova type Ia models (e.g. Dupke & Arnaud 2001). Others, like Baumgartner et al. (2005) used ASCA data to find that Population-III stars should play an important role in the enrichment of the ICM. However, this result is debated (Chapter 4).

With the XMM-Newton observatory (Jansen et al. 2001), which has both a better spectral resolution and a much larger effective area compared to ASCA, it is in principle possible to extend the number of detectable elements to nine. The first abundances determined from a sample of clusters observed with XMM-Newton were published by Tamura et al. (2004). The general picture from the ASCA samples was confirmed, ex-

cept for the fact that the silicon and sulfur abundance show a centrally-peaked spatial profile like iron. The oxygen abundance appears to be more uniformly distributed in the clusters.

In Chapter 4 and 5 we analysed deep XMM-Newton observations of the clusters 2A 0335+096 and Sérsic 159-03, respectively. There we were able to accurately measure the global abundances of about nine elements in the cluster and fit them using nucleosynthesis models for supernovae type Ia and core-collapse supernovae. The fits show that $\sim 30\%$ of all the supernovae in the cluster are type Ia and about 70% are core-collapse supernovae. In their data, they found a clear hint that the calcium abundance in these clusters is higher than expected.

In this paper, we extend the approach of Chapter 4 and 5 to a sample of 22 clusters observed with XMM-Newton. We aim to accurately measure the chemical abundances of all robustly detected elements and fit model yields of type Ia and core-collapse supernovae to the results. Naturally, we discuss the anomalous calcium abundance.

In our analysis we use $H_0 = 70 \text{ km s}^{-1} \text{ Mpc}^{-1}$, $\Omega_m = 0.3$, and $\Omega_\Lambda = 0.7$. The elemental abundances presented in this paper are given relative to the proto-solar abundances from Lodders (2003).

6.2 The sample and methodology

We use XMM-Newton data from a sample of 22 clusters of galaxies in the redshift interval $z=0-0.2$. The clusters are selected primarily from the HIFLUGCS sample (Reiprich & Böhringer 2002), because this sample is well studied and contains the brightest clusters in X-rays. We only select the observations with the best data quality.

6.2.1 Sample selection

Since its launch, XMM-Newton has been used to obtain more than 500 cluster and group observations. However, not all of these observations are suitable to use in a sensitive abundance study. We choose the following selection criteria to ensure that we select a clean and representative sample.

- The redshift of the cluster is between $z=0-0.2$. We select only local clusters and assume that all of these clusters have a comparable enrichment history.
- The cluster core fits inside the field-of-view of XMM-Newton. We need a region on the detector that is not heavily 'polluted' with cluster emission to estimate the local background. This excludes large extended nearby clusters like Virgo and Coma.
- The clusters have reported temperatures between ~ 2 and 10 keV. We exclude groups of galaxies and extremely hot clusters.
- The clusters are part of the HIFLUGCS sample (Reiprich & Böhringer 2002).

Table 6.1: Summary of the cluster properties of this sample. Data are taken from Table 3 and 4 in Reiprich & Böhringer (2002) apart from the classification. We list the following properties: (1) Heliocentric cluster redshift. (2) Column density of Galactic neutral hydrogen gas in units of 10^{20} cm^{-2} . (3) ROSAT flux in the energy range 0.1-2.4 keV in units of $10^{-11} \text{ erg s}^{-1} \text{ cm}^{-2}$. (4) Luminosity in the energy range 0.1-2.4 keV in units of $h_{50}^{-2} 10^{44} \text{ erg s}^{-1}$. (5) X-ray temperature in keV (note: in this table 90% errors are used). (6) Cluster radius (R_{500}) in $h_{50}^{-1} \text{ Mpc}$ as listed in Reiprich & Böhringer (2002). (7) Extraction radius used in this analysis in arcmin ($0.2R_{500}$). (8) Effective XMM-Newton exposure time in ks. (9) Classification (cooling core [cc] or non-cooling core [non-cc]).

Cluster	z (1)	N_{H} (2)	f_{X} (3)	L_{X} (4)	kT (5)	R_{500} (6)	R_{extr} (7)	Exposure (8)	Class (9)
2A 0335+096	0.0349	18.64	9.16	4.79	3.01 ± 0.07	1.15 ± 0.02	3.74	114	cc ^{a,b}
A 85	0.0556	3.58	7.43	9.79	6.9 ± 0.4	1.68 ± 0.06	3.42	12	cc ^{a,b}
A 133	0.0569	1.60	2.12	2.94	$3.8^{+2.0}_{-0.9}$	$1.24^{+0.30}_{-0.16}$	2.46	20	cc ^{a,b}
A 1651	0.0860	1.71	2.54	8.00	6.1 ± 0.4	1.73 ± 0.08	2.26	8	cc ^{a,b}
A 1689	0.1840	1.80	1.45	20.61	9.2 ± 0.3	2.20 ± 0.06	1.31	36	cc ^{a,b}
A 1775	0.0757	1.00	1.29	3.18	$3.69^{+0.20}_{-0.11}$	1.36 ± 0.06	4.04	23	non-cc ^{a,b}
A 1795	0.0616	1.20	6.27	10.12	7.8 ± 1.0	1.89 ± 0.13	3.46	26	cc ^{a,b}
A 2029	0.0767	3.07	6.94	17.31	9.1 ± 1.0	2.01 ± 0.12	2.95	11	cc ^{a,b}
A 2052	0.0348	2.90	4.71	2.45	3.03 ± 0.04	1.10 ± 0.02	3.59	29	cc ^{a,b}
A 2199	0.0302	0.84	10.64	4.17	4.10 ± 0.08	1.43 ± 0.04	5.38	23	cc ^{a,b}
A 2204	0.1523	5.94	2.75	26.94	7.2 ± 0.3	1.82 ± 0.05	1.32	19	cc ^{a,b}
A 2589	0.0416	4.39	2.59	1.92	$3.7^{+2.2}_{-1.1}$	$1.29^{+0.37}_{-0.22}$	3.52	22	non-cc ^c
A 3112	0.0750	2.53	3.10	7.46	$5.3^{+0.7}_{-1.0}$	1.53 ± 0.14	2.29	22	cc ^{a,b}
A 3530	0.0544	6.00	0.99	1.25	3.9 ± 0.3	1.47 ± 0.14	3.06	11	non-cc
A 3558	0.0480	3.63	6.72	6.62	5.5 ± 0.4	1.55 ± 0.07	3.70	43	cc ^{a,b}
A 3560	0.0495	3.92	1.52	1.60	3.2 ± 0.5	1.14 ± 0.12	2.60	25	non-cc ^d
A 3581	0.0214	4.26	3.34	0.66	1.83 ± 0.04	0.87 ± 0.03	4.63	36	cc ^{a,b}
A 3827	0.0980	2.84	1.96	7.96	7.1 ± 1.1	$2.25^{+0.60}_{-0.37}$	2.57	20	non-cc
A 3888	0.1510	1.20	1.10	10.51	8.8 ± 1.3	2.5 ± 0.3	1.82	23	non-cc ^{a,b}
A 4059	0.0460	1.10	3.17	2.87	4.4 ± 0.3	1.40 ± 0.06	3.44	14	cc ^{a,b}
MKW 3S	0.0450	3.15	3.30	2.87	3.7 ± 0.2	1.29 ± 0.05	3.24	35	cc ^{a,b}
S159-03	0.0580	1.85	2.49	3.60	$3.0^{+1.2}_{-0.7}$	$1.22^{+0.23}_{-0.16}$	2.45	113	cc ^{a,b}

^a Peres et al. (1998), ^b White et al. (1997), ^c Buote & Lewis (2004), ^d Bardelli et al. (2002).

- The observation must not suffer from a highly elevated level of soft-protons after flare removal.

We found 22 clusters that meet these requirements. They are listed in Table 6.1. Together, they have a total exposure time of 690 ks. Roughly 40% of the datasets suffer from a high level of so-called residual soft-protons. Soft protons have energies comparable to X-ray photons. They can induce events in the detector that cannot be separated from X-ray induced events. When the soft-proton flux is high, they create a substantial additional background. The soft-proton flare filtering is in general not enough to correct for this. An elevated quiescent level is in some cases only detectable as a hard tail in the spectrum. We check the spectrum in an 8–11' annulus centred on the core of the

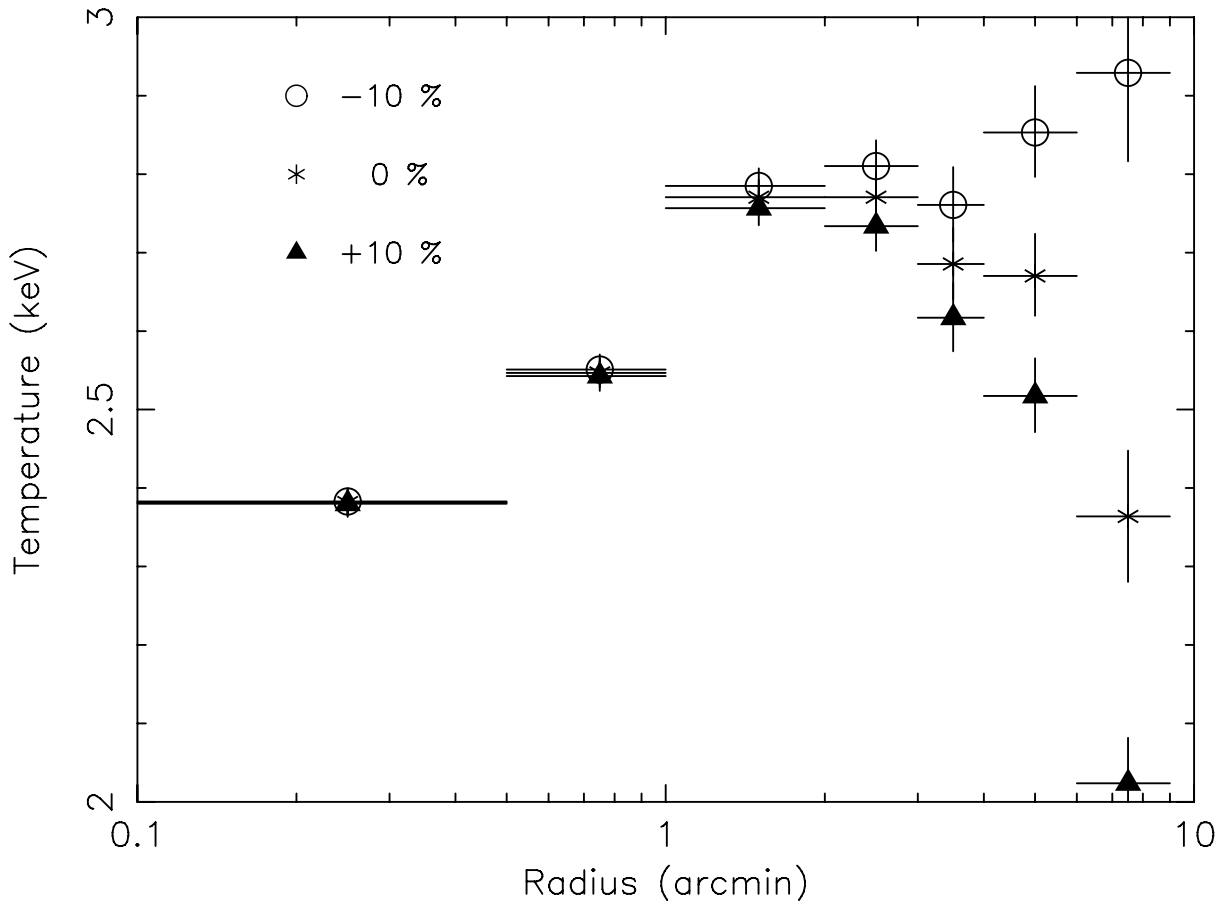


Figure 6.1: Systematic effects in the temperature profile of the cluster of galaxies Sérsic 159-03. We made the three different profiles by subtracting three background spectra with different normalisation. The blank field backgrounds by Read & Ponman (2003) were scaled up and down by a factor of 10% and were subtracted from the EPIC spectra. The impact to the temperature profile is clear: the temperature is well determined in the bright core, but the background subtraction plays an important role in the outskirts.

cluster. If this spectrum shows an obvious hard tail (more than two times the model count rate at 10 keV), then we exclude the cluster from the sample.

The properties of the clusters we selected are diverse. In Table 6.1, we list a few basic properties of the clusters in our sample. The redshifts lie in the range between $z=0.0214$ and $z=0.184$. Sixteen clusters contain a cooling core (cc).

6.2.2 Methodology

Data reduction is done following a procedure that is extensively described in Chapter 4. We first reprocess the data with SAS version 6.5.0. Then, we filter out soft-proton flares which exceed the 2 sigma confidence level. The background subtraction is performed by subtracting a spectrum extracted from a closed filter observation that we scale to the instrumental noise level of the particular cluster observation. Cosmic background components are included in the spectral fitting phase.

We extract the spectra from a circular region around the core of the cluster. In order to sample comparable regions in all clusters, we choose a physical radius of $0.2R_{500}$. The values of R_{500} are taken from Reiprich & Böhringer (2002). When we use the radii of $0.2R_{500}$, we sample the dense core region of the cluster. The radii in arcmin for every cluster are listed in Table 6.1.

The spectral components of the background are fitted to a spectrum extracted from an 8–11' annulus. This region near the edge of the detector generally contains little cluster emission, because we select clusters with a relatively small angular size (see Sect. 6.2.1). This allows us to estimate the local background without a large bias due to cluster pollution. Small (10%) uncertainties in the background do not affect our analysis. Fig. 6.1 shows that the temperature can be robustly measured in the core of Sérsic 159-03, even if the background estimate would be off by 10%. Therefore, we concentrate our analysis on the bright cluster cores.

We fit heuristically the background spectra with four components: two Collisional Ionisation Equilibrium (CIE) components with temperatures 0.07 and 0.25 keV (Chapter 4), a power-law component with $\Gamma=1.41$, and a normalisation fixed to a flux value of $2.24 \times 10^{-11} \text{ erg cm}^{-2} \text{ s}^{-1} \text{ deg}^{-2}$ in the 2–10 keV range (De Luca & Molendi 2004). Another CIE component is added to fit any remaining cluster emission. The results of the background fits are then used in the fits to the spectra of the core.

For the spectral fitting of the cluster spectra we use the *wdem* model (Kaastra et al. 2004, and Chapter 3) which proved to be most successful in fitting cluster cores (e.g. Kaastra et al. 2004, Chapter 4, and Chapter 5). This model is a differential emission measure (DEM) model where the differential emission measure is distributed as a power law ($dY/dT \propto T^{1/\alpha}$) with a high (T_{max}) and low temperature cut-off (T_{min}). We fix T_{min} to 0.1 times T_{max} like in Chapter 4. We quote the emission-weighted temperature kT_{mean} of the distribution (Chapter 4).

6.3 Results

In this section, we apply the *wdem* model to the EPIC spectra of the clusters in the sample. We fix the redshift to the value given in Reiprich & Böhringer (2002) and leave the Galactic neutral hydrogen column density (N_{H}) free in the fit.

6.3.1 Basic properties of the sample

Table 6.2 shows the fit results for N_{H} and the temperature structure. The normalisation (Y), the maximum temperature of the DEM distribution (kT_{max}), and the slope parameter α are directly obtained from the *wdem* fit. The emission-weighted temperature (kT_{mean}), derived from the fit parameters, is a good indicator of the temperature of the cluster core. In our sample these temperatures cover a range between roughly 1.7 keV (A3581) and 9.8 keV (A3888). The sample is slightly biased to low-temperature clusters.

A fit with the *wdem* model does not always lead to an acceptable χ^2 -value (see Table 6.2). This is largely due to systematic errors between the MOS and pn detectors. We

Table 6.2: Basic properties of the sample of clusters obtained from a fit of MOS and pn data. N_{H} is given in units of 10^{20} cm^{-2} , $Y = \int n_e n_{\text{H}} dV$ is in units of 10^{66} cm^{-3} , and kT_{max} and kT_{mean} are in keV. The α parameter is a measure for the slope of the emission-measure distribution.

Cluster	N_{H}	Y	kT_{max}	α	kT_{mean}	χ^2 / dof
2A 0335	25.71 ± 0.09	18.76 ± 0.09	3.486 ± 0.016	0.360 ± 0.007	2.757 ± 0.015	2927 / 1300
A 85	3.25 ± 0.09	30.1 ± 0.2	6.80 ± 0.18	0.50 ± 0.05	5.11 ± 0.17	976 / 739
A 133	1.72 ± 0.10	9.25 ± 0.10	4.29 ± 0.08	0.36 ± 0.03	3.40 ± 0.08	1339 / 775
A 1651	2.10 ± 0.16	24.0 ± 0.4	7.2 ± 0.9	0.3 ± 0.2	5.9 ± 1.0	857 / 756
A 1689	1.96 ± 0.09	88.4 ± 0.8	13.0 ± 1.1	0.52 ± 0.19	9.7 ± 1.0	1106 / 749
A 1775	0.48 ± 0.12	9.82 ± 0.12	3.58 ± 0.19	0.03 ± 0.05	3.5 ± 0.2	1124 / 758
A 1795	1.08 ± 0.04	40.92 ± 0.16	7.05 ± 0.13	0.55 ± 0.04	5.22 ± 0.12	1703 / 877
A 2029	3.23 ± 0.07	72.6 ± 0.5	9.7 ± 0.4	0.51 ± 0.08	7.3 ± 0.3	1279 / 759
A 2052	3.22 ± 0.06	5.24 ± 0.04	3.73 ± 0.04	0.411 ± 0.014	2.89 ± 0.03	1336 / 814
A 2199	1.16 ± 0.04	11.06 ± 0.05	4.93 ± 0.08	0.32 ± 0.03	3.97 ± 0.08	3328 / 1922
A 2204	7.30 ± 0.13	103.8 ± 0.9	10.1 ± 0.5	1.5 ± 0.4	6.5 ± 0.4	982 / 778
A 2589	3.54 ± 0.10	5.067 ± 0.049	3.5 ± 0.3	0.00 ± 0.07	3.5 ± 0.3	1087 / 775
A 3112	1.12 ± 0.07	24.57 ± 0.17	5.76 ± 0.11	0.44 ± 0.04	4.42 ± 0.11	1221 / 806
A 3530	6.1 ± 0.3	2.55 ± 0.06	3.6 ± 0.4	0.03 ± 0.13	3.6 ± 0.6	890 / 709
A 3558	3.5 ± 0.07	10.19 ± 0.06	8.1 ± 0.3	0.61 ± 0.11	5.9 ± 0.3	1190 / 768
A 3560	3.0 ± 0.2	1.83 ± 0.04	3.3 ± 0.3	0.00 ± 0.04	3.3 ± 0.3	996 / 729
A 3581	4.36 ± 0.11	1.85 ± 0.02	2.14 ± 0.02	0.267 ± 0.008	1.765 ± 0.018	1499 / 777
A 3827	2.36 ± 0.12	28.2 ± 0.3	8.0 ± 1.0	0.25 ± 0.19	6.7 ± 1.0	1159 / 791
A 3888	0.43 ± 0.12	39.0 ± 0.5	9.8 ± 1.7	0.0 ± 0.2	9.8 ± 2.6	1018 / 777
A 4059	1.44 ± 0.06	7.85 ± 0.06	4.33 ± 0.19	0.19 ± 0.06	3.7 ± 0.2	1820 / 1426
MKW 3s	2.99 ± 0.06	8.35 ± 0.05	4.35 ± 0.08	0.30 ± 0.03	3.53 ± 0.08	1219 / 822
S 159-03	1.00 ± 0.03	13.7 ± 0.06	3.08 ± 0.02	0.238 ± 0.010	2.59 ± 0.02	3072 / 1495

describe these systematic differences extensively in Sect. 6.3.2. A second reason for the high χ^2 can be the complicated temperature structure that is often observed in cluster cores. Because the *wdem* model is just an empirical DEM model, the real temperature distribution in the core of the cluster may be somewhat different. Finally, because some weak lines are not yet in the atomic database, small positive residuals can arise in line-rich regions like, for example, the Fe-L complex (Brickhouse et al. 2000).

6.3.2 Abundance determination

From each fit to a cluster and from each instrument (MOS and pn), we obtain the elemental abundances of oxygen, neon, magnesium, silicon, sulfur, argon, calcium, iron, and nickel. All these abundances, however, can be subject to various systematic effects. We know, for example, that the oxygen and neon abundances are problematic (Chapter 4 and 5). The spectrum of the Galactic warm-hot X-ray emitting gas (e.g. the local hot bubble) also contains O VIII lines that cannot be separately detected with the spectral resolution of EPIC. The brightest neon lines are blended with iron lines from the Fe-L complex near 1 keV, which makes an accurate determination of the abundance difficult. Therefore, we do not use these two elements in the rest of our discussion. In the following sections we discuss two other possible sources of systematic effects and

Table 6.3: Comparison of the fits using MEKAL and APEC. We fit two CIE models to the spectrum of Sérsic 159-03. Normalisation ($Y = \int n_e n_H dV$) is in units of 10^{66} cm^{-3} .

Parameter	MEKAL	APEC
Y_1	5.5 ± 0.3	5.13 ± 0.11
Y_2	1.4 ± 0.3	2.20 ± 0.07
kT_1	1.99 ± 0.06	1.96 ± 0.05
kT_2	4.4 ± 0.4	3.47 ± 0.08
Si	0.315 ± 0.013	0.331 ± 0.013
S	0.292 ± 0.019	0.310 ± 0.019
Ar	0.20 ± 0.05	0.20 ± 0.05
Ca	0.45 ± 0.08	0.51 ± 0.05
Fe	0.504 ± 0.007	0.514 ± 0.008
Ni	0.63 ± 0.06	0.71 ± 0.05
χ^2/dof	3882/3091	3874/3102

work towards a robust set of abundances.

MEKAL vs. APEC

A possible source of systematic effects is the plasma model that we use. There is an alternative for the MEKAL-based code called APEC (Smith et al. 2001). In Table 6.3 we show a comparison of two spectral fits to the spectrum of Sérsic 159-03 using a two-temperature model. One fit is performed using the MEKAL based CIE model, and the other with APEC.

In general, the differences between the MEKAL and APEC fits are minor. Both plasma models are equally well capable of fitting the spectrum, which is clear from the χ^2 values (3882/3091 [MEKAL] and 3874/3102 [APEC]). We note that there is no standard routine to fit a *wdem*-like emission-measure distribution with APEC. Therefore, we test two-temperature models here, which is often also a good approximation for the temperature structure in a cluster core. The only differences between the best-fit parameters of the two models are in the higher temperature component. MEKAL and APEC find a slightly different mix between the high and low temperature component. Despite the small differences in temperature structure between the two codes, the derived abundances are consistent within errors. This conclusion is in line with a similar comparison of the two codes by Sanders & Fabian (2006).

Cross-calibration issues

EPIC cross-calibration efforts (Kirsch 2006) have shown that there are systematic differences in effective-area between MOS and pn that are of the order of 5–10% in certain bands. Systematic errors of this magnitude can have a large impact on abundance measurements. We fit the MOS and pn spectra separately to investigate the impact on our

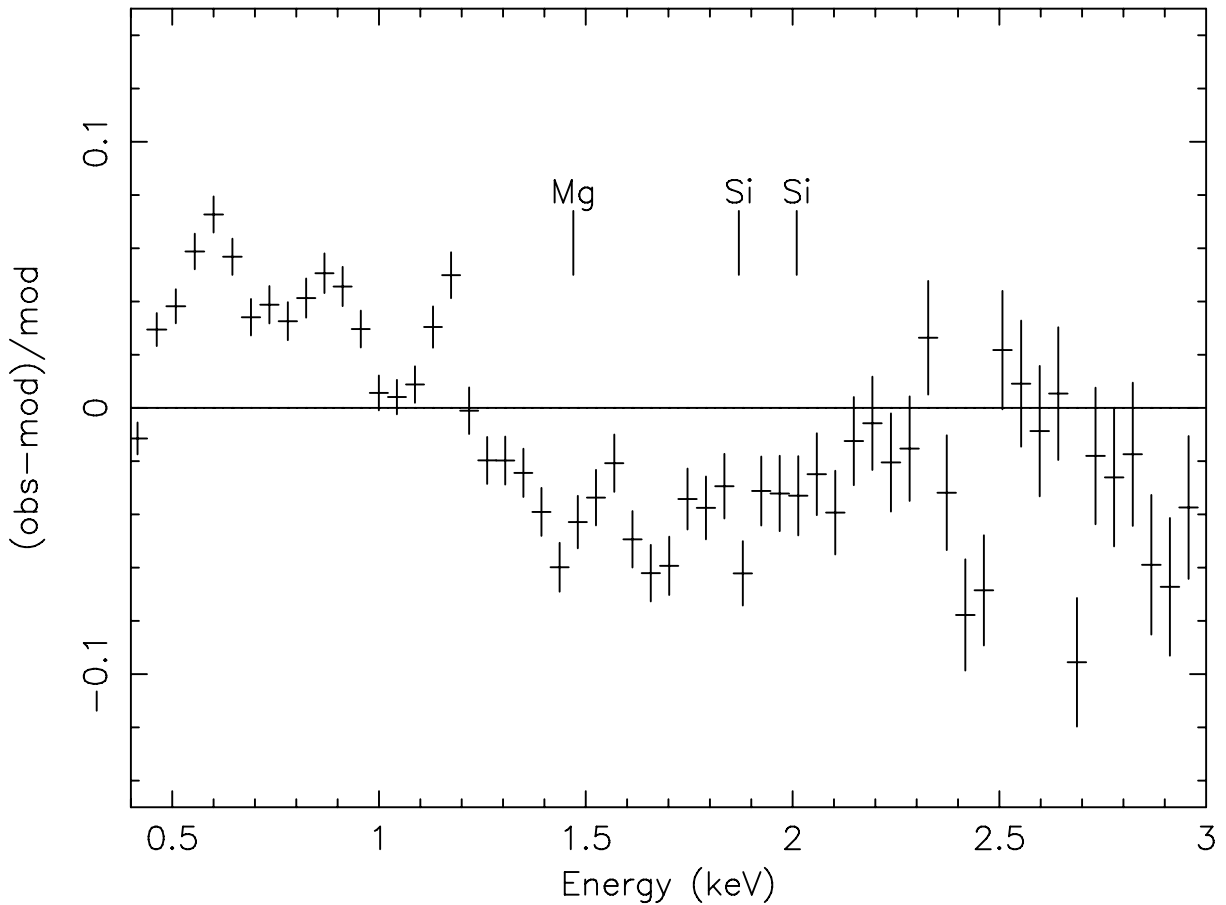


Figure 6.2: Residuals showing the calibration difference between EPIC MOS and pn. We show the residuals of the cluster Sérsic 159-03 as a typical example. The data points in this plot show the difference between the pn data and the best-fit model of MOS: $(\text{observed}[pn] - \text{model}[MOS]) / \text{model}[MOS]$. We indicate the (zero-redshift) line energies for the strongest affected lines in this band: Mg XII $L\alpha$ (1.47 keV), Si XII HE 4 (1.87 keV) and Si XIV $L\alpha$ (2.01 keV).

abundance estimates.

The main differences in calibration between MOS and pn can be found in the 0.3–2 keV band. In Fig. 6.2 we show an example of the differences we observe between the two instruments. The pn instrument shows a positive excess with respect to MOS in the 0.3 to 1.2 keV band. Note that the models fit well to the spectra from both instruments if the spectra are fitted separately. Between 1.2 to 2.2 keV, the pn gives a lower flux than MOS. These differences can have a significant effect on the abundances that are measured in this band, like for magnesium and silicon.

We show the effect in Fig. 6.3 using the spectrum of Sérsic 159-03. The plot shows the line contributions of the elements that contribute the most to the 1.0–4.5 keV band. Between roughly 1 and 2.5 keV, the lines in pn appear to contain less flux than their equivalents in MOS, which is in line with the differences we found between the two instruments. The effect is most notable at 1.4 keV, where the magnesium abundance is used by the fit to make up for the difference in flux. Because the flux of the iron feature

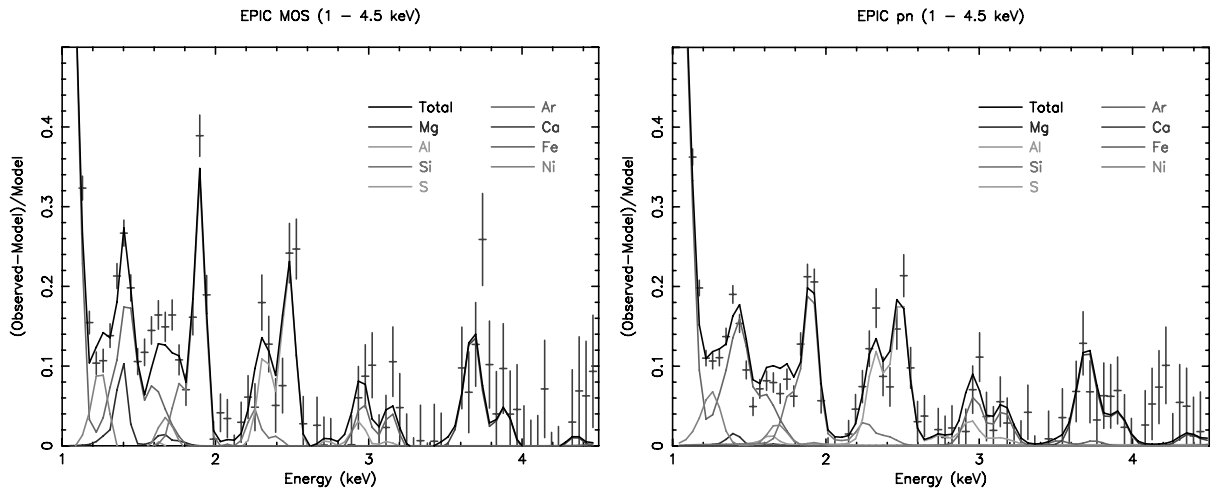


Figure 6.3: Line contributions with respect to the best-fit continuum in the EPIC MOS (left) and pn (right) spectra of Sérsic 159-03. The color version of this figure can be found on page 121.

at that energy is firmly coupled to the iron-K line complex, the magnesium line flux is the only one that can fill the gap in flux. The silicon line, however, is quite clean. But there is still a difference in flux at the position of this line. At higher energies between 2.5 and 4.5 keV, there is no significant effect anymore, which suggests that the sulfur and argon abundances are clean. Above 5 keV, there is a small difference in the slope that can influence the temperature and subsequently the calcium, iron, and nickel line fluxes.

Because abundances are directly derived from these line fluxes, we should be able to see the differences in the measured abundances. In Fig. 6.4, we show the abundance ratios for MOS and pn separately. We use the data of Sérsic 159-03 as an example, because it is representative for the whole sample. The values for the sulfur, argon, and calcium abundances appear to be consistent within errors in the two instruments. However, the silicon and magnesium abundances are clearly not. From spectral fits to the pn spectra we obtain systematically lower abundances for silicon and magnesium relative to MOS.

In order to check whether the systematic differences in the abundances are largely due to effective area effects, we fit the Sérsic 159-03 spectra again with corrected effective areas. We correct the MOS effective area with a simple broad-band spline model such that it nearly matches the pn effective area over the whole band. We do the same for pn. The filled symbols in Fig. 6.4 show the corrected abundances. The corrected MOS abundance is consistent with the original pn abundance and vice versa. Therefore, we can conclude that the effective area is the main contributor to the systematic differences between abundances determined with MOS and pn.

We choose to use a conservative approach and estimate the systematic error from Fig. 6.4. There are three elements that suffer from systematic effects: magnesium, silicon, and nickel. The systematic error in magnesium has such a large magnitude that we can not obtain a significant value for it. For silicon and nickel we calculate the

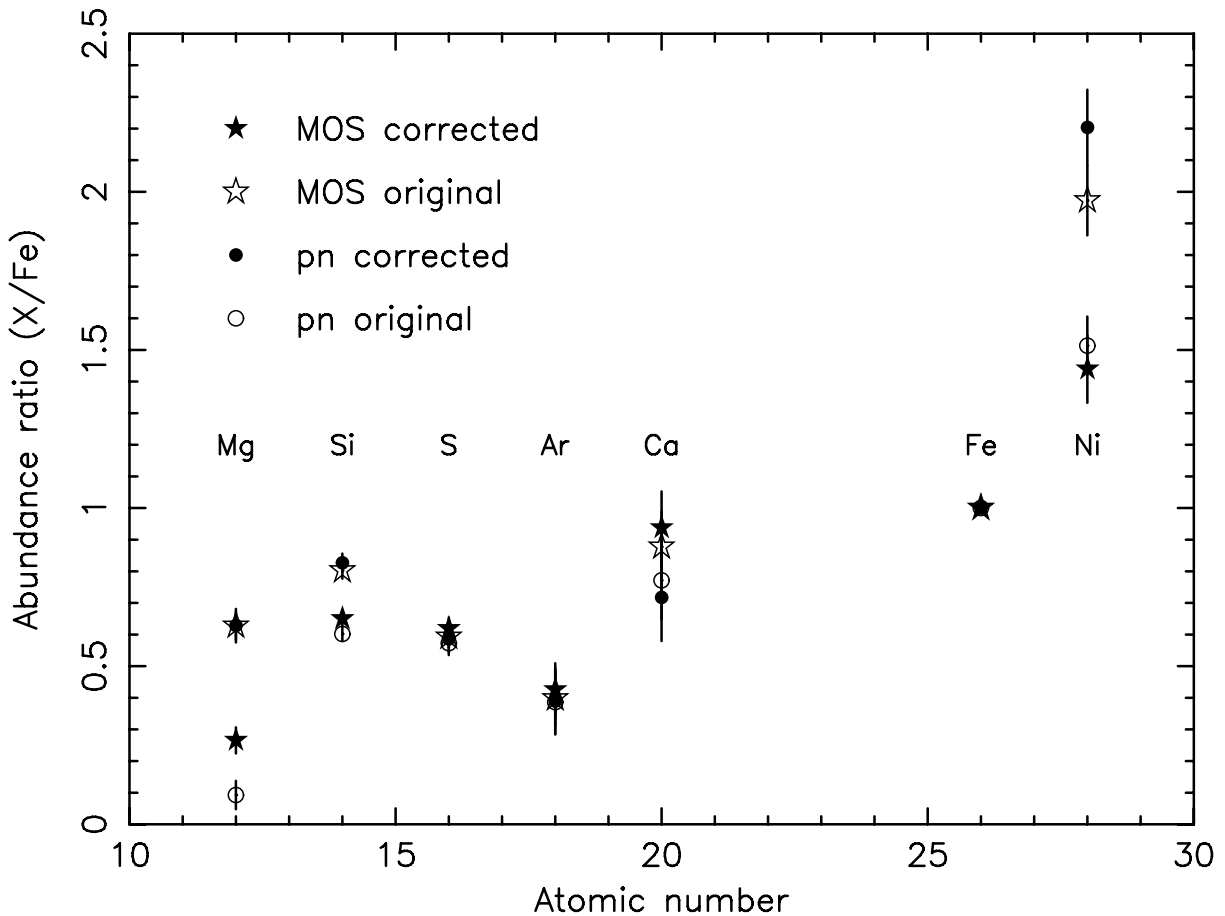


Figure 6.4: Comparison between the abundances measured with the MOS and the pn instruments in the cluster Sérsic 159-03. We plot the abundance ratios with respect to iron. The open symbols correspond to the original data. The filled symbols show the results when the effective area is corrected to match the effective area of the other instrument.

weighted average and add the systematic error linearly to the statistical error. The error should be large enough to cover both the MOS and pn results. Using this method, we derive the following systematic errors (relative error with respect to the average abundance value): Si ($\pm 11\%$) and Ni ($\pm 19\%$).

Intrinsic scatter

In Fig. 6.5 we show the abundance ratios of S/Fe and Ca/Fe for the individual clusters. At first sight, the abundance ratios appear to be consistent with being flat, but they have a small scatter. In principle we expect to find a scatter, because the clusters in our sample are morphologically different and may have had different chemical evolution history. The intrinsic differences between the clusters need to be taken into account if we can detect the scatter with high significance.

In order to quantify this intrinsic scatter in the abundances, we calculate the error-

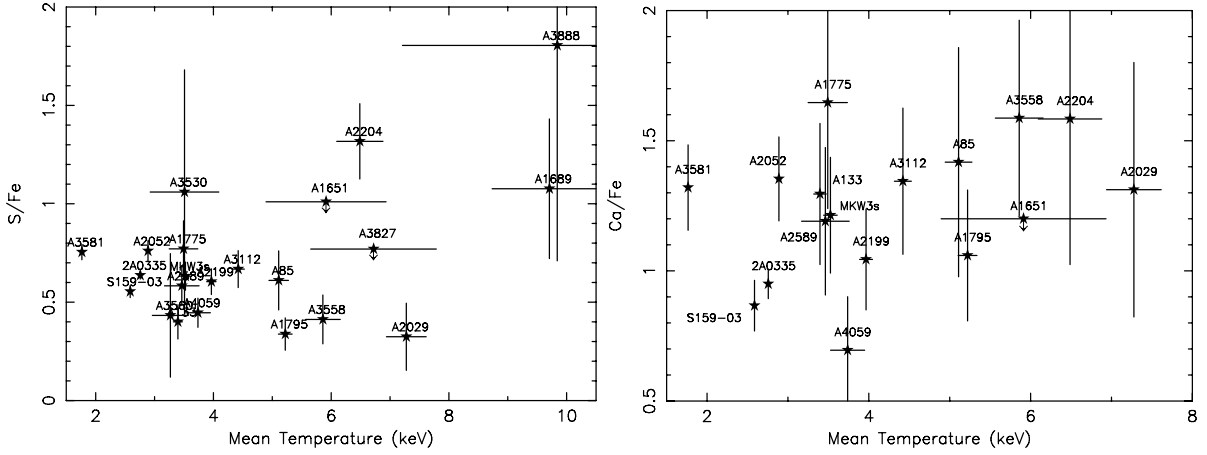


Figure 6.5: Plot of the S-Fe ratio (left) and the Ca-Fe ratio (right). In the Ca/Fe plot we do not plot clusters with 2σ upper limits larger than 2.0 for plotting purposes (A1689, A3530, A3560, A3827 and A3888).

weighted average of the abundances (see Table 6.4) with an error as described in Eq. 6.1:

$$\sigma_{\text{tot}}^2 = \sigma_{\text{m}}^2 + \sigma_{\text{int}}^2 \quad (6.1)$$

The value for the measured uncertainty (σ_{m}) is known from the spectral fits, but the combined uncertainty (σ_{tot}) and the intrinsic scatter in the population of clusters (σ_{int}) are yet to be determined. We do this by varying σ_{int} until the χ^2_{red} of the weighted average is equal to 1. The variance in the χ^2 distribution for n free parameters is $2n$ by definition. We use this variance to find the 1σ limits on our estimate for σ_{int} . The values we derive for σ_{int} are listed in Table 6.4.

We find that the intrinsic scatter (σ_{int}) in the silicon and sulfur abundance ratios differs significantly from zero. This intrinsic scatter in the data needs to be included in the error of the weighted mean. Therefore, we use a new weighted mean for silicon and sulfur with $\frac{1}{\sigma_{\text{tot}}^2}$ as weighing factor (see Table 6.4). Presumably due to lower statistics the σ_{int} of argon, calcium, and nickel does not show a significant deviation ($> 3\sigma$) from zero, hence we may employ the original weighted means.

Final abundance ratios

Now, we have derived values for the most relevant systematic uncertainties that affect our abundances. Using the total statistical uncertainty (σ_{tot}) and the uncertainty in the effective area, we calculate the final abundance values with their errors. This final set of abundance ratios is shown in Table 6.4. Silicon and nickel are both dominated by the systematic uncertainty in the effective area. The sulfur abundance is dominated by the intrinsic scatter.

Table 6.4: Weighted averages of the abundance ratios with respect to solar (Lodders 2003) in our sample. Systematic uncertainties due to the effective-area calibration and uncertainties due to intrinsic scatter are included in the errors. The σ_{int} that we list here is the intrinsic scatter per data point.

X/Fe	Weighted mean (incl. σ_{int})	σ_{int}
Si/Fe	0.66 ± 0.13	0.17 ± 0.05 †
S/Fe	0.60 ± 0.06	0.18 ± 0.06
Ar/Fe	0.40 ± 0.03	0.11 ± 0.05
Ca/Fe	1.03 ± 0.04	0.12 ± 0.08
Ni/Fe	1.41 ± 0.31	0.2 ± 0.2 †

† σ_{int} taken from PN data only.

6.4 Discussion

We determined the elemental abundances in the core of 22 clusters of galaxies with XMM-Newton. Most of the abundances are not consistent with proto-solar abundances (Lodders 2003). The intrinsic scatter in the cluster abundance ratios is between 0–30%, which is quite small. Our sample consists of both relaxed and non-relaxed clusters as well as cooling and non-cooling core clusters. The small intrinsic scatter shows that the effects of merging, cooling and temperature structure on the abundance ratios is limited to 30% in cluster cores. We do not resolve a clear trend of abundances with the presence of a cooling-core.

It is a well established idea that most of the metals from oxygen up to the iron group are generated by supernovae. We construct a few models using elemental yields of supernova type Ia (SNIa) and core-collapse supernova (SNcc). This analysis is similar to the one described in Chapter 4 and 5.

We try several SNIa yields which we obtain from two physically different sets of supernova models (Iwamoto et al. 1999), namely slow deflagration and delayed detonation models. The W7 and W70 models describe a slow deflagration of the stellar core, while the other models are calculated using a delayed-detonation (DD) scenario. WDD2 is the currently favoured SNIa explosion scenario.

For the core-collapse supernovae we use the yields from a recent model by Nomoto et al. (2006). Note that with SNcc we mean all types of core-collapse supernovae including types II, Ib, and Ic. We integrate the yields from the model over the stellar population using an Initial-Mass Function (IMF). We perform the calculation following Tsujimoto et al. (1995):

$$M_i = \frac{\int_{10 M_{\odot}}^{50 M_{\odot}} M_i(m) m^{-(1+x)} dm}{\int_{10 M_{\odot}}^{50 M_{\odot}} m^{-(1+x)} dm}, \quad (6.2)$$

where $M_i(m)$ is the i th element mass produced in a star of main-sequence mass m . We use a standard model with Salpeter IMF ($x=1.35$) and solar-metallicity ($Z=0.02$).

For every element i the total number of atoms N_i is a linear combination of the number of atoms produced by a single supernova type Ia ($Y_{i,\text{Ia}}$) and type cc ($Y_{i,\text{cc}}$).

$$N_i = aY_{i,\text{Ia}} + bY_{i,\text{cc}}, \quad (6.3)$$

where a and b are multiplicative factors of type SNIa and core-collapse supernovae respectively. The total number of particles for an element can be easily converted into a number abundance. This reduces to a system of two variables (a and b) and six data points (Si, S, Ar, Ca, Fe and Ni). The fits are independent of the values for the solar abundances, because they are divided out in the procedure. In essence, we fit the absolute abundances in the cluster. In the following sections, we present the ratio of the relative numbers of SNIa with respect to the total number of supernovae (SNIa + SNcc) that have enriched the ICM.

The supernova number ratios that we present, reflect the supernova ratio that is fitted to the abundances that we measure in the ICM. This does not necessarily correspond to the true ratio of supernova explosions in the entire cluster over its lifetime (Matteucci & Chiappini 2005). Because SNIa explode some time after the initial star burst, there may be a difference between the fractions of type Ia and core-collapse products locked up into stars. However, this delay time ($\lesssim 3$ Gyr, Maoz & Gal-Yam 2004) is probably short with respect to the formation time scale of the cluster. Therefore, it is likely that the bulk of the metals formed before $0.1t_{\text{Hubble}}$. Because this enrichment timescale is an order of magnitude smaller than the Hubble time, the instantaneous recycling approximation (Tinsley 1980) is presumably a reasonable approximation in the case of clusters. Using this approximation implies that we ignore the stellar lifetimes and thus the delay with which some chemical elements are released from stars into the ICM (Matteucci & Chiappini 2005).

We can make a very rough estimate of the systematic uncertainty that we introduce in our supernova ratio when we adopt the instantaneous recycling approximation. Galactic evolution models provide an indication about how the O/Fe ratio behaves in and around galaxies (for example, Calura & Matteucci 2006). However, galactic models are based on specific assumptions and approximations. Therefore, they also contain systematic uncertainties that are not well known. The plots in Calura & Matteucci (2006), for example, suggest that the fraction of oxygen that is locked up in stars is about a factor of two higher than for iron. If this model is a reasonable representation of galactic evolution in clusters of galaxies, then we overestimate our SNIa/(SNIa+SNcc) ratio in clusters with respect to the true supernova ratio with about 40% at maximum.

6.4.1 Solar abundances

The abundance ratios of silicon, sulfur, and argon that we derive from the sample are lower than proto-solar abundance ratios determined by (Lodders 2003). If we fit a constant to the cluster abundance ratios, we obtain a χ^2 of 418 for 5 degrees of freedom. This means that the chemical enrichment in cluster cores differs significantly from that in the solar neighbourhood.

In order to compare the supernova ratios in clusters with the solar ratio, we fit the supernova models to a constructed dataset with solar abundance ratios that have a

Table 6.5: Number ratios of supernovae type Ia over the total number of supernovae derived using SN Ia models by Iwamoto et al. (1999) and by (Badenes et al. 2006). The results are from a fit which contained the elements from silicon to nickel. We also list the results of the comparison to solar abundances.

Model	SNIa/SNIa+SNcc	χ^2/dof
Constant		418/5
Solar	0.15 ± 0.08	64/4
W7	0.22 ± 0.06	152/4
W70	0.26 ± 0.07	104/4
WDD2	0.37 ± 0.09	84/4
WDD3	0.22 ± 0.06	105/4
CDD2	0.32 ± 0.08	86/4
Tycho	0.72 ± 0.17	26/4

nominal error of 5% on every data point. From this fit (with a χ^2/dof of 64/4), we find a supernova type Ia (WDD2) contribution in the solar abundance of 0.15 (± 0.08), which is actually similar to the value for our galaxy found by Tsujimoto et al. (1995). This suggests that the abundances in the Sun are probably dominated by core-collapse supernovae that usually produce nearly flat abundance ratios. However, by adopting the instantaneous recycling approximation we might underestimate the type Ia fraction for the solar neighbourhood with the same factor that we derived from the galactic evolution models by Calura & Matteucci (2006).

6.4.2 Supernova type Ia models by Iwamoto et al.

We now try to fit the current supernova models to the data of the sample. In Table 6.5 we show the fit results using the supernova type Ia models W7, W70, WDD2, WDD3, and CDD2. None of the models provides an acceptable fit. The model with the lowest χ^2 is the delayed-detonation model WDD2 ($\chi^2/\text{dof} = 84/4$).

The reason why the models fail can be found in Fig. 6.6. The calcium abundance is highly underestimated by the models. Moreover, the high calcium abundance forces the fit to increase the SNcc contribution. The current models are clearly not able to produce the observed Ar/Ca and Ca/Fe abundances. This result re-affirms the earlier measurements in 2A 0335+096 (Chapter 5) and S ersic 159-03 (Chapter 4).

6.4.3 Supernova type Ia models based on Tycho

Recently, Badenes et al. (2006) compared type Ia models by Chieffi & Straniero (1989) and Bravo et al. (1996) to XMM-Newton EPIC observations of the Tycho supernova remnant. The Tycho supernova is thought to have been a type Ia supernova. Badenes et al. (2006) empirically modified the parameters of their delayed-detonation model to fit the Tycho observations. The parameter that mainly determines the outcome of their

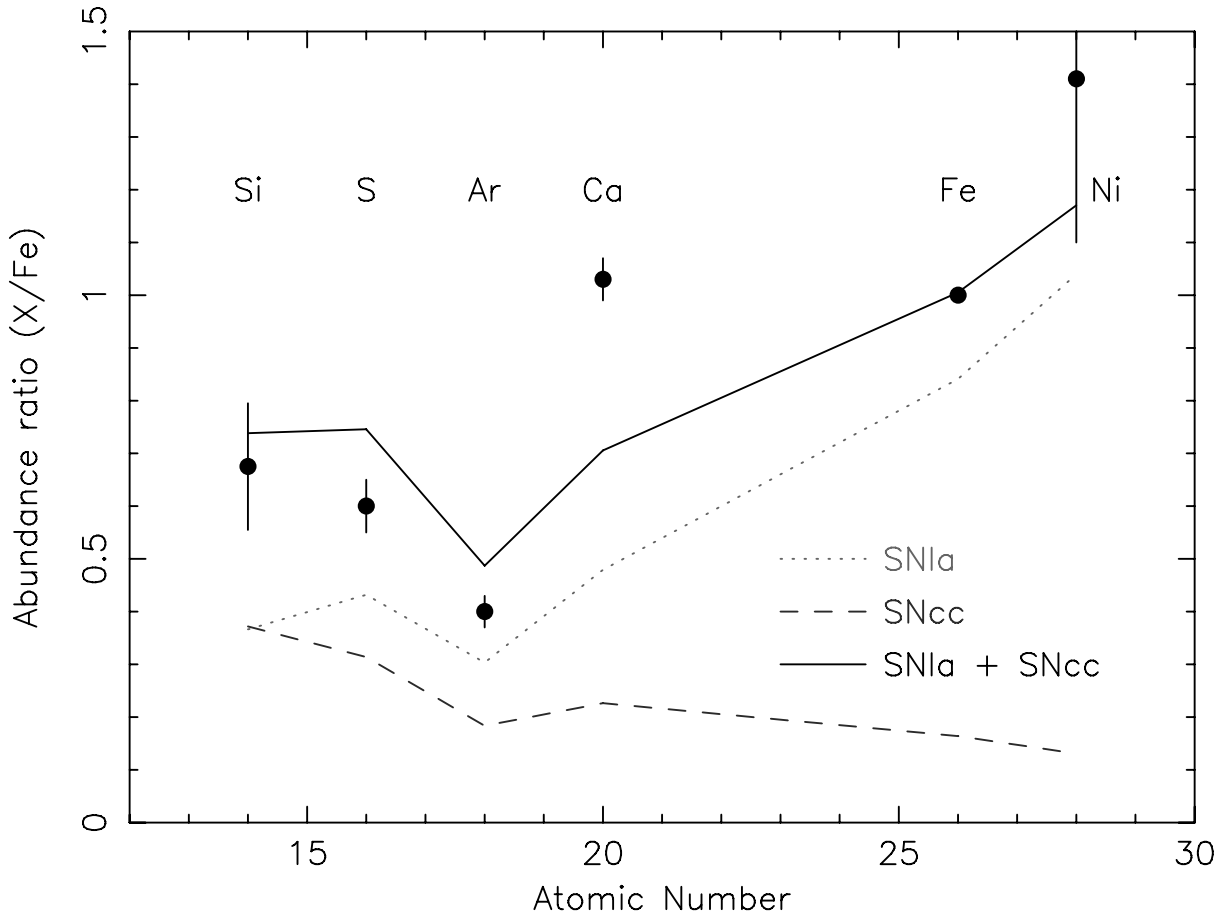


Figure 6.6: Abundance ratios versus atomic numbers for the sample. We fit the supernova yield models for SN Ia (WDD2) and SNcc ($Z=0.02$ and Salpeter IMF). The black line shows the total fit, while the dotted and dashed lines represent the SN Ia and SNcc models respectively.

model is the density where the subsonic wave, which runs through the white dwarf during the explosion, turns into a supersonic shock. This transition from deflagration to detonation is put in by hand in every DD model. By modifying this parameter and the ratio between the specific internal energies of ions and electrons (β), they found a best-fit delayed-detonation model that fitted the Tycho observations.

We take the yields from this best-fit model of Tycho and use them as a supernova type Ia model in our fit to the cluster abundances. Note that in Tycho not all the ejected material is visible in X-rays, because the reverse shock has not ionised all the material yet. Therefore, the Tycho results might not reflect the total SNIa yields yet. Despite this caveat, the Tycho model provides a major improvement in χ^2 compared to the Iwamoto et al. (1999) models (see Table 6.5). In Fig. 6.7, we show that the Tycho model is more successful in fitting the calcium abundance in clusters. Moreover, the supernova ratios change dramatically, the SNIa/(SNIa+SNcc) ratio for this model is 0.72 ± 0.17 .

This shows that the Ar/Ca and Ca/Fe abundance ratios mainly determine how well type Ia models fit. By varying the parameters of the delayed-detonation models, it is

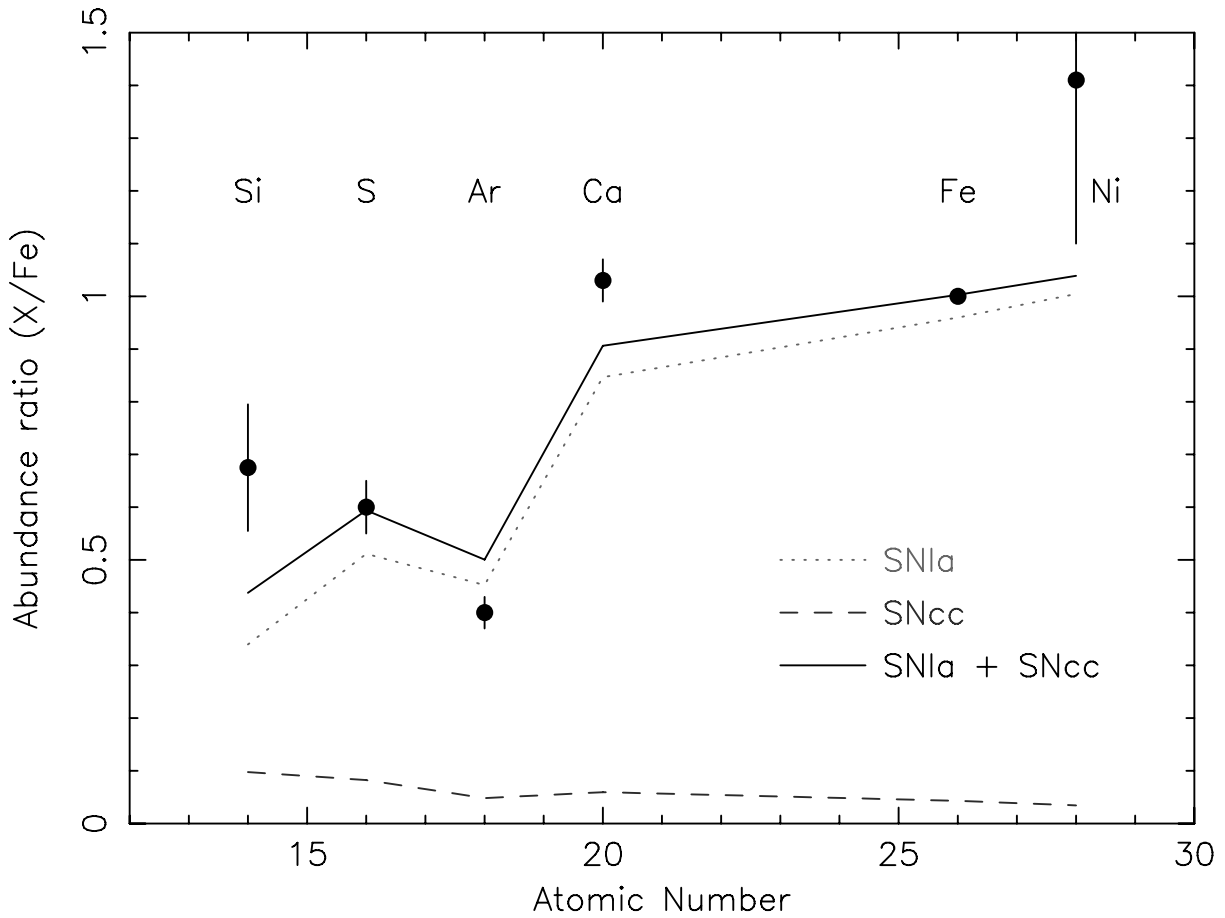


Figure 6.7: Same as Fig 6.6, but now we fit the SNIa yields found in the Tycho supernova remnant by Badenes et al. (2006). The nickel yield of the Tycho SNIa model was kindly provided by Carles Badenes (priv. comm.).

in principle possible to obtain a calcium abundance that fits the observations, which apparently very effectively constrain type Ia models.

6.4.4 Core-collapse models

In order to test whether our models are also reproducing the core-collapse contribution adequately, we need abundances of some typical core-collapse products. Therefore, we estimate the oxygen and neon abundance of the sample using the Reflection Grating Spectrometer (RGS) aboard XMM-Newton. For oxygen, we take the average of the clusters Sérsic 159-03 and 2A 0335+096, because these clusters have the highest exposure in our sample and very good RGS data (Chapter 4 and 5). The O/Fe measurements of the two clusters are not statistically consistent possibly due to systematic differences in the line widths (see Chapter 4 for an explanation of this effect). Therefore, we take the average value and assign an error which covers both results within 1σ . The neon abundance is consistent in both Sérsic 159-03 and 2A 0335+096, hence we take the weighted average of the two neon abundances and use them in the rest of the

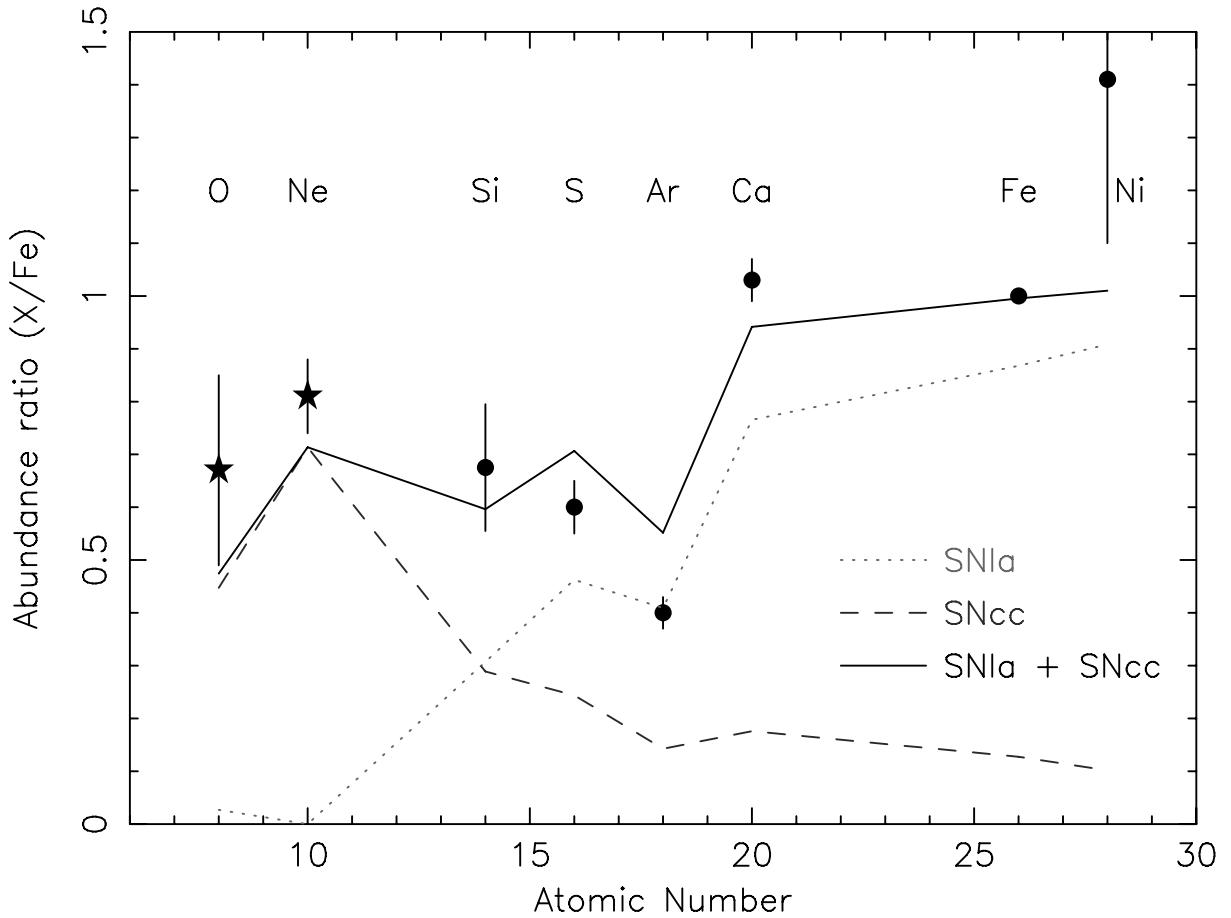


Figure 6.8: Fit using the SNIa yields by Badenes et al. (2006), but now with additional oxygen and neon data points (stars) obtained from the RGS spectra of Sérsic 159-03 and 2A 0335+096. Here, the core-collapse model with $Z=0.02$ and Salpeter IMF is used.

fits.

The fit including O/Fe and Ne/Fe from RGS is shown in Fig. 6.8. We use here a standard core-collapse model ($Z=0.02$ and Salpeter IMF) and the type Ia model based on Tycho. The trend in O/Ne that is predicted by the core-collapse model, is consistent with the O/Ne ratio that we observe. However, the core-collapse contribution needs to increase with respect to the model used in Fig. 6.7 to explain the absolute values for O/Fe and Ne/Fe (see Table 6.6). The typical values that we derive are of the order of 45–60%. Considering the uncertainties, this number is compatible with the current supernova type Ia ratio within $z=0.03$ ($\sim 42\%$) determined by the Lick Observatory Supernova Search (LOSS) (van den Bergh et al. 2005).

In principle, the increase of the core-collapse contribution with respect to the results before we included oxygen and neon results in a smaller predicted Ar/Ca ratio. However, the data suggest that the Ar/Ca ratio is larger. The plot shows that this particular core-collapse model still allows a relatively high Ar/Ca ratio, because the absolute contributions of silicon, sulfur, argon, and calcium are relatively small in this model.

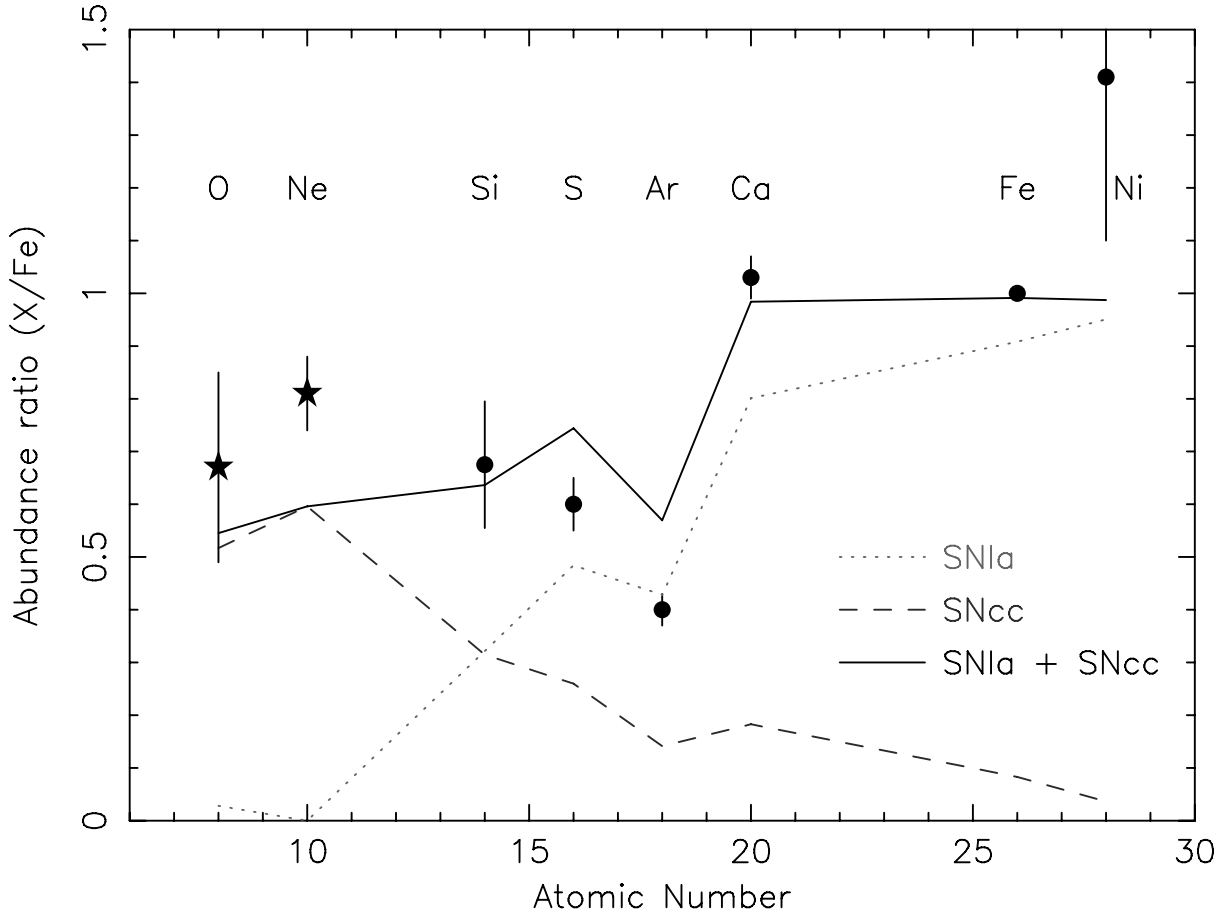


Figure 6.9: Fit using the SNIa yields by Badenes et al. (2006) and SNcc yields for $Z=0.001$ metallicity progenitors (Nomoto et al. 2006).

Table 6.6: Results for a supernova fit to the abundance ratios using SNcc models by Nomoto et al. (2006) that are integrated over a Salpeter ($x=1.35$) or “top-heavy” IMF ($x=0$). $Z=0.02$ is the solar abundance. For the type Ia model we used Badenes et al. (2006).

Z	Salpeter IMF		“Top-heavy” IMF	
	$\frac{SNIa}{SNIa+SNcc}$	χ^2/dof	$\frac{SNIa}{SNIa+SNcc}$	χ^2/dof
0	0.55 ± 0.05	79/6	0.68 ± 0.04	102/6
0.001	0.51 ± 0.05	54/6	0.62 ± 0.04	69/6
0.004	0.49 ± 0.05	55/6	0.62 ± 0.04	58/6
0.02	0.44 ± 0.05	40/6	0.57 ± 0.04	34/6

Effect of progenitor metallicity on core-collapse yields

Up to now, we have used a core-collapse supernova model that assumes that the progenitor had a solar metallicity. Nomoto et al. (2006) also provide models where the

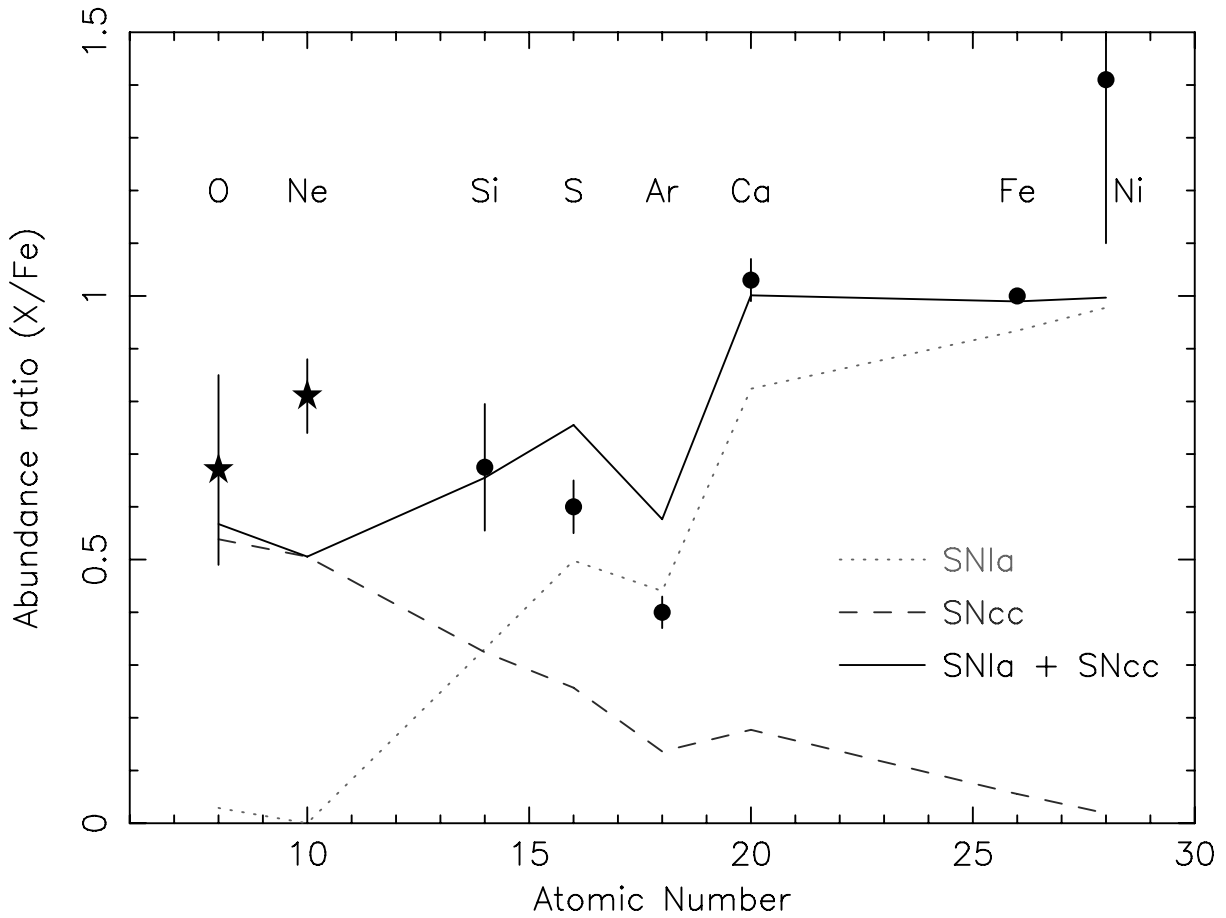


Figure 6.10: Fit using the SNIa yields by Badenes et al. (2006) and SNcc yields for $Z=0.001$ metallicity progenitors (Nomoto et al. 2006) that are integrated over a “top-heavy” IMF.

metallicity (Z) of the supernova progenitor is 0, 0.001, and 0.004. In Table 6.6 we show the results for the fits using progenitor metallicities ranging from 0 to 0.02 (solar). The $Z=0.001$, $Z=0.004$, and $Z=0.02$ models do show a relatively small variation in χ^2 . The data are still compatible with a wide range of metallicities (0.001-0.02).

In Fig. 6.9 we show the fit result for the $Z=0.001$ model. The main difference between this $Z=0.001$ model and the $Z=0.02$ model is the amount of oxygen and neon produced. The neon peak is clearly less pronounced compared to the model in Fig. 6.8, while the plateau from silicon to nickel in the core-collapse contribution is nearly unaffected. That also confirms that the influence of metallicity differences in SNcc models on the Ar/Ca ratio is limited.

Effect of IMF on core-collapse yields

We also fit the data for core-collapse models integrated over a “top-heavy” IMF ($x=0$), because presumably more high-mass stars form in low-metallicity environments. Table 6.6 shows that the fits are similar to the fits using Salpeter IMF. In Fig. 6.10, we show the fit for this metallicity. The main differences with Salpeter IMF models are

in the O/Ne ratio. The abundance peak in the model is shifted from neon to oxygen with respect to the Salpeter models, which is less consistent with the neon abundance from RGS. Again, the plateau from silicon to nickel in the core-collapse model is barely affected.

6.4.5 The fraction of low mass stars that become Type Ia SNe

This study indicates a much higher lifetime averaged ratio of type Ia to core-collapse supernovae than in the Galaxy. The reason for this large contribution of SNIa is likely that in late type galaxies, like our own galaxy, ongoing star formation ensures an ongoing core collapse contribution. For clusters of galaxies, the star formation continued at a very reduced level shortly after the formation of the cluster. This has some interesting consequences. SNIa are likely the result of a thermonuclear runaway explosion of a C-O white dwarf in binary systems, caused by accretion from the secondary star. Since this involves the formation of a white dwarf from a star with mass $M \lesssim 10 M_{\odot}$, there is a considerable delay between the period of star formation and the resulting SNIa explosion. In late type galaxies the subsequent waves of star formation make it difficult to disentangle the SNIa contribution from recent and old star formation periods. However, cluster of galaxies are an interesting laboratory to study the fraction of all stars that will eventually become type Ia supernovae, since the star formation has shut down, and for the last few Gyr since formation, the buffer of potential type Ia progenitors has nearly emptied.

As a result, the fraction of SNIa in clusters must be a good approximation to the fraction of low mass stars that can become type Ia explosions. For a power law initial mass function we can write (Yoshii et al. 1996):

$$\frac{SNIa}{SNIa + SN_{cc}} = \frac{f_{SNIa} \int_{M_{low}}^{M_{cc}} m^{-(1+x)} dm}{f_{SNIa} \int_{M_{low}}^{M_{cc}} m^{-(1+x)} dm + \int_{M_{cc}}^{M_{up}} m^{-(1+x)} dm}, \quad (6.4)$$

with M_{low} the lower limit to the mass of stars that can have contributed to the type Ia production, and M_{up} the mass of the most massive stars. The parameter of interest here is f_{SNIa} , which is defined as the fraction of stars with $M_{low} < M < M_{cc}$ that will eventually explode as SNIa.

It is clear that the absolute lower limit to M_{low} is the mass of stars that can evolve to a C-O white dwarf within a Hubble time, about $0.9 M_{\odot}$. However, there is considerable evidence that the mean delay time between star formation and type Ia explosion is of the order of 1 Gyr. Strolger et al. (2004) find a value of 2-4 Gyr. However, based on a lack of observed SNIa in clusters of galaxies, Maoz & Gal-Yam (2004) find a 2σ upper-limit of about 3 Gyr for the delay time. Very recently Mannucci et al. (2006) argued for two channels for SNIa explosions, one with a very short delay time of 10^8 yr, and the other with 2-4 Gyr. In other words, the majority of the type Ia explosion must come from stars that have lifetimes shorter than 2-4 Gyr, suggesting $M_{low} = 1.5 M_{\odot}$ (c.f. Greggio & Renzini 1983; Yoshii et al. 1996).

Table 6.7 shows the values for f_{SNIa} using different assumptions for M_{low} , M_{cc} and the initial mass function. We use the best fit SNIa rate of 0.44 ± 0.10 (Table 6.6), but with

Table 6.7: The fraction, f_{SNIa} , of low mass stars in the range M_{low} to M_{cc} that will eventually result in SNIa. It is based on our observed SNIa fraction of $\frac{SNIa}{SNIa+SNIc} = 0.44 \pm 0.10$.

	$M_{low} = 0.9 M_{\odot}$	$M_{low} = 1.5 M_{\odot}$
Salpeter IMF ($x = 1.35$)		
$M_{cc} = 8 M_{\odot}$	$4.1 \pm 1.7\%$	$9 \pm 4\%$
$M_{cc} = 10 M_{\odot}$	$2.9 \pm 0.1\%$	$6 \pm 3\%$
Kroupa (2002)		
$M_{cc} = 8 M_{\odot}$	$2.0 \pm 0.8\%$	$4.0 \pm 1.7\%$
$M_{cc} = 10 M_{\odot}$	$1.3 \pm 0.6\%$	$2.7 \pm 1.1\%$

slightly larger errors in order to allow for systematic uncertainties. The values that we find for $M_{low} = 1.5 M_{\odot}$ are high compared to previous results based on other observational data, which suggests $f_{SNIa} = 1 - 5\%$ (Greggio & Renzini 1983; Yoshii et al. 1996; Matteucci & Recchi 2001). Note that these authors sometimes use slightly different definitions for M_{low} and M_{cc} . Our lowest value is 1.3%, which assumes $M_{cc} = 10 M_{\odot}$ and $M_{low} = 0.9 M_{\odot}$ together with the broken power law IMF of Kroupa (2002). Notice also that f_{SNIa} refers to all stars with masses between M_{low} and M_{cc} . We can estimate the probability that a binary produces a type Ia supernova from the value of f_{SNIa} . We assume that roughly 50% of all stars are formed in binaries, which introduces a factor of two. In addition, we need another factor of two because we want to count binaries instead of stars. Together, the probability that a binary produces a SNIa supernova is thus about four times higher than f_{SNIa} .

Our derived supernova ratios therefore suggest that binary systems in the appropriate mass range are very efficient in eventually forming SNIa explosions ($\sim 5-16\%$, depending on the assumptions for the IMF and M_{cc}). We are aware that we ignore several complications in this simple calculation, such as an increased binarity fraction for massive stars that flattens the IMF for binary stars and binary mass ratios that may peak near 1. Also the instantaneous recycling approximation may introduce an additional uncertainty. However, a detailed calculation is beyond the scope of this paper.

6.5 Conclusions

We measure the abundances for silicon, sulfur, argon, calcium, iron, and nickel in a sample of clusters with XMM-Newton (EPIC), and we add a high-resolution oxygen and neon measurement from RGS (Chapter 4 and 5). From these data we conclude that:

- The Ar/Ca ratio in clusters is a good touchstone for determining the quality of type Ia models. The core-collapse contribution, which is about 50% and not

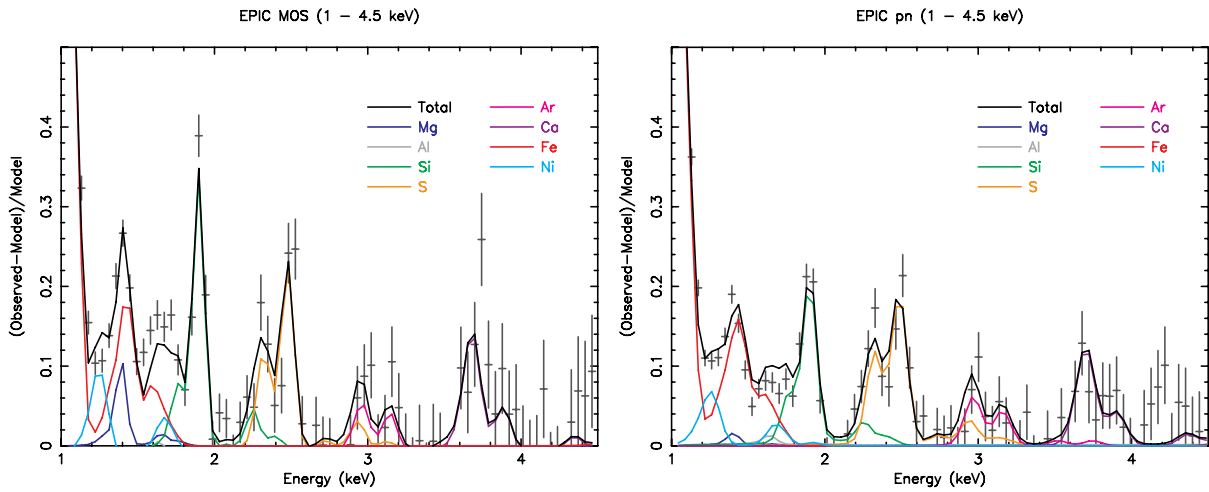


Figure 6.11: Line contributions with respect to the best-fit continuum in the EPIC MOS (left) and pn (right) spectra of Sérsic 159-03.

strongly dependent on the IMF or progenitor metallicity, does not have a significant impact on the Ar/Ca ratio.

- Current supernova type Ia models (Iwamoto et al. 1999) do not agree with our data, because they fail to produce the Ar/Ca and Ca/Fe abundance ratios.
- A major improvement of the supernova fits is obtained, when we use an empirically-modified supernova type Ia model, which is calibrated on the Tycho supernova remnant (Badenes et al. 2006). This model largely solves the problems with the Ar/Ca and Ca/Fe abundance ratios by varying the density where the sound wave in the supernova turns into a shock and varying the ratio of the specific internal energies of ions and electrons at the shock.
- The number ratio between supernova type Ia and core-collapse supernovae suggests that binary systems in the appropriate mass range are very efficient ($\sim 5\text{--}16\%$) in eventually forming supernova type Ia explosions.
- We find that the progenitors of the core-collapse supernovae which contributed to the ICM abundances have probably been enriched. Progenitor abundances range from $Z \sim 0.001$ to $Z \sim 0.02$.
- The intrinsic spread in abundance ratios between clusters is smaller than 30%. That means that the chemical histories of the clusters do not depend a lot on cluster temperature, temperature structure or merging activity.

Acknowledgements

We would like to thank Norbert Langer, Ton Raassen, and Rob Izzard for useful discussions. We are also grateful to Carles Badenes who kindly provided details about his

Table 6.8: Abundance ratios in the sample of clusters with respect to the solar abundances determined by Lodders (2003). The listed ratio is calculated using $\frac{X/X_{\odot}}{Fe/Fe_{\odot}}$. We included a systematic error in the data points of Si/Fe and Ni/Fe. See Sect. 6.3.2 for a discussion about systematic errors.

Cluster	Si/Fe	S/Fe	Ar/Fe	Ca/Fe	Ni/Fe	Fe
2A 0335	0.78 ± 0.09	0.636 ± 0.019	0.43 ± 0.04	0.95 ± 0.06	1.4 ± 0.4	0.741 ± 0.006
A 85	0.72 ± 0.18	0.61 ± 0.15	0.4 ± 0.4	1.4 ± 0.4	1.0 ± 0.7	0.574 ± 0.018
A 133	0.64 ± 0.14	0.40 ± 0.09	0.6 ± 0.2	1.3 ± 0.3	1.6 ± 0.6	0.81 ± 0.02
A 1651	0.0 ± 0.4	0.3 ± 0.4	0.0 ± 0.4	0.0 ± 0.6	1.4 ± 1.3	0.45 ± 0.03
A 1689	0.3 ± 0.4	1.1 ± 0.4	0.8 ± 1.0	0.6 ± 0.9	0.6 ± 1.0	0.40 ± 0.02
A 1775	0.57 ± 0.18	0.77 ± 0.14	0.5 ± 0.3	1.7 ± 0.4	1.6 ± 0.7	0.63 ± 0.02
A 1795	0.75 ± 0.14	0.34 ± 0.08	0.2 ± 0.2	1.1 ± 0.3	1.3 ± 0.5	0.517 ± 0.009
A 2029	0.4 ± 0.2	0.32 ± 0.17	0.00 ± 0.10	1.3 ± 0.5	1.6 ± 0.7	0.587 ± 0.017
A 2052	0.74 ± 0.12	0.76 ± 0.05	0.55 ± 0.11	1.35 ± 0.16	1.4 ± 0.4	0.682 ± 0.011
A 2199	0.73 ± 0.13	0.60 ± 0.07	0.60 ± 0.16	1.04 ± 0.19	1.5 ± 0.5	0.532 ± 0.008
A 2204	0.75 ± 0.18	1.32 ± 0.19	0.0 ± 0.2	1.6 ± 0.6	1.6 ± 0.7	0.59 ± 0.02
A 2589	0.55 ± 0.14	0.58 ± 0.10	0.4 ± 0.2	1.2 ± 0.3	1.8 ± 0.6	0.666 ± 0.019
A 3112	0.70 ± 0.14	0.67 ± 0.09	0.5 ± 0.2	1.3 ± 0.3	1.9 ± 0.6	0.695 ± 0.016
A 3530	1.1 ± 0.6	1.1 ± 0.6	0.3 ± 0.9	1.2 ± 1.5	0.0 ± 2.0	0.28 ± 0.04
A 3558	0.74 ± 0.16	0.41 ± 0.12	0.3 ± 0.3	1.6 ± 0.4	1.5 ± 0.6	0.478 ± 0.017
A 3560	0.9 ± 0.3	0.4 ± 0.3	0.2 ± 0.5	1.0 ± 1.0	1.1 ± 1.3	0.39 ± 0.03
A 3581	0.80 ± 0.10	0.75 ± 0.04	0.66 ± 0.09	1.32 ± 0.16	1.3 ± 0.4	0.654 ± 0.013
A 3827	0.2 ± 0.3	0.0 ± 0.4	0.0 ± 0.7	2.9 ± 1.2	1.1 ± 1.2	0.38 ± 0.03
A 3888	0.1 ± 0.5	1.8 ± 1.1	0.0 ± 1.3	1.0 ± 1.9	0.0 ± 1.8	0.30 ± 0.03
A 4059	0.59 ± 0.13	0.45 ± 0.07	0.16 ± 0.17	0.7 ± 0.2	1.0 ± 0.5	0.687 ± 0.014
MKW 3s	0.84 ± 0.13	0.63 ± 0.07	0.54 ± 0.18	1.2 ± 0.2	1.4 ± 0.5	0.551 ± 0.011
S 159-03	0.67 ± 0.10	0.55 ± 0.03	0.41 ± 0.07	0.87 ± 0.10	1.6 ± 0.4	0.533 ± 0.005

work on the Tycho supernova remnant and to Steve Sembay who provided information about the current calibration status of the EPIC instruments. The work is based on observations obtained with XMM-Newton, an ESA science mission with instruments and contributions directly funded by ESA member states and the USA (NASA). The Netherlands Institute for Space Research (SRON) is supported financially by NWO, the Netherlands Organisation for Scientific Research.

Abundance data

In Table 6.8 we list the abundances obtained from fits to the EPIC data. The MOS and pn spectra are fitted simultaneously. We included a systematic error in the uncertainties on the Si/Fe and Ni/Fe abundance ratios (see Sect. 6.3.2 for a discussion about systematic errors).

Summary & Outlook

In the previous chapters I show that the abundances in the Intra-Cluster Medium (ICM) are able to reveal the clusters enrichment history. In addition, the abundances can also be used to constrain supernova models. The hot X-ray emitting gas clouds in clusters of galaxies are the biggest aggregates of baryons that we know, except for the cosmic web. A typical cluster contains the products of billions of supernovae. Therefore, clusters are very representative objects to study the enrichment of the bulk of the matter in the universe.

Using the current state-of-the-art in high-resolution X-ray spectroscopy, XMM-Newton, I have analysed data of 23 clusters of galaxies in total. I find that detailed knowledge about the X-ray background, spectral lines and the response of the instruments is absolutely necessary to obtain accurate abundances with realistic uncertainties. To improve the accuracy on the abundances and their uncertainties I have developed a method to correct for the soft X-ray background, because the background is different for every position on the sky (Chapter 4). Moreover, systematic differences between the instruments also need to be taken into account. Therefore, analysis of extended sources, like clusters, cannot be done using a black-box approach, but a large effort is needed to extract robust values.

Only when robust values are obtained, one can attempt to derive the enrichment history. In Chapter 4 and 5, I show that EPIC and RGS can be used to obtain information about the spatial abundance distribution in clusters. From the RGS spectrum of Sérsic 159-03 (Chapter 4) I derive that the iron abundance profile (a typical type Ia product) is peaked around the central cluster galaxy, while the oxygen abundance distribution (a typical core-collapse product) is more extended. This confirms the idea that iron is still being added to the ICM specifically in the core by the supernovae type Ia, and that oxygen is an old well-mixed product of the core-collapse supernovae that exploded soon after the first star bursts. The spatial oxygen distribution is not required to be entirely flat, but may exhibit a more shallowly peaked distribution due to ram-pressure stripping of gas from in-falling galaxies. Perhaps this is the case in

2A 0335+096 (Chapter 5), where I find a similar spatial profile for oxygen and iron with RGS.

The abundances that I measure also provide constraints on the supernovae themselves. In Chapter 6, I conclude that the currently favoured supernova models are not able to match our data. An empirically modified supernova type Ia model by Badenes et al. (2006) provides a better fit to the Ar/Ca ratio that I find. By fitting the abundances I am able to constrain physical parameters of a supernova, like the density where the sound wave that is ahead of the explosion turns into a shock.

Core-collapse supernova models are more difficult to constrain because of two reasons. First, the yields of core-collapse supernovae differ from star to star. I use the yields that are integrated over the entire mass range (8–50 M_{\odot}). Secondly, most of the elements that I robustly detect in EPIC are mainly produced in type Ia supernovae. Therefore, also the results for oxygen and neon from RGS are required to constrain the core-collapse contribution. The results do not yet allow me to put strong limits on the core-collapse history, neither on the metallicity of the stars nor on the Initial-Mass Function of the stellar population. But perhaps new deep observations with XMM-Newton or observations with future missions will be able to constrain them.

As expected, signatures of population-III stars are not significantly detected in the cluster data (Chapter 4 and 5). The best uncertainties on the abundances that I obtain are of the order of 10^{-2} times solar, whereas the population-III contribution is expected to be 10^{-3} times solar. New X-ray missions may also be able to detect their contribution in the future.

7.1 Outlook

One of the most important steps forward in the field of X-ray spectroscopy, is the development of the microcalorimeter, and especially the so-called Transition-Edge Sensor (TES). This new type of detector can achieve a spectral resolution of $\lesssim 5$ eV, which is more than 20 times better than the current state-of-the-art CCD technology. The microcalorimeter employs an energy dispersive rather than a wavelength dispersive technique like transmission and reflection gratings. Therefore, it does not lose photons to higher order spectra and retains a detection efficiency close to 1. The major advantage for cluster research is also that its high spectral resolution also applies to extended sources in combination with imaging capability.

With current high-resolution spectrometers based on gratings, like the Reflection-Grating Spectrometer (RGS), the spectral resolution decreases when the source is more extended. Basically, this is because the RGS does not have a slit. All the light from a $\sim 12'$ wide area enters the spectrometer, therefore the resulting spectrum is convolved with the spatial profile of the source. In contrast with this, one detector pixel of a TES can measure the full spectrum of a specific part in the cluster at the intrinsic high spectral resolution.

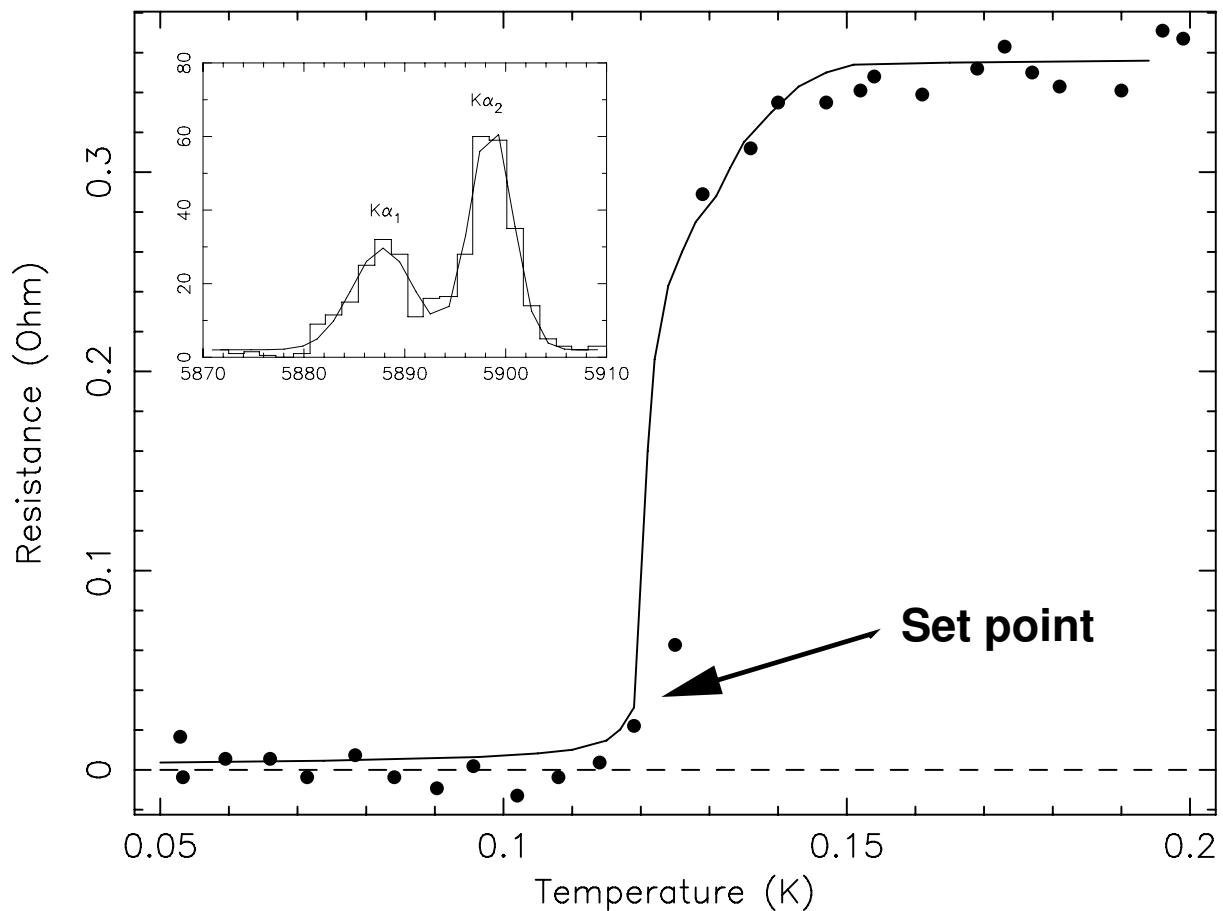


Figure 7.1: The dependence of the resistance of the absorbing material versus temperature. The figure shows a very sharp transition from zero resistance at low temperature to to a high resistance at slightly higher temperatures. The data points represent directly measured resistances at low currents, and the curve shows the resistance of the absorber at high currents. The arrow points to the optimal operation temperature. The inset shows an example of a measured spectrum near 6 keV. The closely spaced Fe $K\alpha_1$ and Fe $K\alpha_2$ lines are clearly resolved. The x-axis and y-axis are in units of eV and counts, respectively.

7.1.1 Transition-Edge Sensors

A Transition-Edge Sensor (TES) is a small microcalorimeter that can measure the energy of individual X-ray photons with high accuracy. To reach this high spectral resolution, the TES uses the transition edge between normal conductivity and superconductivity that is present in a number of suitable materials. At cryogenic temperatures (~ 0.1 K), the conductivity of the absorbing material is very sensitive to temperature. In Fig. 7.1 I show this strong dependence on temperature. The optimal operation temperature (set point) of a TES detector lies at the base the edge. It is the point where the steepest increase of the resistance starts. When an X-ray photon hits the absorber, its temperature rises just enough to get the temperature of the absorber into the transition regime. By measuring the increase of the resistance, one can calculate the energy of the photon with high accuracy.

Table 7.1: Science requirements and goals for the XEUS observatory as formulated in the Science Requirements Document (SRD) for XEUS in May 2006.

Parameter	Requirement	Goal
Effective Area (m ²)	1 @ 0.2 keV	1.5 @ 0.2 keV
	5 @ 1.0 keV	5 @ 1.0 keV
	2 @ 7 keV	3 @ 7 keV
		1 @ 10 keV
		0.1 @ 40 keV
Energy Range (keV)	0.1 – 15	0.1 – 40
FOV Diameter	7' (WFI)	1.7' (NFI)
	45" (NFI)	
Spatial Resolution (")	5 HEW	2 HEW
Energy Resolution	2 eV @ 0.5 keV (NFI)	1 eV @ 0.5 keV (NFI)
	6 eV @ 6 keV (NFI)	3 eV @ 6 keV (NFI)
	150 eV @ 6 keV (WFI)	1 keV @ 40 keV

Presently, the main effort in this field is to make a array of TES detectors, which would allow imaging of a source. Current arrays consist of about 5×5 detectors, but 32×32 arrays will be possible in the coming years.

7.1.2 Future X-ray missions using TES detectors

Since July 2005, an array of microcalorimeters has been flying aboard the Japanese Suzaku satellite (formerly known as Astro-E2). Unfortunately, the liquid helium that was needed for the cooling of the detector boiled away just a few days after the instrument was switched on. No scientific observation was performed. Therefore, we still have to wait before the first TES spectrum of a cluster can be obtained.

The next major European X-ray mission that will have a microcalorimeter array on board is the X-ray Evolving Universe Spectrometer (XEUS). This X-ray observatory is part of ESA's Cosmic Vision programme and is proposed to fly between 2015 and 2025. XEUS is planned to have a large effective area ($\sim 5 \text{ m}^2$), a high spectral resolution ($\lesssim 5 \text{ eV}$) and a spatial resolution of about three arcseconds. The instruments on XEUS that have the largest potential impact for cluster research comprise the Narrow-Field Imager (NFI) and the Wide-Field Imager (WFI). The NFI will probably consist of a TES detector, while the WFI will contain a CCD-type detector. The basic parameters of the mission are summarised in Table 7.1.

In Fig. 7.2 I show a simulated NFI spectrum of the core of Sérsic 159-03. Clearly, many lines are resolved. Compared to the EPIC spectrum of Sérsic 159-03, the improvement is overwhelming. With XEUS, the abundances will be measured with an accuracy of 10^{-3} times solar, which is about an order of magnitude larger than the accuracy with EPIC. This accuracy might be sufficient to detect the contribution of Population-III stars.

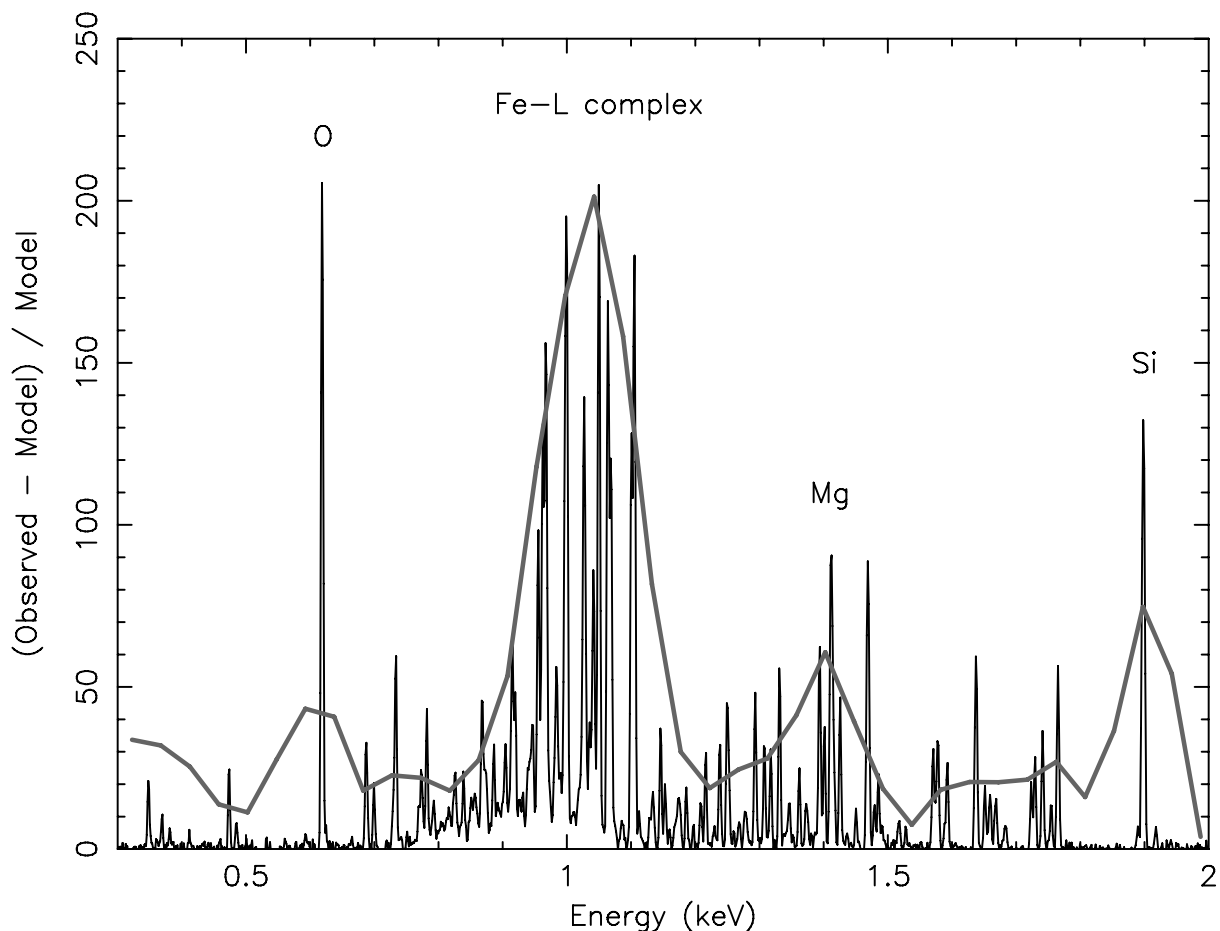


Figure 7.2: Simulated spectrum of the inner 30'' of the cluster of galaxies Sérsic 159-03 in the 0.3–2 keV interval. I subtract the continuum to show the spectral lines. For the simulation I assumed an exposure time of 100 ks with the TES array that is planned for XEUS. The thick line that is plotted on top of the XEUS spectrum represents an EPIC spectrum of the same source for comparison.

A spectral resolution and accuracy of this magnitude will open up an entirely new dimension of cluster research. Spatially resolved high-resolution spectroscopy is very important for deriving the chemical enrichment of clusters. With a TES, we will not only be able to measure the abundances and temperatures of the cluster with higher accuracy, but also lines from other elements will be resolved. The significance of the lines would be about a factor of 10 better with respect to EPIC, just because of the order of magnitude improvement of the spectral resolution and effective area.

When the number of accurately determined elements increases, we will have more accurate tests for supernova models. Of course, individual supernova remnants can be studied in more detail, but also clusters provide excellent tests. The supernova fits that I performed using the XMM-Newton data (Chapter 4, 5, and 6), can be performed again with a much higher accuracy. With this information supernova models will be much better tuned.

The Wide-Field Imager aboard XEUS will be excellent to derive the enrichment history from metal maps and it will show the cluster dynamics. A few theoretical metal-

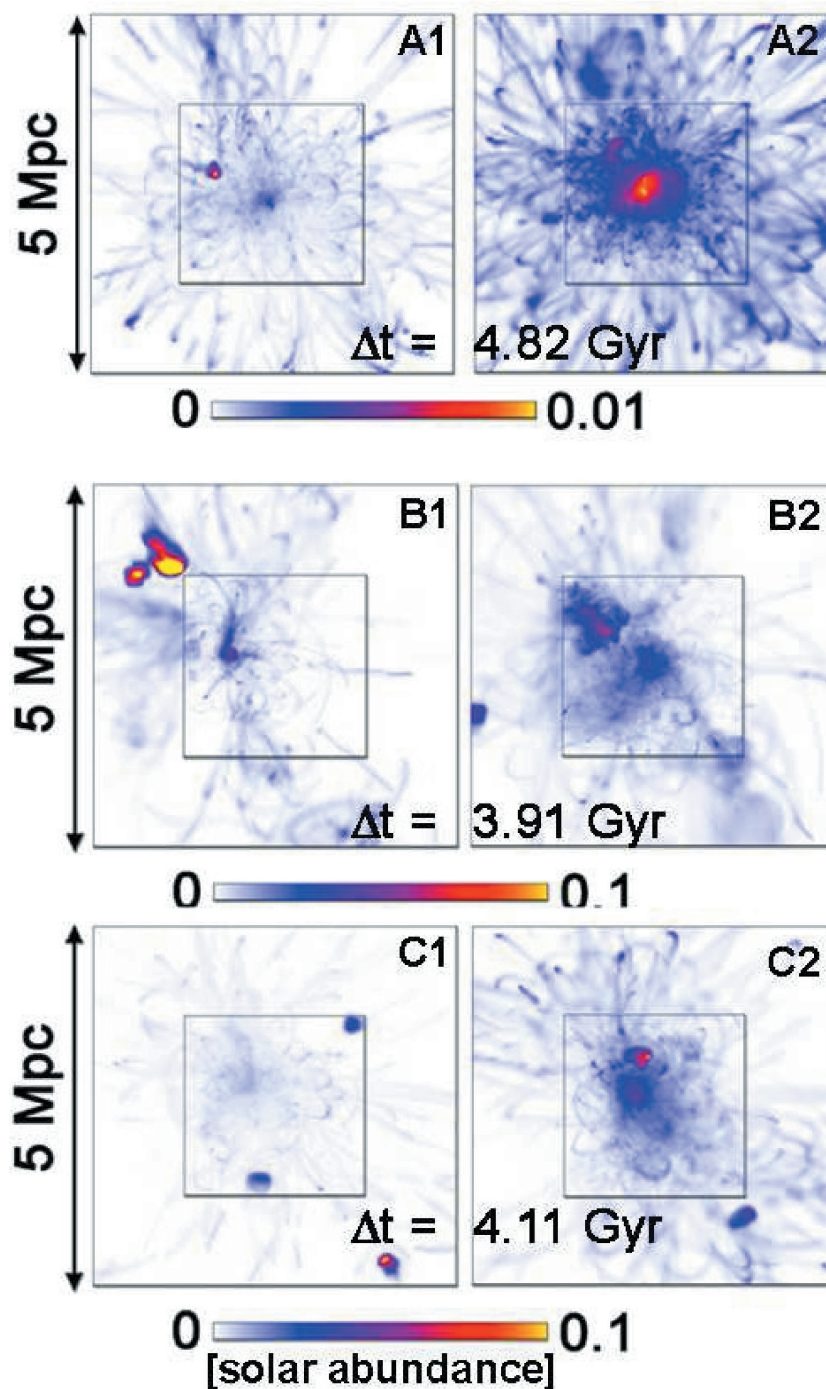


Figure 7.3: Simulated X-ray weighted metal maps for three clusters with slightly different dynamical histories and masses. Clusters A, B, and C have total masses of 13.0, 6.8, and 7.8 times $10^{14} M_{\odot}$, respectively, within a 3 Mpc radius. Between A1 and A2 there is 4.82 Gyr of evolution, between B1 and B2 3.91 Gyr, and between C1 and C2 4.11 Gyr. This figure is adapted from Kapferer et al. (2006).

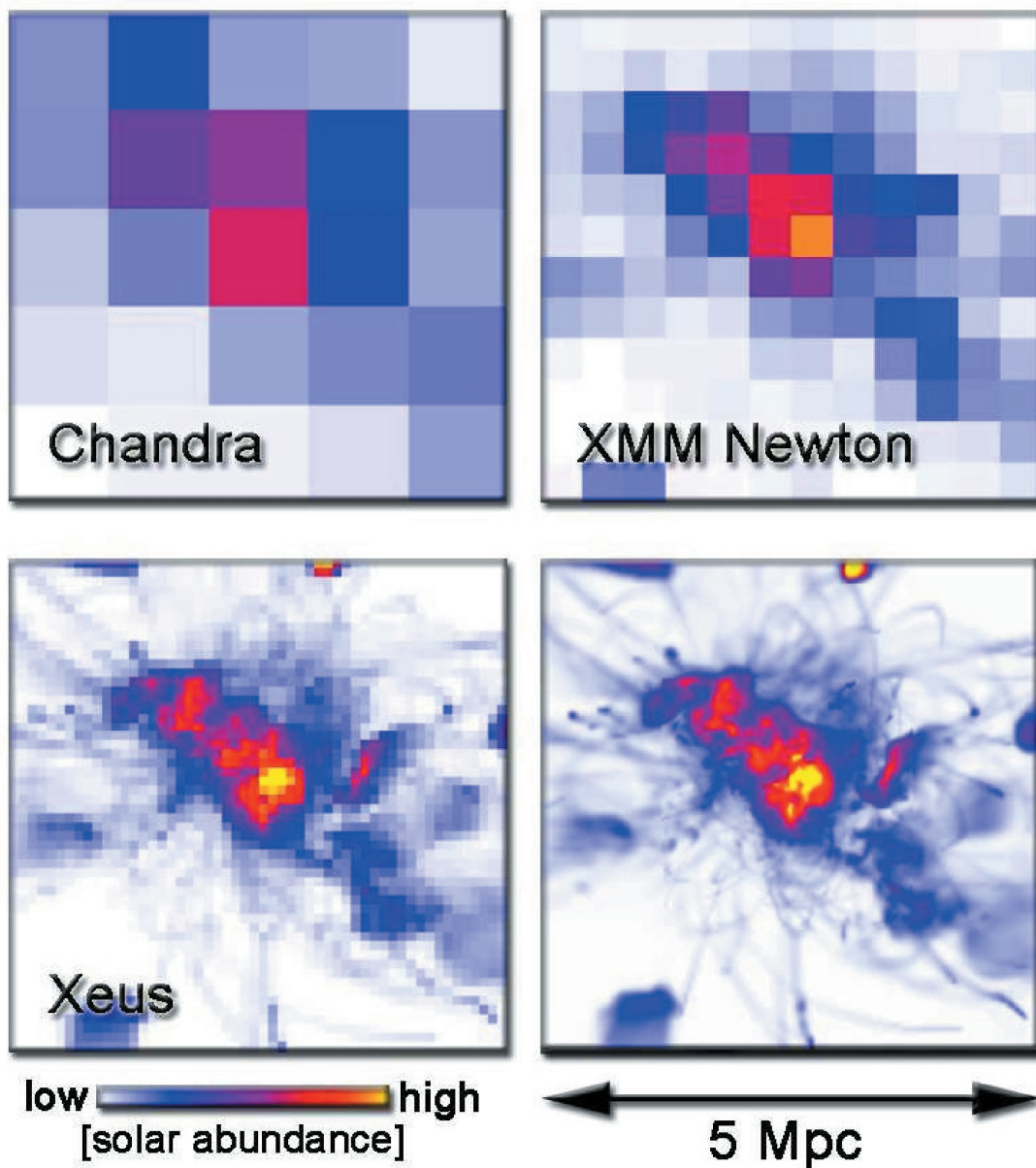


Figure 7.4: Simulated X-ray weighted metal maps as they would be extracted with Chandra, XMM-Newton and XEUS, respectively. In the bottom-right corner, the original numerical simulation is shown. Adapted from Kapferer et al. (2006).

licity maps of clusters, simulated by Kapferer et al. (2006), are shown in Fig. 7.3. These maps show filamentary structures along the paths of individual galaxies. The panels A, B, and C show the results for clusters with different masses. Observing these structures would be a strong indication for enrichment through ram-pressure stripping of in-falling galaxies. In Figure 7.4 I show that XEUS will probably resolve these features. The plot also shows that the current X-ray observatories, XMM-Newton and Chandra, are not able to observe the effects of ram-pressure stripping directly. This shows that

the sensitivity and spectral resolution of the next generation of X-ray telescopes will definitely enlarge our view on the chemical history of clusters.

Nederlandse Samenvatting

Clusters van melkwegstelsels zijn in veel opzichten de grote steden van ons heelal. Ze bestaan uit honderden melkwegstelsels die op hun beurt weer miljarden sterren bevatten. De melkwegstelsels zijn ingebed in een enorme wolk heet gas die als een soort smog in het cluster hangt. Ontploffende sterren, zogenaamde supernova's, hebben het gas in de afgelopen tien miljard jaar verrijkt met zwaardere elementen, zoals zuurstof, silicium en ijzer.

Met behulp van de röntgensatelliet XMM-Newton (ESA) kan je de hoeveelheden van die elementen in het hete clustergas meten. In dit proefschrift beschrijf ik een nieuwe methode om de metingen zo goed mogelijk te doen. Die nieuwe methode maakt het mogelijk om de hoeveelheden zware elementen te vergelijken met de uitstoot van supernova's. Ik heb ontdekt dat veel van de modellen die nu voor supernova's gebruikt worden niet helemaal kloppen. Door een aangepast model te gebruiken, kan ik de hoeveelheden van elementen die ik in clusters vind veel beter verklaren.

8.1 Clusters van melkwegstelsels

Het grootste deel van de ruimte in het heelal is leeg en koud. Maar zo hier en daar hangen er grote wolken materie die verre van koud zijn. Door hun grote zwaartekracht trekken ze voortdurend gas en sterrenstelsels aan uit lange linten materie die de grote wolken met elkaar verbinden. Ze zijn als het ware knooppunten in een gigantisch kosmisch web dat zich uitstrekt tot zover we kunnen kijken. In de grote wolken bevinden zich groepen van honderden tot duizenden sterrenstelsels die we kennen als clusters van melkwegstelsels. Elk van die melkwegstelsels bestaat weer uit honderden miljarden sterren zoals onze zon.

De zwaartekracht, die ervoor zorgde dat het web zijn vorm kreeg, komt vooral van massa die we niet kunnen zien. Die donkere materie, die bij elkaar zeven keer

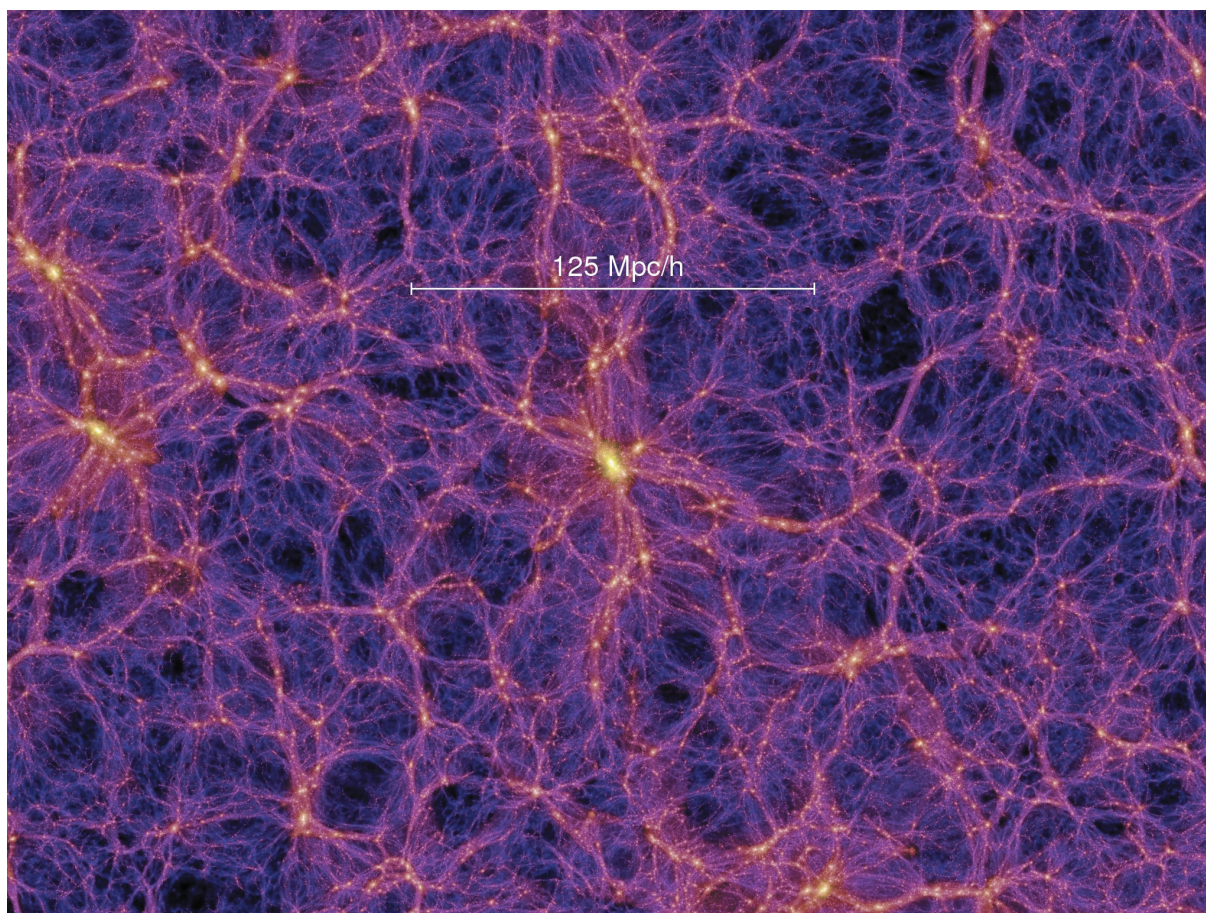


Figure 8.1: Het kosmisch web zoals het eruit ziet volgens computersimulaties door Springel et al. (2005). Het plaatje laat de structuur van de donkere materie in het heelal zien. Omdat normale materie de sterke aantrekkingskracht van de donkere materie voelt, ziet het plaatje er ongeveer hetzelfde uit voor sterren en gas. In het midden van de foto hangt een groot cluster van melkwegstelsels. De witte lijn geeft een grootte van 125 Mpc aan, wat overeenkomt met ongeveer 400 miljoen lichtjaar.

zwaarder is dan alle gewone materie bij elkaar, heeft zo'n grote invloed dat het gas en de melkwegstelsels vrijwel altijd de onzichtbare materie volgen. Vanwege al die donkere materie in een cluster is het totale gewicht zo groot dat licht uit het verre heelal afgebogen wordt. Op foto's van clusters in zichtbaar licht zien we daarom soms vervormde beelden van melkwegstelsels die in werkelijkheid veel verder achter het cluster staan (zie Fig. 8.2).

8.1.1 Heet gas

Wat je in zichtbaar licht niet kan zien, is de hete ijle gaswolk waarin de melkwegstelsels zijn ingebed. Sinds zijn ontstaan heeft het cluster veel gas aangetrokken uit zijn omgeving. Dat gas is vervolgens in z'n zwaartekrachtsveld blijven hangen en heeft een grote wolk gevormd. Doordat het gas door de zwaartekracht is samengeperst en door allerlei schokgolven is verhit, heeft het gas een temperatuur gekregen van rond



Figure 8.2: Foto van het cluster Abell 2218 gemaakt door de Hubble ruimtetelescoop (NASA/ESA). Tussen de grote gele melkwegstelsels zijn vervormde beelden te zien van melkwegstelsels die in werkelijkheid achter het cluster staan. De sterke zwaartekracht werkt als een soort lens. Het is alsof je door het voetje van een wijnglas naar de achterliggende melkwegstelsels kijkt.

de tien miljoen graden Celcius. Vanwege de hitte is de druk in het gas hoog genoeg om tegendruk te bieden aan de zwaartekracht. Daardoor krimpt de wolk niet meer en krijgt hij een mooie ronde vorm.

In een gas dat miljoenen graden heet is, zijn botsingen tussen de gasdeeltjes zo heftig dat er bij elke botsing röntgenstraling uitgezonden wordt. De kans is klein dat deeltjes botsen, want er zitten maar ongeveer honderd deeltjes in een liter cluster gas. Ter vergelijking: in een liter water zitten 10^{25} deeltjes. Maar omdat het totale aantal deeltjes en het volume in het hele cluster zo enorm groot is, vinden er toch genoeg botsingen plaats om het cluster helder in röntgenlicht te laten schijnen.

Het hete gas heeft ook invloed op de geboorte van sterren in een cluster. Melkwegstelsels die het cluster in vallen verliezen een groot deel van hun gas, omdat het er door wrijving vanaf waait. Bovendien blijven koude gaswolken door de hitte en straling te warm om in elkaar te storten en nieuwe sterren te maken. De meerderheid van de sterren die we in clusters zien, behoren waarschijnlijk tot de oudste sterren in het heelal. Ze zijn ontstaan toen het cluster nog jong was en weinig heet gas bezat. We kunnen dat ook aan de gele kleur van de stelsels in Fig. 8.2 zien, omdat oude sterren relatief koel zijn en daardoor een rood-gele kleur hebben.

8.1.2 Koele kern

In tegenstelling met wat je zou verwachten is het in het centrum van de hete gaswolk vaak kouder dan aan de rand. De temperatuur is in de kern ongeveer de helft lager dan aan de buitenkant. Dat komt omdat het gas daar sterk aan het afkoelen is. Dat

afkoelen heeft op het eerste gezicht veel weg van een sneeuwbaaleffect. De energie die in die röntgenstraling zit, blijft niet in het cluster, maar vliegt ver het heelal in. Het gas in het cluster koelt daardoor af en krimpt een beetje, net als een spoorstaaf die uitzet en krimpt als het heet of koud is. Door het krimpen hebben de deeltjes in het gas ineens minder ruimte en neemt het aantal botsingen, en daarmee ook de productie van röntgenstraling, toe. Het cluster verliest daardoor weer energie en zo gaat het afkoelen steeds maar harder.

Het afkoelen gaat niet eeuwig door, omdat clusters nog een hittebron achter de hand hebben. In de melkwegstelsels zitten vaak hele zware zwarte gaten die met groot geweld materie opzuigen en met bijna de lichtsnelheid weer de ruimte in slingeren. De bundel met materie die eruit komt, blaast grote bellen in het hete gas (zie Fig. 8.3). De energie die in die bellen zit is genoeg om het gas zodanig te verwarmen dat het de afkoeling stopt.

8.2 De oorsprong van elementen

Vrijwel alle chemische elementen waar we uit bestaan, zijn ooit in sterren gevormd. In het vroege heelal was er alleen nog maar waterstof, helium en een hele kleine hoeveelheid lithium en berillium. Pas toen de eerste sterren ontbrandden, konden er zwaardere elementen ontstaan. In het centrum van sterren heerst een zodanig hoge druk en temperatuur dat atoomkernen samen kunnen smelten tot zwaardere elementen. Dat proces, dat kernfusie heet, levert vrijwel alle energie die een ster in z'n leven uitzendt.

In eerste instantie zet de ster alleen waterstof om in het zwaardere helium. Maar zodra het waterstof in het centrum op is, kan ook helium omgezet worden naar nog zwaardere kernen zoals koolstof en zuurstof. Zware sterren, die meer dan acht keer de massa van de zon hebben, gaan door met fuseren totdat er ijzer ontstaat. Het samensmelten van ijzerkernen levert namelijk geen energie meer op, maar kost energie. Op dat moment stopt de productie van energie in het centrum en daardoor kan het binnenste van de ster geen tegendruk meer leveren aan de buitenlagen. De gigantische druk perst het centrum in elkaar tot een neutronenster of een zwart gat. De schokgolf die op de implosie volgt, zorgt ervoor dat de kernfusie in de aangrenzende lagen letterlijk explosief toeneemt. De ster ontploft dan als een zogenaamde *core-collapse* supernova.

Voor de explosie, die het einde van de ster betekent, zijn er in het binnenste van de ster lagen ontstaan met de verschillende producten van kernfusie. Dat komt omdat de temperatuur naar het centrum toe steeds hoger oploopt. Hoe hoger de temperatuur is, des te verder is de kernfusie gekomen. De gelaagde structuur lijkt op die van een ui. In het midden zit een bol ijzer en daaromheen lagen van silicium, zuurstof, koolstof, helium en waterstof. Bij een supernova explosie ontploffen de lagen die direct om de bol ijzer zitten, daardoor worden de buitenste lagen van de ster, die vooral lichtere elementen bevatten, de ruimte ingeblazen.

8.2.1 Type Ia supernovae

Naast de zogenaamde *core-collapse* supernovae, die vaak ook type II supernovae worden genoemd, is er nog een andere soort supernovae die type Ia (één-a) supernova heet. Dat laatste type ontstaat niet uit een enkele zware ster, maar uit twee middelzware sterren die dicht om elkaar heen draaien. Door het uitwisselen van materie tussen de twee sterren kan de zwaarste van de twee uiteindelijk als supernova ontploffen.

In eerste instantie verloopt het leven van de twee sterren zoals normaal. Beide sterren zetten in hun binnenste waterstof om naar helium. De zwaarste van de twee zal dat echter sneller doen dan de andere, omdat de temperatuur en druk in de zware ster hoger is. De brandstof is daar eerder op. Voor een ster met een massa lager dan 8 zonsmassa's betekent dat een einde als witte dwerg. In de dwerg vindt geen kernfusie meer plaats, waardoor hij niet meer is dan een hete bal van helium, koolstof en zuurstof die langzaam afkoelt.

Zodra de andere ster, de buurman van de witte dwerg, aan het eind van z'n leven komt, zwelt hij flink op. Als de afstand tussen de twee sterren kort genoeg is, kan er materie van de opgezwollen ster naar de witte dwerg toe vallen. Door de effecten van de zwaartekracht zuigt de witte dwerg zijn begeleider als het ware leeg, met als gevolg dat er een dikke laag waterstof en helium om de witte dwerg komt te liggen. Zo nu en dan is de temperatuur in de laag hoog genoeg om het waterstof en soms ook helium te laten fuseren. Het oppervlak van de witte dwerg wordt dan tijdelijk ontzettend helder. Sterrenkundigen noemen dat ook wel een nova, omdat zo'n ster op dat moment ineens als een nieuw lichtpunt aan de hemel verschijnt.

Die novae kunnen geregeld plaatsvinden zonder dat de witte dwerg helemaal ontploft. De kernfusie zet aan het oppervlak van de witte dwerg nieuwe zuurstof en koolstof af. Omdat er steeds maar weer nieuwe materie van de begeleidende ster aangevoerd wordt, blijft de massa van de witte dwerg toenemen. Het groeien gaat goed totdat de witte dwerg zwaarder is dan zo'n 1.4 keer de massa van de zon. Dan kan de materie in het binnenste van de witte dwerg niet meer genoeg druk leveren om de ster in stand te houden. De ster implodeert en ook hier zorgt een schokgolf ervoor dat de buitenlagen exploderen. In de hitte van de explosie maakt de ster veel zwaardere elementen aan, vooral nikkel en ijzer.

8.2.2 Chemische handtekening

Omdat *core-collapse* en type Ia supernovae op verschillende manieren ontstaan, zijn er ook verschillen in de hoeveelheid en soort chemische elementen die ze maken. In een *core-collapse* supernova verdwijnen vrijwel alle zware elementen (calcium, ijzer en nikkel) in het zwarte gat of neutronenster, terwijl vrijwel alle zuurstof en koolstof in een type Ia wordt omgezet naar diezelfde zware elementen. Aan het aantal elementen in een gas kan je dus zien welk type supernovae het gas hebben verrijkt. De supernova laat als het ware een chemische handtekening achter in het omliggende gas.

Supernovae van het type Ia zijn het meest constant, omdat ze allemaal ontploffen als de massa van de witte dwerg de natuurkundige limiet van 1.4 zonsmassa overschrijdt.

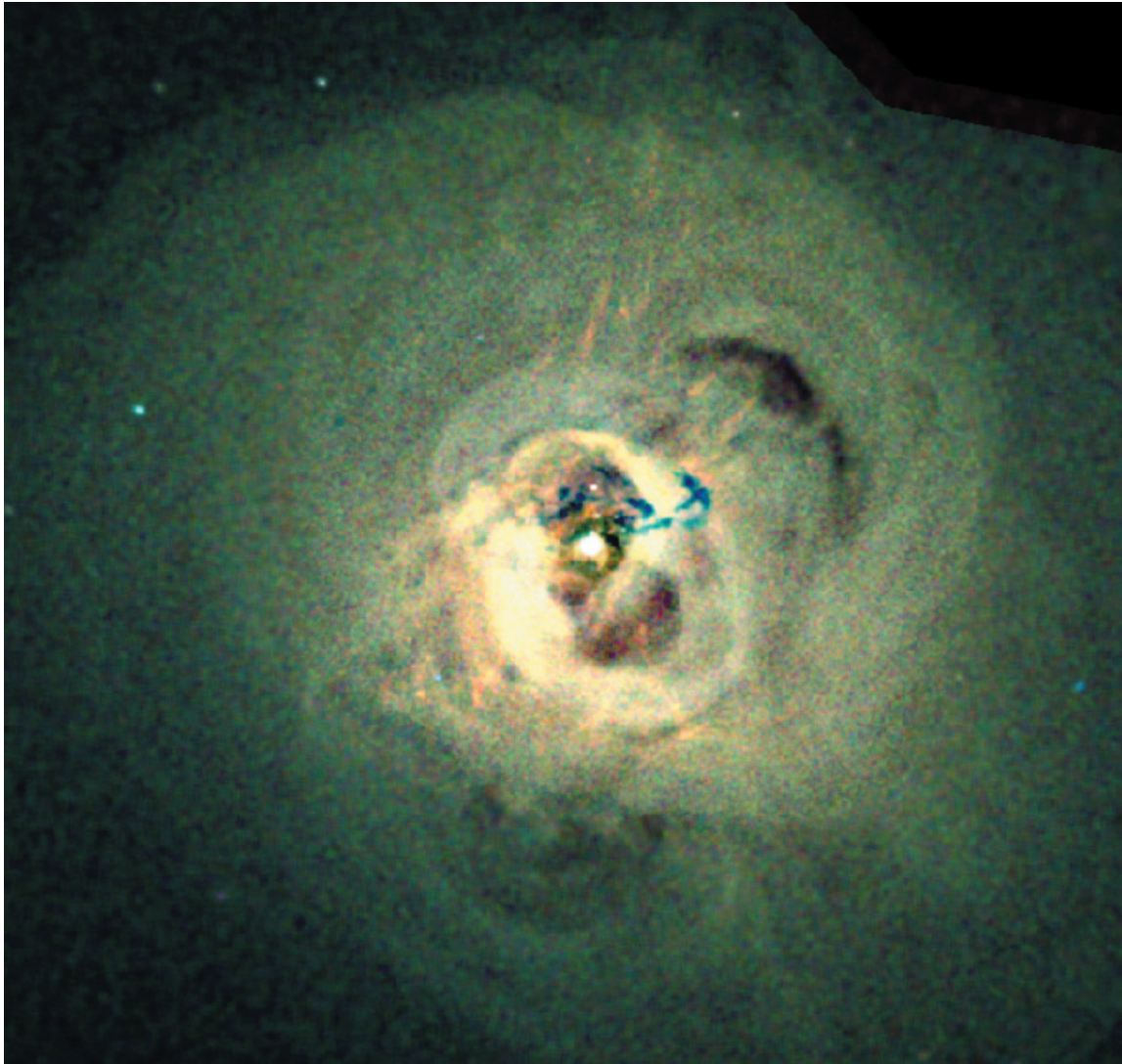


Figure 8.3: In het Perseus cluster blaast een zwart gat bellen in het hete clustergas. Op deze röntgenfoto van Chandra zijn de bellen duidelijk te zien. (Foto: Chandra X-ray Observatory, NASA)

Mensen die computermodellen van supernovae maken zijn er nog niet precies uit hoeveel een type Ia supernova van een element produceert, maar de producten bestaan vooral uit calcium, ijzer en nikkel. Dat betekent dat de calcium in onze botten, het ijzer in het hek en het nikkel in onze munten hoogstwaarschijnlijk in een type Ia supernova zijn gevormd.

Core-collapse supernovae zijn lastiger, omdat de verhoudingen tussen de verschillende geproduceerde elementen afhangen van de massa van de ster. Over het algemeen produceren ze vooral lichtere elementen, zoals zuurstof, neon, silicium en zwavel. Dat komt omdat de buitenste schillen in de ster, waar die elementen in zitten, vrijwel geheel weggeslingerd worden. De zwaardere elementen eindigen voor een groot deel in het zwarte gat of de neutronenster en zijn dan niet meer te zien. Dat

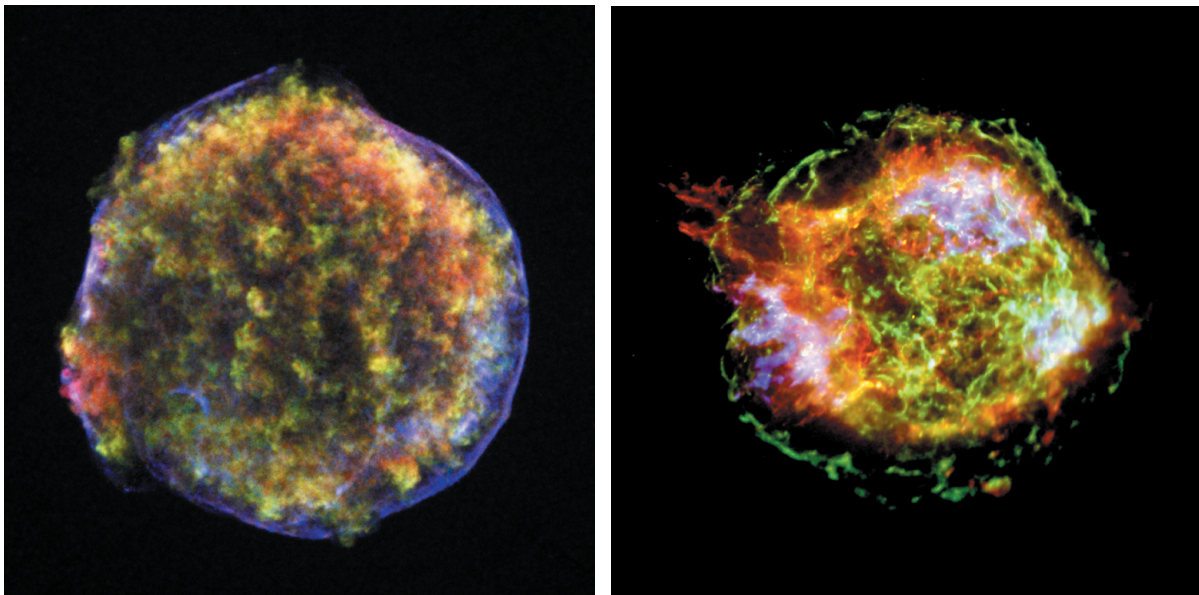


Figure 8.4: Twee supernovarestanten gezien in röntgenstraling. Het Tycho supernovarestant (links) was waarschijnlijk een supernova van het type Ia die in 1572 ontplofte. Cassiopeia A (rechts) explodeerde waarschijnlijk rond 1680 en wordt gezien als een typische core-collapse supernova. (Foto: Chandra X-ray Observatory, NASA)

maakt ze duidelijk onderscheidbaar van de type Ia's.

8.3 De chemische historie van clusters

Zo'n honderd à tweehonderd miljoen jaar na de oerknal ontstonden de eerste sterren. Op het moment dat die sterren als supernova ontploften, ontstonden ook de eerste zwaardere elementen. De producten van de eerste generaties *core-collapse* supernova's konden zich in die tijd over een relatief groot gebied verspreiden, omdat de onderlinge afstanden – vanwege de uitdijing van het heelal – toen kleiner waren dan nu. Aangezien de type Ia supernova's er langer over doen om te ontploffen, is het meeste gas uit die tijd alleen 'vervuild' geraakt met elementen die in *core-collapse* supernova's gemaakt zijn (zuurstof, silicium en zwavel).

Clusters waren er nog niet toen de eerste sterren ontstonden. De grootste groepen van melkwegstelsels waren pas één à twee miljard jaar na de oerknal groot genoeg geworden om ze een cluster te kunnen noemen. Ze hadden sinds lange tijd voortdurend gas en sterrenstelsels uit de omgeving aangetrokken. Dat gas is dus vooral 'vervuild' door *core-collapse* supernova's. In diezelfde periode begonnen ook de type Ia supernovae af te gaan. Omdat het maken van zo'n supernova niet even lang duurt voor elke dubbelster, gaan ze niet allemaal tegelijk af, maar één voor één over een lange periode. Zelfs nu ontploffen er nog type Ia supernova's waarvan de sterren al in het vroege heelal gevormd zijn. Omdat er meer sterrenstelsels in het centrum van het cluster zitten dan aan de buitenkant, komt de uitstoot van de type Ia supernova's ook vooral in het centrum terecht. De hoeveelheden van elementen zoals ijzer en nikkel

zullen dus afnemen naarmate het gas verder van het centrum af ligt.

Behalve vervuiling door de supernova's die in het cluster zelf afgaan, komen er ook zwaardere elementen in het hete gas terecht via invallende melkwegstelsels. Als een melkwegstelsel zoals het onze in een cluster valt, dan wordt al het gas in het stelsel door wrijving eruit geblazen. Een groot deel van de producten van de supernova's die gedurende de evolutie van het stelsel zijn ontploft komen op die manier in het hete gas terecht. Het meeste gas komt vrij op de plek in de wolk waar de dichtheid en de snelheid (en dus de weerstand) het hoogst zijn. Dat is eigenlijk altijd het centrum van de wolk. Daarom verwacht men dat dat het afblaas-effect een lichte toename van alle zware elementen naar het centrum toe laat zien. In het invallende stelsels zijn immers zowel *core-collapse* als type Ia supernova's ontploft.

8.4 De vooruitgang met XMM-Newton en Chandra

Sinds 1999 hebben sterrenkundigen de beschikking over twee nieuwe röntgentelescopen, XMM-Newton (ESA) en Chandra (NASA). Beide satellieten hebben superieure eigenschappen ten opzichte van hun voorgangers. Chandra beschikt over een zeer goede spiegel waarmee hele scherpe plaatjes kunnen worden gemaakt. Daarmee kan je bijvoorbeeld in clusters de gasbellen zien die zwarte gaten in het hete gas blazen. XMM-Newton, daarentegen maakt iets minder scherpe foto's, maar is veel gevoeliger dan Chandra. Door het grote oppervlak van de spiegels van XMM-Newton vangt hij veel meer röntgenstraling op. Bovendien kan XMM-Newton veel nauwkeuriger de golflengte van de röntgenstraling van clusters meten. Het spectrum, dat je krijgt als je de hoeveelheid licht per golflengte op volgorde van golflengte ordent, bevat ontzettend veel informatie over het hete gas in clusters.

Uit de gedetailleerde spectra van XMM-Newton kan je aflezen wat de temperatuur van een cluster is, maar ook welke elementen erin zitten. Atomen van verschillende elementen geven namelijk op hele specifieke golflengten licht. In een spectrum lijkt het een beetje op een streepjescode. Natuurkundigen kunnen de golflengten waarop die verschillende elementen licht geven nauwkeurig uitrekenen en aan de hand daarvan kunnen sterrenkundigen bepalen welke elementen ze in clusters zien. In Fig. 8.5 staat een voorbeeld van een spectrum genomen met XMM-Newton. Hierop zijn duidelijk pieken zichtbaar. We weten dankzij berekeningen dat die pieken overeenkomen met magnesium, ijzer en zuurstof.

Die pieken in het spectrum vertellen niet alleen welk element het is, maar met de juiste modellen kan je ook bepalen hoeveel atomen er van dat element zijn. Die modellen zijn in de afgelopen jaren ontwikkeld op het SRON Netherlands Institute for Space Research in Utrecht. Samen met de grote nauwkeurigheid van XMM-Newton hebben die modellen ons nieuwe inzichten gegeven in het hete gas in clusters van melkwegstelsels.

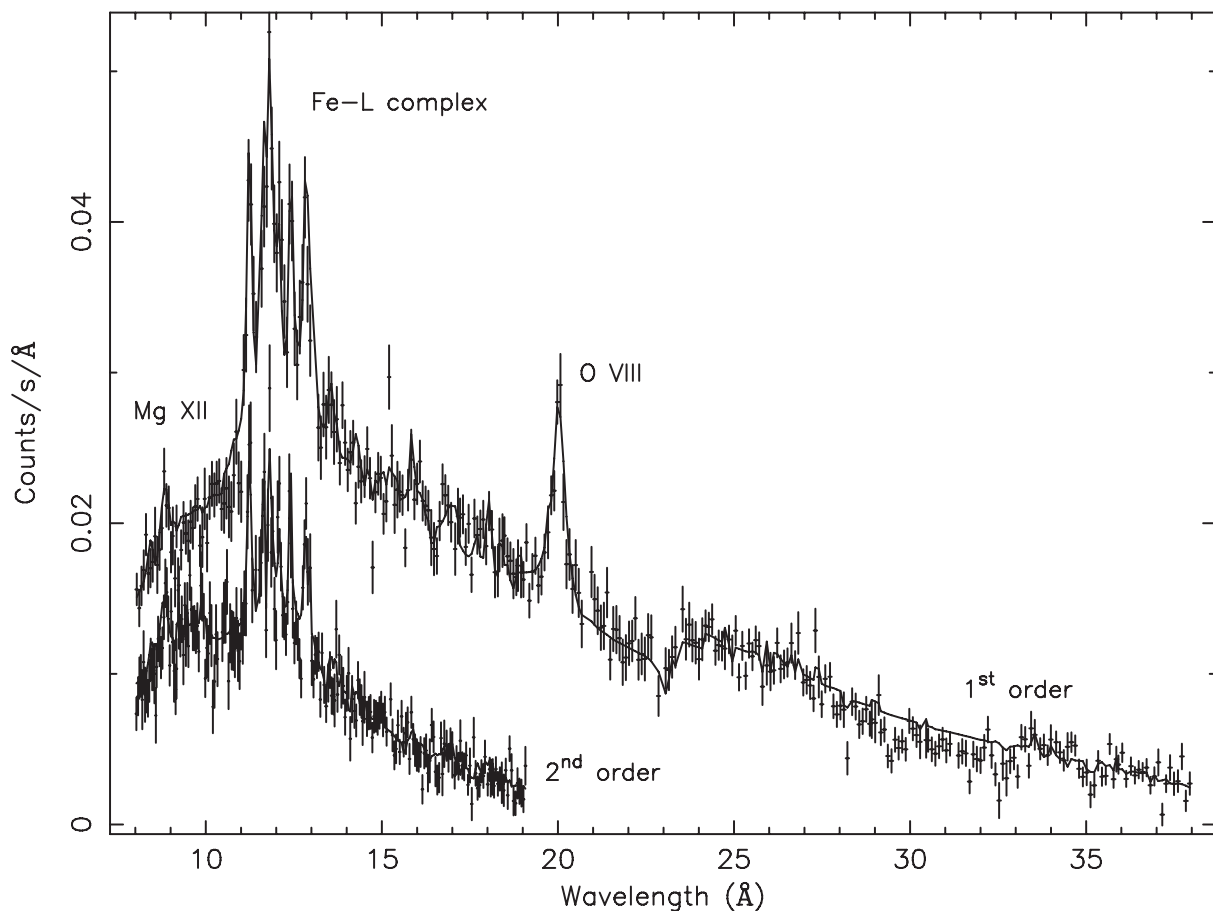


Figure 8.5: Een spectrum van het hete clustergas gemaakt door het RGS instrument aan boord van XMM-Newton. Hierop zijn spectraallijnen te zien van magnesium (Mg), ijzer (Fe) en zuurstof (O).

8.5 Nieuwe ontdekkingen

Voor dit proefschrift heb ik XMM-Newton waarnemingen van 23 clusters van melkwegstelsels bekeken. Dat klinkt misschien makkelijker dan het is. Voordat je betrouwbare gegevens uit de waarnemingen kan halen, moet je ook precies weten hoe de instrumenten werken en wat voor storingsbronnen invloed op de data hebben. Gas in ons eigen melkwegstelsel zendt bijvoorbeeld ook röntgenstraling uit die als een soort waas voor het cluster hangt. Bovendien er zit ruis in de camera's zelf. Omdat er nog geen manier was om al die storende invloeden eruit te halen, heb ik daarvoor zelf een methode ontwikkeld. Met behulp van die nieuwe methode kunnen we met grotere zekerheid de hoeveelheden van elementen in het hete clustergas bepalen.

In 22 clusters kon ik op die manier van zes elementen de hoeveelheid bepalen: silicium, zwavel, argon, calcium, ijzer en nikkel. Uit waarnemingen met het RGS instrument kwamen daar nog eens twee elementen bij: zuurstof en neon. Voor die acht elementen heb ik de hoeveelheid vergeleken met de uitstoot van de twee typen supernova's. Het blijkt dat ontploffingen van die twee typen ongeveer even vaak voorkomen. Het totaal aantal supernova's van het type Ia is ongeveer gelijk aan het

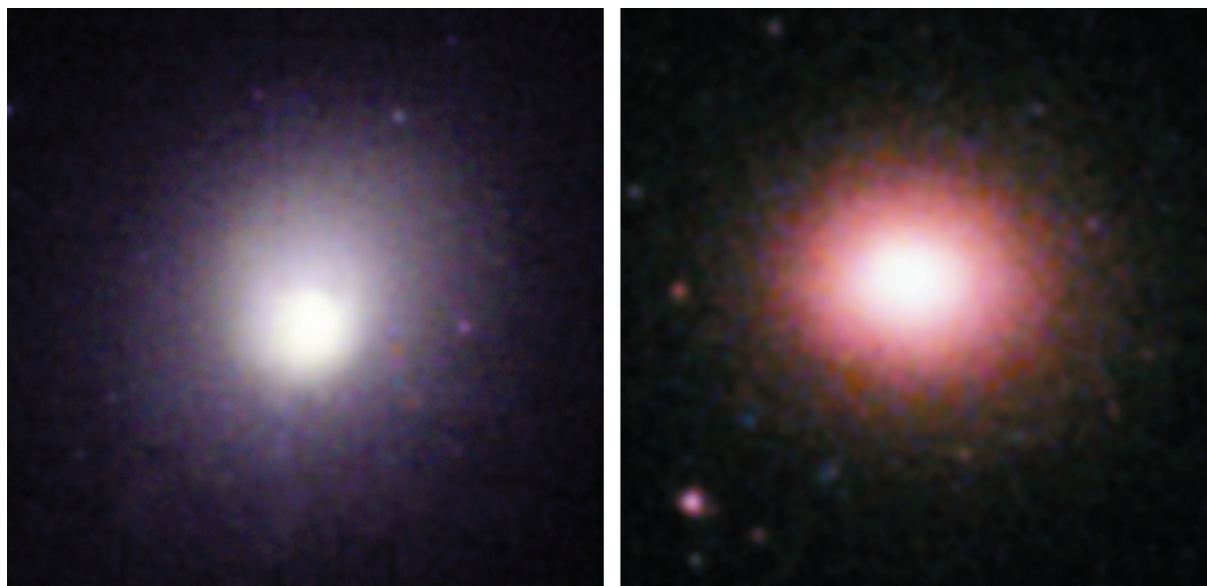


Figure 8.6: Twee clusters van melkwegstelsels, 2A 0335+096 (links) en Sérsic 159-03 (rechts), zoals je ze ziet in röntgenstraling. Beide foto's zijn gemaakt met EPIC camera's aan boord van XMM-Newton.

aantal *core-collapse* supernova's. In vergelijking met de verhouding in ons eigen melkwegstelsel, waar maar 15% van het type Ia is, is dat best veel. Dat komt omdat er in de laatste miljarden jaren geen sterren meer gevormd zijn in een cluster, zodat er nu alleen nog maar type Ia supernova's ontploffen. In ons melkwegstelsel worden nog wel sterren gevormd en daarom hebben de *core-collapse* supernova's nog steeds de overhand boven de tragere type Ia's.

Uit dezelfde vergelijking volgde nog iets opmerkelijks. De modellen voor type Ia supernova's die men op dit moment het meest gebruikt, konden de hoeveelheid calcium in clusters niet verklaren. Ik vond dat er maar liefst anderhalf keer zoveel calcium in clusters aanwezig is dan het model voorspelt. Een nieuw model, dat gebaseerd is op recente waarnemingen van de restanten van de supernova die de Deense astronoom Tycho Brahe in 1572 zag (zie Fig 8.4), blijkt veel beter te werken. De metingen die ik gedaan heb, sluiten voor het eerst een aantal supernovamodellen uit. Omdat mijn metingen een gemiddelde zijn van miljarden supernova's, geeft dat een nog beter beeld van de uitstoot van type Ia's dan een supernovarestant zelf. Met behulp van mijn metingen moet het mogelijk zijn om meer te leren over hoe een supernova van het type Ia precies ontploft.

Een ander voordeel van de XMM-Newton satelliet die ik voor dit onderzoek kon gebruiken is dat je ook op verschillende plaatsen in het cluster hoeveelheden van elementen kan meten. Ik heb gekeken hoe vooral zuurstof en ijzer in het cluster verspreid zijn. Het moet immers mogelijk zijn om verschil te zien tussen de verspreiding van zuurstof (*core-collapse*) en ijzer (type Ia). In het cluster Sérsic 159-03 vond ik inderdaad verschillen. De zuurstof was daar beter door het cluster verspreid dan het ijzer, dat vooral in het centrum te vinden was. De resultaten komen goed overeen met de ideeën die daar al over bestonden. Een deel van het zuurstof komt van vroege *core-collapse* su-

pernova's en het andere deel wordt in het cluster gebracht doordat het van invallende sterrenstelsels afgeblazen wordt. In het grote centrale ellipsvormige stelsel in het centrum van S3c 159-03 gaan voornamelijk type Ia supernova's af en die zorgen voor een grotere hoeveelheid ijzer in het midden van het cluster.

De resultaten die ik heb gevonden geven goede hoop voor de toekomst. Met nieuwe telescopen, zoals de röntgensatelliet XEUS die waarschijnlijk na 2015 gelanceerd zal worden, zal het mogelijk zijn om nog meer te leren over de elementen in clusters. Misschien kunnen we dan direct de sporen zien die de invallende stelsels in het hete clustergas achterlaten. Bovendien kunnen nieuwe camera's nog beter de golflengte van röntgenstraling meten waardoor we nog meer lijnen in het spectrum van clusters kunnen zien. Met al die nieuwe informatie leren we wellicht nog beter hoe supernova ontploffingen in elkaar zitten en waar de atomen om ons heen precies zijn gemaakt.

References

- Allen, S. W. & Fabian, A. C. 1997, *MNRAS*, 286, 583
- Allen, S. W., Fabian, A. C., Johnstone, R. M., et al. 1993, *MNRAS*, 262, 901
- Allende Prieto, C., Lambert, D. L., & Asplund, M. 2001, *ApJ*, 556, L63
- Anders, E. & Grevesse, N. 1989, *Geochim. Cosmochim. Acta*, 53, 197
- Badenes, C., Borkowski, K., Hughes, J., Hwang, U., & Bravo, E. 2006, *ApJ*, 645, 1373
- Bardelli, S., Venturi, T., Zucca, E., et al. 2002, *A&A*, 396, 65
- Baumgartner, W. H., Loewenstein, M., Horner, D. J., & Mushotzky, R. F. 2005, *ApJ*, 620, 680
- Bonamente, M., Lieu, R., Mittaz, J. P. D., Kaastra, J. S., & Nevalainen, J. 2005, *ApJ*, 629, 192
- Bradt, H., Mayer, W., Naranan, S., Rappaport, S., & Spada, G. 1967, *ApJ*, 150, L199+
- Bravo, E., Tornambe, A., Dominguez, I., & Isern, J. 1996, *A&A*, 306, 811
- Brickhouse, N. S., Dupree, A. K., Edgar, R. J., et al. 2000, *ApJ*, 530, 387
- Bromm, V., Ferrara, A., Coppi, P. S., & Larson, R. B. 2001, *MNRAS*, 328, 969
- Bromm, V. & Larson, R. B. 2004, *ARA&A*, 42, 79
- Buote, D. A. 2000, *MNRAS*, 311, 176
- Buote, D. A. & Lewis, A. D. 2004, *ApJ*, 604, 116
- Byram, E. T., Chubb, T. A., & Friedman, H. 1966, *Science*, 152, 66
- Calura, F. & Matteucci, F. 2006, *MNRAS*, 369, 465
- Cavaliere, A., Gursky, H., & Tucker, W. 1971, *Nature*, 231, 437
- Cen, R. & Ostriker, J. P. 1999, *ApJ*, 514, 1
- Chieffi, A. & Straniero, O. 1989, *ApJS*, 71, 47
- Cooke, B. A., Ricketts, M. J., Maccacaro, T., et al. 1978, *MNRAS*, 182, 489
- Couchman, H. M. P. & Rees, M. J. 1986, *MNRAS*, 221, 53
- Cowie, L. L., Songaila, A., Kim, T.-S., & Hu, E. M. 1995, *AJ*, 109, 1522
- Davé, R., Cen, R., Ostriker, J. P., et al. 2001, *ApJ*, 552, 473
- Davis, J. E. 2001, *ApJ*, 548, 1010
- De Grandi, S. & Molendi, S. 2001, *ApJ*, 551, 153
- De Grandi, S. & Molendi, S. 2002, *ApJ*, 567, 163
- De Luca, A. & Molendi, S. 2004, *A&A*, 419, 837

- De Young, D. S. 1978, *ApJ*, 223, 47
- den Herder, J. W., Brinkman, A. C., Kahn, S. M., et al. 2001, *A&A*, 365, L7
- Dickey, J. M. & Lockman, F. J. 1990, *ARA&A*, 28, 215
- Domainko, W., Mair, M., Kapferer, W., et al. 2006, *A&A*, 452, 795
- Dubinski, J. 1998, *ApJ*, 502, 141
- Dupke, R. A. & Arnaud, K. A. 2001, *ApJ*, 548, 141
- Edge, A. C. 2001, *MNRAS*, 328, 762
- Edge, A. C. & Stewart, G. C. 1991, *MNRAS*, 252, 414
- Ellison, S. L., Songaila, A., Schaye, J., & Pettini, M. 2000, *AJ*, 120, 1175
- Enßlin, T. A., Lieu, R., & Biermann, P. L. 1999, *A&A*, 344, 409
- Ettori, S., De Grandi, S., & Molendi, S. 2002, *A&A*, 391, 841
- Fabian, A. C. 1994, *ARA&A*, 32, 277
- Fabian, A. C., Sanders, J. S., Taylor, G. B., et al. 2006, *MNRAS*, 366, 417
- Finoguenov, A., Arnaud, M., & David, L. P. 2001, *ApJ*, 555, 191
- Finoguenov, A., Briel, U. G., & Henry, J. P. 2003, *A&A*, 410, 777
- Finoguenov, A., David, L. P., & Ponman, T. J. 2000, *ApJ*, 544, 188
- Fukazawa, Y., Makishima, K., Tamura, T., et al. 2000, *MNRAS*, 313, 21
- Fukazawa, Y., Ohashi, T., Fabian, A. C., et al. 1994, *PASJ*, 46, L55
- Fusco-Femiano, R., Dal Fiume, D., De Grandi, S., et al. 2000, *ApJ*, 534, L7
- Fusco-Femiano, R., dal Fiume, D., Feretti, L., et al. 1999, *ApJ*, 513, L21
- Fusco-Femiano, R., Landi, R., & Orlandini, M. 2005, *ApJ*, 624, L69
- Fusco-Femiano, R., Orlandini, M., Brunetti, G., et al. 2004, *ApJ*, 602, L73
- Gastaldello, F. & Molendi, S. 2004, in *Proceedings of The Riddle of Cooling Flows in Galaxies and Clusters of Galaxies*, held in Charlottesville, VA, May 31 - June 4, 2003, Eds. T. Reiprich, J. Kempner, and N. Soker. Published electronically at <http://www.astro.virginia.edu/coolflow/>
- Giacconi, R., Murray, S., Gursky, H., et al. 1972, *ApJ*, 178, 281
- Gibson, B. K., Loewenstein, M., & Mushotzky, R. F. 1997, *MNRAS*, 290, 623
- González-Riestra, R. 2004, <http://xmm.vilspa.esa.es/docs/documents/CAL-TN-0058-1-0.ps.gz>
- Greggio, L. & Renzini, A. 1983, *A&A*, 118, 217
- Grevesse, N. & Sauval, A. J. 1998, *Space Science Reviews*, 85, 161
- Gunn, J. E. & Gott, J. R. I. 1972, *ApJ*, 176, 1
- Hansen, L., Jørgensen, H. E., Nørgaard-Nielsen, H. U., et al. 2000, *A&A*, 356, 83
- Heger, A. & Woosley, S. E. 2002, *ApJ*, 567, 532
- Hwang, C. 1997, *Science*, 278, 1917
- Irwin, J. A. & Sarazin, C. L. 1995, *ApJ*, 455, 497
- Iwamoto, K., Brachwitz, F., Nomoto, K., et al. 1999, *ApJS*, 125, 439
- Jansen, F., Lumb, D., Altieri, B., et al. 2001, *A&A*, 365, L1
- Johnstone, R. M., Allen, S. W., Fabian, A. C., & Sanders, J. S. 2002, *MNRAS*, 336, 299
- Johnstone, R. M., Fabian, A. C., Edge, A. C., & Thomas, P. A. 1992, *MNRAS*, 255, 431
- Kaastra, J. S., Ferrigno, C., Tamura, T., et al. 2001, *A&A*, 365, L99
- Kaastra, J. S., Lieu, R., Tamura, T., Paerels, F. B. S., & den Herder, J. W. 2003a, *A&A*, 397, 445
- Kaastra, J. S., Mewe, R., & Nieuwenhuijzen, H. 1996, in *UV and X-ray Spectroscopy*

- of Astrophysical and Laboratory Plasmas : Proceedings of the Eleventh Colloquium on UV and X-ray ... held on May 29-June 2, 1995, Nagoya, Japan. Edited by K. Yamashita and T. Watanabe. Tokyo : Universal Academy Press, 1996. (Frontiers science series ; no. 15)., p.411, 411
- Kaastra, J. S., Mewe, R., & Raassen, A. A. J. 2003b, in *New Visions of the X-ray Universe in the XMM-Newton and Chandra Era*, ed. F. A. Jansen, Vol. in press (ESA)
- Kaastra, J. S., Tamura, T., Peterson, J. R., et al. 2004, *A&A*, 413, 415
- Kapferer, W., Ferrari, C., Domainko, W., et al. 2006, *A&A*, 447, 827
- Katayama, H., Takahashi, I., Ikebe, Y., Matsushita, K., & Freyberg, M. J. 2004, *A&A*, 414, 767
- Kawara, K., Murayama, T., Taniguchi, Y., & Arimoto, N. 1996, *ApJ*, 470, L85+
- Kellogg, E., Gursky, H., Leong, C., et al. 1971, *ApJ*, 165, L49+
- Kellogg, E. M. 1973, in *IAU Symp. 55: X- and Gamma-Ray Astronomy*, ed. H. Bradt & R. Giacconi, 171–+
- Kikuchi, K., Furusho, T., Ezawa, H., et al. 1999, *PASJ*, 51, 301
- Kirsch, M. 2003, <http://xmm.vilspa.esa.es/docs/documents/CAL-TN-0018-2-1.pdf>
- Kirsch, M. 2006, <http://xmm.vilspa.esa.es/docs/documents/CAL-TN-0018.pdf>
- Kroupa, P. 2002, *Science*, 295, 82
- Kuntz, K. D. & Snowden, S. L. 2000, *ApJ*, 543, 195
- Lieu, R., Mittaz, J. P. D., Bowyer, S., et al. 1996, *ApJ*, 458, L5
- Lodders, K. 2003, *ApJ*, 591, 1220
- Loewenstein, M. 2001, *ApJ*, 557, 573
- Loewenstein, M. 2004, in *Origin and Evolution of the Elements*, ed. A. McWilliam & M. Rauch, 422–+
- Loewenstein, M. 2006, *ApJ*, 648, 230
- Lumb, D. H., Warwick, R. S., Page, M., & De Luca, A. 2002, *A&A*, 389, 93
- Maia, M. A. G., da Costa, L. N., Willmer, C., Pellegrini, P. S., & Rite, C. 1987, *AJ*, 93, 546
- Mannucci, F., Della Valle, M., & Panagia, N. 2006, *MNRAS*, 370, 773
- Maoz, D. & Gal-Yam, A. 2004, *MNRAS*, 347, 951
- Markevitch, M., Forman, W. R., Sarazin, C. L., & Vikhlinin, A. 1998, *ApJ*, 503, 77
- Markevitch, M., Ponman, T. J., Nulsen, P. E. J., et al. 2000, *ApJ*, 541, 542
- Matteucci, F. & Chiappini, C. 2005, *Publications of the Astronomical Society of Australia*, 22, 49
- Matteucci, F. & Recchi, S. 2001, *ApJ*, 558, 351
- Mazzotta, P., Edge, A. C., & Markevitch, M. 2003, *ApJ*, 596, 190
- Mittaz, J. P. D., Lieu, R., & Lockman, F. J. 1998, *ApJ*, 498, L17
- Molendi, S. & Gastaldello, F. 2001, *A&A*, 375, L14
- Moretti, A., Campana, S., Lazzati, D., & Tagliaferri, G. 2003, *ApJ*, 588, 696
- Nomoto, K., Tominaga, N., Umeda, H., Kobayashi, C., & Maeda, K. 2006, *Nucl. Phys. A*, in press.
- Peres, C. B., Fabian, A. C., Edge, A. C., et al. 1998, *MNRAS*, 298, 416
- Peterson, J. R., Kahn, S. M., Paerels, F. B. S., et al. 2003, *ApJ*, 590, 207
- Peterson, J. R., Paerels, F. B. S., Kaastra, J. S., et al. 2001, *A&A*, 365, L104
- Pettini, M. 2004, in *Cosmochemistry. The melting pot of the elements*, ed. C. Esteban,

- R. García López, A. Herrero, & F. Sánchez, 257–298
- Pointecouteau, E., Arnaud, M., Kaastra, J., & de Plaa, J. 2004, *A&A*, 423, 33
- Portinari, L., Moretti, A., Chiosi, C., & Sommer-Larsen, J. 2004, *ApJ*, 604, 579
- Pratt, G. W. & Arnaud, M. 2002, *A&A*, 394, 375
- Raymond, J. C. & Smith, B. W. 1977, *ApJS*, 35, 419
- Read, A. M. & Ponman, T. J. 2003, *A&A*, 409, 395
- Reiprich, T. H. & Böhringer, H. 2002, *ApJ*, 567, 716
- Renzini, A. 2004, in *Clusters of Galaxies: Probes of Cosmological Structure and Galaxy Evolution*, ed. J. S. Mulchaey, A. Dressler, & A. Oemler, 260–+
- Romanishin, W. & Hintzen, P. 1988, *ApJ*, 324, L17
- Rossetti, M. & Molendi, S. 2004, *A&A*, 414, L41
- Sérsic, J. L. 1974, *Ap&SS*, 28, 365
- Sanders, J. S. & Fabian, A. C. 2002, *MNRAS*, 331, 273
- Sanders, J. S. & Fabian, A. C. 2006, *MNRAS*, 875
- Sarazin, C. L., Baum, S. A., & O’Dea, C. P. 1995, *ApJ*, 451, 125
- Sarazin, C. L. & Lieu, R. 1998, *ApJ*, 494, L177
- Sarazin, C. L., O’Connell, R. W., & McNamara, B. R. 1992, *ApJ*, 397, L31
- Schindler, S., Kapferer, W., Domainko, W., et al. 2005, *A&A*, 435, L25
- Schwartz, D. A., Schwarz, J., & Tucker, W. 1980, *ApJ*, 238, L59
- Singh, K. P., Westergaard, N. J., & Schnopper, H. W. 1986, *ApJ*, 308, L51
- Singh, K. P., Westergaard, N. J., & Schnopper, H. W. 1988, *ApJ*, 331, 672
- Smith, R. K., Brickhouse, N. S., Liedahl, D. A., & Raymond, J. C. 2001, *ApJ*, 556, L91
- Springel, V., White, S. D. M., Jenkins, A., et al. 2005, *Nature*, 435, 629
- Stanford, S. A., Romer, A. K., Sabirli, K., et al. 2006, *ApJ*, 646, L13
- Strüder, L., Briel, U., Dennerl, K., et al. 2001, *A&A*, 365, L18
- Strolger, L.-G., Riess, A. G., Dahlen, T., et al. 2004, *ApJ*, 613, 200
- Sun, M., Jones, C., Murray, S. S., et al. 2003, *ApJ*, 587, 619
- Takahashi, S. & Yamashita, K. 2003, *PASJ*, 55, 1105
- Takei, Y., Fujimoto, R., Mitsuda, K., Futamoto, K., & Onaka, T. 2003, in *Astrophysics of Dust*
- Tamura, T., Bleeker, J. A. M., Kaastra, J. S., Ferrigno, C., & Molendi, S. 2001a, *A&A*, 379, 107
- Tamura, T. & den Herder, J. W. A. 2003,
<http://xmm.vilspa.esa.es/docs/documents/CAL-TN-0034-1-0.ps.gz>
- Tamura, T., Kaastra, J. S., den Herder, J. W. A., Bleeker, J. A. M., & Peterson, J. R. 2004, *A&A*, 420, 135
- Tamura, T., Kaastra, J. S., Peterson, J. R., et al. 2001b, *A&A*, 365, L87
- Taniguchi, Y., Arimoto, N., Murayama, T., et al. 1997, in *Quasar hosts*, edited by David L. Clements, Ismael Perez-Fournon. Berlin : Springer-Verlag, c1997 Proceedings of the ESO-IAC Conference held on Tenerife, Spain, p. 122., ed. D. L. Clements, 122–+
- Tegmark, M., Silk, J., Rees, M. J., et al. 1997, *ApJ*, 474, 1
- Tinsley, B. M. 1980, *Fundamentals of Cosmic Physics*, 5, 287
- Tsujimoto, T., Nomoto, K., Yoshii, Y., et al. 1995, *MNRAS*, 277, 945
- Turner, M. J. L., Abbey, A., Arnaud, M., et al. 2001, *A&A*, 365, L27
- van den Bergh, S., Li, W., & Filippenko, A. V. 2005, *PASP*, 117, 773

-
- Verner, D. A., Ferland, G. J., Korista, K. T., & Yakovlev, D. G. 1996, *ApJ*, 465, 487
- Weisskopf, M. C., O'Dell, S. L., Paerels, F., et al. 2004, *ApJ*, 601, 1050
- White, D. A. 2000, *MNRAS*, 312, 663
- White, D. A., Fabian, A. C., Allen, S. W., et al. 1994, *MNRAS*, 269, 589
- White, D. A., Fabian, A. C., Johnstone, R. M., Mushotzky, R. F., & Arnaud, K. A. 1991, *MNRAS*, 252, 72
- White, D. A., Jones, C., & Forman, W. 1997, *MNRAS*, 292, 419
- Woosley, S. E. & Weaver, T. A. 1995, *ApJS*, 101, 181
- Yoshii, Y., Tsujimoto, T., & Nomoto, K. 1996, *ApJ*, 462, 266
- Zabludoff, A. I., Huchra, J. P., & Geller, M. J. 1990, *ApJS*, 74, 1
- Zhang, Y.-Y., Finoguenov, A., Böhringer, H., et al. 2004, *A&A*, 413, 49
- Zwicky, F., Karpowicz, M., & Kowal, C. T. 1965, in *Catalog of Galaxies and Clusters of Galaxies* Vol. 5 (Pasadena: California Institute of Technology)

Curriculum Vitae

Ik ben op 1 december 1979 geboren in Vlissingen, maar opgegroeid in Middelburg. Halverwege de middelbare school kwam ik in aanraking met de sterrenkunde via de Volkssterrenwacht “Philippus Lansbergen” in Middelburg. Ik volgde daar eerst een basiscursus sterrenkunde en werd vervolgens al snel medewerker. Nadat ik in 1998 mijn VWO diploma haalde, ben ik aan de Universiteit Utrecht sterrenkunde gaan studeren. Ondanks dat ik in Zeist woonde, ben ik naast die studie ook bestuurslid bij de Volkssterrenwacht in Middelburg geweest van 1999 tot 2002.

Mijn afstudeeronderzoek, dat ik in oktober 2002 afrondde, deed ik bij Wim Hermsen en Lucien Kuiper op SRON. Ik analyseerde waarnemingen van de pulsar PSR 0540-69 die gedaan waren met de röntgensatelliet RXTE. De pulsar bleek verrassend veel overeen te komen met de bekende Krab-pulsar en dat leidde tot mijn eerste publicatie in het vaktijdschrift *Astronomy & Astrophysics*.

Vanaf november 2002 ben ik begonnen met mijn promotie-onderzoek op SRON, maar ditkeer in de röntgenspectroscopie-groep van Jelle Kaastra en Mariano Méndez. Dit proefschrift is een bundeling van de resultaten van het werk wat ik tussen november 2002 en februari 2007 gedaan heb.

